UNIVERSITY OF CALIFORNIA, SAN DIEGO

The Geomagnetic Field Over the Last 5 Myr From Lava Flows,

and

Properties of the Venusian Lithosphere From Magellan Data

A dissertation submitted in partial satisfaction of the requirements

for the degree Doctor of Philosophy in Earth Sciences

by

Catherine Johnson

Committee in charge:

Professor Catherine G. Constable, Co-Chair

Professor David T. Sandwell, Co-Chair

Professor John M. Goodkind

Professor Robert L. Parker

Professor Lisa Tauxe

1994

The dissertation of Catherine Johnson is approved, and it is acceptable in quality and form for publication on microfilm:

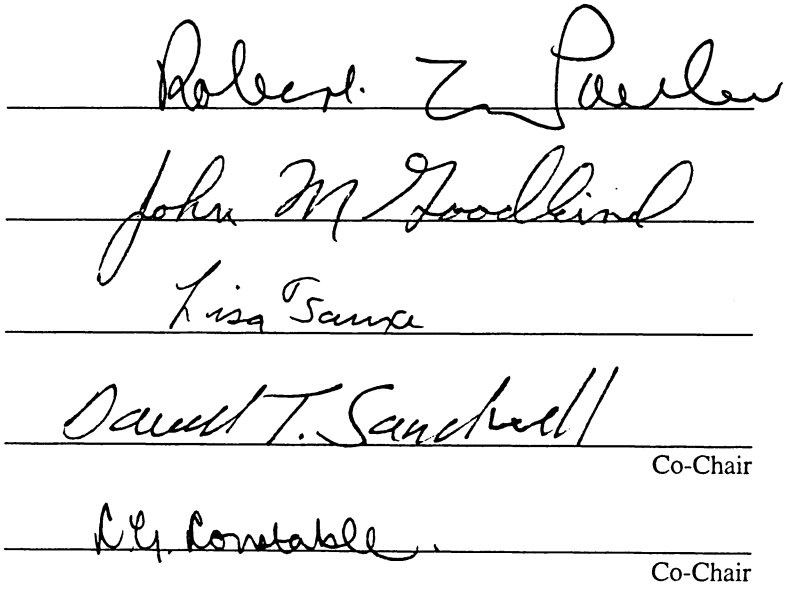

Co-Chair

Co-Chair

University of California, San Diego

1994

Table of Contents

List of Figures and Tables

Chapter 2

Chapter 3

Chapter 4

Chapter 5

Chapter 6

ACKNOWLEDGEMENTS

I would like to thank all the members of my committee for allowing me to assemble this rather strange hotpotch of topics for my thesis. In particular, I would like to thank my co-chairs, Cathy Constable and Dave Sandwell for their support and encouragement during the last 5 years. My thesis is divided into two distinct halves, and Cathy and Dave each supervised one half. There were many periods when progress was not made concurrently on the two parts and I am very grateful for the patience which Cathy and Dave had during these times! Both Cathy and Dave have always been available and willing to answer questions and provide input, and this has been much appreciated. Dave Sandwell also made sure that I did not graduate from Scripps without some sea-going experience! Bob Parker and Lisa Tauxe both povided considerable input into the first two chapters of this thesis. Lisa made sure that I understood what can and cannot be said from paleomagnetic data. In addition to his involvement in my thesis work, Bob taught three of the best classes I have ever taken.

One other IGPP faculty member deserves special mention. Guy Masters has provided constant support during my time as a graduate student, and has contributed either directly or indirectly to four chapters of this thesis. I never thought I would thank anyone for a homework problem, however Guy's spherical harmonic homework problem which was the bane of the first weeks of graduate school has been used extensively in chapters 2, 3 and 6 of my thesis. Frank Vernon kindly allowed me to use his multi-taper spectral analysis code for the resolution analysis presented in chapter 6. I would also like to thank Dan McKenzie for his advice and friendship over the past 4 years. He instigated the global study of flexural features on Venus in chapter 5 and provided helpful suggestions during the course of this work.

As in any job, there are numerous people who work behind the scenes to try to ensure that daily life progresses smoothly. I am especially grateful to Karen, Elaine, Anne, Janeyl, Yvonne and Arlene for their respective roles in dealing with administration.

Five years ago Maya Tolstoy came to the airport to pick me up and has been unable to get rid of me since then. Maya's friendship has been invaluable. Chris Small helped me debug the above-mentioned spherical harmonic code so that I could leave work and go and play instead! I am greatly indebted to Chris for his support both inside and outside of work, and for ensuring that I saw as much of the southwestern U.S. as possible while I was at Scripps. Adrienne Ertl, Denae O'Brien, and Harold and Helen Bolton have also given much-appreciated friendship during my time in San Diego. I would also like to acknowledge Lesley Normand for her friendship and support. Above all, I thank my family for their love and encouragement.

VITA

June 19th, 1967	Born, Stafford, England
1989	Bachelor of Science in Geophysics, University of Edinburgh, Scotland
1989, 1990, 1991	Exploration Geophysicist, Esso Exploration and Production, Leatherhead, England
1989 – 1994	Research Assistant, Scripps Institution of Oceanography, University of California, San Diego, La Jolla, California
1994	PhD. Earth Sciences, University of California, San Diego

PUBLICATIONS

Johnson, C. L. & C. G. Constable, 1994. The time-averaged field as recorded by lava flows over the past 5 Myr. submitted to *Geophys. J. Int.*.

Sandwell, D.T., Winterer, E.L., Mammerickx, J., Duncan, R. A., Lynch, M. A., Levitt, D. A. & C. L. Johnson, 1994. Evidence for Diffuse Extension of the Pacific Plate: No Mini Hot Spot, No Convection. submitted to *J. Geophys. Res.*.

Johnson, C. L. & C. G. Constable, 1994. Palaeosecular variation recorded by lava flows over the last 5 million years. *Philos. Trans. R. Soc. London Ser. A* , in press.

Johnson, C. L. & D. T. Sandwell, 1994. Lithospheric flexure on Venus. *Geophys. J. Int.*, in press.

Johnson, C. L. & D. T. Sandwell, 1992. Joints in venusian lava flows. *J. Geophys. Res.*, **97**, 13601–13610.

McKenzie, D., P. G. Ford, C. Johnson, B. Parsons, D. Sandwell, S. Saunders, & S. C. Solomon, 1992. Features on Venus Generated by Plate Boundary Processes. *J. Geophys. Res.*, **97**, 13533–13544.

ABSTRACTS

Johnson, C. & C. Constable, 1994. Observational Constraints on Long Term Properties of the Geomagnetic Field. *SEDI 94*, **Abstract Volume**, 109–111.

Johnson, C. L. & D. T. Sandwell, 1994. Resolution Analysis of Magellan Cycle 5 Gravity Data. *LPSC*, **XXV**, 625–626.

Johnson, C. & C. Constable, 1993. Paleosecular Variation and the Time Averaged Field: 0-5 Ma. *EOS, Trans AGU*, **74, #43**, 218.

D. Sandwell, C. Johnson, D. Levitt, M. Lynch, J. Mammerickx, C. Small, E.L. Winterer & M. Simons, 1993. Morphology of Pukapuka Volcanic Ridge System, Southeast Pacific. *EOS Trans AGU*, **74, #16**, 285.

Winterer, E. L., C. Johnson, D. Levitt, M. Lynch, J. Mammerickx, D. Sandwell, C. Small & M. Simons, 1993. Morphology of Pukapuka Volcanic Ridge System, Southeast Pacific. *EOS Trans AGU*, **74, #16**, 285.

Constable, C. & C. Johnson, 1993. Can we Observe Core-Mantle Control over Geomagnetic Reversal Paths?. *EOS Trans AGU*, **74, #16**, 51.

Johnson, C. L. & D. T. Sandwell, 1993. Estimates of Lithospheric Thickness on Venus. *LPSC*, **XXIV**, 721–722.

Johnson, C. & C. Constable, 1992. The Time Averaged Geomagnetic Field: 0-5 Ma. *EOS Trans AGU*, **73, #43**, 63.

Schubert, G., D. T. Sandwell, & C. L. Johnson, 1992. Subduction Trenches on Venus: A Global Assessment. *EOS Trans AGU*, **73, #43**, 329.

Johnson, C. L. & D. T. Sandwell, 1992. Variations in Lithospheric Thickness on Venus. *International Colloqium on Venus*, **Abstract Volume**, 51–52.

McKenzie, D., P. G. Ford, C. L. Johnson, D. T. Sandwell, B. Parsons, S. Saunders & S. C. Solomon, 1992. Features on Venus Generated by Plate Boundary Processes. *EOS Trans AGU*, **73, #14**, 304.

Johnson, C. L. & D. T. Sandwell, 1992. Flexure on Venus: Implications for Lithospheric Elastic Thickness and Strength. *LPSC*, **XXIII**, 619–620.

Johnson, C. & C. Constable, 1991. A Statistical Model for Geomagnetic Secular Variation. *EOS Trans AGU*, **72, #44**, 126.

Johnson, C. L. & D. T. Sandwell, 1991. Residual Thermal Stress: A Mechanism for Joints in Venusian Lava Flows. *LPSC*, **XXII**, 645–646.

FIELDS OF STUDY

Major Field: Geophysics

Studies in Geomagmetism and Palaeomagnetism
Professors George Backus, Catherine Constable, Robert Parker, Lisa Tauxe (IGPP/SIO, UCSD)

Studies in Potential Theory
Professors George Backus, Robert Parker, David Sandwell (IGPP, UCSD)

Studies in Inverse Theory
Professor Robert Parker (IGPP, UCSD)

Studies in Satellite Remote Sensing
Professor David Sandwell (IGPP, UCSD)

Studies in Geophysical Data Analysis
Professor Robert Parker (IGPP, UCSD)

Studies in Geodynamics
Professor David Sandwell (IGPP, UCSD)

Studies in Seismology
Professors Leroy Dorman, Freeman Gilbert, Bernard Minster, Guy Masters (IGPP/SIO, UCSD)

Studies in Solid Earth Geophysics
Professors Guy Masters, David Sandwell (IGPP, UCSD)

Studies in Marine Geophysics
Professor Leroy Dorman, John Hilderbrand (SIO, UCSD)

Studies in Exploration Geophysics
Roger Scrutton (University of Edinburgh, Scotland)

ABSTRACT OF THE DISSERTATION

The Geomagnetic Field Over the Last 5 Myr from Lava Flows

and

Properties of the Venusian Lithosphere from Magellan Data

by

Catherine Johnson

Doctor of Philosophy in Earth Sciences

University of California, San Diego, 1994

Professor Catherine G. Constable, Co-Chair

Professor David T. Sandwell, Co-Chair

The dissertation consists of two unrelated parts. Chapters 2 and 3 investigate long-term properties of the geomagnetic field. Chapters 4 – 6 are studies of Venus using data from the Magellan mission.

Chapter 2 presents a new database comprising palaeomagnetic directions from lava flows over the past 5 Myr. Existing palaeosecular variation models fail to take account of time-averaged field structure and do not adequately describe the properties of the database. In chapter 3 regularized models of the time-averaged field are constructed from Brunhes, normal and reverse polarity subsets of the new database. Non-zonal models are required to fit the data. Normal and reverse stable polarity field structures are significantly different. Normal polarity field models are similar to historical field maps; differences may be real or due to data quality and distribution. Jackknife estimates of the models suggest that data from a few sites contribute significant structure; removing these sites yields conservative estimates of the time-averaged field.

Chapter 4 presents an investigation of polygonal fracture patterns observed in radar images of volcanic plains on Venus. The patterns are similar to jointing in lava flows on Earth, but the scale of the venusian networks is much larger than their terrestrial counterparts. The venusian networks may be the result of increased heat flux to the base of the lithosphere, during the formation of flood basalt provinces.

Chapter 5 is a study of topographic flexural features on Venus. These are modeled using a thin-elastic plate model. Reliable estimates of mechanical lithospheric thickness are in the range 21 – 37 km.

Dynamical models predict a thick viscous lithosphere. Numerical simulations are used to explore the validity of a 2-D cartesian approximation to an axisymmetric load geometry.

Chapter 6 presents a preliminary resolution analysis of Magellan cycle 5 gravity data. Multi-taper spectral coherence estimates show the best resolution available from the Doppler residuals to be 450 – 500 km. Thus in some regions it should be possible to distinguish between local compensation, flexural or dynamic support of topography.

CHAPTER 1

INTRODUCTION AND ORGANIZATION OF THE THESIS

The work presented in this thesis consists of studies in two distinct fields - geomagnetism and the geophysics of Venus. The main reason for this apparently strange combination of investigations is timing. When I started my PhD the Magellan spacecraft had just been launched, and it was hoped that the Magellan mission would provide high resolution altimetry, emissivity, synthetic aperture radar and gravity data for Venus. By the time Magellan started sending back radar images and altimetry data from Venus, I was firmly entrenched in the world of geomagnetism. The success of the Magellan mission has surpassed the expectations of almost all of those who were involved in its original conception. As a result, many more possibilities for geophysical studies of Venus have arisen and so roughly half of my thesis work comprises investigations using the Magellan data. In this section I present a brief introduction to the two parts of the thesis.

PART A: The geomagnetic field over the last 5 Myr from lava flows

Observations of the Earth's magnetic field come from many different data sources. Historically, the geomagnetic field has been measured at sea, in surveys on land and also at observatories specifically dedicated to this purpose. Satellite measurements of the field, in particular those available from MAGSAT (which operated for 7 months during 1979 and 1980), have been extremely useful in producing high resolution maps of the present-day field. Magnetic directions recorded in archaeological materials also provide information on historical variations in the magnetic field. Investigations of long-term properties of the geomagnetic field rely on magnetic directions retained by geological materials - this area of study is known as palaeomagnetism. Palaeomagnetic data are available from both igneous and sedimentary rocks; however the process by which the remanent magnetization is acquired in these two rock types is different. In general, palaeomagnetic directions from lava flows provide an improved temporal resolution picture of the geomagnetic field than directions from sediments, but this is at the expense of a poorer global spatial distribution of lavas relative to sediments.

Most of the power in the geomagnetic field at the Earth's surface is due to the internally generated field – *i.e.*,that part of the field which is due to fluid motions in the (predominantly) iron liquid outer core. Additional power in the field at the surface is the result of externally generated magnetic fields – *i.e.*,those due to currents in the ionosphere and magnetosphere. Although the present-day and historical

field morphologies are quite complicated, the dominant signal in the field observed at the Earth's surface can be represented by a dipole at the center of the Earth and aligned with the rotation axis (a geocentric axial dipole). This first order description is also true of the geomagnetic field over geological timescales. One of the outstanding questions in geomagnetism concerns the nature of the second order structure in the field over these longer timescales. The nature of the time-averaged geomagnetic field over the last few million years and the variability about this average structure may at first seem a rather isolated problem, however it has implications for other areas of geophysics, notably those of mantle dynamics and plate reconstructions. Persistent longitudinal structure in the geomagnetic field (over timescales of millions of years) would not be expected from fluid motions in a spherical outer core. The characteristic timescales of convection in the lower mantle are much greater than those in the outer core. As a result, one possible explanation for such longitudinal structure in the field is that fluid flow in the top of the outer core is influenced by heterogeneities and convection in the lower mantle through core-mantle coupling. Plate motion models are based on the assumption that over time the average geomagnetic field morphology can be described by an axial geocentric dipole. Second order spatial structure in the field thus also has some implications for plate reconstructions.

Part A of the thesis is concerned with the long-term properties of the field, both in terms of the time-averaged field morphology and the statistical variations about this average field structure. One of the major problems in attempting this type of study is the availability of a self-consistent database. During the course of the studies presented here, it was realized that it was necessary to compile a palaeomagnetic database which would be suitable for all the investigations being pursued. As a result, chapter one of the thesis presents a new database comprising palaeomagnetic directions from lava flows spanning the last 5 million years. This database is suitable for use in studies of the time-averaged field and long period temporal variations (palaeosecular variation) of the field. Palaeosecular variation as recorded by the new database is discussed and previous studies reviewed. Chapter 2 presents the results of an investigation of the time-averaged field morphology, using the new database.

PART B: Properties of the venusian lithosphere from Magellan data

The second part of the thesis comprises three independent studies using data collected by the Magellan spacecraft. The studies are based on analyses of synthetic radar images (primarily chapter 3), altimetry data (primarily chapter 4) and gravity data (chapter 5).

Prior to the Magellan mission knowledge of Venus was based on data from the Mariner 2 spacecraft, Soviet Venera and Vega landers, Earth-based radiotelescopes, Soviet Venera orbiters and the U.S. Pioneer Venus orbiter. Venus is very similar in mass and density to the Earth, and the landers established that dry basaltic rocks occur at the surface. However, there are notable differences from Earth – the surface temperature on Venus is approximately 455°C, the atmosphere is predominantly carbon dioxide, the surface pressure is about 90 atmospheres, and the period of rotation of Venus is 243 Earth days. Pioneer Venus carried an altimeter, and so the topography of Venus was measured to a vertical resolution of about 200 m and a horizontal resolution of 150 km. It was discovered that most of the venusian surface lies within 1 km of the mean elevation (6051.9 km), although there are regions of high topography. Radar images available from Earth-based telescopes and the Pioneer Venus and Venerea missions showed a variety of styles of tectonic and volcanic deformation. Low resolution gravity data returned by Pioneer Venus indicated a high correlation of long wavelength gravity with topography on Venus, unlike on Earth. The aims of the Magellan mission were to collect higher resolution altimetry data, gravity data and radar images than already existed.

The studies presented in this part of the thesis were conducted in the order they are presented, which is a result of the changing data availability over the course of the last 4 years. All are based on the data collected by Magellan. Radar images and altimetry data were returned first, gravity data only became available as of September 1992. The first study (chapter 3) is an investigation of deformation patterns observed in some of the volcanic plains on Venus, and a discussion of the possible mechanisms for their production. The second study (chapter 4) comprises the bulk of the research in part B of the thesis and is an investigation of lithospheric flexure on Venus based on flexural signatures observed in the topography. Part of this study involved a numerical investigation of the circumstances in which a 2-D cartesian repesentation of a topographic load (which is assumed to be the cause of the flexural signature) is a good approximation to a 2-D axisymmetric load geometry. This is also relevant to studies of terrestrial lithopsheric flexure, as many observations of flexure come from subduction zones which are arcuate in planform, with varying planform radii of curvature. The final study of this section, and of the thesis (chapter 5) is an investigation of the maximum resolution attainable from the Magellan gravity data. This is an important question because it has implications for the possibility of investigating lithospheric thickness from combined gravity/topography studies.

CHAPTER 2

PALAEOSECULAR VARIATION RECORDED BY LAVA FLOWS OVER THE LAST 5 MYR

ABSTRACT

We present a new global palaeomagnetic database, comprising lava flows and thin intrusive bodies, suitable for studying palaeosecular variation and the time-averaged field. The database is presented in some detail in the appendix and is available on-line from the authors. We review palaeosecular variation models to date, emphasising the assumptions required and the rather arbitrary construction of many of these models. Preliminary studies of the statistical properties of the new database suggest that existing palaeosecular variation models are inadequate to explain the long-term temporal variations in the field. It is increasingly apparent that data distribution and quality are pivotal in determining the characteristics of the secular variation. The work presented here demonstrates the need for revised models of the time-averaged field structure for both normal and reverse polarities before reliable models for palaeosecular variation can be made.

INTRODUCTION

A New Database for Palaeosecular Variation Studies

Geomagnetic palaeosecular variation (PSV) describes the spatial and temporal variability of the field on time scales of $10^2 - 10^5$ years, that is long period variations of the field during stable polarity times. Long period temporal variations are controlled by the changes in the geodynamo which in turn may be controlled in part by conditions at the core-mantle boundary (CMB). PSV studies rely on remanent magnetisations retained by either archaeomagnetic materials or by sedimentary and igneous rocks, and are thus limited by the temporal and spatial distribution of data. Each of these three data sets has advantages and disadvantages. The remanence carried by archaeomagnetic materials and igneous rocks is primarily thermal in origin. It is acquired during cooling, either after firing of pottery or bricks, or after emplacement of igneous rocks. The remanence is thus acquired "instantly" on geological timescales and provides a spot recording of the geomagnetic field direction. Archaeomagnetic data span only the last 10^3 years or so and provide no information on longer period PSV. Igneous rocks provide secular variation information spanning periods of up to millions of years, but the data distribution is determined by the occurrence of volcanism and the present day accessibility of the lava flows. Sedimentary rocks have the advantage that a fairly continuous record of PSV can be obtained from specific locations if sedimentation has continued over a long period of time. The main disadvantages of sedimentary records are the temporal smoothing inherent in the remanence acquisition and the need for independent determinations of the sedimentation rate. Useful sedimentary records come from lakes and from the oceans, making these data expensive to acquire.

There have been many PSV studies reported over the past thirty years [see the summaries in *e.g., Merrill and McElhinny*, 1983; *McElhinny and Merrill*, 1975, and also the references for the database presented in this paper] but the data analysis methods employed fall into two broad categories. In a few cases it has been possible to examine continuous sedimentary records spanning the last 50,000 years using traditional time series analysis approaches [*e.g., Creer et al.*, 1983]. More commonly, PSV studies rely heavily on statistical approaches where the variance (dispersion) in the field is quantified in some way. The two most commonly used descriptions of PSV are the angular dispersion in the field directions or the angular dispersion in the virtual geomagnetic pole (VGP) positions. A VGP is computed assuming that the instantaneous field directions are due to a geocentric dipole.

In this paper we present an updated database, spanning the time interval 0 – 5 Ma, suitable for

both studies of palaeosecular variation from lavas (PSVL) and time-averaged field modeling. We review previous PSV models and their shortcomings to place this database in context with previous work. We discuss briefly the time-averaged field problem and the need for improved estimates of the timescales for secular variation. Selection criteria for the new database are reported - the resulting database differs significantly from others used in PSVL work owing to these stringent selection criteria. A summary of the data is given in the appendix with a brief outline of each contributing study and stereographic plots of VGP positions divided according to geographical region. The distributions of VGP latitudes and longitudes are reported, together with a discussion of the relative contributions of normal and reverse polarity data. The data distributions are compared with the predictions of recent statistical models [*Constable and Parker*, 1988; *Egbert*, 1992]. Angular dispersions in directions and in VGP positions have been computed for the last 5 Ma and are compared with the results from more recent studies [*McFadden et al.*, 1991, *McFadden et al.*, 1988] and with the predictions of the global statistical model [*Constable and Parker*, 1988]. We summarise the state of the art in PSV studies relating the results to the revised database.

Palaeosecular Variation Models

Over the last 3 decades several models for PSV have been proposed which attempt to account for the angular dispersion observed in sedimentary and volcanic records. Traditionally, these models have attributed secular variation to 3 sources – variations in the intensity of the dipole part of the field, variations in the direction of the dipole (dipole wobble) and variations in the non-dipole field. Later statistical descriptions of palaeosecular variation have used present day properties of the field to constrain the model; for example, *McFadden et al.* [1988] used the present day field to establish the general form of a VGP dispersion curve, whilst *Constable and Parker* [1988] used the present day power spectrum as a constraint on the palaeo-power spectrum. It is important to note that none of these models were based on any physical theory: earlier models were based on the empirical observation that most of the power in the geomagnetic field observed at the earth's surface can be accounted for by a geocentric dipolar field structure, whilst later models were based on statistical properties of the field.

Models A [*Irving and Ward*, 1964] and B [*Creer et al.*, 1959; *Creer*, 1962] considered only dipole wobble. Later models (model C [*Cox*, 1962], model D [*Cox*, 1970], model E [*Baag and Helsley*, 1974], model M [*McElhinny and Merrill*, 1975] and its modification [*Harrison*, 1980], model F [*McFadden and McElhinny*, 1984]) considered both dipole and non-dipole variations. These PSV models are defined by a set of statistical parameters describing the random variations in the non-dipole field, the dipole wobble

(typically described by assuming the VGP distribution produced by the wobble is Fisherian with a specified angular dispersion) and the intensity variations. Many of the assumptions built into these models (*e.g.*, the form of the dipole intensity variations [*Cox*, 1968]) are now known to be incorrect. Also important is the way in which the dipole wobble and non-dipole/dipole intensity parts of PSV are combined. This varies according to whether the total angular variance of the field directions or the VGPs is presumed to be Fisherian. Most studies have modeled the dispersion in VGPs rather than field directions since firstly the VGPs are generally assumed to have a more Fisherian distribution than the field directions, and secondly the VGP dispersion due to dipole wobble is latitude invariant, simplifying the analyses. Finally, correlations between the three sources of variations must be considered; *e.g.*, model F assumes the non-dipole field intensity increases with the latitudinal increase in intensity of the axial dipole field. In addition to the large number of assumptions necessary in PSV models A, B, C, D, E, M and F the distinction between dipole and non-dipole sources for PSV is purely mathematical rather than being based on physics.

Some of these concerns were recognised by *McFadden et al.* [1988] who put forward a different representation of PSV. Their model G invokes a result from dynamo theory, in which under certain conditions the solution to the magnetohydrodynamic equations results in a magnetic field consisting of 2 independent families – the dipole family and quadrupole family. If these two families are independent, the total variance in the field is the sum of the variances due to the dipole family and the quadrupole family. The general form of the dispersion in the VGPs was established using the present day field. It was found that the dispersion due to the quadrupole family was constant with latitude, whereas the dispersion due to the dipole family varied linearly with latitude up to a latitude of 70° . At the equator the contribution due to the variance from the dipole family is zero. *McFadden et al.* [1988] used this form for VGP dispersion to establish the dipole and quadrupole family contributions to SV over the last 5 Ma. *McFadden et al.* [1991] extended this study back to 195 Ma, with plate motion corrections applied to data older than 5 Ma. Although this model is appealing because of its simplicity and possible interpretation in terms of a particular class of dynamo models, it is not clear whether the assumptions on which it is based are valid.

An alternative statistical approach was presented by *Constable and Parker* [1988], who considered the present day spatial geomagnetic power spectrum to be a realisation of a white noise process near the CMB. Their description of PSV relies on the spherical harmonic representation of the geomagnetic field, and allows the statistical variation in any palaeomagnetic data type to be predicted. In the *Constable and Parker* model all the non-dipole spherical harmonic coefficients (except for the axial quadrupole) of a given degree are identically, independently distributed zero mean Gaussian variables with a variance determined

by the white spectrum at the CMB. Physically this translates into temporal field variations with no average longitudinal dependence and the variance in each of the local orthogonal components of the field vector is independent of latitude. The dipole terms in the model have a lower variance than predicted using the spectrum at the CMB, and the axial dipole term has an expected magnitude specified by its present day value. The model also includes a non-zero mean axial quadrupole, in agreement with previous studies [*e.g., Wilson*, 1971; *Creer et al.*, 1973; *Merrill and McElhinny*, 1977; *Livermore et al.*, 1983; *Schneider and Kent*, 1990].

The *Constable and Parker* model [1988] illustrates a crucial assumption involved in modeling of PSV, that of the structure of the time-averaged geomagnetic field. While it has been noted by several investigators that the time-averaged field can be approximated by an offset axial dipole, many applications of palaeomagnetism (*e.g.*, plate tectonics) rely on the assumption that over time the geomagnetic field can be described by a geocentric axial dipole (the GAD hypothesis). Most PSV studies have also assumed that the GAD hypothesis holds, so VGP dispersion is easily computed as the angular variance about the geographic pole. This assumption has been justified by the fact that small perturbations in the mean pole position have a very small effect on the calculated VGP dispersion [*McFadden et al.*, 1988]. Recent studies of reversal records [*Tric et al.*, 1991; *Clement et al.*, 1991; *Laj et al.*, 1991] have suggested that there may be structure in the geomagnetic field, other than the axial dipole and axial quadrupole terms, with a longer timescale than PSV. The findings of these studies are currently under hot debate due to uncertainties associated with the fidelity of the reversal records and the rather small number of records available [*Valet et al.*, 1992; *Langereis et al.*, 1992; *Laj et al.*, 1992; *McFadden et al.*, 1993]; however, the controversy surrounding the results is indicative of our lack of understanding of the long period temporal variations in the field. It was suggested by *Constable* [1992] that the non-zonal field structure seen in some reversal records is also observed in the palaeosecular variation record. As we shall show, the new database presented here does not support this claim, however the data do still appear to require non-zonal structure in the time-averaged field.

The most recent PSV studies [*McFadden et al.*, 1988, 1991; *McFadden and McElhinny*, 1984] have used a database comprising solely igneous rocks compiled by *Lee* [1983]. This database is a compilation of previous reported palaeomagnetic work, particularly from the 1970s, which was edited to be suitable for PSV studies. It comprises data spanning the last 195 million years. Studies of the time-averaged field have used either sedimentary data alone [*e.g., Opdyke and Henry*, 1969; *Schneider and Kent*, 1990] or combinations of sedimentary and igneous data [*e.g., Wilson*, 1971; *Merrill and McElhinny*, 1977;

Livermore et al., 1983,1984; *Merrill et al.*, 1990].

Problems with Existing PSV Models

It can be seen that PSV studies are hindered by several factors, not least of all the current palaeomagnetic data distribution and our own preconceived notions concerning the behaviour of the geomagnetic field both temporally and spatially. We have noted that several models are based on the rather arbitrary separation of the field into dipole and non-dipole parts. Another model considers the secular variation to be due to two (assumed) independent sources – the dipole and quadrupole families. The majority of PSV studies have used VGP positions as the palaeomagnetic observable. Intuitively this seems reasonable as the major component of the field at the Earth's surface is the dipole term and for a dipolar field it is simpler to think in terms of the VGP positions rather than the field directions. However, the VGP representation is also potentially confusing, especially for complex field structures, since the transformation between field directions and VGP positions is non-linear. PSV dispersion analyses to date have assumed symmetry about the equator, even though this is not true for the present day field and we will show that this assumption does not hold for PSV data over the last 5 Ma. Dispersion calculations require some knowledge of the time-averaged field structure, and although it is generally accepted that the time-averaged field cannot be adequately described by an axial dipole term alone, the GAD hypothesis is still used in PSV studies. References to the time-averaged field in the palaeomagnetic literature are often confusing, as the definition of "time-averaged" is usually not rigorous, and varies from one study to another. In this paper we use the term "time-averaged" to mean the average field direction at a particular site over a given time interval, that is $\langle \hat{B} \rangle = \int_{t_1}^{t_2} \hat{B}\, dt \,/\, (t_2 - t_1)$. ($\hat{B}$ is the unit vector in the direction of the magnetic field at a given location.) The evaluation of $\langle \hat{B} \rangle$ at a particular site would be quite straight forward if we knew t_1 and t_2 and we had a good temporal distribution of data over this time interval. However, as noted at the beginning of this paper, palaeomagnetic studies rely on data which is unevenly distributed in time and space, and so the estimation of $\langle \hat{B} \rangle$ is a statistical problem. We assume that if we can make an estimate of the time interval, $t_2 - t_1$, (discussion of this issue below), and if we have a sufficient temporal distribution of data (see criteria 7-9 of section 2a) over this time interval, then we can approximate $\langle \hat{B} \rangle$ by the average field direction computed from our finite set of palaeomagnetic directions. Obviously, this assumption can lead to problems if the data do not adequately sample the palaeosecular variation of the field over the time interval used for averaging. Another problem is that this uneven temporal sampling differs from one location to another, and so our estimates of $\langle \hat{B} \rangle$ may be of variable reliability. This issue can be addressed somewhat by careful data selection during the compilation phase, and by careful assignment of uncertainties to the

estimated mean directions. We discuss this later in the context of the database presented here.

One problem encountered when we attempt to describe the time-averaged field is that we do not have a good estimate for characteristic timescales of secular variation, and hence it is not clear over what time period we need to examine the geomagnetic field to obtain a reliable average field model. In other words, we do not know what t_1 and t_2 are in our definition of time-averaged. Ideally, we would like to have a mathematical description for PSV based on physics, this model being supported by the available data. Characteristic timescales of this model would provide a theoretical, rather than empirical basis for establishing time windows over which we could obtain an estimate of the average field configuration, given sufficient high quality data. Unfortunately, to date only empirical estimates for such characteristic timescales are available, and often these estimates are based on few data. Conservative bounds on PSV timescales can be obtained by looking at individual PSV records; *e.g.*, , a power spectral analysis [*Barton*, 1983] of observatory, archaeomagnetic and sedimentary PSV data gave a broad peak in the spectrum over periods of $10^3 - 10^4$ years. Although some of the results of this analysis are artefacts due to the wide variety of variable quality data used, the presence of the broad peak in the spectrum is supported by individual lake sediment records. For example lake sediment records from Australia [*Barton and McElhinny*, 1981] and Great Britain [*Thompson and Turner*, 1979] suggest that periods of at least a few thousand years are necessary to obtain an estimate of the average field at these locations. These results provide some constraints on the minimum period necessary to average out PSV; an upper limit on this time period is suggested by the database presented here. Statistical testing suggests that the Brunhes (0 – 0.78 Ma) and the remaining normal polarity data (0.78 – 5.0 Ma) do not exhibit statistically significant different average field properties (Kolmogorov-Smirnov test, [*Kendall and Stuart*, 1979]). Details of the application of this test to the new database are presented in another paper, specifically concerning the question of the time-averaged field structure [*Johnson and Constable*, 1994]. The important result for our purposes here is that we can place conservative bounds of 1,000 – 780,000 years on the time period which should be sampled to obtain a good estimate of PSV and the time-averaged field.

Figure 1 illustrates at least two of the concerns mentioned above. Both the upper and lower figures show the VGP dispersion for the palaeosecular variation from lavas (PSVL) data used by *McFadden et al.* [1988, 1991] and the best fit model (model G) to the data with 95% confidence limits. All VGP positions are mapped into the northern hemisphere and the dispersion is averaged in latitude bands as described in *McFadden et al.* [1991]. The GAD hypothesis was assumed and so VGP dispersion was calculated about the geographic pole. The upper figure also shows the latitudinally averaged VGP dispersion for the

new database presented in this paper, where the dispersion is calculated about the geographic pole. In the lower figure the dispersion for the new database is calculated about the mean pole position for each group of data as a crude way of estimating dispersion when the time-averaged field is not the GAD. This figure illustrates the importance of the data coverage in PSV studies and the effect of the time-averaged field we assume in the study.

DATABASE

Selection Criteria

The database presented in this paper contains palaeomagnetic directions tabulated in refereed journals and which satisfy the following criteria: (1) only extrusives and thin intrusives (*i.e.*,thin dikes) were used; (2) the individual magnetically cleaned flow directions must be published; (3) the reference from which the data are taken was published during the period 1965 – 1992; (4) at least 3 samples per flow were taken in the field; (5) the VGP latitude corresponding to each field direction must be at least 55° in magnitude; (6) the estimate of the precision parameter must be greater than 30 for directions to be accepted as significant; (7) there is sufficient information in the reference to establish temporal independence of the flows; (8) temporal sampling from a given location must span at least 10,000 years; (9) require at least 5 flows satisfying criteria (1) – (8) at any given location.

Extrusives and thin intrusives are required to ensure that the thermal remanence was acquired instantly on geological timescales, and the individual magnetically cleaned (to remove overprinting) flow data must be published to obtain an estimate of the statistics of the temporal variation of the field at a given location. Data published prior to 1965 were not included on the grounds that laboratory methods, specifically the magnetic cleaning of samples, were less advanced and these data may be unreliable.

In any PSV study it is necessary to be able to estimate field and experimental uncertainties, so we required at least 3 cores per flow to have been taken. Typically 2 – 8 cores per flow are taken during palaeomagnetic field work. Some studies have attempted to estimate the minimum number of samples required to average out field measurement uncertainties *e.g., Ellwood et al.* [1973] estimated that the largest number of samples per flow required to obtain a reliable mean direction was four. We found that a high percentage of flows where only 2 samples were taken did not meet other selection criteria such as the VGP latitude cut-off, and so we decided to exclude all 2 samples per flow data.

Low VGP latitudes may indicate unusual secular variation, but are also associated with excursions

and reversals which are not considered part of the normal secular variation record. PSV studies generally assume a cut-off VGP latitude of between 45° and 60°; we used a value of 55° and flows with field directions corresponding to VGP latitudes less than this were excluded from the database. Often, one or two low latitude VGP data are reported from a series of flows which otherwise have palaeodirections associated with high latitude VGPs. These low latitude VGPs are usually the result of field or laboratory measurement errors, rather than being indicative of either a field excursion or anomalously high secular variation. In such cases we found that VGP latitude data in the range 45° – 55° often failed other selection criteria. On the other hand, several low latitude VGPs from one site may indicate high secular variation or an excursion. We used a VGP cut-off of 55° in order to try to ensure that estimates of secular variation from this database would be conservative rather than anomalously high due to the inclusion of excursion data. Previous secular variation models have suggested that VGP dispersion at high latitude sites can be as large as 20° – 25°, thus our choice of a 55° cut-off for VGP latitude is intended to include normal secular variation data from high latitudes.

The Fisherian precision parameter provides information on whether a given set of directions are statistically different from a random population, a precision parameter of zero indicating a completely random population. Thus for each flow we would expect the set of directional measurements, corresponding to the cores from that flow, to have a high precision parameter, assuming correct orientation of the samples and reliable laboratory techniques. Choosing a cut-off value for the precision parameter is somewhat ad hoc - we used a value of 30, with a few exceptions where many records counteracted the lower quality of some of the contributing data. Obviously, reliable estimates of secular variation require sufficient data spanning the longest timescales of the variation and criteria (7) – (9) represent an attempt to ensure adequate sampling. Of all the criteria, (7) and (8) are the most difficult to enforce as they are subjective and dependent on age dating of the flows and/or good geological descriptions of the study areas in the original reference.

Data Sources

The data sources used to obtain the references for this compilation were the *Lee* database [1983], the Global Paleomagnetic Database (GPMDB) [*Lock and McElhinny*, 1991], and additional library search by the authors for post-1988 data. The final data set comprises 2187 records from 104 distinct locations – 1528 normal polarity records and 659 reverse polarity records. Of the 2187 records only 1272 were taken from the original *Lee* database, which comprises 2244 records in its original form. The severe editing of

the *Lee* database was largely a result of the presence of many records (323) consisting of fewer than 3 samples per flow. After consulting the original references we also decided that in some cases there was insufficient information to determine whether the flows sampled were temporally independent or whether they covered a sufficiently long time span to provide a good estimate of secular variation. A few records in the *Lee* database had VGPs with latitudes less than 55°, others had values of the precision parameter which we considered unacceptably low, or the precision parameter could not be estimated. 729 records were added from references in the GPMDB but not in the *Lee* database. Another 186 records were added which were not referenced in either the *Lee* database or the GPMDB. Relevant details of the individual studies contributing to the database are given in the appendix. The study locations are shown in figure 2.

Local Properties of the Database

Prior to considering global properties of the palaeofield and PSV we mention some local properties of the field observed in the new database. Mean declinations, inclinations, VGP positions and the associated 95% confidence cones [*Fisher*, 1953] are given in table 1 for the normal and reverse polarity data separately. Note that these VGP positions, with their 95% confidence cones are plotted in the figures in the appendix. First, we observe that all but 10 of the data groups have 95% confidence cones of less than 10°, and 8 of these 10 locations have less than 10 flows contributing to the estimate of the mean direction. Based on the selection criteria we had no reason for excluding these sites with rather poorly constrained mean directions: it is important to note that other sites with less than 10 flows do have a well-constrained mean direction. However, these sites are noted here as a reminder that they should be considered carefully in any global analyses. Second, we note that the 95% confidence cones about the mean direction are in most cases much less than our estimates for secular variation (described in the next section). This is important because it implies that our secular variation estimates should be reasonably robust with respect to the mean direction at a given location. Third, we can see from table 1 that there are some large differences (10° – 15°) in the mean directions calculated for neighbouring sites. In most of these cases the 95% confidence cones about the mean directions intersect. In a few cases neighbouring mean directions do appear to be significantly different and this may indicate that the palaeomagnetic sampling at one or both sites is insufficient (in a temporal sense) to obtain a reliable estimate of PSV and the mean field direction at that location. Again, these cases should be treated with care in global analyses.

Availability

The database itself is available on-line, subdivided according to geographical region and normal or reverse polarity. A "README" file provides file format details. The data can be obtained from the authors by anonymous ftp as follows:

% ftp 132.239.154.12

% login: anonymous

% password: username@usermachine

> cd pub/pmag5

> mget *

> quit

PALAEOSECULAR VARIATION

Previous PSV models and the data used in these models were discussed in the introduction. Several concerns were raised which fall into four main categories: data distribution, quality control of data, the structure of the time-averaged field and problems associated with using VGP positions. In this section we review various statistical properties of the revised database, especially those which highlight one or more of the four major concerns outlined above. We compare properties of the database with the *Constable and Parker* [1988] model as it is the most recent global PSV model and is constructed in a manner which allows us to distinguish between the effect of long-period bias and temporal variability in the data. This section presents some global properties of the database, as opposed to local features described in the previous section.

Data Distributions

VGP latitude and longitude distributions for the revised data set are given in Figures 3 and 4 together with the smoothed predictions of the *Constable and Parker* [1988] model at the database site locations. Reverse polarity VGP positions are mapped into the antipodal pole position.

The *Constable and Parker* [1988] model fits the general shape of the combined polarity VGP latitude distribution (Figure 3), with the exception of the low latitude VGP data. The fit of the model to the normal polarity data alone is similar, but the model does not predict even the general shape of the reverse polarity data distribution: the mode for the model is about 5° greater than for the data, the variance in the model

distribution is too low and the low latitude VGPs in the data distribution are not modeled. The main signal common to all the VGP latitude distributions is the location of the mode at around 80° latitude. As discussed earlier several previous studies have suggested that the time-averaged geomagnetic field has a non-zero mean axial quadrupole component, causing a "far-sided" effect in VGP locations (the VGP plots on the other side of the geographic pole from the site location). Obviously, VGP latitude distributions alone cannot distinguish between a "far-sided" and a "near-sided" effect; however, the distributions in Figure 3 coupled with Figure 4 and the VGP stereo plots shown in the appendix do indicate that the strongest signal in the time-averaged field is the "far-sided" effect. Figure 3 also suggests that there may be differences between the average field during normal and reverse polarities. Such a difference has been suggested by other workers, but using other datasets, *e.g., Schneider and Kent* [1990] proposed different average field configurations for normal and reverse fields based only on inclination data from deep sea cores. Direct comparisons between such studies are difficult since different datasets have different abilities to resolve temporal and spatial structure in the field.

Differences between the normal and reverse polarity data are also seen in the VGP longitude distributions (Figure 4). The combined polarity distribution shows peaks at longitudes of 70° and 125° and a trough at 150° but is otherwise fairly homogeneous with longitude. The peak at 70° is due to both reverse and normal polarity data, that at 125° is due primarily to the normal polarity data. It is evident that the *Constable and Parker* model [1988] predicts the general shape of the longitude distributions, but is unable to predict the amplitude of the distribution peaks. We attribute part of this discrepancy in the VGP longitude distributions to having insufficient data from a statistical sampling standpoint. The VGP latitude distributions (Figure 3) are mapped onto a 35° interval, whereas the VGP longitude distributions (Figure 4) span 360°. This effect is particularly noticeable in the model predictions. The model distributions for VGP latitudes are much smoother than those for the VGP longitudes indicating that the current data distribution is still not ideal for investigating longitudinal spatial field variations. The general homogeneity seen in the VGP longitude distribution for normal and reverse polarity data combined is in general agreement with that obtained by *Quidelleur et al.* [in press] in an independent revision of the *Lee* database, although their final database differs from that presented here because of the different selection criteria used. The distribution of VGP longitudes for both this new revised database and that of *Quidelleur et al.* is significantly different from that reported by *Constable* [1992]. Implications of this are discussed briefly in the summary section of this paper and in a separate paper concerning the structure of the time-averaged field [*Johnson and Constable*,1994]. For now, it suffices to say that the difference between the VGP longitudes obtained

from this database and those reported by *Constable* [1992], plus the statistical sampling considerations mentioned, emphasise the importance of a reasonable data distribution and the importance of consistent quality control on data to be used for PSV studies.

Figure 4 also shows VGP longitudes for normal and reverse polarities combined, plotted relative to their site longitudes. This type of plot is often referred to as a "common site longitude" plot and is a crude attempt to remove the effect of uneven sampling. The predominant feature of this plot in Figure 4 is that VGP longitudes generally lie at least 90° away from the site longitude. VGP positions having a latitude less than 90° and a VGP longitude 180° away from the site longitude are pure "far-sided" VGPs. The database presented here demonstrates this "far-sided" effect, although the strength of the signal appears to vary on a regional basis (see appendix), and there are more near-sided VGPs than predicted by the *Constable and Parker* [1988] model.

Egbert [1992] showed that the VGP longitude distribution is related solely to the secular variation for the non-axial-dipole part of the field and that there is a tendency for VGP longitudes to be biased 90° away from the sampling site for rotationally symmetric (homogeneous or isotropic) field models. The magnitude of this bias depends upon the field model, specifically upon the ratio of the variance in the vertical field to the variance in the horizontal field. This ratio is referred to as κ^2. For homogeneous field models this parameter falls in the range $2 < \kappa^2 \leq 4$, where κ^2 is equal to 4 for a purely dipolar model and κ^2 tends to 2 for fields dominated by short wavelength features. The *Constable and Parker* [1988] model has a value for κ^2 of 3.2. The tendency of VGP longitudes to be 90° away from the site longitudes is least (flat VGP longitude distribution) for $\kappa^2 = 4$ and increases as κ^2 decreases. Important in palaeomagnetic work is the effect of measurement uncertainty on the study in hand. Measurement error can be modeled as isotropic noise where the vertical and horizontal variances in the field are equal, *i.e.*, $\kappa^2 = 1$. This produces the greatest bias in VGP longitude distributions. Figure 5 shows the results of these different models, where the model VGP longitude distributions are calculated for the site distribution in the new database. We can see qualitatively that the incorporation of isotropic measurement noise ($\kappa^2 = 1$) into a given field model could produce substantial variations in the VGP longitude distributions. The presence of such isotropic noise could be one reason why the common-site longitude plot in Figure 4 does not exhibit a pure "far-sided" effect. The difference between the distributions predicted by the *Constable and Parker* model [1988] for 2 time-averaged field structures (with and without an axial quadrupole term) demonstrates that knowledge of the time- averaged field structure and reliability of the palaeomagnetic measurements are critical in PSV studies. We note here that non linear least squares fits for a time-averaged

field structure (up to spherical harmonic degree 10) to the palaeodirections presented in this paper yield spatially complex field models [*Johnson and Constable*, 1994]. In such models the magnitudes of some of the higher degree and order spherical harmonic coefficients are comparable to the magnitudes of low degree coefficients such as the axial quadrupole and octopule terms. In contrast, inversions for a spatially smooth time-averaged field model suggest that the predominant non-axial-dipole signal in the current database is the axial quadrupole term, although there is still evidence for other non-dipole terms [*Gubbins and Kelly*, 1993; *Johnson and Constable*, 1994].

Calculation of Dispersion

Traditionally the measure of secular variation which has been modeled is the angular dispersion in either the field directions or the VGP positions. First it is necessary to define some terminology. Suppose we sample a series of N temporally independent lava flows at a given location. From each flow we take n_i palaeomagnetic samples and calculate a mean field direction for that flow. We thus have N pairs of measurements of declination (D) and inclination (I) at a given location. We can now investigate the secular variation record retained by this series of flows as follows. The total angular variance (dispersion) in the field directions and VGPs respectively are given by

$$s_t{}^2 = \frac{1}{N-1}\sum_{i=1}^{N}\delta_i{}^2 \tag{1}$$

$$S_t{}^2 = \frac{1}{N-1}\sum_{i=1}^{N}\Delta_i{}^2 \tag{2}$$

δ_i is the angle between the direction vector from the ith flow and the time-averaged mean direction vector at our study location. Δ_i is the corresponding angle between the ith VGP position and the time-averaged mean pole. Immediately apparent is the necessity for a time-averaged field model before secular variation can be modeled. As explained in the introduction, PSV studies have generally assumed that the geocentric axial dipole (GAD) describes the time-averaged field. Hence the mean VGP position to be used in calculating Δ_i in (2) conveniently corresponds to the geographic north pole. The mean field direction to be used in calculating δ_i in (1) is the field direction at the ith location which would be produced by a GAD field.

The dispersion obtained by calculating (1) or (2) cannot be directly compared with that predicted

by secular variation models. The total field dispersion is made up of two components, the within-site dispersion (due to experimental uncertainty) and the true field dispersion known as the between-site dispersion. Thus (1) and (2) can also be written

$$s_t{}^2 = s_b{}^2 + \frac{s_w{}^2}{n} \tag{3}$$

$$S_t{}^2 = S_b{}^2 + \frac{S_w{}^2}{n} \tag{4}$$

where n is the average number of samples per site (flow) and $s_w{}^2$ and $S_w{}^2$ are respectively the average within-site dispersion in field directions and VGPs at this location, that is

$$n = \frac{1}{N}\sum_{i=1}^{N} n_i \tag{5}$$

$$s_w{}^2 = \frac{1}{N}\sum_{i=1}^{N} s_{w_i}{}^2 \tag{6}$$

$$S_w{}^2 = \frac{1}{N}\sum_{i=1}^{N} S_{w_i}{}^2 \tag{7}$$

The within-site dispersion can be estimated using Fisher statistics, where the Fisher distribution is the spherical analogue of the Gaussian distribution [*Fisher*, 1953]. This is justifiable in that it is reasonable to assume some isotropy in the distribution of measurement error. We quote the result without proof [*Cox*, 1970]: for the directional data the within-site dispersion for the ith flow can be calculated using

$$s_{w_i}{}^2 = \frac{6561}{k_i} \tag{8}$$

where the best estimate of k_i (the precision parameter) is

$$k_i = \frac{n_i - 1}{n_i - R_i} \tag{9}$$

R_i is the magnitude of the vector resultant of the n_i individual sample direction vectors from the ith lava flow. Hence the average within-site dispersion in the directions can be calculated and the true field dispersion at the particular study location obtained. In theory the same approach can be used to obtain S_{w_i} and hence S_w (average within-site scatter) for VGP positions; however in practice this is not usually possible as the VGP equivalent of R_i is not recorded in most published palaeomagnetic studies. Sometimes an average value for S_w is recorded: typically the value is in the range 7° – 13° [*McElhinny and Merrill*, 1975]. Where there is no recorded value investigators sometimes estimate a rough figure. *Cox* [1970] derived expressions which could be used to transform dispersion in directions into dispersion in VGPs, with either the directional data or VGPs assumed to be samples from a Fisherian distribution. This transformation approach is sometimes used to obtain an estimate of the VGP within-site dispersion from the within-site dispersion in the directions. This is not entirely satisfactory as the expressions of *Cox* [1970] require the Fisherian distribution to have a very small variance – a criterion which is not always met. Fortunately, in most studies for which a reasonable estimate of the within-site variance in the VGPs is available, the difference between the total scatter, S_t, and the between-site scatter, S_b, is small (usually less than about 1°). As a result of this and in order to minimise the number of assumptions made we use the total scatter S_t when discussing VGP dispersion. For the directional data we have direct estimates of both s_w and s_t and so we can calculate s_b. This discussion illustrates one advantage of using directional data rather than VGP positions to model secular variation.

So far we have considered the secular variation record at only one location. For comparison with previous studies we plot dispersion (in the directions and the VGPs) as a function of latitude. Dispersion values are averaged in latitude bands. Suppose there are N_λ study locations in a given latitude band. The band-averaged dispersion is calculated as a weighted mean dispersion from the N_λ locations, where the weights are the number of flows at each location [*McFadden et al.*, 1991]. The average dispersion is plotted at the weighted mean latitude for that band.

Dispersion Results

Figures 6 and 7 show the raw dispersion results for directional data and VGP positions respectively, *i.e.*,the dispersion calculated for each data group in Table (A1). The corresponding band-averaged dispersion results are shown in Figures 8 and 9, where the mean dispersion for each latitude band is plotted at the mean latitude. It should be remembered that the true scatter in the field, s_b, is plotted for the directional data, whereas the total scatter, S_t, is plotted for the VGP positions. The results for the revised dataset are

compared with predictions made from the *Constable and Parker* [1988] model.

The raw dispersion in the directions for the data (Figure 6, lower) shows considerable scatter. A general trend of decreasing dispersion with increasing latitude is evident, although the raw data indicate that this trend is poorly constrained at both high and low latitudes. The lack of data at high southern latitudes with the exception of two points from Antarctica means that secular variation in the southern hemisphere is only resonably constrained as far as about 50°S. The northernmost latitude data is from Iceland (Figure 2) and the large quantity of data of varying age from this location (see appendix) provides a good estimate of secular variation. The low latitude southern hemisphere data shows considerable scatter in the estimates of dispersion. Asymmetry between the northern and southern hemispheres can be seen in both the dispersion in the data and the dispersion predicted at the site locations by the *Constable and Parker* [1988] model. Dispersion results for the normal polarity data alone are very similar to the combined polarity results; those for the reverse polarity show the same general trend, although the data distribution for the reverse data is more restricted. At this stage it would be premature to discuss the details of differences in PSV recorded by normal and reverse polarity data due to the fact that thereare roughly twice as many normal data as reverse, and the fact that the time-averaged field may be different for the two polarities.

In contrast to the behaviour of the direction data, the dispersion in the VGPs predicted by the *Constable and Parker* [1988] model is almost uniform with latitude (Figure 7, upper). This is purely a result of the VGP transformation but is important as any small latitudinal signal in the VGP dispersion may be masked by noise. The VGP dispersion calculated from the data shows a trend of increasing dispersion with increasing latitude, the signal being stronger in the northern hemisphere than the southern hemisphere. If real, this trend demonstrates that the *Constable and Parker* [1988] model is inadequate. The dispersion in the data is calculated about both the axial dipole and the mean pole (where the mean pole is calculated separately for each group of data). Using the mean pole obviously produces a lower value for the dispersion at each location than using the axial dipole, and provides a minimum estimate of the total dispersion for each group of data. As we have not taken into account within-site dispersion in calculating VGP scatter, our S_t values will be slight overestimates of the true VGP dispersion. Some asymmetry in the VGP scatter between the two hemispheres can be seen.

The dispersions averaged in latitude bands illustrate the N-S hemisphere asymmetry more clearly, for both the directions (Figure 8) and the VGPs (Figure 9). The latitudinal variation in dispersion is greater for the direction data than for the VGPs: this observation coupled with the problems in accounting for

within-site scatter in estimating VGP dispersion strongly implies that it is advisable to model dispersion in field directions rather than VGP dispersion. Neither the dispersion in the directions or in the VGPs is modeled very well by the *Constable and Parker* [1988] model, although the fit to the directional data appears to be slightly better than to the VGPs.

Earlier we noted that the addition of an isotropic noise component (*e.g.,* uncertainties in the orientation of samples) to a particular field model could produce substantial variations in the expected VGP longitude distributions for a given data distribution. We investigated the effect of incorporating orientation uncertainty into the *Constable and Parker* [1988] model, on both the VGP longitude distributions and the predicted latitudinal variation in dispersion. As before, the predicted dispersion was calculated at each location in the database from N simulations of VGP positions, where N represents the number of lava flows at that location in the database. In the previous dispersion calculations, this procedure was repeated several times (10 times in the case of Figures 6 and 7, and 100 times in the case of Figures 8 and 9) at each location to obtain an estimate of the variability in dispersion expected from the *Constable and Parker* [1988] model. To incorporate the effect of orientation uncertainty into the statistical model each statistical sample from the *Constable and Parker* model [1988] was taken to define the mean direction of a Fisherian distribution with a given precision parameter. This Fisherian distribution was then sampled once and this new sample replaced the original *Constable and Parker model* [1988] sample. It was found that this representation of orientation uncertainty produced an improved fit to the VGP longitude distributions and an improved fit to the latitudinal variation seen in the data dispersion curves, however the total magnitude of the dispersion was too great. The variance in the *Constable and Parker* [1988] model was then reduced to combat this. Figure 10 shows the results for one such modified model. In this figure the *Constable and Parker* [1988] model has been modified so that the total power in the secular variation has been reduced to approximately 40% of its original value. The standard deviation in the horizontal field components is 3.51 μT compared with 5.4 μT in the original model, and the standard deviation in the vertical component is 6.24 μT compared with 9.6 μT originally. At each location the orientation uncertainty is modeled by sampling from a Fisherian distribution with a mean direction predicted by the *Constable and Parker* [1988] model and a precision parameter of 100, corresponding to an angular standard deviation of 8.1°. Although we do not wish to attach particular significance to the particular model shown in Figure 10, it can be seen that reducing the contribution of the *Constable and Parker* [1988] model to variance in the field, and incorporating a locally isotropic noise component provides a much better fit to the data. A possible explanation for this could be that orientation errors need to be better accounted for in PSV studies. However,

the angular standard deviation of 8.1° for the locally isotropic distribution seems too large to be entirely due to this experimental uncertainty. The local isotropic contribution cannot be modeled by a homogeneous statistical model for spherical harmonics of the kind described by *Constable and Parker* [1988] (*i.e.*, one in which the secular variation has no preferred coordinate system for the spherical harmonics). An alternative explanation to that of large orientation errors is that the secular variation is inhomogeneous and influenced by a particularly oriented coordinate system (the spin axis or the shape of the CMB). However, before such an issue can be properly addressed we need a better model for the average field configuration. One final point to note is that whilst investigating the effect of adding isotropic noise to the statistical model we noticed that there was often an obvious difference in the goodness of fit of a particular model to the dispersion in the directions or in the VGPs. This is important because it suggests that the "shape" of the *Constable and Parker* [1988] model may not adequately describe PSV, as the fit to the data is not robust with respect to the VGP transformation.

The problems inherent in Figure 1 should now be apparent. First, the data distribution is constrained by the availability of suitable volcanics for palaeomagnetic work. Previous studies have assumed that PSV can be investigated by averaging scatter in the field directions and/or VGPs in latitude bands. This reduces the data coverage requirements but requires the time-averaged field to have certain geometric properties. Second, most previous PSV work has involved the use of VGP positions, which we have seen can incorporate several problems not least of all the non-linear mapping between field directions and VGPs. Third, the technique of combining northern and southern hemisphere data may not be applicable for PSV studies where the time-averaged field requires a non-zero mean axial quadrupole term. Dispersion results for the data presented in this paper are not symmetrical about the equator. The concerns discussed above indicate that, in many cases of PSV modeling, the apparent agreement between data and models can be misleading and is rather sensitive to the assumptions made during the data analysis.

SUMMARY

We have presented a new database suitable for palaeosecular variation and time-averaged field studies. This database has been compiled using strict criteria regarding both the temporal extent of sampling and the data quality, and has superior spatial coverage to previous PSVL databases. Details of the contributing references are summarised on a regional basis in the appendix. Some properties of the database have been given, particularly those statistical parameters which are used in PSV work. Previous PSV models have

been described, and we have compared the results from our new database with predictions of two of these models. Several problems with existing PSV models have been noted, mainly connected with the use of VGPs and assumptions concerning the time-averaged field. Earlier PSV models were based on databases quite different from that presented here, and our research indicates that many data included in these studies are unsuitable for PSV modeling. Existing PSV models cannot explain the statistical properties of the database presented here. Model G (Figure 1, *McFadden et al.* [1988, 1991]) does not accurately predict the dispersion and cannot account for north-south hemisphere asymmetry in the dispersion record. The *Constable and Parker* [1988] model does not predict the latitudinal dependence in the VGP dispersion and provides only poor agreement with the dispersion in the directions. Part of the poor agreement of this latter model with the data may be due to an inadequate average field model, this is supported by the VGP latitude and longitude distributions. The VGP longitude distribution obtained from this database has similar gross features to those observed in the distribution reported by *Quidelleur et al.* [in press], but it is much more homogeneous than the distribution reported by *Constable* [1992], using the Lee database alone. The main conclusion of *Constable* [1992] still holds – that is, there is evidence for non-zonal structure in the time-averaged palaeofield [*Gubbins and Kelly*, 1993; *Johnson and Constable*, 1994]. However, there is no longer an obvious link between PSVL VGP longitude distributions and the preferred VGP longitude bands observed in some field reversal records [*Clement et al.*, 1991; *Tric et al.*, 1991; *Laj et al.*, 1991]. We have proposed that PSV studies should use the dispersion in the field directions rather than the dispersion in the VGP positions as a measure of temporal field variability. The main non-dipolar signal in the 0 – 5 Ma data recorded by lava flows is the far- sided effect, however we noted that the non-dipolar signal may be different for normal and reverse polarities. As a result PSV studies need to investigate variations about the average field for the northern and southern hemispheres, and possibly normal and reverse data, separately. This study emphasises the need for an improved understanding of the time-averaged field, for both normal and reverse polarities, before we can understand the statistics of palaeosecular variation.

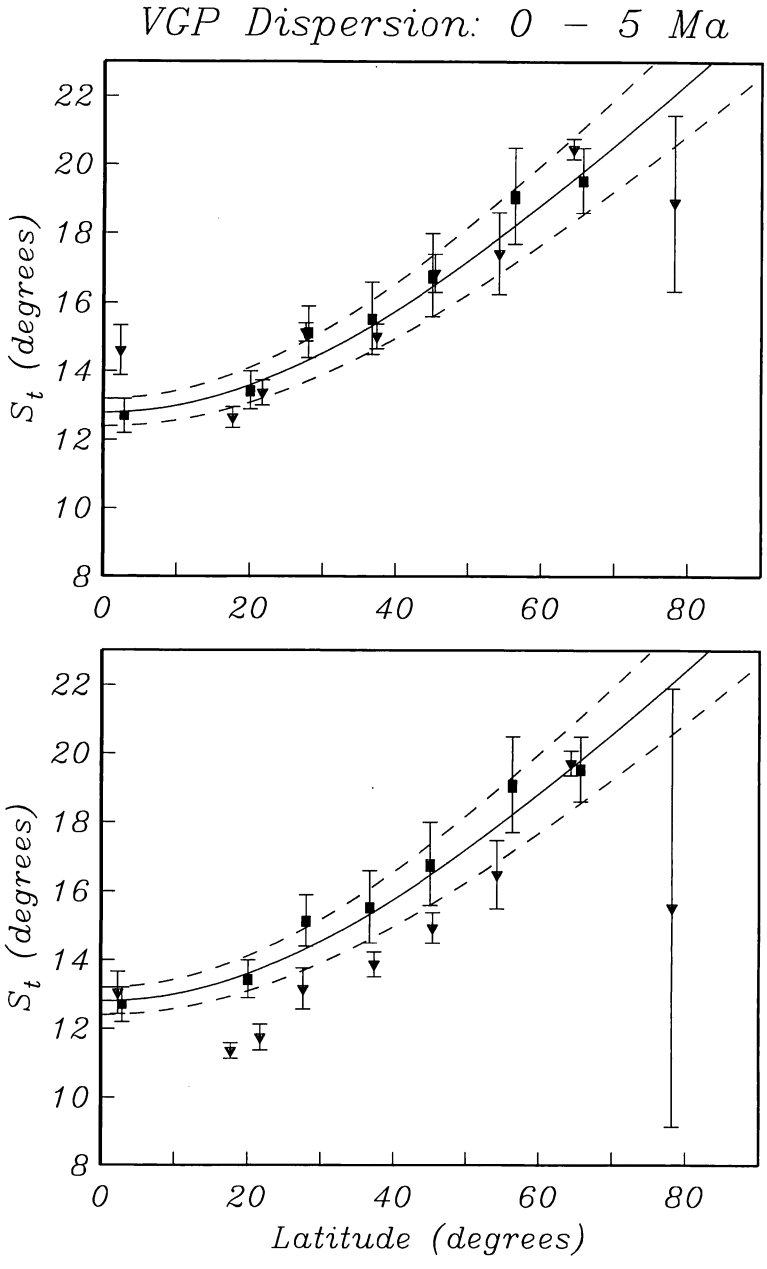

Figure 2.1: VGP dispersion fo the last 5 Myr. Squares represent data of *McFadden et al.* [1988, 1991]. Uncertainties are two standard errors in the mean, computed using a jackknife. Best-fit Model G of *McFadden et al.* [1991] (solid) with 95% confidence limits (dashed). In the upper figure, triangles are the VGP dispersion for the revised data set computed about the GAD. In the lower figure a different time-averaged field is mimicked by computing the VGP dispersion about the mean pole. VGP scatter for the new data set includes some experimental error which is not taken into account here.

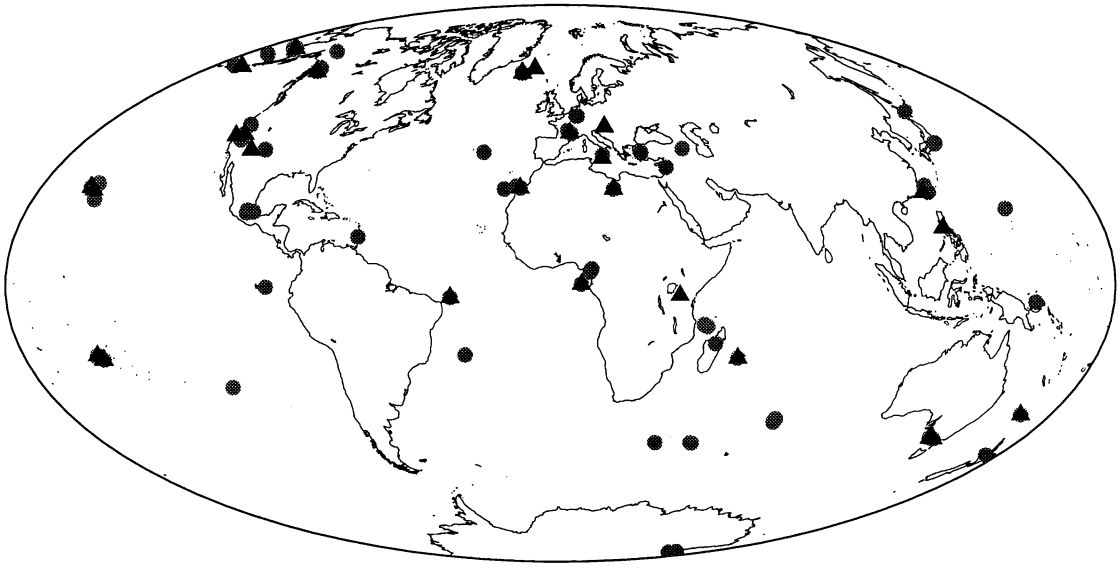

Figure 2.2: Location map for the data comprising the revised database. The circles denote normal polarity data locations, the triangles denote reverse polarity data locations.

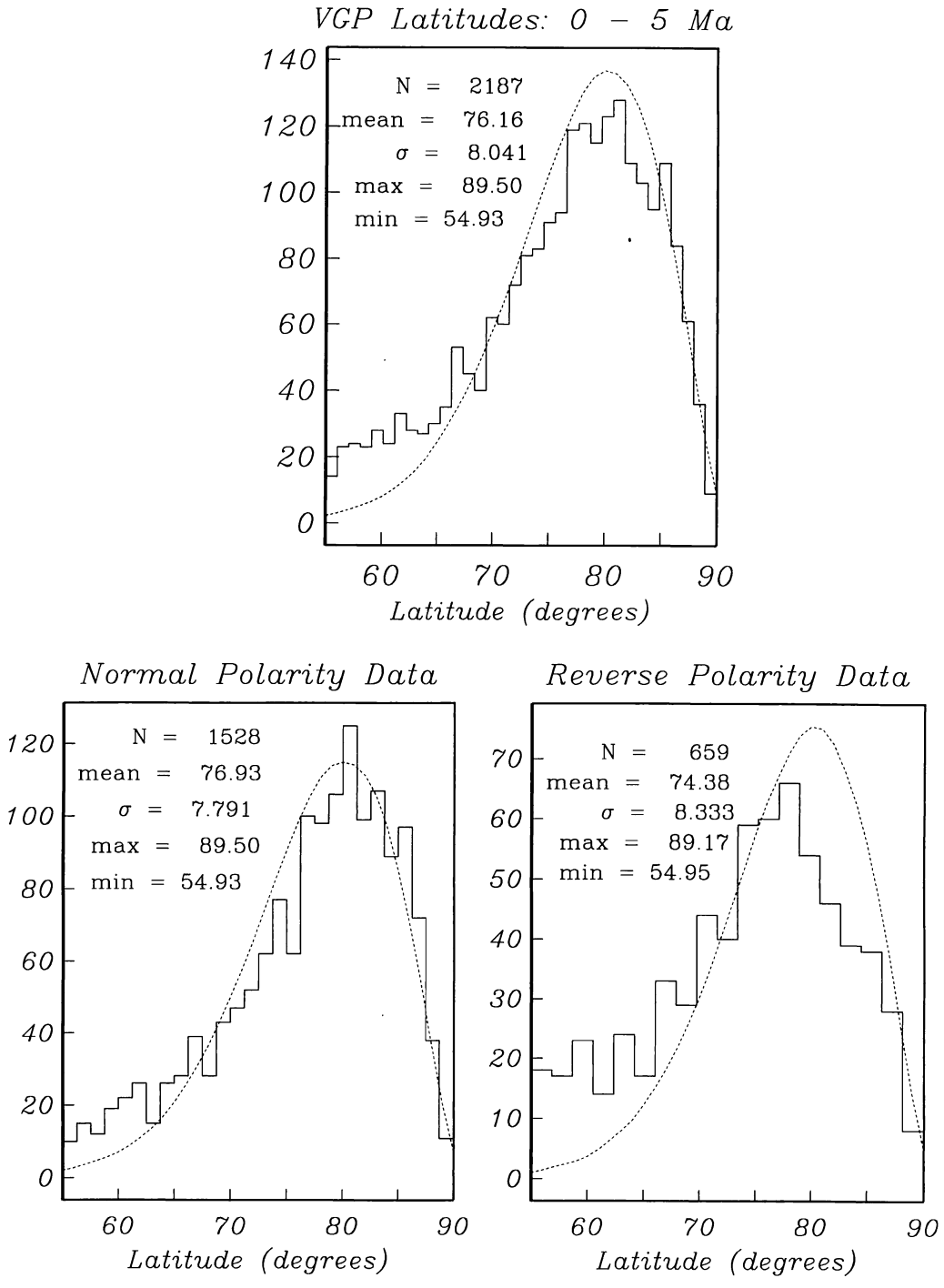

Figure 2.3: VGP latitude histograms for the revised database (solid lines) compared with the smoothed predictions of the Constable and Parker [1988] secular variation model (dashed curves), calculated at the site locations. The statistics given on each plot apply to the data distribution.

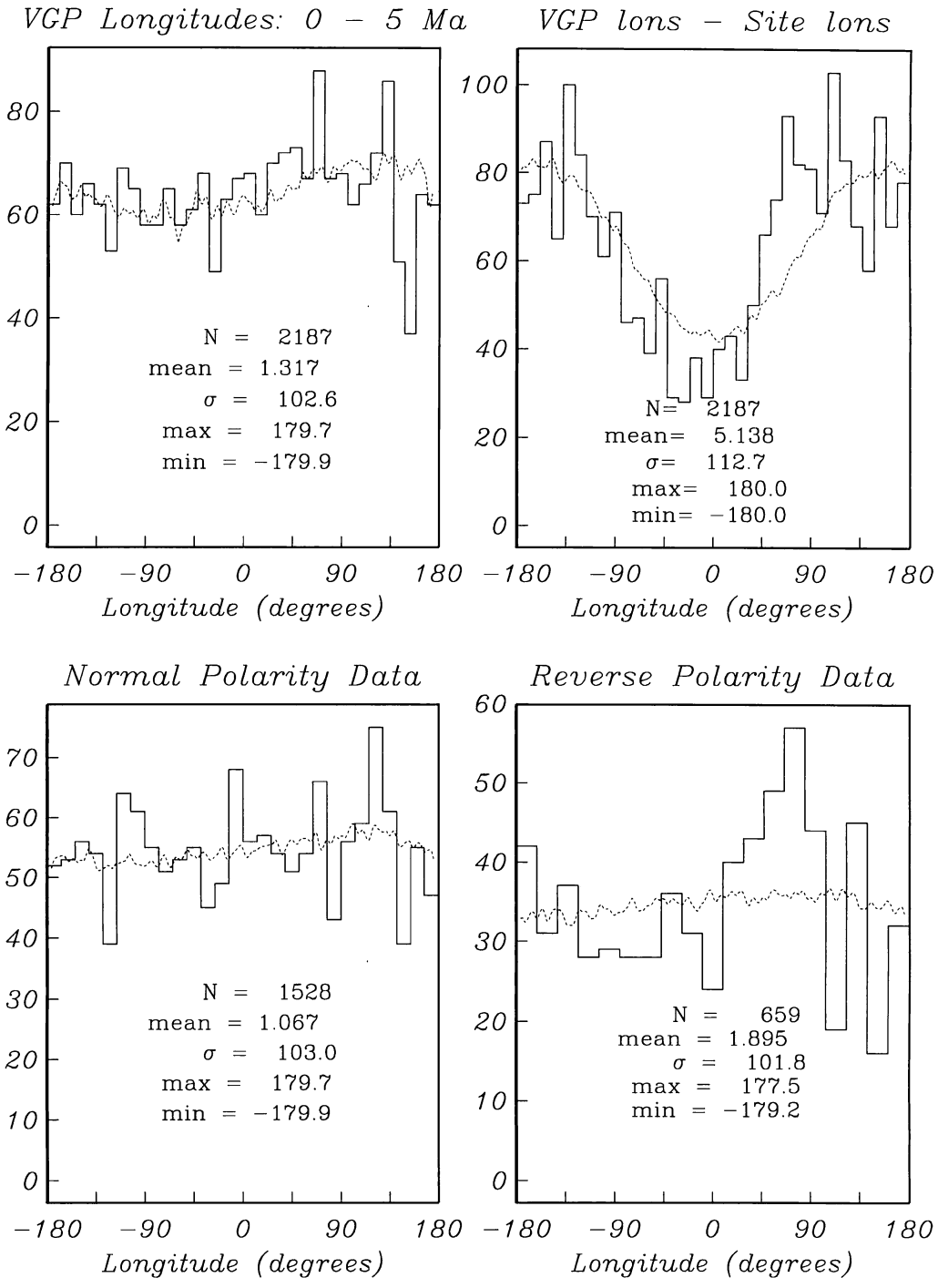

Figure 2.4: As in figure 2.3 but for the VGP longitude distributions. Also shown is the distribution of VGP longitudes minus site longitudes ("common site longitude" plot), together with the prediction of the *Constable and Parker* [1988] model.

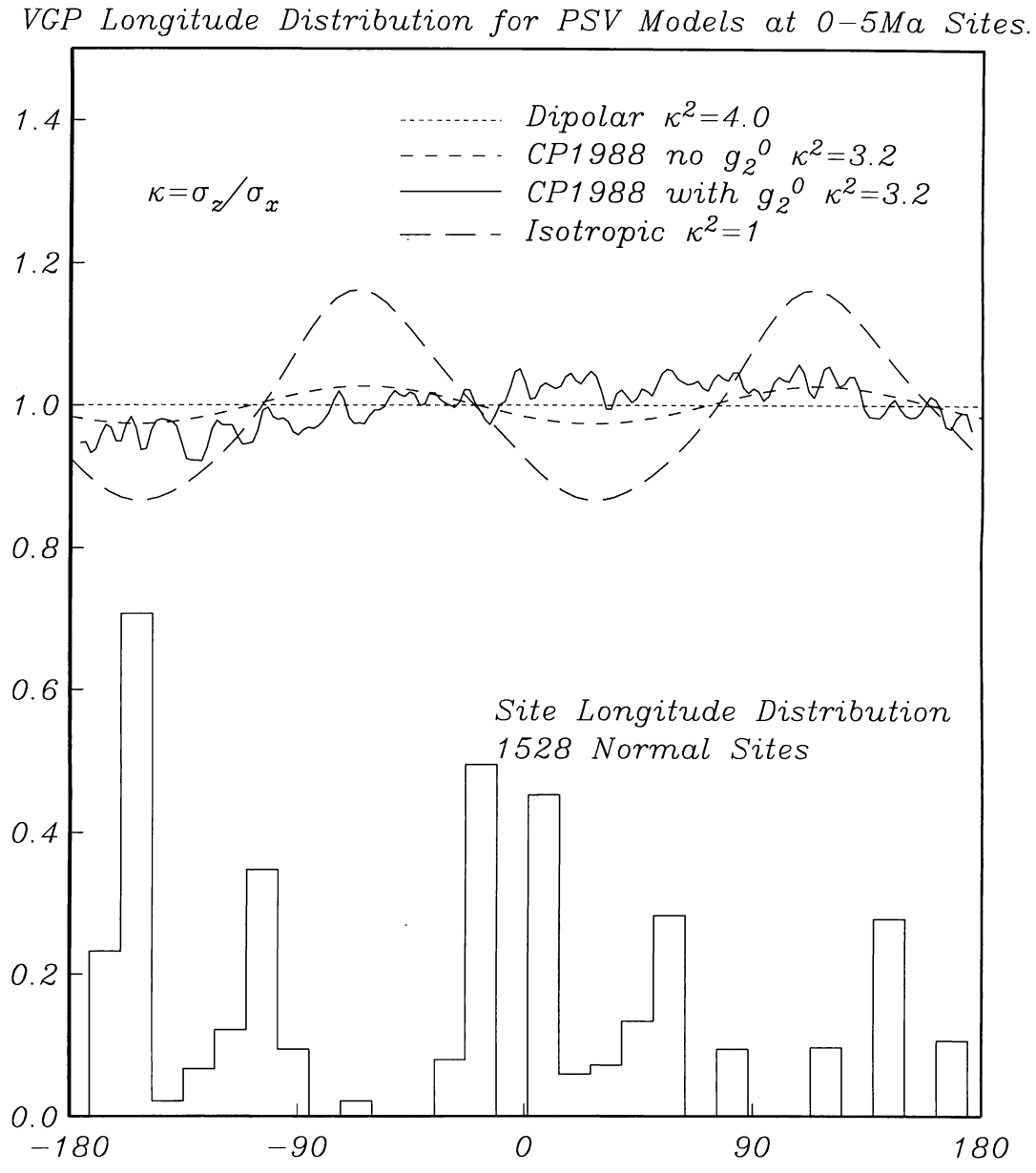

Figure 2.5: VGP longitude distributions for 4 PSV models. The data site longitude distribution is shown in the lower part of the figure. The smoothed predictions of the *Constable and Parker* [1988] model both with and without a zero mean axial quadrupole are shown. The uniform distribution is for a purely dipolar field and the long dashed line shows the predictions of an isotropic secular variation model in which the vertical and horizontal variances are equal [*Egbert*, 1992].

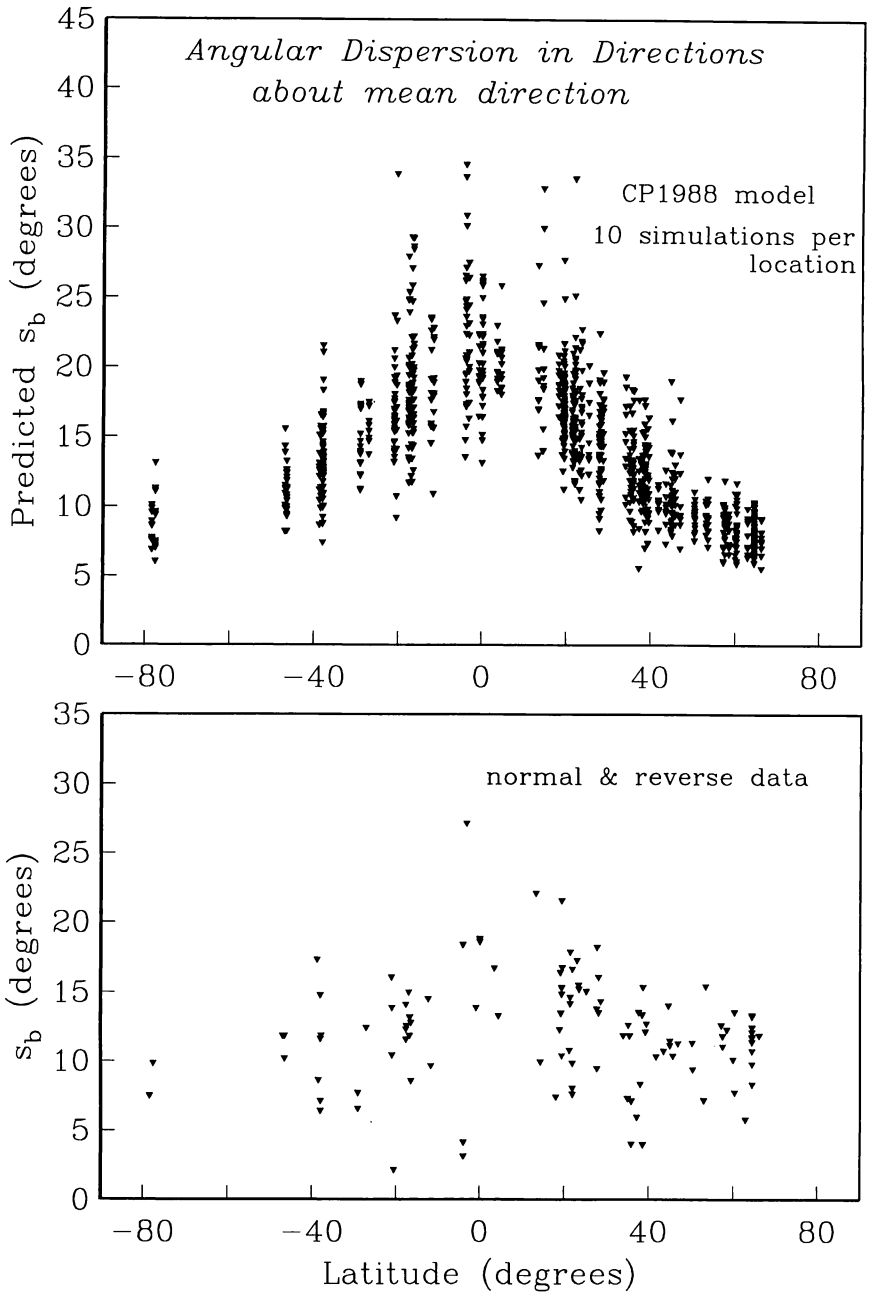

Figure 2.6: Angular dispersion in directions, computed about the mean direction. Lower figure shows combined normal and reverse polarity data. Upper figure shows predictions of the *Constable and Parker* [1988] model, where 10 simulations are made at each database site, to obtain an estimate of the variability expected in dispersion. For each simulation the dispersion is computed from N VGP positions (N is the number of lava flows at that location in the database). The true scatter in the field, s_b, is plotted as the within-site dispersion can be estimated.

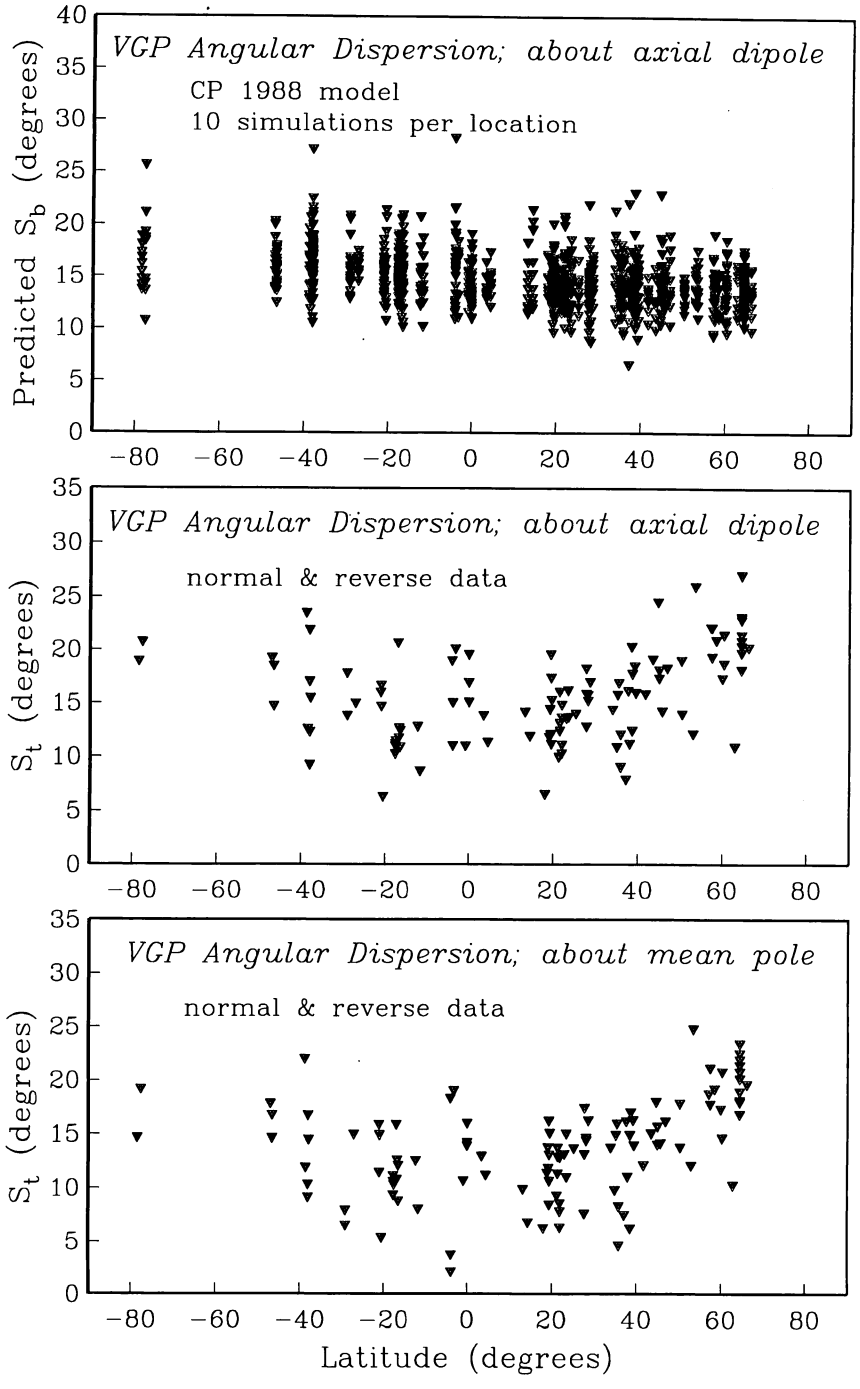

Figure 2.7: Angular dispersion in VGPs. The upper figure shows the model predictions calculated as in figure 2.6. The lower figures are the data dispersion computed about the mean pole for each group of data, and about the geocentric axial dipole, for normal and reverse polarity data combined. The total dispersion, *St*, is plotted for the data, rather than the between-site dispersion as in figure 2.6.

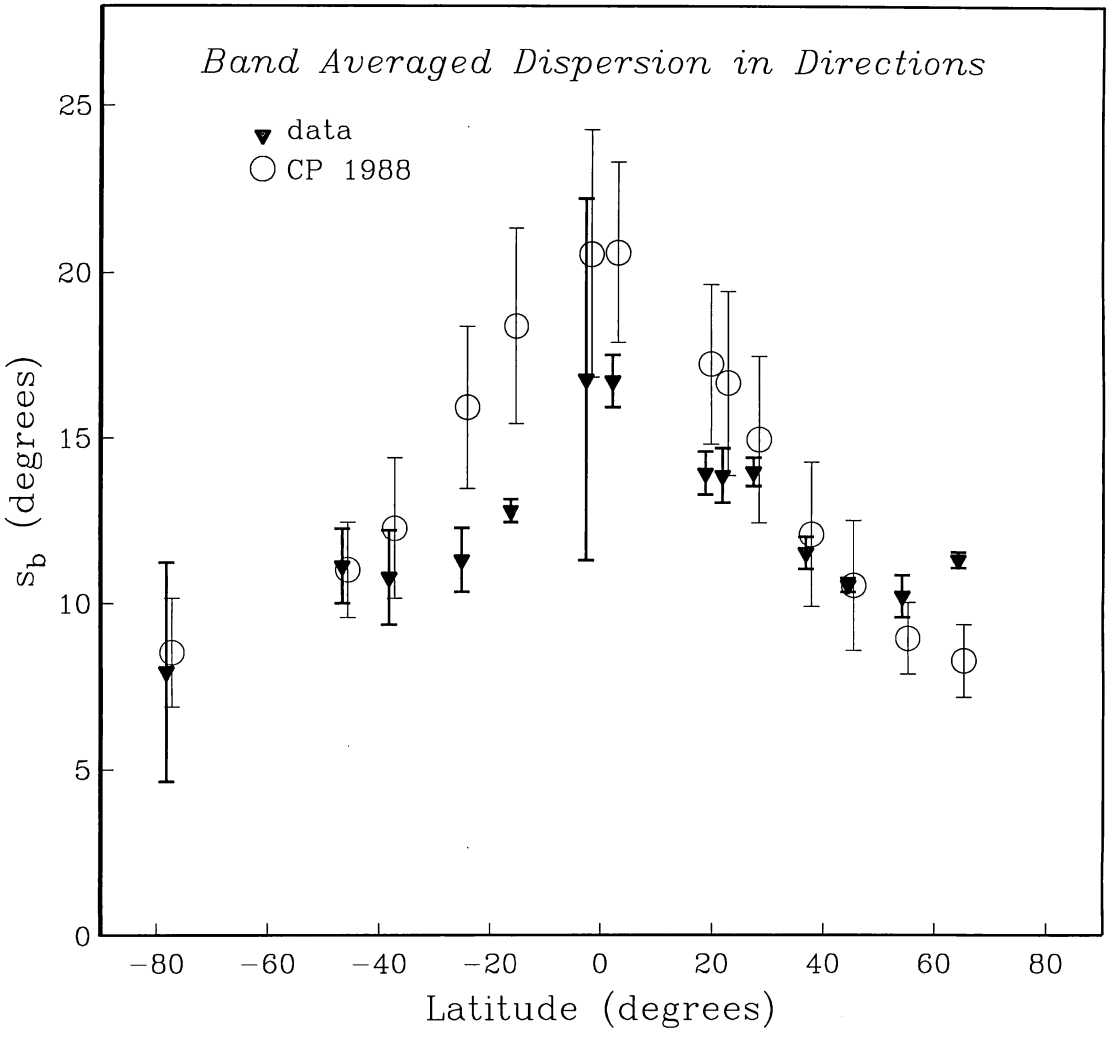

Figure 2.8: Angular dispersion about the mean direction, averaged in latitude bands. The weighted mean dispersion is plotted at the mean latitude for each band. 100 simulations at each location are computed to obtain a reliable estimate of the mean. Triangles are the data, open circles are the model predictions. The model predictions are offset from the data by 1 degree of latitude for clarity. Uncertainties for the data are 2 standard errors, computed with a jackknife. Uncertainties for the model are 1 standard deviation.

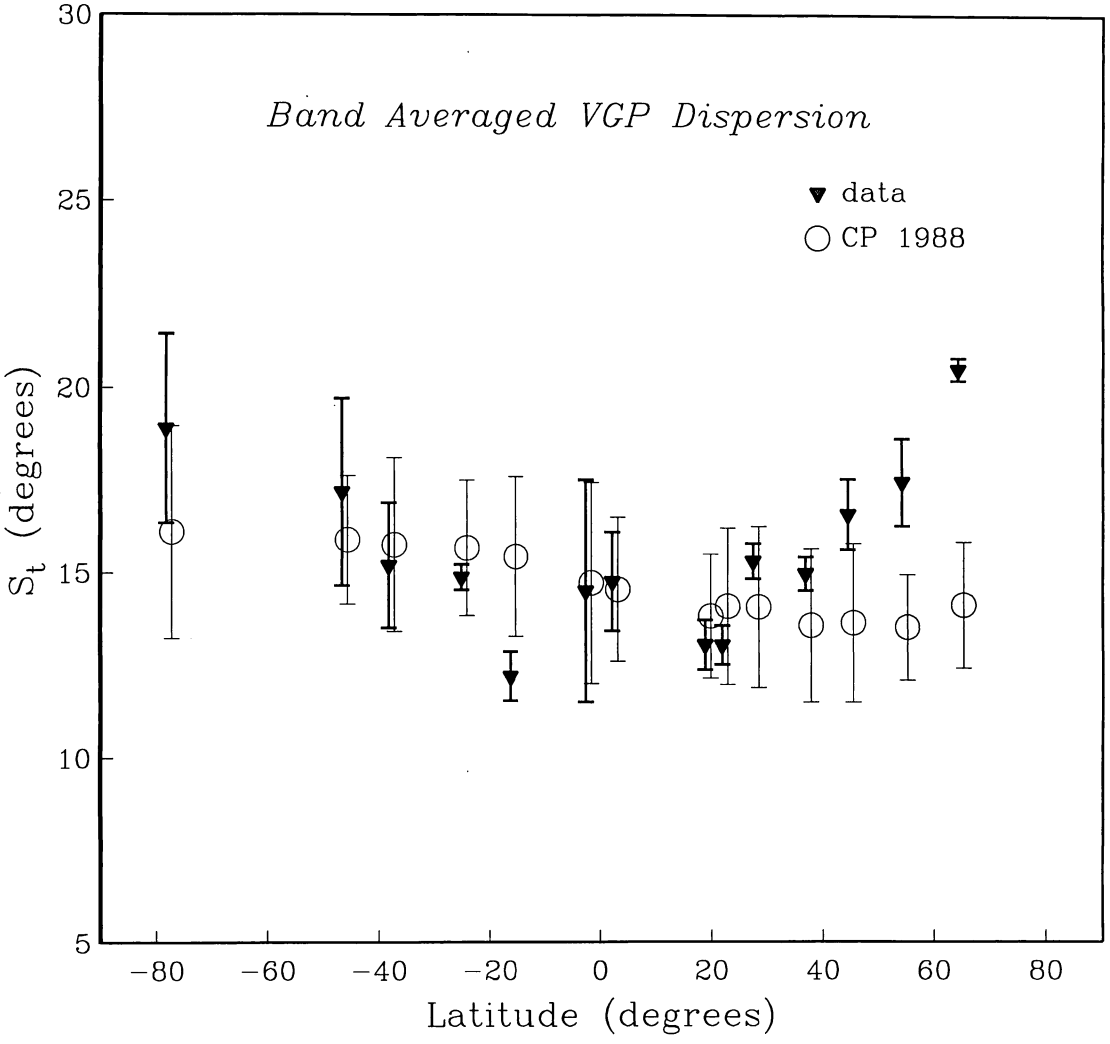

Figure 2.9: As in figure 2.8 but for VGP dispersion. The dispersion is computed about the geocentric axial dipole, rather than the mean pole.

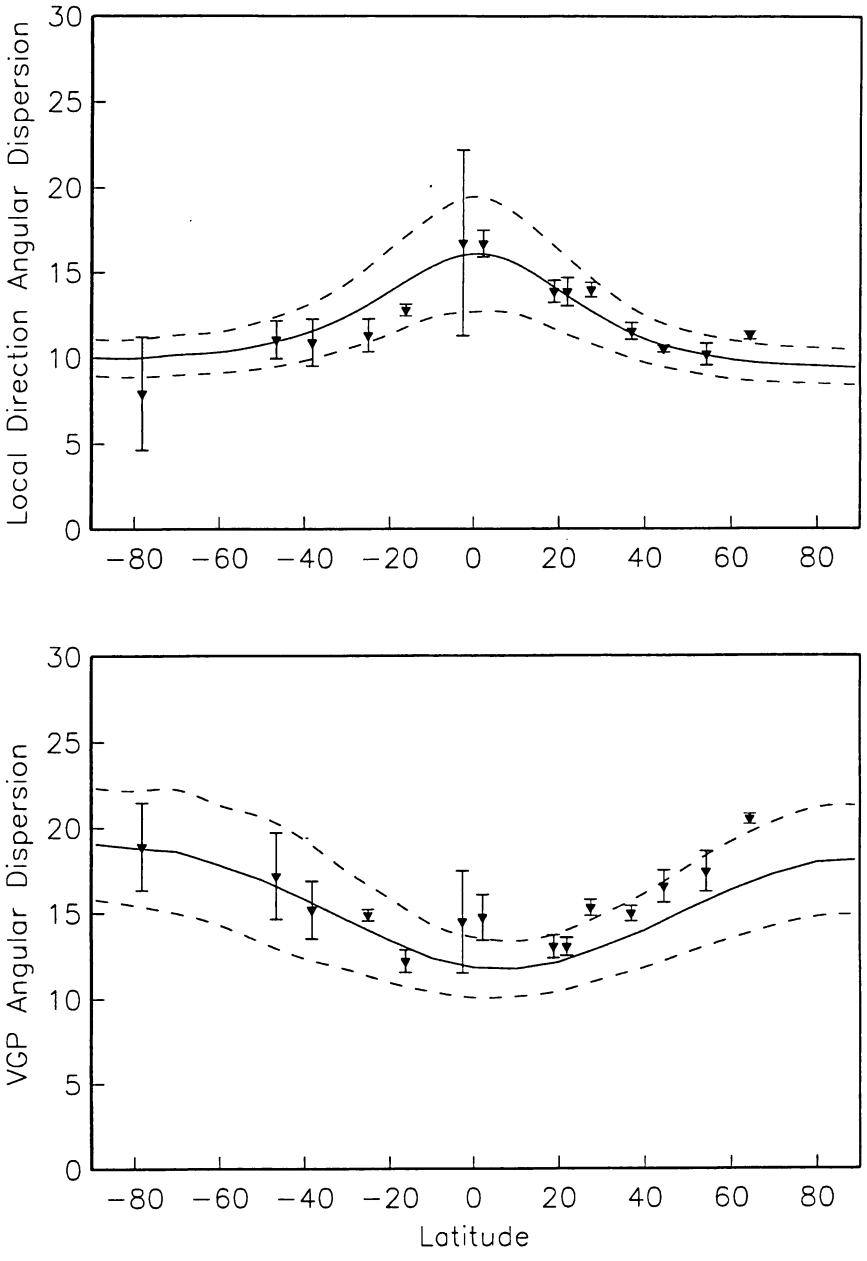

Figure 2.10: Latitudinally averaged VGP and direction dispersions for the data as in Figures 2.8 and 2.9. Also shown is the corresponding variation predicted by a modified Constable and Parker [1988] model, in which the variance in the original model is reduced, but a component of local isotropic noise is added. The isotropic noise is represented by a Fisher distribution (see text) at each location superposed on the Constable and Parker [1988] model. Dispersions for the revised model are calculated every 10 degrees of latitude with 1000 simulations per location. The solid line is the mean of the 1000 simulations, each with 15 points, and the dashed lines represent 95% confidence limits on the mean.

Table 2.1: Mean Directions and Mean VGP Positions for Data Groups, with 95% confidence cone

λ_s	ϕ_s	N	n	I	D	α_d	λ_v	ϕ_v	α_v
				A. Normal Polarity					
-78.39	164.23	13	7	-83.85	-59.10	3.733	78.41	46.36	7.042
-78.39	164.23	13	7	-83.85	-59.10	3.733	78.41	46.36	7.042
-77.56	166.26	5	8	-87.32	6.90	7.759	83.02	-16.34	14.777
-46.90	37.80	15	7	-67.30	7.89	5.500	83.00	173.21	7.952
-46.50	51.70	32	4	-64.50	-2.66	3.230	88.46	-66.70	4.476
-46.50	52.20	37	4	-60.52	10.14	3.480	82.17	115.37	4.751
-38.80	77.50	14	7	-58.14	-10.81	8.039	81.91	-27.75	10.101
-38.50	175.00	19	8	-60.73	0.53	3.470	86.15	-6.33	4.738
-38.00	142.80	5	3	-55.03	-1.33	9.243	87.34	116.01	12.954
-38.00	144.50	17	3	-61.14	5.90	2.933	83.56	-80.33	4.351
-37.83	77.52	24	7	-59.25	5.33	4.275	84.61	-152.33	5.116
-29.10	167.90	25	3	-42.14	11.42	2.840	78.86	-122.98	2.769
-27.10	-109.20	53	3	-45.00	1.05	3.125	89.58	-17.09	3.551
-21.10	55.50	17	7	-38.94	-1.17	6.800	87.94	-90.72	6.657
-21.00	55.50	27	5	-47.20	-4.28	3.610	80.97	-98.11	3.841
-20.52	-29.33	5	3	-40.99	-0.44	3.781	86.97	158.54	4.216
-17.67	-149.58	23	5	-29.09	3.92	4.525	85.86	-81.95	3.399
-17.67	-149.58	8	4	-31.03	-2.65	7.509	87.37	133.00	6.522
-17.00	47.50	14	5	-43.63	-10.20	7.150	77.14	-92.11	7.330
-16.83	-151.45	8	4	-30.87	4.45	7.444	85.75	-59.99	6.644
-16.75	-151.00	32	4	-31.93	-0.07	4.078	89.01	20.91	3.864
-16.50	-151.27	7	3	-34.03	5.64	6.120	84.05	-37.56	5.802
-12.20	44.40	23	5	-22.09	2.81	5.402	87.53	126.58	4.539
-11.60	43.30	12	5	-20.16	-2.97	5.032	86.85	-27.65	4.053
-4.00	150.00	5	3	-14.95	-2.39	15.626	85.52	2.55	14.138
-3.85	-32.40	7	8	-8.56	-9.68	3.084	80.34	-125.47	2.498
-0.83	-88.42	18	8	2.91	-1.00	5.661	87.49	-113.07	4.366

0.00	6.50	14	3	-5.37	3.94	8.789	80.87	-115.91	8.021
0.00	6.50	9	3	-8.91	-7.33	10.848	85.13	137.66	6.555
3.50	9.00	38	3	-2.31	-0.35	4.830	85.20	-166.80	3.638
4.50	9.50	15	3	5.18	-0.58	7.211	88.12	-151.63	5.024
13.30	-61.20	9	4	18.10	-9.14	8.341	80.37	-172.48	5.742
18.10	145.70	23	6	32.16	1.97	2.780	88.11	-110.13	2.284
19.00	-99.00	30	6	29.43	1.31	4.090	86.94	62.99	3.617
19.20	-98.60	21	7	34.17	3.73	6.257	85.78	-18.15	5.201
19.30	-96.90	20	9	30.83	-0.73	5.296	87.83	97.78	4.601
19.40	-155.50	7	7	31.45	10.19	14.044	79.71	-60.39	10.598
19.50	-155.50	25	6	25.05	0.47	5.337	78.62	-22.14	4.289
19.50	-155.50	28	5	21.66	8.38	4.919	82.77	-51.01	2.736
19.50	-155.50	29	5	31.72	7.50	3.393	84.28	21.94	3.703
19.60	-99.00	23	6	33.94	1.95	6.169	87.42	-10.05	5.426
21.30	-157.80	25	7	32.10	-0.08	3.810	86.42	20.77	3.233
21.50	-158.10	31	7	33.98	-0.43	4.458	87.69	37.16	4.022
22.00	-159.50	46	4	27.45	-3.57	4.253	82.62	48.44	3.287
22.00	-160.00	11	6	26.79	-7.23	5.308	79.79	63.19	4.509
23.10	-158.00	14	7	35.62	2.70	7.960	86.82	-26.56	6.094
23.50	121.40	12	4	31.99	3.86	8.228	83.98	-96.66	7.462
25.30	121.50	27	5	38.50	1.27	5.159	87.05	-76.77	4.562
27.80	-18.00	10	4	45.62	6.72	10.034	84.66	66.36	9.469
27.80	17.30	10	3	34.09	5.07	5.336	80.16	168.70	4.203
28.20	-12.80	18	4	40.55	-2.05	5.633	85.08	-169.16	5.873
28.70	-14.20	14	5	41.94	3.27	6.843	85.14	129.23	7.486
34.00	36.00	9	5	49.09	-3.66	7.151	85.86	-105.59	7.936
35.00	139.00	13	7	53.71	-5.52	3.979	85.40	48.89	4.726
35.21	138.77	35	4	49.82	-4.99	3.893	84.75	6.46	4.359
35.90	-106.50	6	7	43.88	-1.77	3.267	79.74	82.85	3.314
35.90	-106.50	6	8	51.44	0.38	5.844	86.66	65.09	5.909
37.67	-119.00	33	7	55.80	-0.59	4.125	89.68	141.40	4.860
38.00	15.00	14	14	56.26	-1.74	3.888	88.31	-107.87	5.135

38.60	28.70	5	8	61.60	11.60	3.929	80.32	87.91	4.876
38.70	-27.20	20	7	52.48	-2.83	5.969	84.92	-177.57	6.558
39.50	44.00	5	6	51.33	3.44	10.301	83.04	-155.36	10.822
41.75	-121.85	16	6	50.82	4.50	4.719	79.97	36.12	5.251
43.50	143.50	13	17	57.45	-13.48	5.257	78.60	31.84	7.234
44.69	4.30	5	7	51.51	-10.52	10.961	74.87	-136.05	13.915
45.00	3.80	7	3	61.56	8.18	7.543	83.10	102.18	10.266
45.71	2.99	26	6	61.90	-0.18	3.597	88.38	-168.61	4.802
50.30	6.75	37	14	67.97	10.03	3.275	83.39	78.85	5.050
50.40	7.25	30	13	67.17	3.06	3.009	87.78	87.21	4.361
53.00	-172.00	53	6	69.35	0.07	1.879	89.25	-150.38	2.882
57.18	-170.36	8	6	63.31	3.82	7.810	78.77	0.80	11.424
57.50	-130.00	16	3	75.00	-6.21	5.370	83.74	-162.93	9.103
58.50	-131.50	11	4	69.82	13.48	6.652	82.08	-21.95	9.989
59.99	-165.87	13	7	73.20	1.69	4.920	89.01	-48.33	8.287
60.33	-166.09	8	7	78.46	18.09	4.858	79.09	-128.28	8.964
62.92	-143.16	9	4	75.97	-6.99	3.702	86.45	147.57	5.942
64.50	-21.50	29	3	73.61	-7.37	4.444	82.44	139.00	4.518
64.50	-21.50	52	3	71.44	4.44	2.871	85.26	-153.82	7.176
64.50	-22.00	10	3	71.73	26.56	5.488	74.80	85.46	9.197
64.50	-22.00	65	3	75.87	5.64	2.223	87.23	77.37	3.831

B. Reverse Polarity

-38.00	142.80	5	3	59.11	-165.20	11.584	-77.28	74.68	12.937
-38.00	144.50	14	3	57.81	-179.38	3.614	-88.71	106.92	4.262
-29.10	167.90	12	3	38.62	-164.08	3.576	-74.07	54.77	3.294
-21.00	55.50	13	3	45.84	178.81	6.868	-82.78	66.03	7.159
-17.67	-149.58	39	6	32.36	179.31	3.947	-88.86	-93.41	3.103
-17.53	-149.85	6	3	34.94	-175.58	9.155	-85.43	152.35	7.332
-16.50	-151.27	6	4	32.99	178.18	9.415	-87.46	-108.02	8.587
-3.85	-32.40	5	4	26.93	171.44	2.218	-76.60	6.03	1.704

-3.20	35.50	12	5	-5.22	179.97	13.672	-83.88	-143.58	9.467
0.00	6.50	14	3	14.29	172.11	8.858	-79.09	52.78	7.388
4.45	120.58	5	7	-17.40	172.85	7.888	-81.21	173.35	5.317
21.50	-158.10	27	7	-24.31	177.44	5.969	-81.68	-141.70	4.574
21.50	-158.10	33	7	-29.83	178.86	4.429	-85.02	-141.91	3.435
22.00	-159.50	42	6	-29.87	-176.73	2.198	-83.34	171.62	2.107
22.00	-160.00	5	7	-38.26	-171.03	6.132	-81.79	110.04	4.944
23.60	119.50	7	8	-28.67	-179.80	10.054	-82.41	118.99	7.242
27.80	17.30	54	3	-47.09	-170.71	3.302	-81.06	-84.95	3.101
28.20	-12.80	6	4	-38.94	178.04	10.790	-84.55	0.84	10.370
35.50	-111.60	9	8	-51.87	173.52	7.290	-84.50	-43.15	9.164
37.20	14.80	6	10	-54.03	178.61	4.948	-87.61	40.89	5.330
38.50	-122.50	13	8	-42.78	-178.36	6.469	-76.61	-129.50	7.133
39.25	-120.00	6	5	-54.91	170.76	9.094	-81.98	-50.31	11.499
45.00	3.80	13	3	-56.47	-169.12	5.720	-78.89	-52.321	6.745
46.90	17.50	6	7	-65.17	168.67	8.394	-82.12	124.59	11.434
53.50	-168.10	8	5	-71.92	-171.47	9.571	-82.47	56.16	15.03
57.50	-130.00	44	4	-68.96	-168.66	3.007	-82.30	165.88	4.616
60.33	-166.09	8	7	-74.95	-171.61	8.324	-85.06	56.11	12.643
64.50	-21.50	12	3	-78.19	-169.984	6.320	-77.02	-8.38	14.210
64.50	-21.50	68	3	-75.78	-179.24	2.656	-83.85	-154.88	10.874
64.50	-21.50	8	3	-67.91	175.89	9.200	-89.68	-76.92	4.459
64.50	-22.00	103	3	-74.66	179.48	2.193	-78.90	-56.13	8.963
64.50	-22.00	15	3	-69.70	-170.44	5.772	-82.31	-49.44	7.809
64.50	-22.00	16	3	-71.51	-174.78	5.042	-88.23	-37.60	3.517
66.20	-15.20	19	4	-74.29	-174.70	4.802	-85.23	-44.90	7.762

Code: λ_s, ϕ_s = site latitude, longitude, N = # flows, n = mean # of samples per flow, D, I = mean declination, inclination, λ_v, ϕ_v = mean VGP latitude, longitude, α_d, α_v = 95% confidence cone for mean direction & VGP.

APPENDIX - *Contributing References*

References contributing to the revised PSVL database are summarised and grouped by region. The database can be summarised on a regional basis in terms of the VGP positions. Figures A1 – A11 are stereo projections of VGP positions calculated for all the data in each geographical region. Previous studies have compared palaeomagnetic results from different continents and ocean basins so we have tried to use similar regional divisions in analysing the data. As Iceland and Hawaii contribute 14.8% and 18.2% of the data respectively we have separated these data from the rest of the Pacific Ocean data and Atlantic Ocean data. We chose to display the data in terms of VGPs also for comparison with previous studies. For each region we show the individual flow VGPs (left side of figures A1 – A11). For each PSV study a mean VGP is calculated together with the corresponding α_{95} (α_{95} defines the 95% cone of confidence for the mean) and these mean VGPs are also shown for each region on the right side of figures A1 – A11. Note that although VGP positions are given in many references, some were computed on hand calculators for the older studies and may be inaccurate by up to a few degrees. The VGP positions presented and discussed in this paper have been recalculated from the directional data, however those in the on-line database are the VGPs quoted in the original references. Figure A12 summarises the age distribution of the contributing data. A few poorly constrained age ranges have a maximum age slightly greater than 5 Ma, but we have retained these data on the basis that the most probable ages for these flows are less than 5 Ma. The majority of the data is of Brunhes age as can be seen in Figure A12. It should also be mentioned that in many cases where radiometric ages are available, the range of radiometric ages may not be entirely consistent with the polarity of the data, *e.g.*, a group of Brunhes age flows may have radiometric ages (including uncertainties) spanning 0.0 – 1.0 Myr, rather than the expected 0.0 – 0.78 Myr. We have retained the original radiometric ages in the database. A summary of each reference is given where the code used in the first column of Table A1 is provided together with the (sometimes abbreviated) title of the paper. The corresponding authors, journal, site location and age ranges are given in Table A1. Pertinent field and experimental information from the original reference is reported. Reasons for excluding / including specific data are given and differences from the *Lee* database mentioned. If data from a particular reference were included in the original *Lee* database an asterisk is placed before the reference code. For data referred to by both the *Lee* and *McElhinny* databases, the *Lee* code is given first in the description header, with the *McElhinny* code following in parentheses. References for which no summary is available are marked by a '$' sign in table A1. The descriptions below are in note form and are intended to serve solely as a guide to the database, not as a complete review of the contributing palaeomagnetic literature.

AFRICA

*** G14-52; (M35) Geophysical studies of north African Cenozoic volcanic areas I: Libya**

Summary Paper part of a larger study to determine Neogene absolute motion of the N. African plate. Sampled 70 volcanic units for combined K-Ar, palaeomagnetic study. Obtained a mean pole position significantly different (at 95% level) from geographic pole, which may indicate insufficient temporal sampling. 4 cores per unit, AF demagnetisation performed. Radiometric ages, 0.4–2.2 Ma.

Database 10 normal polarity records (Site 22 removed from *Lee* database – only 2 samples). Three (10,14,20) reverse polarity sites removed from *Lee* database (only 2 samples /site), leaves 54 reverse records.

*** G13-09; (M672) Palaeomagnetism and K-Ar ages of Ngorongoro caldera, Tanzania**

Summary Sampled Gauss-Matuyama boundary and Matuyama epoch. 23 flows and 1 tuff sampled, 5 cores per unit. AF demagnetisation up to about 200 Oe generally sufficient to remove secondary magnetisations. Thermomagnetic properties investigated. K-Ar dating on one flow and tuff. Mean pole is displaced 10.5° from geographic pole but the 95% confidence cone in the mean is 11°. VGP dispersion is large and apparently non-Fisherian.

Database 12 Matuyama age records

*** G14-21,22,46; (M15) Palaeomagnetism of the Gulf of Guinea Province, W. Africa**

Summary Palaeomagnetic sampling carried out in 3 main areas: Cameroun, Fernando Poo, Sao Tome and all suggest no detectable movement of the plate relative to the geographic pole for the last 25 Ma. Sao Tome mostly basaltic lavas, but largely inaccessible. Fernando Poo young volcanic island with alkali olivine basalts. Cameroun has 3 main stages of volcanism exposed. Up to 5 cores per site collected, AF demagnetization up to 400 Oe. Palaeopole for Fernando Poo significantly different from geographic pole, even though all the flows sampled (and the whole island) are less then 700,000 years old.

Database (a) Cameroun: 15 Brunhes age records (sites 4,13,15,29 removed from *Lee* database (low k). Site 29 added); (b) Fernando Poo: 38 Brunhes age sites (Sites 9,30 removed due to 2 samples

/site; sites 25,36,41 omitted due low k; site 36 added); (c) Sao Tome: 14 Brunhes age (sites 1,45 removed, 2 samples /site). 9 sites with age range 2.5–4.0 Ma. 14 reverse polarity sites (site 20 removed, 2 samples /site; site 51 removed – intrusive).

ANTARCTICA

M1319 Paleomagnetic Investigation of some volcanics from McMurdo Province, Antarctica

Summary Volcanism covers Gauss-Brunhes epochs. Total of 303 cores from 39 localities obtained. No evidence for tectonic disruption. Very few samples showed any change on AF demagnetising, probably the result of little alteration in the extremely arid environment. Detailed results for each location given in paper. Mean VGP position is 86.6°N, 334.8°E with α_{95} = 6.6°. Total dispersion of the VGPs is 23.7°, and the dispersion corrected for within-site scatter is 23.5°, with 95% confidence limits of 20.5° and 27.4°.

Database 18 records grouped in two locations (5, 13) of Brunhes /Jaramillo age.

ASIA

* G9-06, G9-07, G9-08; (M409) Paleomagnetic Investigation of Taiwan Igneous Rocks

Summary Paper deals with palaeomagnetic investigations in 8 geologically different areas in Taiwan: data from only 3 areas could be used in the database. Laboratory methods included a.c. demagnetisation up to 800 Oe of all the specimens, thermal magnetic treatment of selected samples and petrographic analyses.

Database (a) Tatun Volcanic Group: 27 N polarity mid Plio-Pleistocene andesite flows. 9 records removed from *Lee* database (only 2 specimens /flow); (b) Shiukuran River: 12 N polarity andesites of Plio- Pleistocene age. In the *Lee* database these were combined with Penghu Islands data although these 2 locations are more than 100 km apart. The 6 R polarity records in the *Lee* database were removed as they are Miocene age.; (c) Penghu Islands: 7 R polarity Plio-Pleistocene basalts. N polarity Penghu Islands records removed from *Lee* database after separating from Shiukuran river data since there are only 4 suitable flows. (d) We also removed all data from Keelung area (6 N, 19 R polarity records) originally in *Lee* database since intrusives and extrusives were not distinguished.

Concern Lack of good age constraints.

C0001 Paleomagnetism of Pleistocence Usami Volcano, Izu Peninsula, Japan

Summary Palaeomagnetic study of a section of andesite flows and pyroclastic deposits at Usami Volcano. Flow thicknesses generally 3–5m. Probable that tilting of the strata occurred after emplacement and this is corrected for (based on field observations) in the final palaeomagnetic analysis. Two specimens from each site were stepwise a.c. demagnetised up to 480 Oe. Field intensity measured, standard thermomagnetic analyses performed and X-ray diffraction experiments carried out.

Database 5 normal polarity, probably Brunhes but possibly Matuyama age, andesite flows included in database. Note that the data from this paper (Kono, 1968) were combined with data from the following reference, C0002 (Kono, 1971) and given an age range of 0 – 1.6 Ma.

C0002 Intensity of the Earth's Magnetic Field in Geological Time

Summary Palaeointensity study of flows from 3 locations: Hakone Volcano (Izu Peninsula), Mt Fuji Volcano (Izu Peninsula) and Kita-Matsuura basalts (NW Kyushu). Experimental procedures applied as in previous reference, C0001. No record of post deposition tilting of strata.

Database 1 record from Mt. Fuji, 7 from Hakone. All Brunhes age normal polarity basalts, but combined with data from Kono [1968], so given collective age range of 0 – 1.6 Ma.

M1588 Palaeomagnetic Study of the Ashitaka Dike Swarm in Central Japan

Summary Hand samples collected from 35 narrow (0.2 – 4 m) dikes which form a radial swarm from Ashitaka Volcano, Izu Peninsula. Stepwise AF demagnetisation up to 100mT. Mean direction determined using minimum dispersion criterion (i.e. mean direction given by the remanence at the demagnetisation level which has the lowest dispersion, or equivalently the greatest precision parameter). All dikes inferred to be Brunhes age.

Database Include all data.

M1301 Palaeomagnetic Results from Luzon and Central Philippines

Summary Detailed study involving collection of 550 samples from 86 sites from the Philippine Arc. Ages span Jurassic to present and study aimed at investigating tectonic rotations of the islands in the Philippine Arc. Main conclusion of study applicable to this database is that there has been

no rotation of the arc during the Plio-Pleistocene. Bedding corrections applied to older sites, but not required for late Miocene and younger samples. Many different lithologies sampled. Lab work involved AF demagnetisation, Curie temperature analysis, thin sections, hysteresis measurements.

Database Only 5 of Plio-Pleistocene records suitable for inclusion in the database after discounting tuffs and sediments, and applying the criteria given in the main text to the tabulated results. All 5 are normal polarity basalt flows from the island of Mindanao. No detailed age information is available, so limits of 0.0 and 5.0 Ma had to be used.

Concern Lack of age constraints, small number of data.

ATLANTIC OCEAN

*** G14-17; (M13) Brunhes Geomagnetic Secular Variation on Terceira Isl., Central N. Atlantic**

Summary At least 6 cores per igneous body taken from 33 bodies (flows and ignimbrites) yielding a mean VGP dispersion for the Brunhes of 13.9° with 95% confidence limits of 16.3° and 12.2°. Investigated effect of reducing number of specimens per flow on the estimate of within site dispersion and concluded that for this particular study could have reduced sampling by about half without significantly affecting the results. 4 stratovolcanoes (Pico Alto [PA], Cinquo Picos [CP], Guilherme Moniz [GM] & Santa Barbara [SB]) comprise most of the island, and are cut by NW-SE trending fissures associated with the Terceira rift. Volcanics associated with PA mostly pumice, with few basaltic flows. More basalts associated with CP & GM, pyroclastics also associated with GM. SB intially developed as lavas and ash with some late stage pumice. 236 cores from 33 separate bodies oriented to ± 2.5° and with lateral separation typically > 10m. Details of sampling sites given in their appendix. We assume tectonic corrections made to the slopes mentioned in their appendix. AF demagnetisation up to 200 Oe and minimum dispersion criterion used.

Database 9 records (flows 1,3,6,11,16,20,22,27,32,33) removed from Lee database due to low precision parameter. Flow 4 removed since welded ignimbrite. Leaves 20 Brunhes age flows.

*** G14-31; (M19) Brunhes Epoch Geomagnetic Secular Variation on Marion Island**

Summary Palaeomag survey of 30 Marion Isl. flows gives broad 95% confidence interval for Brunhes VGP

dispersion. Marion & Prince Edward islands part of single volcanic platform. Marion island exposures alternate between effusive and explosive; the lavas are alkali basalts or trachybasalts. Older volcanic series has K-Ar dates of 100 - 300 kyr and the Younger Series is < 23 kyr. The 2 series are separated by a glacial period. 220 cores from 30 flows oriented to ± 2.5°. AF demagnetisation up to 200 Oe and minimum dispersion criterion used.

Database 15 contributing flows

*** G14-39,64 (M25) Palaeomagnetism of the Canary Islands and Madeira**

Summary Palaeomagnetic results from 1144 specimens from 359 igneous bodies for the Pliocene, Pleistocene & Miocene give mean VGP positions not significantly different from axial dipole. K-Ar dates on 90 of the bodies. Geology in earlier references. The Pliocene data in this paper includes the Brunhes age data presented in Watkins et al., 1972. Samples collected during 1965, 1966, 1968. Cores oriented to ± 3° and 2–8 collected per igneous body. AF demagnetisation up to 300 Oe and minimum dispersion criterion used. K-Ar dating details in earlier references.

Database Data subdivided according to individual contributing islands. (a) all 14 N polarity Pleistocene Lanzarote records removed from Lee database (2 samples per site) (b) 5 N Pleistocene Tenerife data removed (2 samples /site); leaves 18 Brunhes records (c) 18 N Pleistocene Hierro records removed (2 samples /site), flow 28 (low k); leaves 10 Brunhes (d) 2 N Pleistocene La Palma sites removed (Flow 9, intrusive; Flow 14, low k); leaves 14 Brunhes (e) all N Pliocene data removed (mostly 2 samples /site). (f) 14 R Pleistocene Tenerife flows removed (2 intrusive, others 2 samples /flow); 6 Matuyama left (h) All remaining reverse data removed, mostly because only 2 samples /site

M1404 Palaeomagnetism and rock magnetism of Fernando de Noronha, Brazil

Summary Pole positions obtained from seven basaltic sites from Quixaba Formation (3.4 ± 1.7 my, K-Ar) on Fernando de Noronha and from seven sites from Remedios formation (9.5 ± 1.1 my, K-Ar). Also sampled seven Cretaceous (28.7 ± 2.5 my, K-Ar) basaltic sites from mainland province of Fortaleza. 5–13 samples from each site. Pilot samples AF demagnetised up to 1000 Oe, other samples cleaned accordingly. Some Quixaba sites (55,61 & 69,70) gave directions not significantly different (F- test) and so were combined to give 7 independent measurements in total. For the Remedios, 2 sites were rejected due to VGP latitudes < 50°, and an additional

one site rejected due to contamination by VRM, leaving seven useful sites. Forteleza sites poor quality – large within site scatter and low remanence stability.

Database All 7 Quixaba sites ok (N, basalts). Remedios mostly pyroclastics & intrusives, so unsuitable

M799 Paleomagnetism and K-Ar ages of some igneous rocks from Trindade Isl., Brazil

Summary Palaeomagnetic and K-Ar study of 7 thin intrusive igneous units on Trindade Isl. support Gauss- Matuyama transition age of 2.41 ± 0.05 Ma. Island 1,150 km off Brazil and 1,800 km west of the Mid-Atlantic Ridge. Pyroclastics, intrusives and extrusives. Oriented hand samples collected. AF demag, K-Ar determinations.

Database 5 suitable normal polarity sites. Age range 2.3 – 3.3 My.

M1654 K-Ar chronology & palaeomagnetism of volcanic rocks in the Lesser Antilles Arc

Summary Detailed study of 16 islands in the arc. K-Ar dates for the outer arc are in range 38 – 10 Ma, for the inner arc they are less than 7.7 Ma. Only data useful here are from St. Vincent Isl. Flows sampled mainly associated with Richmond and Soufriere volcanic centers. Ages in range 0.29 – 2.85 Ma for dated samples. Both normal and reverse polarities sampled. AF demagnetisation and optimum fields selected using criterion of minimum proportional change in magnetisation vector between successive demagnetisation steps. Rock magnetic studies done.

Database 9 N polarity records from St. Vincent. Age range 0.29–1.28 Ma but probably Brunhes.

M442 Palaeomagnetism of Atlantic Islands: Fernando Noronha

Summary VGP poles for 9 sites from Quixaba formation (4 N, 5 R) and 15 from Remedios formation (11 N, 4 R). Some sites overlap with later study of *Schultz et al.* [1986]. At least 4 cores drilled from each of 28 sites. NRMs measured. Paper states that there is no overprinting, so ok to use NRM. 4 sites rejected due to poor quality data.

Database Quixaba sites 1–5 (R) & 7 (N) distinct from *Schultz et al.* [1986] sites. Although NRM, *Schultz et al.* [1986] added these results to their own so presume NRMs ok.

AUSTRALIA

*** G11-09 A paleomagnetic study of secular variation in New Zealand**

Summary 22 Brunhes formations gave VGP scatter of 19.6° with 95% confidence limits of 16.2° and 24.7°, larger than model predictions at time of paper (1969) but comparable with studies at similar latitude in N. America. Corresponding scatter in directions was 13.2° with 95% limits of 10.9° and 16.7°. 8 cores per flow. AF demagnetisation.

Database 19 Brunhes records. Originally 21 in Lee database, but 1 record (NZ4) removed due to low VGP and another removed (NZ2) since >300 km away from remaining sites.

*** G13-11 Paleomagnetic Secular Variation from the Newer Volcanics of Victoria, Australia**

Summary Study of 46 alkali olivine basalts from the Newer Volcanics, which are Pliocene to Holocene in age and outcrop over area of 25,000 km^2 . The 25 N and 21 R sites showed no significant difference in VGP scatter (11.4°). Oriented hand samples with average of 3 samples /site. AF demagnetisation.

Database All 46 sites originally in *Lee* database. Removed 3 N, 2 R records with only 2 samples per site. Remaining data subdivided into two locations: sites 27 – 36, 38 @ 142.8°E, 38.0°S (5 N, 5 R); the rest @ 144.5°E, 38.0°S (17 N, 14 R).

EUROPE

*** G11-12; (M554) Etude paleomagnetique des basaltes du Plateau du Velay**

Summary Both N and R polarities found in flows (basalts apart from 1 andesite). Stratigraphic dating indicates substantial volcanism during the Matuyama. Inferred that the N polarity rocks observed here are from either the Jaramillo event or the beginning of the Brunhes. Stepwise AF demagnetisation to 400-600 Oe.

Database 7 Normal polarity records (Brunhes /Jaramillo) - A2,B4,D1,D3,D5,D6,E3. 13 Matuyama R records

*** G12-09; (M618) Paleomagnetic Secular Variation Study , the Massif Central, France**

Summary VGP scatter from 31 Brunhes-age lava flows is 15.2° referenced to an axial dipole mean. Confidence limits are 18.4° and 12.9°. Most Brunhes samples from Chain des Puys (near Clermont- Ferrand), some from the valleys and tributaries of the Ardeche. Some pre-Brunhes stuff from Chain des Puys and S.W. of Montpellier. Eight cores per flow, with maximum lateral

separation of a few 100 m. Progressive AF demagnetisation on one specimen per core 25–800 Oe. Compare sequential directions during demagnetisation for each core from single flow and omit specimens which do not appear to reach a stable remenanence. Of 33 original flows 31 retained.

Database All 31 flows OK. 26 grouped as one location, 5 as another, as flows separated by more than 100 km.

*** G10-09; (M517) A Palaeomagnetic Study of Quaternary Volcanic Rocks from Turkey**

Summary Brunhes and Matuyama epoch volcanics give mean VGP consistent with a GAD at the 95% confidence level. Estimated standard deviation in directions is 10.0° - 11.5° for Brunhes (depending on whether used simultaneous or successive 2-tier analysis) and 16.2° for Matuyama. At least 4 oriented hand samples /flow. Thermomagnetic and ore microscopy studies. AF demagnetisation.

Database 16 suitable Brunhes flows but separated by several 100kms. Use 10 records which can be grouped into 2 locations with 5 records per location

M1072 PSV studies of the Brunhes in the volcanic province of the East-Eifel, Germany

Summary Mean pole derived for Brunhes from 31 independent events consistent with the GAD hypothesis. VGP dispersion = 15.1°. Palaeomag samples from 46 sites, 6–17 cores per site each giving 2–3 specimens. Several sites dated radiometrically as well as stratigraphically. 2–3 samples per site AF demagnetised up to 700 Oe. NRM stability varied; classified 4 types, relate to grainsize. Most VRM removed by 100–200 Oe fields. Used a stability index [*Symons & Stupavsky*, 1974] to investigate best demagnetisation level – all other samples for given site demagnetised in this range. Take site mean direction from the stable region at alternating fields yielding minimum α_{95}. Several sites give directions not significantly different (F-test), combining these yielded 31 independent sites.

Database Site EEL5 omitted due to low VGP latitude (52.6°), leaving 30 Brunhes age sites.

M1513 Paleomagmagnetic Investigation of Quaternary West Eifel Volcanics (Germany)

Summary 64 VGPs gave asymmetric longitude distribution with low latitude VGPs (< 60°) concentrated

in the longitude band 30°E – 120°E. Mean VGP significantly different from GAD. Anomalous VGPs possibly represent an event /excursion within the Brunhes epoch. Volcanism began during the Pleistocene with the main activity at 0.7 Ma. 85 sites sampled representing 73 of the West Eifel eruption centres. Sites in lava flows, dikes, scoria cones, sill-like flows, plugs and 2 tuffs. A few samples thermally demagnetised. AF demag of 3 or more specimens /site up to 1200 Oe. Remaining specimens demagnetised in 3–5 steps after a stable direction reached in pilot samples. Sites suspected from being from same eruption centre subjected to F-test and directions combined if necessary.

Database Sills excluded leaving a total of 37 Brunhes sites, 5 are combinations of more than 1 original site.

*** G12-22; (M638) Secular Changes, Polarity Epochs & Tectonic Movements, Hungary**

Summary Palaeomagnetic investigations of Plio-Pleistocene basalts, Miocene andesites, Lower Cretaceous volcanics. Results described separately for each age group with emphasis on the correlation of magnetic polarity with the geology. 6 cores per outcrop taken. Stepwise AF demagnetisation in fields increasing by 100 Oe. Site mean direction computed for the demagnetisation stage for which the dispersion on a stereo plot was estimated visually to be a minimum. Thin sections and thermal demagnetisation also. No significant post deposition tectonics.

Database 6 R records from Transdanubia included (N polarity data ok but only 4 records)

M34 Evolution of a section of the Africa-Europe plate boundary: ... evidence from Sicily.

Summary Palaeomag data from Upper Cretaceous, Neogene and Quaternary volcanics indicates that Sicily is part of the African plate which collided with the European plate in Middle Miocene times. The geochemistry suggests different episodes of volcanism since the late Tertiary. 8 Upper Cretaceous dykes (Capo Passero) and 10 Plio-Pleistocene lavas from Mt. Ilbei. Mt. Ilbei lavas vary from allkali basalts to tholeites – uncertain whether this is due to different degrees of partial melting at the same depth or partial melting at different mantle depths. Field and lab details omitted here except that overprints generally removed by a 150 – 200 Oe field. AF demagnetisation resulted in lower scatter without significantly changing the mean directions.

Database D, I only given to nearest degree but data retained as overall analysis seems ok. 6 suitable

R Plio- Pleistocene Mt. Ilbei sites, only 4 N so N data omitted. 4 of R sites are dated: 3 are Matuyama the 4th is Gauss, implying an incorrect age or flow from a R polarity event during the Gauss.

HAWAII

M285 Paleomagnetism of Hawaiian Lava Flows

Summary 148 flows from the Island of Hawaii, with ages from around 300 BP to 350 ka. 112 flows have multiple samples. Data are from 5 different volcanic series on the island, some of whch erupted repeatedly over very short time intervals and thus provide poor samples of the range of directions expected for PSV. Original age estimates provided in this paper are largely based on plausibility arguments, and the data presented in *McWilliams et al.*, [1982] supercedes these. No evidence for tectonic tilt; rock magnetic studies used to infer that the NRM represents the field at the time of cooling of the lava flows; AF demagnetisation did not reduce scatter. The volcanic series are (1) Puna: 18 flows, age range 300-500 BP, based on C14 (2) Kahuka: 28 flows older than 10 ka (based on stratigraphy to an ash flow) believed to represent a time interval of 5000-75000 yrs (based on amount of dispersion in data) (3) Hamakua: 11 flows older than 10 ka, believed to sample only 100-200 yrs because of the low dispersion, but no data is available for direct comparison (4) Ninole: 25 flows older than 10 ka (5) Pololu: 29 flows with K-Ar ages in the 200-300ka age range.

Database Puna and Hamakua series omitted (insufficient temporal sampling). Others included.

M667 Paleomagnetism of Lava Flows from Kauai, Hawaii

Summary Study of 571 cores from 120 flows indicated (1) far-sided mean palaeopole, (2) low secular variation. Ages range 3.5-5.6 Ma. 8 samples per flow in the Makaweli formation and 5 per flow in the Napali formation and Koloa volcanic series. AF demagnetisation up to 400 Oe.

Database 46 normal and 42 reverse flows. Single samples and asterisked data in paper omitted. Latitude in *Lee* database corrected to 22.0 (from 20.0)

M31 Paleomagnetism of volcanic rocks from Niihau, Nihoa & Necker Isls., Hawaii

Summary Sampling of 39 flows gave far-sided palaeopole for Niihau, although that for Nihoa was very

close to geographic axis. Necker island gave low latitude VGPs. The VGP dispersion is low, consistent with low dispersion observed at other Hawaiian islands (*e.g.,* reference above). 8 cores per flow on all 3 islands. AF demagnetisation.

Database 7 flows from Necker excluded since 10 Ma. Nihoa: 14 flows, all about 3 Ma, all normal. Niihau: 16 flows – Kieke series 0.3–0.7 Ma (11 normal flows); Paniau series 3Ma (5 reverse flows).

M42 K-Ar ages and paleomagnetism of the Waianae & Koolau Volcanic Series, Oahu

Summary Waianae active from 3.6–24. Ma. 99 flows sampled from the Waianae and Koolau series. Stepwise AF cleaning. Five low latitude VGPs possibly indicate an excursion.

Database 31 N, 27 R from Koolau series (2.6–1.8 Ma). Also 33 R, early Matuyama age.

C0003 Paleointensities from C14 dated flows on Hawaii and the Pacific non-dipole low

Summary Palaeointensity and directional data from 9 radiocarbon dated lava flows on Hawaii; age range 2600 BP to at least 17,900 BP. 2600–4000 BP flows yield high VDMs relative to global average. Angular dispersion for this subset is 15.5° (high compared with whole data set). At 18ka there is a low measured VDM with unusually shallow inclinations, while around 10 ka, the VDMs are close to the global average values. Comparison made with other Holocene volcanic series and historic flows

Database Results from 7 reliable flows included

M668 Paleosecular Variation of the Honolulu Volcanic Series, Oahu, Hawaii

Summary 25 flows from the Honolulu series on Hawaii sampled. AF demagnetisation. K-AR ages from 30– 850 ka, with some evidence that the upper part of the series is < 70 ka and the older is 350 ka.

Database 25 N flows.

ICELAND

*** G16-19,20,29,30; (M1139) Upper Miocene and Pliocene geomagnetic SV, W. Iceland**

Summary Study of VGP dispersion from 362 flows extruded at approximately regular rate. Used to extend geomagnetic polarity scale back to 6.5 Ma. Geological, stratigraphic details in *McDougall et al.* [1977]. Stratigraphic column sampled about 3.5km and covers period 1.6 – 6.7 Ma. Flow thicknesses vary considerably and some have been affected by recent hydrothermal alteration. Intrusives occupy only a small percentage of exposed volcanic pile. Lavas dip between 2° and 8° to the southeast except in one area where they dip eastward. Extensive normal faulting parallel to strike of flows and some faulting perpendicular to strike. AF demagnetisation up to 200 Oe. K-Ar dates. Paper concludes has been no long-term changes in inclination over the 6.7-1.6 Ma period in contrast to a previous study by *Wilson and McElhinny* in E. Iceland [1974] which suggested an increase in inclination over the same period. Also conclude the mean VGP positions for 4 polarity epochs are almost identical, suggesting similar average field structure for both polarities.

Database Original data from this paper was re-analysed by Kristjansson, who made tectonic corrections and excluded certain data based on high values of within-site dispersion. We updated the *Watkins et al.* [1977] data in the Lee database with this revised Kristjansson data [*Kristjansson*, 1987, personal communication with C. Constable]. (a) Normal polarity: 52 Gauss flows (2.4–3.4 Ma), 29 Gilbert (1.8–2.4 Ma) flows; (b) Reverse polarity: 68 Gilbert (3.4–5.0 Ma), 12 Gauss (2.4-3.4 Ma) flows, 8 Matuyama (1.57–2.4Ma) flows.

M1496 Stratigraphy & Paleomagnetism of the Esja, Eyrarfjall & Akrafjall mountains, SW Iceland

Summary Mapping and sampling of a 2.1 km section (353 igneous units) in SW Iceland spanning 4.2–1.8 Ma and incorporating more than 10 glaciations. Mean field consistent with a geocentric axial dipole. Regional dip is 5°–8° southeastwards, volcanic activity suggested to be fairly constant over the last 7 Ma. Area mapped is bisected by a major fjord, and some difficulties in correlation of strata across it. Most igneous units are basaltic, several glacial horizons. Stratigraphy confirmed by K-Ar dating. At least 3 cores per site drilled, AF demagnetisation up to 200 Oe, minimum dispersion criterion used. 77 flows considered to overlap in time from geological correlations, details of overlaps given in reference.

Database Only one flow used where possible temporal overlap occurs, as defined in paper. (a) Normal polarity: 65 Gauss flows (2.4–3.4 Ma), 10 Matuyama age flows (1.8–2.4 Ma); (b) Reverse polarity: 16 Gilbert (3.4–4.0 Ma), 15 Gauss age (2.4–3.4 Ma) flows, 103 Matuyama (1.8–2.4)

flows

*** G14-40 A detailed survey of the type location for the Gilsa geomagnetic polarity event**

Summary 163 cores from 40 flows in 3 distinct sections of Jokuldalur, Iceland. No mention of tectonic corrections. Conclude that Gilsa and Olduvai cannot be distinguished as distinct normal events within the Matuyama reverse epoch.

Database 19 reverse polarity Matuyama age flows

INDIAN OCEAN

*** G14-24; (M16) Paleomagnetism and K-Ar Age of St. Paul Island, SE Indian Ocean**

Summary 135 cores from 18 separate bodies give an estimate for VGP dispersion for St. Paul Island greater than that for Amsterdam Island. St. Paul Isl. is a volcanic cone with circular central caldera breached to the sea by a large normal fault. It lies 3km SE of the mid-ocean ridge axis. Core complex is composed of pyroclastics and is overlain by tholeiitic flows. Up to 8 cores drilled from each of 15 flows and 3 intrusives. Samples oriented to $\pm$ 2.5°. AF demagnetisation up to 200 Oe. Fresh unaltered samples from 3 flows in known stratigraphic sequence selected for K-Ar dating. Age estimates range from 0.01 – 0.64 My.

Database 14 suitable Brunhes age records. 3 intrusives are not distinguished from the flows, but included as only 3 of them.

*** G14-27; (M18) Brunhes Epoch Geomagnetic Secular Variation on Reunion Island**

Summary VGP dispersion estimated as 17.7° with 95% confidence interval of 14.4° – 22.8°, based on at least 7 samples per flow from 21 flows. Within each flow lateral separation of cores 5m. Suggest that Brunhes SV higher than present which could be due to inadequate temporal distribution of data or to real SV changes. Also detect a large excursion at 0.51–0.61 My. AF demagnetisation at 100 Oe and 200 Oe, and minimum dispersion criterion used.

Database 17 flows with VGP lat > 55°

*** G14-05 /23; (M4) Age of the Comore Isls, W. Central Indian Ocean**

Summary Data from Grande Comore, Anjouan, Mayotte give K-Ar ages in range 0.01–3.65 My, with

age increasing southeastwards along the chain. Mean VGP for each island not significantly different from axial dipole at 95% level. No raw data published in this paper. Data from Grande Comore, Anjouan published in *Watkins et al.*, [1972]

Database 23 Brunhes age flows from Anjouan, 12 Brunhes age flows from Grande Comore.

*** G14-28 /29; (M11) Brunhes Geomagnetic Secular Variation - Indian & Atlantic Oceans**

Summary Data from 401 igneous units (more than half previously unpublished) divided into first order data (more than 4 samples per flow) and second order (no requirement on the number of samples). Both data sets indicate that VGP dispersion increases with latitude. Couldn't reject Pacific non-dipole low hypothesis. Consider Indian Ocean data here – see Atlantic section notes for the Atlantic data from this paper. (1) Comore Islands - Anjouan, Grande Comore: Samples from these 2 of the 4 Comore Islands: 23 samples from Anjouan from the younger flows – 6 are melanocratic-ankaramitic, the remainder are basaltic; 14 samples are from Grande Comore – 5 from fissures in the northern volcanic centre and 9 from the west and central coasts which are ankaramites or feldsparphyric flows from fissure eruptions. Inferred that this data is also that used by Hajash and Armstrong [1972], but the raw data is not published in Hajash and Armstrong [1972]. This paper infers Brunhes age based on stratigraphy and polarity, which is consistent with the 1 radiometric age reported in Hajash and Armstrong [1972] for Grande Comore (0.01 ± 0.01 My) and the one normal polarity age reported for Anjouan (0.39 ± 0.2 My). (2) Amsterdam Island: Lies on transform fault, young looking volcanic cone. 12 flows sampled. (3) Crozet Islands – Possession and East Island: Possession Island is the largest of the Crozet group. Series of horizontal to sub-horizontal basaltic flows at surface; similar geochemically and geomorphologically to East Island. K-Ar dating places Brunhes-Matuyama boundary in the lower part of 3 of sequences sampled on Possession. All flows from East Island from Brunhes. 43 flows sampled on East Island (mostly 1 sequence) and 38 on Possession. Data presented in this paper collected over 5 years. Number of specimens per body varies. Orientation accuracy 2.5°. One specimen per core AF demagnetised at 100, 200, 300 Oe and mean direction computed using minimum scatter criterion.

Database (a) Crozets (Possession) – 32 Brunhes (assume no overlap of different sequences); 2 low VGP lat sites removed and another with only 2 samples removed; (b) Crozets (East) – 37 Brunhes flows, 3 low VGP lat sites removed.

Concern Amsterdam Isl. data was removed (11 records) from *Lee* database because of possible overlap with that in *Watkins and Nougier* [1973]. Lower precision parameter associated with some records, but these records retained due to extensive study in this area

M17 Excursions and secular variation during the Brunhes in the Indian Ocean

Summary 33 flows on Amsterdam Island sampled, all Brunhes age. Six flows record 50°–80° latitudinal departure of the VGP from the present geographical pole – probably recording 1 or 2 excursions. Remaining 27 lavas give a VGP angular standard deviation of 14.6° with 95% confidence interval of 12.5° – 17.7°. Amsterdam Island comprises an older volcanic episode in the SW of the island and younger extrusives elsewhere. Lavas range in composition from olivine tholeites to high alumina basalts. No radiogenic ages, but geology consistent with Brunhes age. 237 cores, 2.5 cm diameter from 33 lava flows. Cores oriented to ± 3° in situ. Sites 11, 20–29 from the geomorphologically older parts of the sland. Sites 30–33 from Recent summit crater and remaining sites from the younger flows draping the old volcanic center. AF demagnetisation at 100 Oe and 200 Oe. Flows 2,13,17,18,19,24 have VGP lats in the range 24.5° to 32.2°, possible evidence for excursion(s).

Database Flows 1, 3-10, 12, 14-16, 20,21,23, 25, 27-33 ok. All Brunhes.

C0004 Paleointensity recorded by 2 late Quaternary volcanic sequences, La Reunion

Summary Investigation of two sequences associated with the volcano Piton de la Fournaise. One sequence gave radiometric dates of 5–12 ka, the other 82–98 ka. Detailed rock magnetic studies and Thellier palaeointensity experiments performed. VDMs show very little variation for youngest sequence and are comparable with worldwide VDM fluctuations for this period. Data from older sequence the only data for this time interval and gave VDMs comparable with younger sequence. Results indicate intermittent emplacement of flows.

Database 27 Brunhes age flows

*** G14-48; (M32) Age and Duration of the Reunion Geomagnetic Polarity Event**

Summary Reunion polarity event is dated at 2.02 ± 0.02 My with a duration of 10–50 Kyr. Omit event data in case of insufficient temporal distribution for estimation of secular variation. Two sequences sampled: Grande Chaloupe and Riviere St. Denis. Riviere St. Denis (RD) section

stratigraphically lower than Grande Chaloupe (GC) section. GC – 3 oriented samples from each of 7 flows. RD section - 3 cores per flow from 29 flows. Oriented to ± 3°. AF demagnetisation up to 300 Oe. K-Ar dates for 8 of the flows. Lowest 2 samples in GC section normal polarity, next had random magnetisation, upper 4 reverse polarity. 16 lower samples of RD section reverse polarity, next 11 normal, top transitional. Presumably seeing Matuyama to the end of Reunion in RD.

Database 13 R magnetised flows of RD section. Omit N data (Reunion) due to insufficient temporal sampling. Omit GC section since insufficient stable polarity data.

NORTH AMERICA

*** G11-08 Paleomagnetism, K-Ar ages and geology of Valles Caldera rhyolites, New Mexico**

Summary Rhyolites and tuffs of Valles Caldera sampled to compare with previously established geomagnetic polarity timescale. Bandelier Tuff deposited about 1.4 my ago, rhyolites subsequent to this – both Matuyama and Brunhes epoch. AF demagnetisation. K-Ar dates.

Database 6 Brunhes age normal polarity rhyolites suitable.

*** G14-33; (M20) Palaeomagnetic Investigations of Tertiary and Quaternary Igneous Rocks**

Summary Investigated palaeomagnetism of volcanics from the Valley of Mexico, partly to study any possible relationship between oxidation state and magnetic polarity (didn't find any). Use the frequency of polarity changes observed to establish the temporal distribution of their sampling. Plio-Pleistocene data is from the Chinchinautzin volcanic group. Valley of Mexico is a basin surrounded by volcanic rocks Upper Oligocene to Recent in age. Little published on the geology of the Valley. Relevant formation here is the Chinchinautzin group (Upper Pliocene – Pleistocene to Recent). 5–10 cores per site. 2 specimens per site AF demagnetised up to 1200 Oe. Remaining samples demagnetised at the level at which stable remanence reached in the pilot samples and at one level higher. Mean directions then taken from the demagnetisation stage which gave the highest magetization value and the smallest cone of confidence.

Database Removed flows 11,13,22,26,27,32 leaving 30 Brunhes records. Only a handful of these data are used in a later compilation by *Herrero-Bervera et al.* [1986] – not clear why.

M1429 Negative Inclination Anomalies from the Medicine Lake Highland Lavas, N. Ca.

Summary Data from 21 Quaternary age flows from Medicine Lake Highlands give a mean VGP at 78.0°N, 42.4°E – far sided and right-handed. Mean inclination is 49.3°, 12° shallower than predicted by a GAD. Volcanic activity (Recent) is dominantly andesitic with some high-alumina olivine tholeiites and some low-Si andesite. Most flows 1–5 kyrs old, all the volcanics probably less than 100,000 yrs old (K-Ar ages). No maghaemite observed in the 21 Brunhes age flows sampled, suggesting post-solidification oxidation not a significant factor. 6 – 8 cores per flow. Care taken to sample only sites which had not undergone post deposition rotation. Stepwise AF demagnetisation (25–800 Oe) on several samples, NRM generally very stable. Remaining samples demagnetised at 200 Oe.

Database Remove 1,4,17,20 due to low value of precision parameter. Remove flow 7 due to low VGP lat. Leaves 16 records.

M1749 Palaeomagnetic Results from rocks from the E.Trans-Mexican Volcanic Belt.

Summary E. TMVB classified into 4 geological units. 55 sites sampled, AF demagnetised. Used stability index [*Symons and Stupavsky*, 1974] to establish optimum demagnetising field. Rock magnetic studies done. Sites 1–33 of quaternary age and thus of interest here.

Database 20 Brunhes age records suitable.

C0005 Paleomagnetic directions from the Iztaccihuatl volcano, Mexico

Summary This 1985 paper refers to a 1971 paper by the same author for details of palaeomagnetic sampling and lab work. AF demagnetisation and thermal demagnetisation. Magnetic carrier essentially pure magnetite, flows normally magnetised. 24 flows yield a value for VGP dispersion consistent with that expected for Brunhes epoch. Results consistent with K-Ar dates for volcano.

Database 21 of the 24 flows suitable

C0006 Paleomagnetism and K-Ar ages of volcanic rocks from Long Valley Caldera, Ca

Summary K-Ar dates indicate post-caldera eruptions began about 0.73 Ma and continued intermittently until about 50,000 yrs ago. Mean pole position from 33 volcanic units is indistinguishable

from the geographic pole. VGP scatter about this mean pole is 16.0° with 95% confidence limits of 13.6° and 19.3°. Rocks sampled mostly rhyolities or basalts with 3–8 cores per site. AF demagnetisation performed with optimum field chosen on basis of behaviour during demagnetisation.

Database 33 Brunhes age flows (2 flows excluded on the basis of low k)

C0007 Magnetostratigraphy and secular variation at Level Mountain, N. British Columbia

Summary Results from 50 flows indicate eruptive behaviour began about 6.5 Ma and continued intermittently until very recent times. Most flows from stable polarity periods, but 2 record Gauss /Matuyama transition (as confirmed by K-Ar dates) and 4 possibly represent an excursion during the early Gauss. Average VGP position not significantly different from geographic pole, but is near-sided rather than far-sided. VGP scatter (about the mean direction) is 21.9° with 95% confidence limits of 19.9° and 24.4°. Two distinct sections, separated by 10 km sampled. Field evidence suggests sections don't overlap and there is no significant hiatus between them. AF demagnetisation and minimum dispersion citerion used.

Database Only 11 suitable flows as all of section A may be > 5 Ma

Concern Flows span age range 0 – 5 Ma so may be insufficient temporal sampling of each epoch

M713 Evidence for excursions and secular variation from the Wrangell Volcanics,Alaska

Summary Sampled 36 late Tertiary (3–4 my) flows from 3 sections of Wrangell volcanics. Data from 1 section purely from an excursion (11 flows); from another (16 flows) is partly excursion, partly stable polarity; from another all stable polarity (9 flows). All stable polarity data is normal – Gauss epoch. Exclusion of excursion data yields value for PSV consistent with model predictions (14.0° with respect to the geographic north pole). Age of all 3 sections 3.4 my. 3 – 7 cores per flow. Stepwise AF demagnetisation. For section with some excursion data & some stable polarity data pilot AF demagnetisation was done on 24 samples from 13 of the 16 flows and a value of 380 Oe chosen for blanket demagnetisation of remaining samples. Since fewer samples collected from other 2 sections 1 specimen per sample demagnetised until an end-point reached (below 340 Oe). Mean direction calculated using minimum dispersion criterion.

Database All 9 flows from Air II location ok.

Concern Secular variation estimate may be less reliable due to limited temporal data distribution.

*** G9-13 Paleomagnetism of Pliocene Basalts from the SW USA**

Summary Flows from Rio Grande Gorge near Taos, N.M. and near Flagstaff, Az sampled. Taos plain covered by Tertiary-Quaternary olivine basalts – 14 flows and 2 baked sediments cored. Seven basalts and 2 baked sediments sampled near Flagstaff. Rock magnetic studies and AF demagnetisation performed. Early study (1967) so just interested in detecting reversals and investigating general magnetic stratigraphy.

Database Data only given to nearest degree but otherwise ok. Arizona data removed since only 4 sites. 2 sub-sequence flows (Rio Grande) removed since may overlap main sequence. Leaves nine records with K-Ar dates in range 3.62–4.38 Ma.

C0008 Revised paleomagnetic pole for the Sonoma volcanics, California

Summary Study is an update of a 1972 study in the same area by *Mankinen*. Data from 25 flows yields a mean VGP position significantly different from the present day geographic pole. It is speculated that this is due to insufficient sampling of PSV rather than a different average field direction. VGP scatter is 18.6° with 95% confidence limits of 15.4° and 23.1°. Results not significantly different from those from the earlier 1972 study. Data spans 8 – 3 Ma. AF demagnetisation.

Database 13 andesite flows from Andesite Peak, spanning 4 – 5.5 Ma

C0009 Paleomagnetism of Plio-Pleistocene Louisetown formation, Virginia City, Nevada

Summary 61 flows sampled and their remanence directions fall into 2 distinct groups, both different from those predicted by an axial dipole field. One set of flows probably represents a polarity transition, the remaining flows suggest the late Pliocene field was significantly different from an axial dipole field. 6 cores per flow, AF demag, rock magnetic studies.

Database 6 R polarity flows from Carson Range and Truckee Basin suitable.

Concern No detailed age information (0–5Ma)

PACIFIC OCEAN

*** G14-35; (M22) Palaeosecular variation of the geomagnetic field in the Aleutian Isls., Alaska**

Summary Palaeomagnetic samples taken from 6 Aleutian Isl sites to investigate the geographical limits of the low SV observed in the Pacific in other studies. Angular standard deviation in field directions is 10.8°, compatible with other low values from the Pacific region. Data from all sites need to be combined to obtain reasonable SV estimate. Age range of flows is late Tertiary to Quaternary. At least 5 cores per flow. AF demagnetisation. Individual site descriptions given.

Database 53 N polarity flows, 8 R polarity flows.

Concern Lack of age information

*** G14-09; (M8) Paleosecular Variation of Lavas from the Mariana in the Western Pacific**

Summary Study of 24 flows from Pagan Island gave a mean VGP consistent with GAD. Estimate of VGP dispersion of 6.2° with 95% confidence limits of 5.2° and 7.8°. Conclude either insufficient temporal sampling, or there is a Pacific dipole low, or a belt of low latitude VGP dispersion. Note that the authors could not obtain radiometric dates or get a reliable palaeointensity estimate (Thellier method). Brunhes age is inferred based on geology and polarity. 7 cores per flow taken for 22 of the flows and 6 cores per flow for the remaining two flows. Time span = historical (1925) – mid /late Quaternary. AF demagnetisation done up to 200 Oe, minimum dispersion criterion used.

Database 23 flows of inferred Brunhes age

*** G15-14; (M741) Paleomagnetism and Secular Variation of Easter Island Basalts**

Summary Study of 65 Brunhes age flows. Mean VGP not significantly different from GAD at 95% confidence level. VGP dispersion estimated to be 12.8° with upper and lower limits of 14.8° and 11.3°; consistent with, but less pronounced than, the low SV observed at Hawaii. Lower latitude VGPs cluster in longitude range 90°-150° – possible excursion? Lavas intermediate between island tholeiites and alkali basalts and difficult to correlate across the entire island due to volcanic vents and pyroclastic centres. 3 major volcanic episodes (and volcanoes)

recognised: the youngest (<= 0.24 My) is sampled here from outcrops along sea cliffs. Four samples per flow collected. AF demagnetisation up to 800 Oe on at least 2 specimens per flow. Directions in about 2 /3 of 65 flows changed little on demagnetisation.

Database 53 Brunhes age flows

*** G14-75; (M45) PSV on Lavas from Norfolk & Philip Islands, SW Pacific**

Summary Samples from 87 sites on the two islands gave a mean VGP dispersion of 7.5° and a mean VGP 14° away from rotation axis. Volcanism concentrated in two episodes – one at 3.05 Ma and the other between 2.8 & 2.35 Ma. Low VGP dispersion could be due to insufficient temporal sampling rather than Pacific dipole low. Norfolk island comprises basalts and tuffs, generally flat-lying or with an original dip of a few degrees. Flow thicknesses are 1–30 m. K-Ar dates indicate volcanism over period 3.1–2.35 Ma. Earliest flows during Mammoth reverse event (3.05 Ma), remaining flows span late Gauss and early Matuyama (2.75 – 2.35 Ma). Philip Island about 6.5 km south of Norfolk Island. Mostly tuffs but some basalts. K-Ar dates indicate volcanism occuring in latter part of Gauss (2.8 –2.6 Ma). Assume authors just collected from basalts. Mostly only 2 samples per site. AF demagnetisation in fields 50 Oe – 600 Oe.

Database No VGP lats given in paper. 25N, 12 R polarity records suitable

Concern Possibly insufficient temporal sampling of data

M663 Paleomagnetism of San Cristobal Island, Galapogos

Summary Island is most easterly of Galapogos and comprises large volcano in SW and flows and small cones in NE. Surrounding seafloor estimated to be 9–10 my old. Minimum age of island based on R magnetised samples from S. part of island is 0.7 my. Samples from N. coast give a VGP dispersion of 11.3°, consistent with S.V. models. Sampling confined to 27 sites on N. coast (couldn't land on S. coast); 24 are from Brunhes. In paper sites assigned an 'age group' (0–4) based on relative degradation of flows from field observations and air photos. Eight samples per site. Most cores drilled in or near the intertidal zone; almost none of samples affected by rotation during cooling and /or lightning. Orientation accuracy 2°. Specimens from 12 sites AF demagnetised in fields 12.5 – 800 Oe. In general fields of 50 –100 Oe raise precision parameter to at least 380. Doesn't say if /why didn't clean all samples. Some flows may be

very closely spaced in time, so number of independent Brunhes sites reduced to 17, retaining the more accurate of overlapping flows. Dispersion = 11.3°.

Database Appear to be 18 records in table rather than the 17 mentioned in the text. Brunhes age. Minimum VGP lat = 66.9°. Omit reverse data points since only 2.

C0010 Geomagnetic reversals from volcanic islands of French Polynesia: (1) Huahine

Summary Aim of paper is to look at structure of the field during a reversal. Sampling done in two field seaons. First season involved a general survey around Huahine at same locations as those visited by Duncan [1975], so older data replaced from this reference. Second field season involved detailed study of Mahuti Bay on the southern part of Huahine Iti. No tectonic corrections necessary. Five new K-Ar ages in range 2.91 – 3.08 Ma. Most transitional flows observed in Mahuti area, but no reverse directions sampled indicating most of the volcanic activity on Huahine occurred during the Gauss normal polarity epoch. Some directions close to normal or reverse field directions had low palaeointensities - authors suggest these data actually indicate a transitional field. Flows that record the same average field direction grouped together.

Database Data for Huahine in *Duncan* [1975] and *Lee* database replaced with data from this paper. 32 normal polarity flows suitable: Gauss age.

C0011 Geomagnetic reversals from volcanic islands of French Polynesia: (2) Tahiti

Summary Sequence in the Punaruu Valley, western part of Tahiti Nui, sampled to investigate field structure during reversals. All data Matuyama and younger, spanning Matuyama /Brunhes transition and upper and lower Jaramillo boundaries. Some data reproduced from Duncan [1975]. 123 flows sampled with an average of 6–7 cores per flow. Natural dip of flows of 10° toward ocean. No indication of differences in stratigraphy between different sides of the river. Stepwise AF demagnetisation. Non-transitional normal data are 31 Jaramillo flows, 2 Brunhes flows and 2 dikes. Jaramillo flows yield a mean VGP not significantly different from geographic axis at 95% level. Similarly for the non-transitional reverse flows. Estimate of VGP scatter identical to that of *Duncan* [1975] (13.8°).

Database 23 N (Jaramillo), 39 R polarity Matuyama flows

M1652 Paleolatitudes determined from paleomagnetic data from vertical cores

Summary Paper presents new method for determining the palaeocolatitude of a sampling site and the associated confidence limits, using inclination only data. Method is tested on data for which both inclination and declination are available: lava flows from the Pribilof Islands and Nunivak Island in the Bering Sea. Flows all of Matuyama or Brunhes age. AF demagnetisation. Some directions very similar, suggesting data not independent.

Database 8 Brunhes age N records from Pribilof Isls; 13 Brunhes age N records from Nunivak Isl.; 8 Jaramillo age N records from Nunivak; 8 Matuyama R flows from Nunivak Isl. Care taken not to duplicate flows which are possibly not temporally independent.

*** G14-13,569,188,570,571 (M268) PSV at the Society Islands, French Polynesia**

Summary PSV study involving palaeomagnetic data from 5 of the younger islands of the Society Islands. All samples less than 3.4 Ma. Mean VGP scatter about the geographic axis is 13.8°. Mean VGP is indistinguishable from the geographic axis at 95% confidence level. Flows mostly olivine basalts.

Database Bora Bora (3.1 - 3.4 Ma) - 7 N, 6 R flows Raiatea (2.3 - 2.5 Ma) - 8 N flows Huahine (2.3 - 2.6 Ma) - 7N flows replaced from Roperch and Duncan [1990] Tahiti (0.4 - 1.3 Ma) - 8 N flows suitable - T1,T2,T3,T5,T6,T10,T11,T13 Moorea (1.4 - 1.6 Ma) - 6 R flows

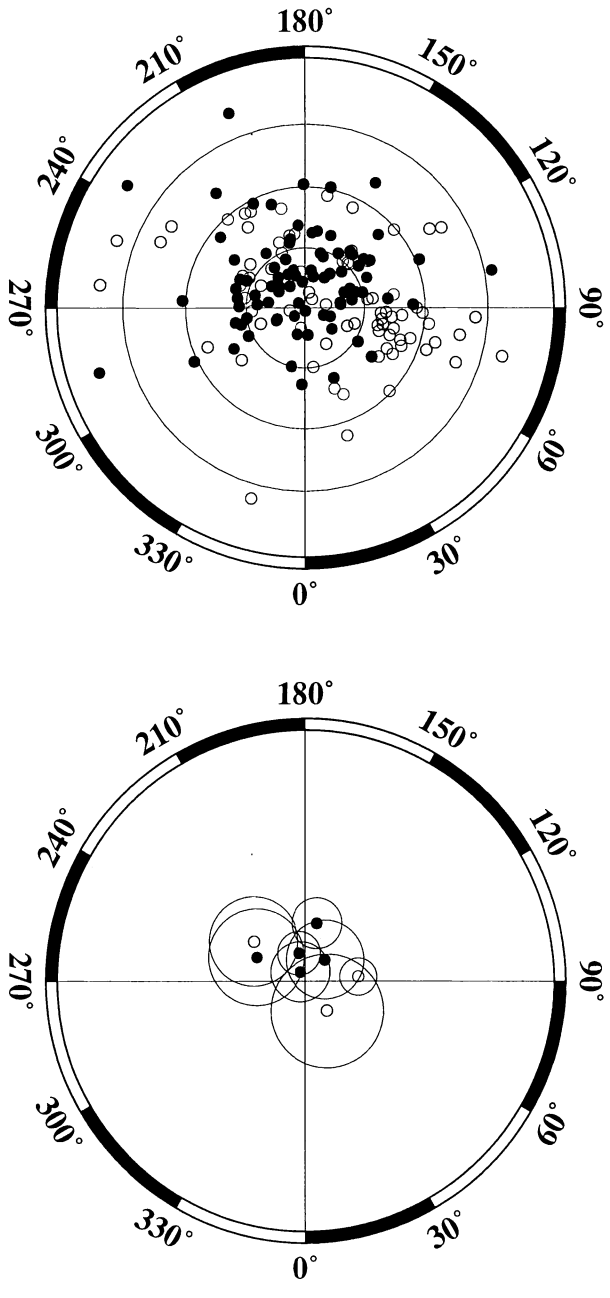

Figure 2.A1: Africa, 86 N (normal polarity records), 80 R (reverse polarity records). In each figure in the appendix the upper plot shows the individual VGP positions calculated for each group of data listed in Table 2.A1. The lower plot shows the mean VGP position for each group together with the 95% confidence cone for the mean. Filled circles represent normal polarity data, open circles represent reverse polarity data. Latitude grid lines are every 10°. For Africa, all bar one of the mean VGP positions are far-sided, and all have corresponding α_{95}s less than 10°. The one near-sided VGP also has has the largest α_{95} and corresponds to 12 Matuyama age reversely magnetised flows from Tanzania.

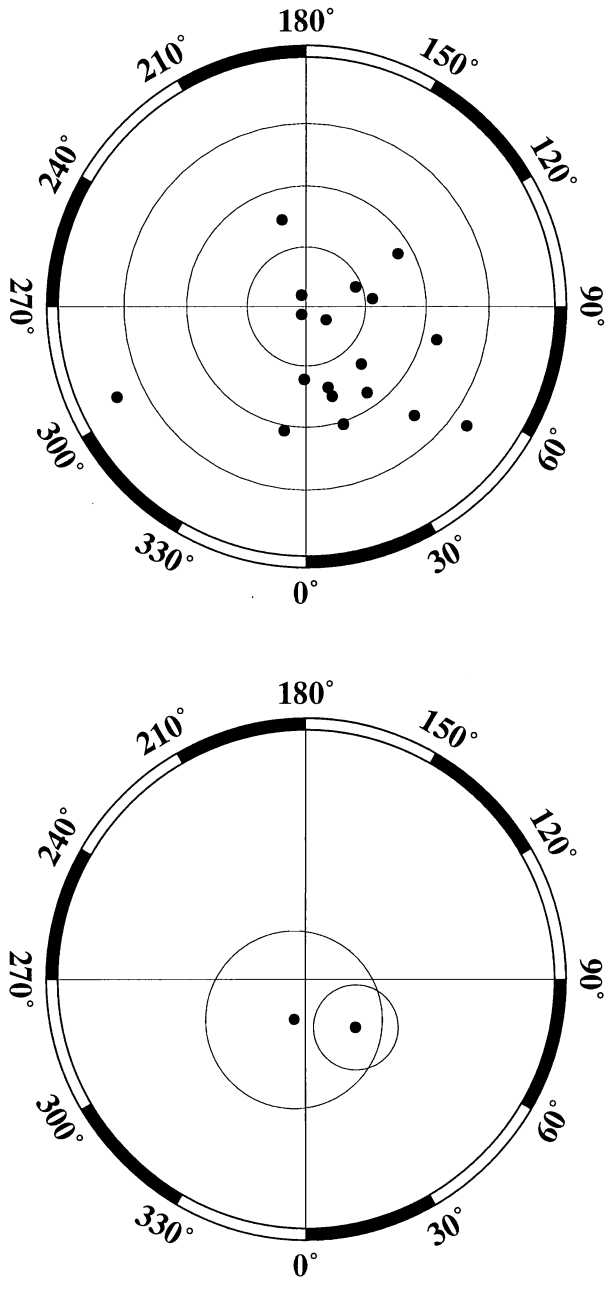

Figure 2.A2: Antarctica, 18 N. Data are only available from two locations, both in McMurdo Province. One pole has an α_{95} of 14.8° and is markedly different from the second pole. These are the highest latitude site locations in the database, but the VGPs indicate that these data cannot provide very good constraints for PSVL studies.

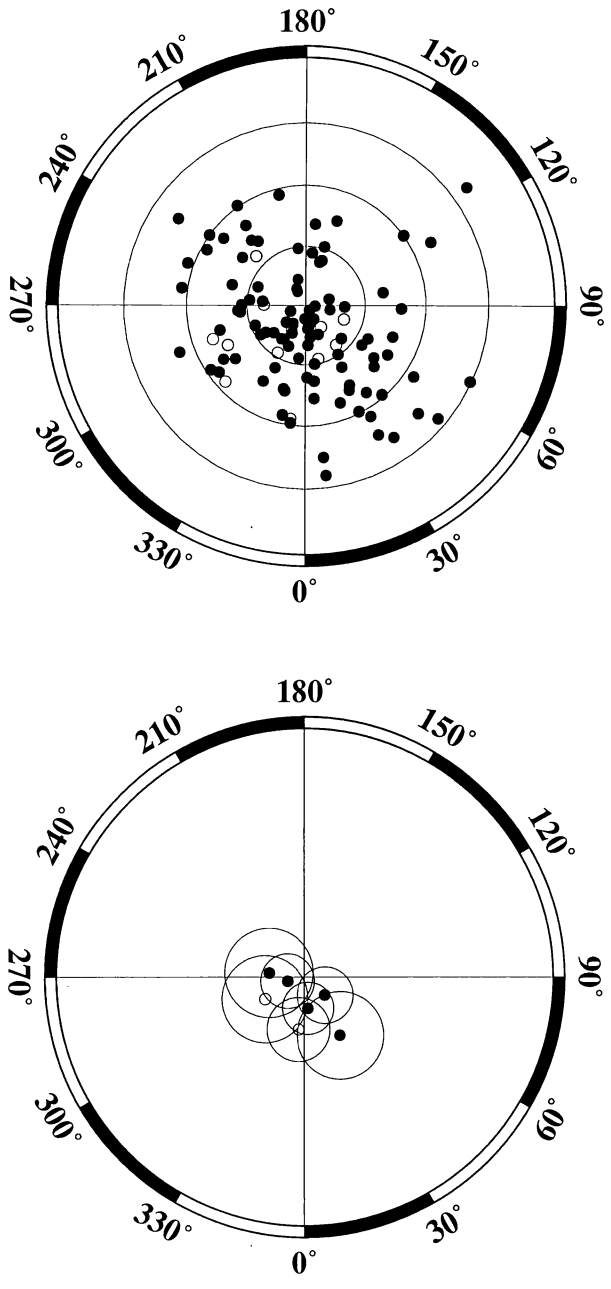

Figure 2.A3: Asia, 100N, 12 R. The mean VGPs are all far-sided and all have α_{95}s less than 8°. Most α_{95}s do not include the geographical pole.

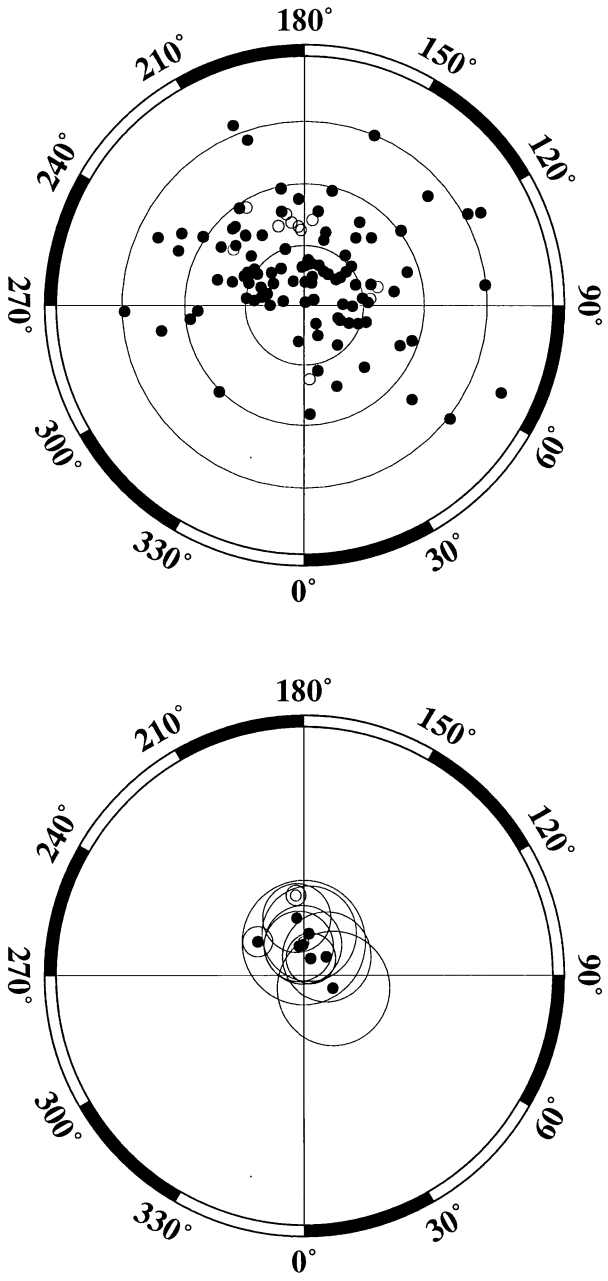

Figure 2.A4: Atlantic Ocean, 98 N 11 R. All except one of the mean VGPs are far-sided. Typical α_{95}s are 7° and most α_{95}s include the geographical north pole. One normal and one reverse polarity mean VGP have extremely small (less than 3 °) α_{95}s.

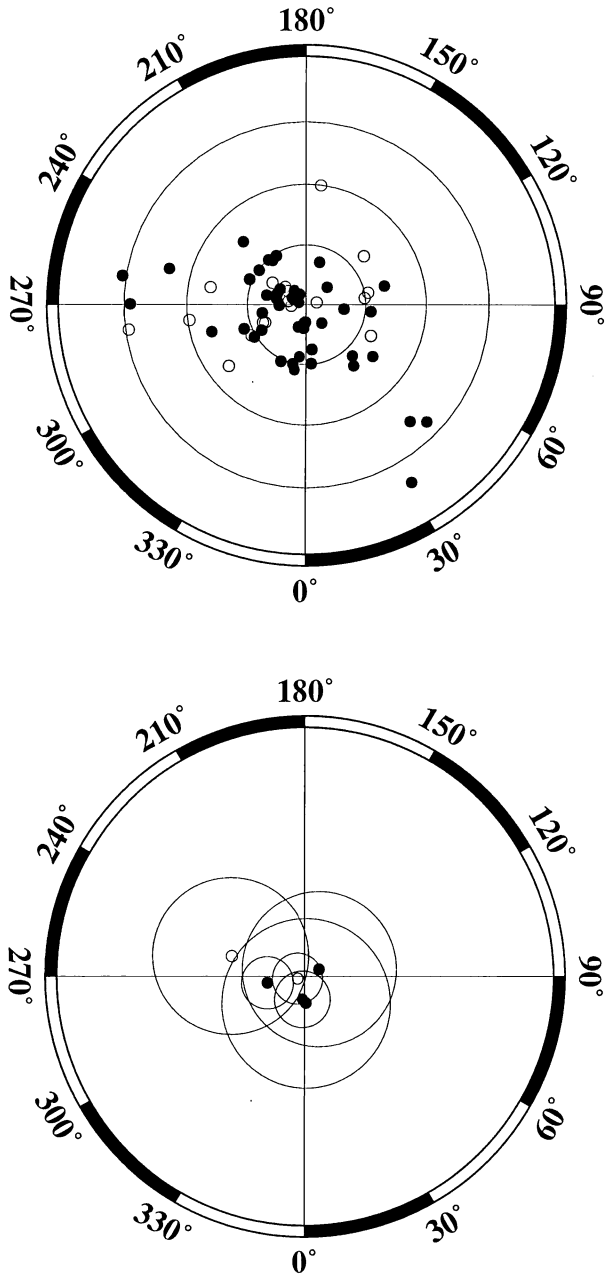

Figure 2.A5: Australia, 46 N, 19 R. Individual flow VGPs appear to indicate far-sided effect, but there is substantial scatter and three of the mean VGPs have corresponding α_{95}s of 4° whilst the other three have α_{95}s of 12° - 15°. The largest α_{95}s correspond to locations where only 5 records contribute to the mean direction - the temporal sampling of the data from these 3 locations is probably insufficient to provide good constraints on PSV in this region.

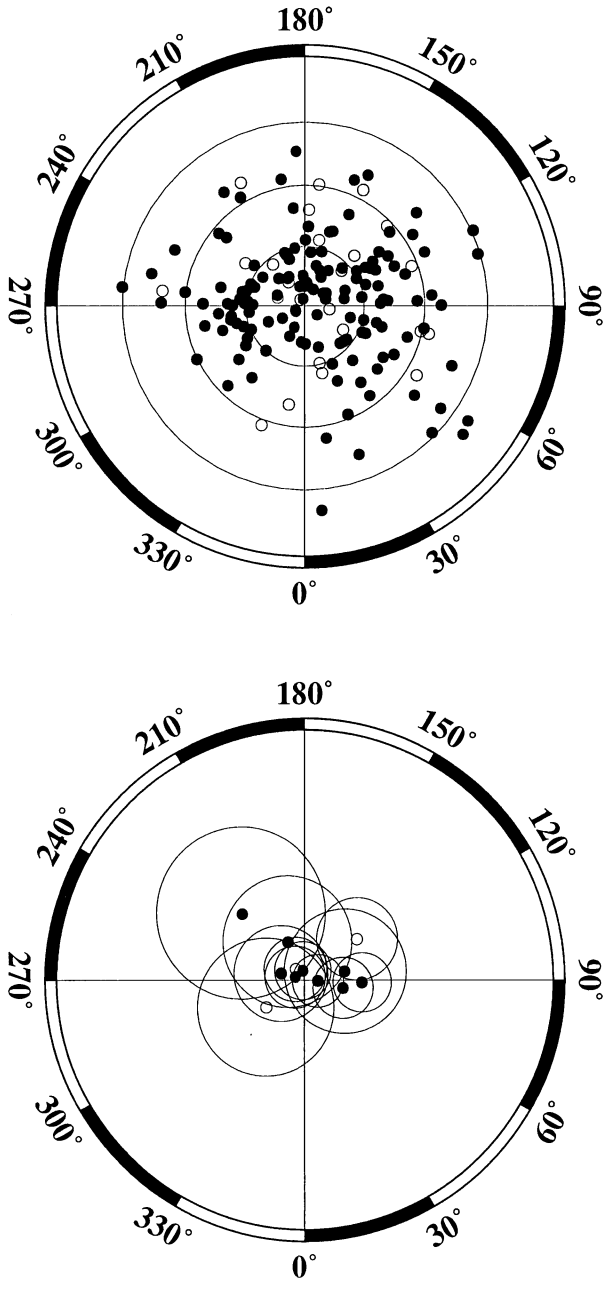

Figure 2.A6: Europe, 138 N, 25 R. Most of the mean VGPs are far-sided and there is a large range of α_{95}s (4° - 14°). The largest α_{95} corresponds to 5 normal polarity Brunhes age flows from the Plateau du Velay in France. The large α_{95} corresponding to a reverse polarity mean VGP is associated with 6 Hungarian flows with the only age constraint being that they are 0 - 5 Ma.

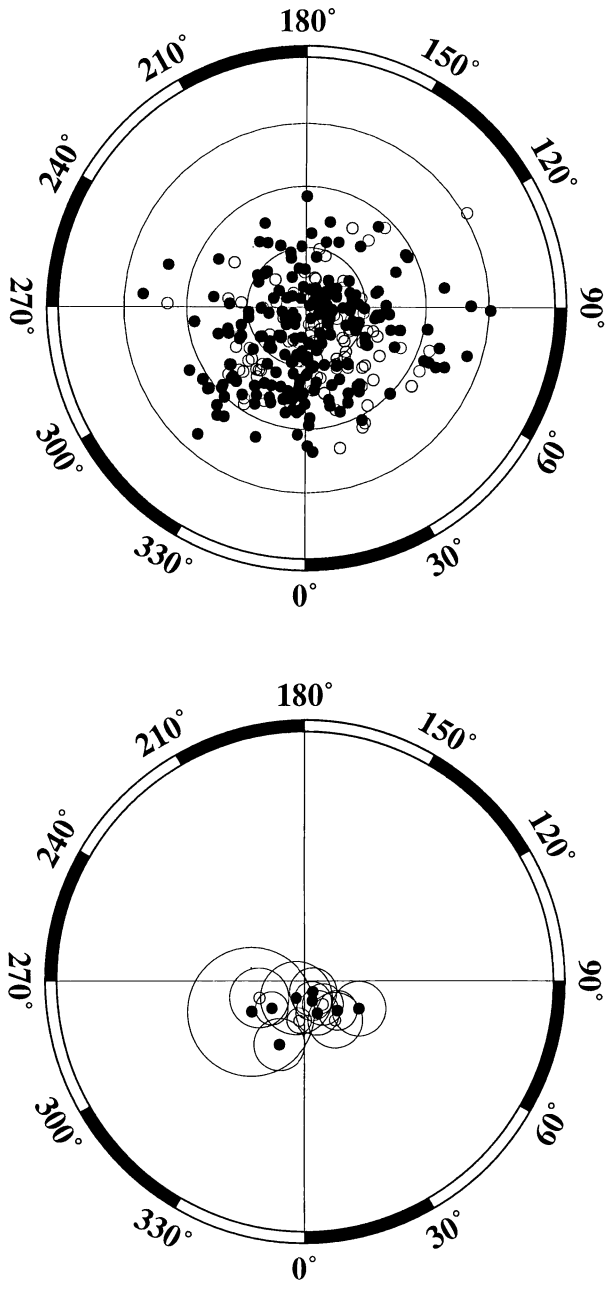

Figure 2.A7: Hawaii, 216N, 107 R. Hawaii contributes the second largest number of points to the database after Iceland. The indivdual flow data appear to exhibit far-sided VGPs, and this is confirmed by the mean VGP positions. All the mean VGPs except one have α_{95}s of 6° or less. The one exception has an α_{95} of 11° and is from 7 dated Holocene flows. Low VGP dispersion in the Pacific has been noted previously [Doell and Cox, 1972; Aziz-ur-Rahman and MacDougall, 1973; U.S. Japan Paleomagnetic Cooperation Program in Micronesia, 1975] and the data from Hawaii in this database support these observations to a first order approximation.

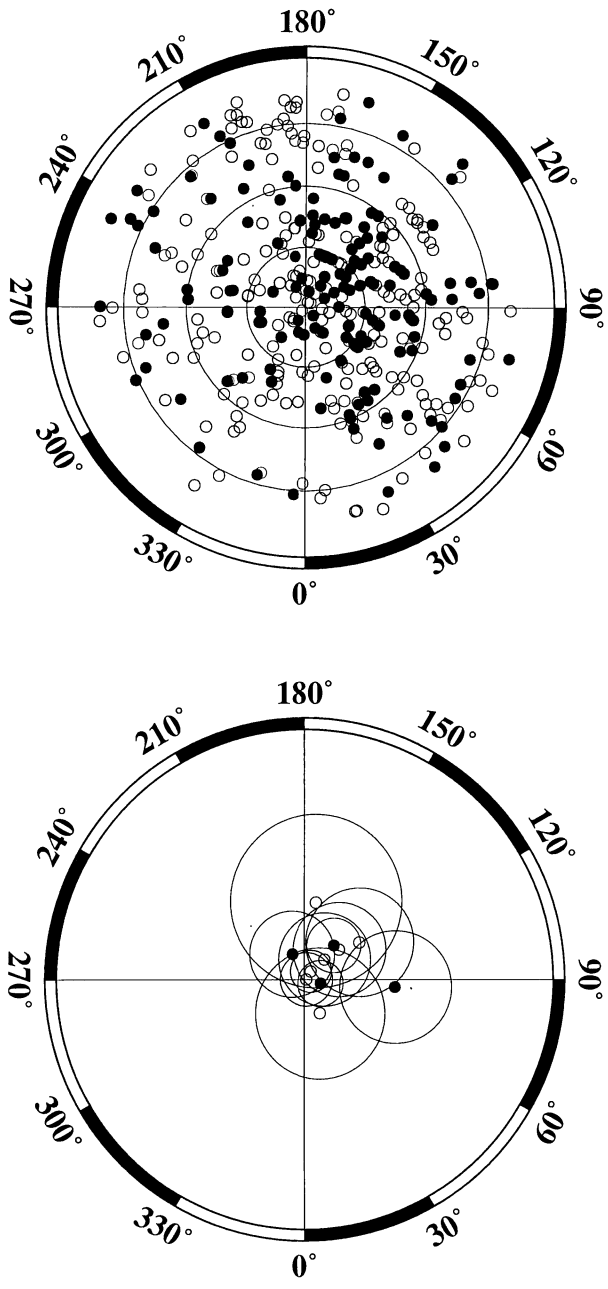

Figure 2.A8: Iceland, 156 N, 241 R. Iceland contributes the most data to the database: most flows are of Matuyama or older age. The large number of data make it difficult to distinguish trends in the individual VGPs, but the mean VGPs are generally far-sided. The α_{95}s are variable, again correlating with the number of points contributing to the mean VGP estimate. One reverse polarity mean VGP with an α_{95} of 11° corresponds to reverse polarity data within the Gauss period. The other reverse polarity mean VGP with a high α_{95} (14°) has just 8 records contributing to the mean VGP estimate. The highest α_{95} for normal polarity data corresponds to 10 normal polarity, but Matuyama age records.

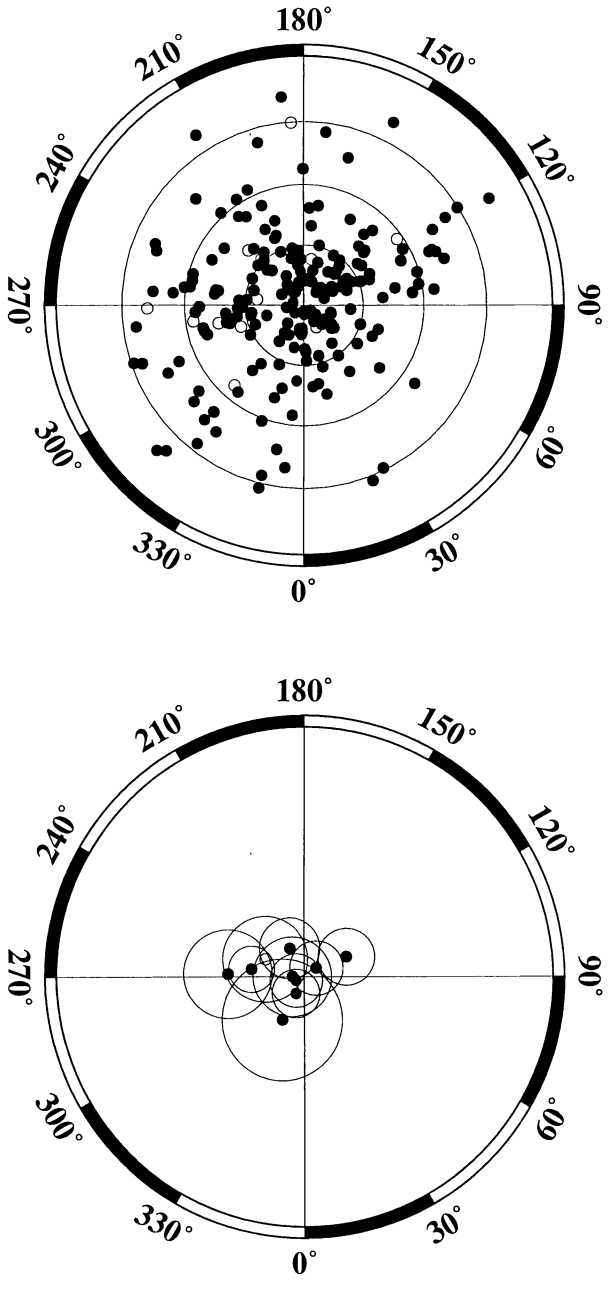

Figure 2.A9: Indian Ocean, 200 N, 13 R. Most mean VGP positions are far-sided and many have α_{95}s which do not include the geographical north pole. All the α_{95}s except one are in the range 4° - 7°. The one anomalous α_{95} is 10° and is associated with a moderate number of contributing flows (14) with large scatter in directions.

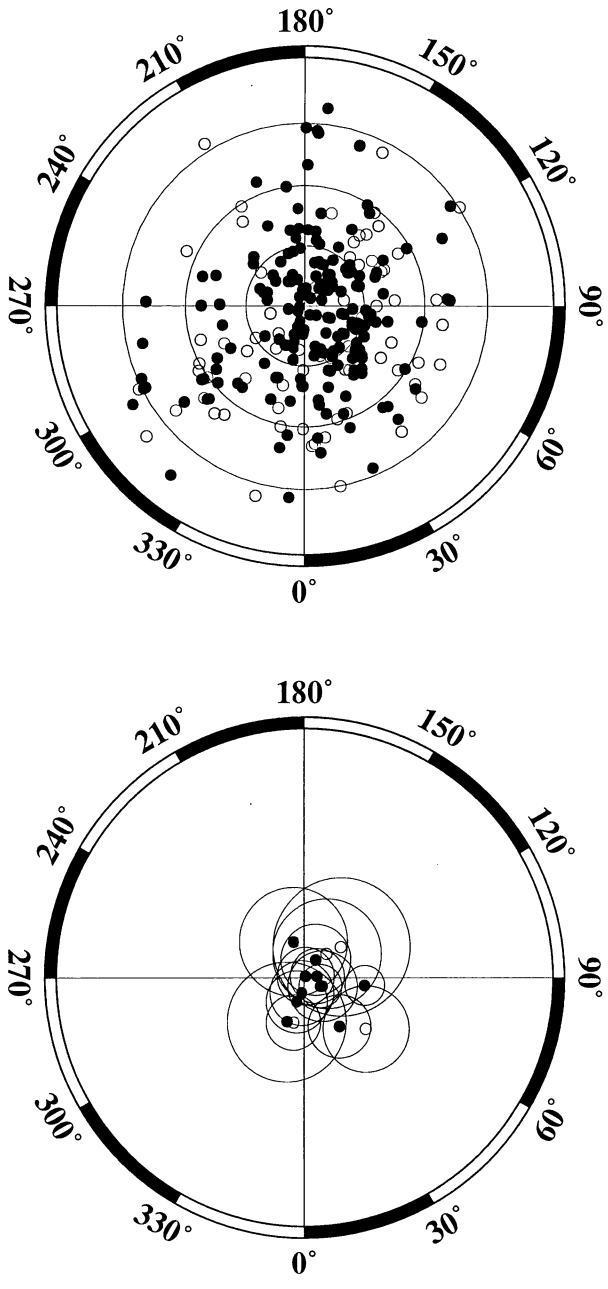

Figure 2.A10: North America, 191 N, 72 R. North America data includes data from a very wide latitudinal band from as far south as Central Mexico up to Alaska. The data are constrained in longitude, being concentrated along the western U. S. The majority of the mean VGPs are far-sided and the α_{95}s vary from 2° - 11°, with the majority being less than 7°.

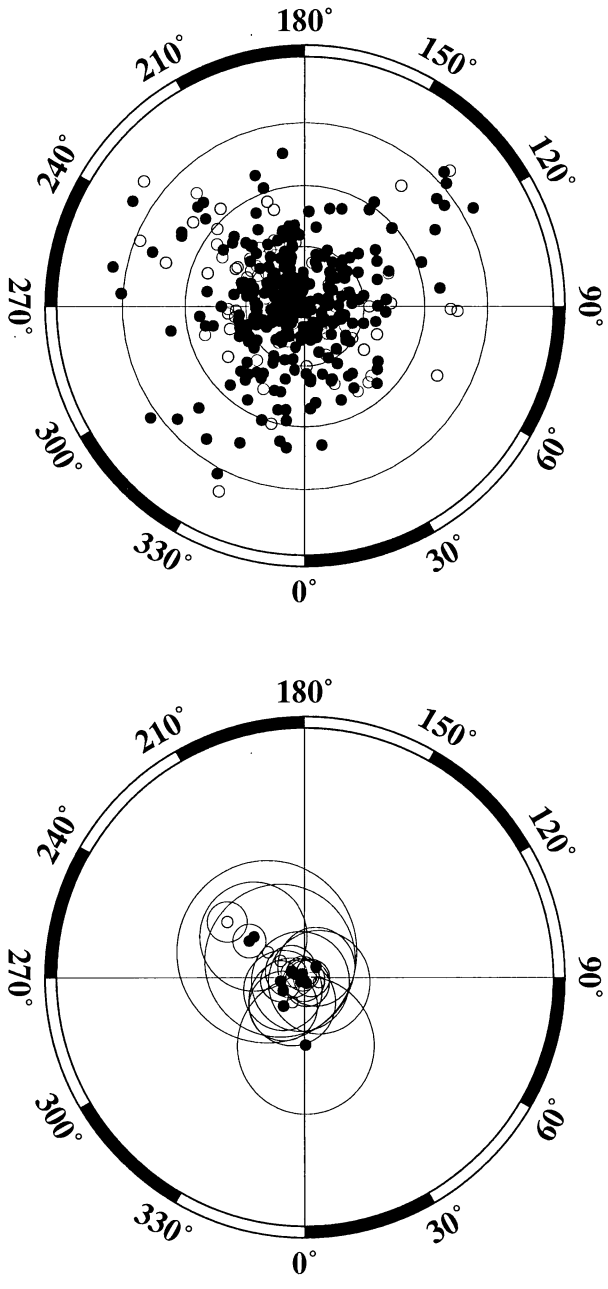

Figure 2.A11: Pacific Ocean, 279 N, 79 R. Most mean VGP postions for the Pacific Ocean (excluding Hawaii) are not far-sided, in contrast to data from all the other geographical regions. Most α_{95}s are less than 7° with 3 being in the range 8° - 9°, and a further one being 11°. The largest α_{95}, 15°, corresponds to reversely magnetised data of Matuyama age from the Aleutians.

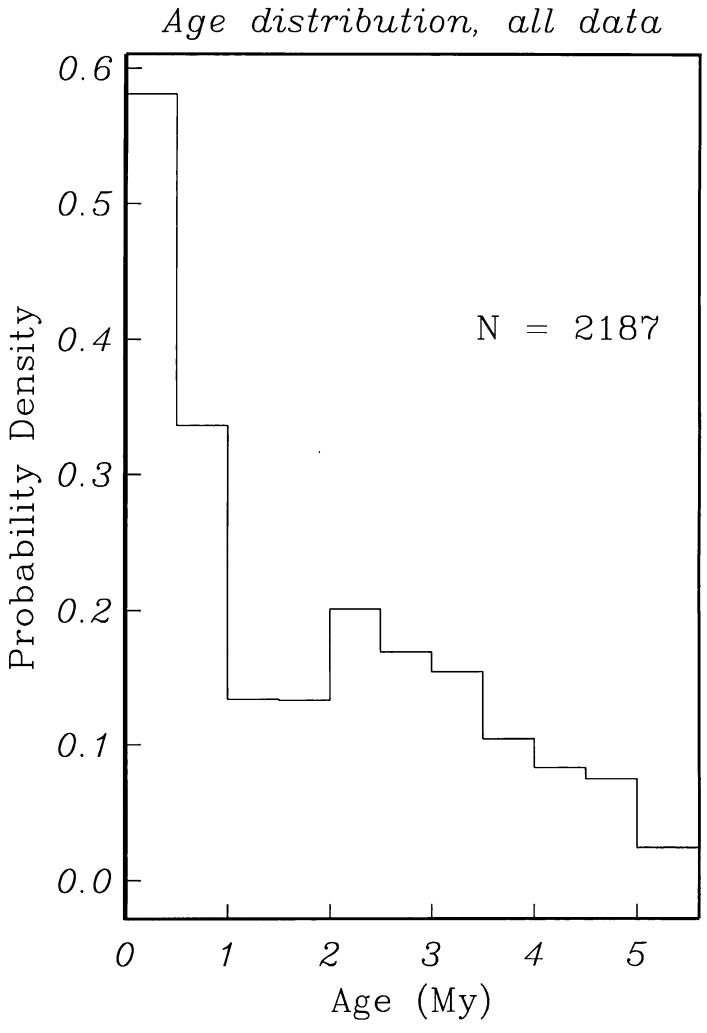

Figure 2.A12: Age distribution of data, normal and reverse polarities combined. Data from each location is assumed to be uniformly distributed over the age interval quoted, and is binned into 0.5 Myr bins. Normalized so that total area under histogram is unity.

Table 2.A1

Ref.	*N*	*First Author*	*Journal*	*Pages*	*Lat*	*Lon*	*Ages*
			Africa				
G14-52	10	Ade-Hall, 1974	C.J.E.S., 11	998–1006	27.80	17.30	0.40 – 2.20
G14-52	54	Ade-Hall, 1974	C.J.E.S., 11	998–1006	27.80	17.30	0.40 – 2.20
G13-09	12	Gromme, 1970	G.J.R.A.S., 22	101–115	-3.20	35.50	0.70 – 2.45
G14-21	15	Piper, 1972	G.J.R.A.S., 29	147–171	4.50	9.00	0.00 – 0.70
G14-22	38	Piper, 1972	G.J.R.A.S., 29	147–171	3.50	9.00	0.00 – 0.70
G14-46	14	Piper, 1972	G.J.R.A.S., 29	147–171	0.00	6.50	0.00 – 0.70
G14-46	9	Piper, 1972	G.J.R.A.S., 29	147–171	0.00	6.50	2.50 – 4.00
G14-46	14	Piper, 1972	G.J.R.A.S., 29	147–171	0.00	6.50	0.00 – 4.00
			Antarctica				
M1319	5	Mankinen, 1988	J.G.R., 93	11,599–11,612	-77.56	166.26	0.56 – 1.39
M1319	13	Mankinen, 1988	J.G.R., 93	11,599–11,612	-78.39	164.23	0.00 – 1.54
			Asia				
G9-06	27	Hsu, 1966	B.G.S.A., 17	27–81	25.30	121.50	0.0 – 3.40
G9-07,8	12	Hsu, 1966	B.G.S.A., 17	27–81	23.50	121.40	0.01 – 5.00
M1588	35	Tsunakawa,1988	J.G.G., 40	221–226	35.21	138.77	0.00 – 0.70
C0001	5	Kono, 1968	J.G.G., 20	353–366	35.00	139.00	0.00 – 1.60
C0002	8	Kono, 1971	J.G.G., 23	1–9	35.00	139.00	0.00 – 1.60
G9-07,8	7	Hsu, 1966	B.G.S.A., 17	27–81	23.60	119.50	0.01 – 5.00
M1301	5	McCabe, 1987	J.G.R., 92	555–580	14.45	120.58	0.00 – 5.00
$O12-262	13				43.50	143.50	0.00 – 1.60
			Atlantic Ocean				
G14-17	20	Ellwood, 1973	J.G.R., 78	8699–8710	38.70	-27.20	0.00 – 0.70
G14-31	15	Amerigian, 1974	J.G.G., 26	429–441	-46.90	37.80	0.00 – 0.70
G14-39	18	Watkins, 1973	G.J.R.A.S., 32	249–267	28.20	-12.80	0.00 – 1.60

G14-39	10	Watkins, 1973	G.J.R.A.S., 32	249–267	27.80	-18.00	0.00 – 1.60
G14-39	14	Watkins, 1973	G.J.R.A.S., 32	249–267	28.70	-14.20	0.00 – 1.66
M1404	7	Schultz, 1986	E.P.S.L., 79	208–216	-3.85	-32.40	1.70 – 5.10
M799	5	Valencio, 1974	R.B.d.G., 4	124–132	-20.52	-29.33	2.30 – 3.30
M1654	9	Briden, 1979	P.T.R.S., 291	485–527	3.30	-61.20	0.29 – 1.28
G14-39	6	Watkins, 1973	G.J.R.A.S., 32	249–267	28.20	-12.80	0.81 – 1.74
M442	5	Richardson,1967	Nature, 215	1470–1473	-3.85	-32.40	1.70 – 5.10

Australia

G11-09	19	Cox, 1969	E.P.S.L., 6	257–267	-38.50	175.00	0.00 – 0.70
G13-11	17	Aziz-ur-Rahman, 1971	G.J.R.A.S., 24	255–269	-38.00	144.50	0.00 – 4.50
G13-11	5	Aziz-ur-Rahman, 1971	G.J.R.A.S., 24	255–269	-38.00	142.80	0.00 – 4.50
G13-11	14	Aziz-ur-Rahman, 1971	G.J.R.A.S., 24	255–269	-38.00	144.50	0.00 – 4.50
G13-11	5	Aziz-ur-Rahman, 1971	G.J.R.A.S., 24	255–269	-38.00	142.80	0.00 – 4.50
$G13-02	5				-4.00	150.00	0.00 – 0.01

Europe

G11-12	7	Bobier, 1969	C.R.A.S., 268	20–23	45.00	3.80	0.00 – 2.30
G12-09	26	Doell, 1970	E.P.S.L., 8	352–362	45.71	2.99	0.00 – 0.70
G12-09	5	Doell, 1970	E.P.S.L., 8	352–362	44.69	4.30	0.00 – 0.70
G10-09	5	Sanver, 1968	P.E.P.I., 1	403–421	38.60	28.70	0.00 – 1.60
G10-09	5	Sanver, 1968	P.E.P.I., 1	403–421	39.50	44.00	0.00 – 1.60
M1072	30	Kohnen , 1978	J.G., 44	545–555	50.40	7.25	0.00 – 0.70
M1513	37	Bohnel , 1987	J.G., 62	50–61	50.30	6.75	0.00 – 0.70
G11-12	13	Bobier, 1969	C.R.A.S., 268	20–23	45.00	3.80	0.70 – 2.41
G12-22	6	Marton ,'70	P.A.G., 81	151–162	46.90	17.50	0.00 – 5.00
M34	6	Barberi, 1974	E.P.S.L., 22	123–132	37.20	14.80	1.40 – 3.60
$O12-257	14				38.00	15.00	0.00 – 1.60
$G14-73	9				34.00	36.00	1.60 – 5.00

Hawaii

M285	28	Doell, 1965	J.G.R., 70	3377–3405	19.50	-155.50	0.01 – 0.02
M285	25	Doell, 1965	J.G.R., 70	3377–3405	19.50	-155.50	0.01 – 5.00
M285	29	Doell, 1965	J.G.R., 70	3377–3405	19.50	-155.50	0.20 – 0.30
M667	46	Doell, 1972	J.G.R., 77	862–876	22.00	-159.50	3.50 – 5.60
M31	14	Doell, 1972	J.G.R., 77	3725–3730	23.10	-158.00	0.00 – 3.00
M31	11	Doell, 1972	J.G.R., 77	3725–3730	22.00	-160.00	0.30 – 0.70
M42	31	Doell, 1972	B.G.S.A., 84	1217–1242	21.50	-158.10	2.40 – 3.60
C0003	7	Coe, 1978	J.G.R., 83	1740–1756	19.40	-155.50	0.00 – 0.02
M668	25	Doell, 1972	J.G.R., 77	2129–2138	21.30	-157.80	0.03 – 0.85
M667	42	Doell, 1972	J.G.R., 77	862–876	22.00	-159.50	3.50 – 5.60
M42	33	Doell, 1972	B.G.S.A., 84	1217–1242	21.50	-158.10	1.80 – 2.60
M31	5	Doell, 1972	J.G.R., 77	3725–3730	22.00	-160.00	3.00 – 5.00
M42	27	Doell, 1972	B.G.S.A., 84	1217–1242	21.50	-158.10	2.40 – 3.60
			Iceland				
M1496	65	Kristjansson, 1980	J.G., 47	31–42	64.50	-22.00	2.40 – 3.40
M1496	10	Kristjansson, 1980	J.G., 47	31–42	64.50	-22.00	1.80 – 2.40
M1139	52	Watkins, 1977	G.J.R.A.S., 49	609–632	64.50	-21.50	2.40 – 3.40
M1139	29	Watkins, 1977	G.J.R.A.S., 49	609–632	64.50	-21.50	3.40 – 5.00
G14-40	19	Watkins, 1975	E.P.S.L., 27	436–444	66.20	-15.20	1.09 – 2.00
M1496	16	Kristjansson, 1980	J.G., 47	31–42	64.50	-22.00	3.40 – 4.00
M1496	15	Kristjansson, 1980	J.G., 47	31–42	64.50	-22.00	2.40 – 3.40
M1496	103	Kristjansson, 1980	J.G., 47	31–42	64.50	-22.00	1.80 – 2.40
M1139	8	Watkins,1977	G.J.R.A.S., 49	609–632	64.50	-21.50	1.57 – 2.40
M1139	12	Watkins, 1977	G.J.R.A.S., 49	609–632	64.50	-21.50	2.40 – 3.40
M1139	68	Watkins, 1977	G.J.R.A.S., 49	609–632	64.50	-21.50	3.40 – 5.00
			Indian Ocean				
G14-24	14	Watkins, 1975	E.P.S.L., 24	377–384	-38.80	77.50	0.00 – 0.70
G14-27	17	Watkins, 1973	J.G.R., 78	7763–7768	-21.10	55.50	0.00 – 0.70
G14-05	12	Hajash, 1972	E.P.S.L., 16	231–236	-11.60	43.30	0.00 – 0.70

G14-23	23	Hajash, 1972	E.P.S.L., 16	231–236	-12.20	44.40	0.00 – 1.62
G14-28	37	Watkins, 1972	G.J.R.A.S., 28	1–25	-46.50	52.20	0.00 – 0.70
G14-29	32	Watkins, 1972	G.J.R.A.S., 28	1–25	-46.50	51.70	0.00 – 0.70
M17	24	Watkins, 1973	J.G.R., 78	6060–6068	-37.83	77.52	0.00 – 0.70
C0004	27	Chauvin, 1991	J.G.R., 96	1981–2006	-21.00	55.50	0.00 – 0.98
G14-48	13	McDougall, 1973	E.P.S.L., 19	443–452	-21.00	55.50	2.00 – 2.11
$G15-3,4,9	14 , 1971		PhD. Thesis		-17.00	47.50	0.00 – 1.60

North Ammerica

G11-08	6	Doell, 1969	G.S.A.M., 116	211–248	35.90	-106.50	0.40 – 0.60
G14-33	30	Mooser, 1974	G. Runds, 63	452–483	19.00	-99.00	0.00 – 0.70
M1429	16	Brown, 1979	E.P.S.L., 42	121–126	41.75	-121.85	0.00 – 0.70
M1749	20	Bohnel, 1981	G.I.V., 20	235–248	19.30	-96.90	0.00 – 0.70
C0005	21	Steele, 1985	G.I.V., 24	159–167	19.20	-98.60	0.00 – 0.70
C0006	33	Mankinen, 1986	J.G.R., 91	633–652	37.67	-119.00	0.00 – 0.75
C0007	11	Hamilton, 1983	G.J.R.A.S.,73	39–49	58.50	-131.50	0.00 – 5.00
M713	9	Bingham, 1976	C.J.E.S., 13	547–554	62.92	-143.16	3.00 – 4.00
G9-13	9	Kono, 1967	J.G.G., 19	357–375	35.50	-111.60	3.62 – 4.38
C0008	13	Mankinen, 1989	G.R.L., 16	1081–1084	38.50	-122.50	4.00 – 5.50
C0009	6	Heinrichs, 1967	J.G.R., 72	3277–3294	39.25	-120.00	0.70 – 5.00
$G14-38	16	Southier			57.50	-130.00	0.00 – 5.00
$G14-38	44	Southier			57.50	-130.00	0.00 – 5.00
$M1316	6	Geissman			35.90	-106.50	0.00 – 1.60
$O11-362	23				19.60	-99.00	1.60 – 5.30

Pacific Ocean

G14-09	23	US-Japan Prog, 1975	J.G.G., 27	57–66	18.10	145.70	0.00 – 0.70
G14-35	53	Bingham, 1972	G.J.R.A.S., 28	317–335	53.00	-172.00	0.00 – 5.00
G15-14	53	Isaacson, 1976	J.G.R., 81	1476–1482	-27.10	-109.20	0.00 – 0.70
G14-75	25	Aziz-ur-Rahman, 1973	G.J.R.A.S., 33	141–155	-29.10	167.90	2.40 – 3.10
M663	18	Cox, 1971	E.P.S.L., 11	52–160	-0.83	-88.42	0.00 – 0.70

C0010	32	Roperch, 1990	J.G.R., 95	2713–2726	-16.75	-151.00	2.01 – 3.00
C0011	23	Chauvin, 1990	J.G.R., 95	2727–2752	-17.67	-149.58	0.60 – 1.20
C0011	23	Chauvin, 1990	J.G.R., 95	2727–2752	-17.67	-149.58	0.60 – 1.20
G14-75	12	Aziz-ur-Rahman, 1973	G.J.R.A.S., 33	141–155	-29.10	167.90	2.40 – 3.10
G14-35	8	Bingham, 1972	G.J.R.A.S., 28	317–335	53.50	-168.10	1.50 – 2.30
M1652	8	Cox, 1984	R.G.S.P., 22	47–72	57.18	-170.36	0.00 – 0.80
M1652	13	Cox, 1984	R.G.S.P., 22	47–72	59.99	-165.87	0.00 – 0.80
M1652	8	Cox, 1984	R.G.S.P., 22	47–72	60.33	-166.09	0.80 – 2.40
M1652	8	Cox, 1984	R.G.S.P., 22	47–72	60.33	-166.09	0.80 – 2.40
G14-13,569	8	Duncan, 1975	G.J.R.A.S., 41	245–254	-17.67	-149.58	0.40 – 1.60
G14-13,569	6	Duncan, 1975	G.J.R.A.S., 41	245–254	-17.53	-149.85	1.40 – 1.60
G14-188,570,571	7	Duncan, 1975	G.J.R.A.S., 41	245–254	-16.50	-151.27	3.10 – 3.40
G14-188,570,571	8	Duncan, 1975	G.J.R.A.S., 41	245–254	-16.83	-151.45	2.30 – 2.50
G14-570,571,188	6	Duncan, 1975	G.J.R.A.S., 41	245–254	-16.50	-151.27	3.10 – 3.40

Key to Table A1 Data "groups" contributing to the revised database. A group is defined by at least 5 flows within a specified age range from the same sampling area. N is the # of contributing flows, Lat, Lon are the mean site latitude and longitude and $LoAge, HiAge$ are the minimum and maximum ages of the contributing flows in Myr.

'$' sign before reference code => reference unavailable & hence no summary provided

Ref Code is the source for the original reference and should be interpreted as follows:

(a) GX-Y = Geophysical Journal, Royal Astronomical Soc., Pole Compilation, pole Y in compilation X

(b) MX = Global Paleomagnetic Database (GPMDB) database reference code X

(c) OX-Y = Ottowa Pole Compilation, pole Y in compilation X

(d) CX = this study reference X

Journal reference codes are as follows:

(a) B.G.S.A. = Bulletin of the Geological Society of America

(b) C.J.E.S. = Canadian Journal of Earth Sciences

(c) C.R.A.S. = Comptes Rendues Academie Science Paris, Series D

(d) E.P.S.L. = Earth and Planetary Science Letters

(e) G.I.V. = Geofisica Internationale

(f) G.J.R.A.S. = Geophysical Journal of the Royal Astronomical Society

(g) G.R.L. = Geophysical Research Letters

(h) G. Runds = Geologische Rundschau

(i) G.S.A.M. = Geological Society of America, Memoirs

(j) J.G. = Journal of Geophysics

(k) J.G.G. = Journal of Geomagnetism and Geoelectricity

(l) J.G.R. = Journal of Geophysical Research

(m) P.A.G. = Pure and Applied Geophysics

(n) P.E.P.I. = Physics of the Earth and Planetary Interiors

(o) P.T.R.S. = Philosophical Transactions of the Royal Society of London

(p) R.B.d.G. = Revista de Brasileira de Geociencias

(q) R.G.S.P. = Reviews of Geophysics and Space Physics

REFERENCES - MAIN TEXT

Baag, C., & Helsley, C. E., 1974. Geomagnetic Secular Variation model E. *J. Geophys. Res.*, **79**, 4918–4922.

Barton, C. E., 1983. Analysis of palaeomagnetic time series - techniques and applications. *Geophys. Surv.*, **5**, 335–368.

Barton, C. E. & McElhinny, M. W., 1981. A 10, 000 yr geomagnetic secular variation record from three Australian maars. *Geophys. J. R.. Ast. Soc.*, **67**, 465–485.

Clement, B. M. , 1991. Geographical distribution of transitional VGPs: evidence for non-zonal equatorial symmetry during the Matuyama-Brunhes geomagnetic reversal. *Earth. Planet. Sci. Lett.*, **104**, 48–58.

Constable, C. G., & Parker, R. L., 1988. Statistics of the Geomagnetic Secular Variation for the Past 5 m.y. *J. Geophys. Res.*, **93**, 11,569–11,581.

Constable, C., 1992. Link between geomagnetic reversal paths and secular variation of the field over the past 5 My. *Nature*, **358**, 230–233.

Cox, A., 1962. Analysis of the present geomagnetic field for comparison with paleomagnetic results. *J. Geomagnetism and Geoelectricity*, **13**, 101-112.

Cox, A., 1968. Lengths of geomagnetic polarity intervals. *J. Geophys. Res.*, **73**, 3247–3260.

Cox, A., 1970. Latitude Dependence of the Angular Dispersion of the Geomagnetic Field. *Geophys. J. R. Ast. Soc.*, **20**, 253–269.

Creer, K. M., Irving, E., & Nairn, A.E.M., 1959. Paleomagnetism of the Great Whin Sill. *Geophy. J. R. Ast. Soc.*, **2**, 306–323.

Creer, K. M., 1962. The dispersion of the geomagnetic field due to secular variation and its determination for remote times from paleomagnetic data. *J. Geophys. Res.*, **67**, 3461–3476.

Creer, K.M., Tucholka, P. & Barton C.E., 1983. *Geomagnetism of baked clays and recent sediments*. Oxford: Elsevier.

Egbert, G.D., 1992. Sampling Bias in VGP Longitudes. *Geophys. Res. Lett.*, **19**, 2353–2356.

Ellwood, B. B., Watkins, N. D. & Amerigian, C., 1973. Brunhes epoch geomagnetic secular variation on Terceira Island, Central North Atlantic. *J. Geophys. Res.*, **78**, 8699–8710.

Fisher, R., 1953. Dispersion on a sphere. *Proc. Roy. Soc.*, **217, A**, 295–305.

Gubbins, D. & Kelly, P., 1993. Persistent patterns in the geomagnetic field over the past 2.5 Myr. *Nature*, **365**, 829–832.

Harrison, C. G. A., 1980. Secular Variation and Excursions of the Earth's Magnetic Field. *J. Geophys. Res.*, **85**, 3511–3522.

Irving, E. & Ward, M.A., 1964. A statistical model of the geomagnetic field. *Pure Appl. Geophys.*, **57**, 47–52.

Johnson, C. L. & Constable, C. G., 1994. The time-averaged geomagnetic field as recorded by lava flows over the past 5 million years. submitted to *Geophys. J. Int.*.

Kendall, M. & Stuart, M., 1979. *The advanced theory of statistics, vol. 2, Inference and relationship 4th ed.*. MacMillan, New York.

Langereis, C.G., van Hoof, A.A.M. & Rochette, P., 1992. Longitudinal confinement of geomagnetic reversal paths as a possible sedimaentary artifact. *Nature*, **358**, 226–230.

Laj, C., Mazaud, A., Weeks, R., Fuller, M., & Herrero-Bervera, E., 1991. Geomagnetic reversal paths. *Nature*, **351**, 447.

Laj, C., Mazaud, A., Weeks, R., Fuller,M. & Herrero-Bervera, E., 1992. Statistical assessment of the preferred longitudinal bands for recent geomagnetic reversal records. *Geophys. Res. Lett.*, **19**, 2003–2006.

Lee, S., 1983. A study of the time-averaged paleomagnetic field for the last 195 million years. *PhD. Thesis*. Australian National University

Livermore, R.A., Vine, F.J. & Smith, A.G., 1983. Plate motions and the geomagnetic field - I. Quaternary and late Tertiary. *Geophys. J. R. Ast. Soc.*, **73**, 153–171.

Lock, J. & McElhinny M. W., 1991. The global paleomagnetic database. *Surveys in Geophysics*, **12**, 317–491.

McElhinny, M. W., & Merrill, R. T., 1975. Geomagnetic Secular Variation Over the Past 5 m.y. *Rev. Geophys. Space Phys.*, **13**, 687–708.

McFadden, P. L., & McElhinny, M. W., 1984. A physical model for secular variation. *Geophys. J. R .Ast. Soc.*, **78**, 809–830.

McFadden, P. L., Merrill, R. T., & McElhinny, M. W., 1988. Dipole/Quadrupole Family Modeling of Paleosecular Variation. *J. Geophys. Res.*, **93**, 11,583–11,588.

McFadden, P.L., Merrill, R.T., McElhinny, M.W. & Lee, S., 1991. Reversals of the earth's magnetic field and temporal variations of the dynamo families. *J. Geophys. Res.*, **96**, 3923–3922.

McFadden, P.L., Barton, C.E. & Merrill, R.T., 1993. Do virtual geomagnetic poles follow preferred paths during geomagnetic reversals?. *Nature*, **361**, 342–344.

Merrill, R. T., & McElhinny, M. W., 1977. Anomalies in the Time Averaged Paleomagnetic Field and Their Implications for the Lower Mantle. *Rev. Geophys. Space Phys.*, **15**, 309–323.

Merrill, R. T., & McElhinny, M. W., 1983. *The Earth's Magnetic Field.* Academic Press.

Merrill, R. T., McFadden, P. L., & McElhinny, M. W., 1990. Paleomagnetic Tomography of the Core-Mantle Boundary. *Phys. Earth Planet. Int.*, **64**, 87–101.

Opdyke, N. D., & Henry, K. W., 1969. A Test of the Dipole Hypothesis. *Earth Planet. Sci. Lett.*, **6**, 139–151.

Quidelleur, X, Valet, J-P, Courtillot, V. & Hulot, G., 1994. Long-term geometry of the geomagnetic field for the last 5 million years; an updated secular variation database from volcanic sequences. *Geophys. Res. Lett.*, in press.

Schneider, D. A., & Kent, D. V., 1990. The Time-Averaged Paleomagnetic Field. *Rev. Geophys.*, **28**, 71–96.

Thompson, R. & Turner, G.M., 1979. British geomagnetic master curve 10,000 – 0 yr B.P. for dating European sediments. *Geophys. Res. Lett.*, **6**, 249–252.

Tric, E., Laj, C., Jehanno, C., Valet, J., Kissel, C., Mazaud, A., & Iaccarino, S., 1991. High-resolution record of the Upper Olduvai transition from Po Valley (Italy) sediments: support for dipolar transition geometry?. *Phys. Earth Planet. Int.*, **65**, 319-336.

Valet, J.P., Tucholka, P., Courtillot, V. & Meynadier, L., 1992. Palaeomagnetic constraints on the geometry of the geomagnetic field during reversals. *Nature*, **356**, 400–407.

Wilson, R. L., 1971. Dipole offset – the time averaged field over the past 25 million years. *Geophys. J. R. Ast. Soc.*, **22**, 491–504.

REFERENCES - APPENDIX

All references cited in the appendix are given in Table A1, with the exception of the following:

Herrero-Bervera, E., Fucugauchi, J.U., Martin Del Pozzo, A.L., Bohnel, H. & Guerrero, J., 1986. Normal amplitude Brunhes paleosecular variation at low-latitudes: a paleomagnetic record from the Trans-Mexican Volcanic Belt. *Geophys. Res. Lett.*, **13**, 1442–1445.

McDougall, I., Saemundsson, K., Johannesson, H., Watkins, N. & Kristjansson, L., 1977. Extension of the geomagnetic polarity time scale to 6.5 m.y.: K-Ar dating, geological and paleomagnetic study of a 3,500 m lava succession in western Iceland. *Geol. Soc. Am. Bull.*, **88**, 1–15.

McWilliams, M.O., Holcomb, R.T. & Champion, D.E., 1982. Geomagnetic secular variation from C14-dated flows on Hawaii and the question of the Pacific non-dipole low. *Phil. Trans. R. Soc. Lond.*, **306 (series A)**, 211–222.

Symons, D.T.A. & Stupavsky, M., 1974. A rational paleomagnetic stability index. *J. Geophys. Res.*, **79**, 1718–1720.

Wilson, R.L. & McElhinny, M.W., 1974. Investigation of the large scale palaeomagnetic field over the past 25 million years. Eastward shift of the Icelandic spreading ridge. *Geophys. J. R. Ast. Soc.*, **39**, 571–586.

CHAPTER 3

THE TIME-AVERAGED GEOMAGNETIC FIELD RECORDED BY LAVA FLOWS OVER THE PAST 5 MYR

ABSTRACT

A recently compiled lava flow database spanning the last 5 million years is used to investigate properties of the time-averaged geomagnetic field. More than 90% of the power in the palaeofield can be accounted for by a geocentric axial dipole; however, there are significant second order structures in the field. Declination and inclination anomalies for the new database indicate that the main second order signal is the "far-sided" effect, and there is also evidence for non-zonal structure. VGP latitude distributions indicate that normal and reverse polarity field morphologies are different, and that any changes in the normal polarity field morphology over the last 5 million years are undetectable, given the present data distribution. Regularized non-linear inversions of the palaeomagnetic directions support all these observations. Non-zonal models are required to fit the data to within the required tolerance level. Normal and reverse polarity field models obtained are significantly different. Field models obtained for the Brunhes epoch data alone are much smoother than those obtained from combining all the normal polarity data; synthetic tests indicate that these differences can be explained by the less extensive data distribution for the Brunhes epoch. The field model for all of the normal polarity data (MN1) contains features observed in the historical field maps, although the details differ. MN1 suggests that although the two northern hemisphere flux lobes observed in the historical field are stationary to a first order approximation, they do show changes in position and amplitude. A third, less pronounced flux lobe is observed in MN1 over central Europe. The lack of structure in the southern hemisphere is due in part to the paucity of data. Jackknife estimates of the field models for different subsets of the data suggest that a few sites contribute significant structure to the final field models. More conservative estimates of the time-averaged field morphology are obtained by removing these sites.

INTRODUCTION

The structure of the present-day geomagnetic field is well constrained by observatory data and also by MAGSAT satellite measurements taken during a 7 month period in 1979 and 1980 [*Langel*, 1989]. Most of the power in the present-day field, as observed at (or near) the earth's surface, can be described by a geocentric axial dipole (GAD). One of the basic assumptions concerning the geomagnetic field is that the GAD hypothesis is valid over long timescales; although this appears to be an excellent first order approximation, the residual field (relative to a GAD) contains second order structure for the present-day, the historical and the palaeo field. Natural questions then are, what is the nature of this second order structure and, what do we mean by "long timescales" in terms of obtaining a reliable time-averaged field morphology? Some information on the latter question is obtained by considering convection timescales. If the internally generated geomagnetic field is solely the result of dynamo action in the outer core, then we might expect the observed field to average out to an axisymmetric (although not necessarily dipolar) geometry over timescales typical of convection in the outer core. Unfortunately, we have little information from which to estimate these convection timescales, however observations of westward drift (see below) predict flow velocities of approximately 10^{-4} ms^{-1} at the top of the outer core, corresponding to timescales of 10^3 - 10^4 years. These are consistent with diffusive decay timescales estimated for flow in the outer core, although they are probably a minimum estimate of convection timescales, since westward drift is not observed everywhere. Longer period variations in the geomagnetic field have been observed in palaeomagnetic records, which also indicate that the field needs to be averaged over at least 10^5 years to obtain a robust estimate of the average field morphology.

Maps of the historical magnetic field (1715–1980) have been made using observatory measurements, shipboard survey data, and land survey data [*Bloxham and Gubbins*, 1985; *Gubbins and Bloxham*, 1987; *Bloxham et al.*, 1989]. These historical maps display some features that appear to drift westward with time, and other features (flux lobes) that have remained virtually stationary over the last few hundred years. This has led to the suggestion that these flux lobes may have remained quasi-stationary over much longer time periods, resulting in longitudinal structure in the geomagnetic field which has persisted over timescales longer than those associated with dynamo action in the outer core. One possible cause of these features is control of fluid flow in the top of the outer core by conditions at the base of the lower mantle, *e.g.*, lateral thermal variations at the core-mantle boundary (CMB) [*Bloxham and Gubbins*, 1985]. If this is the case, then we can expect certain features in the geomagnetic field to persist over timescales consistent with convection in the lower mantle (approximately 10^7 years). Over the past few years there has been much controversy surrounding the

question of whether palaeomagnetic records of geomagnetic polarity transitions support this notion of mantle influence on outer core flow. One approach to investigating this question further is to construct field maps from palaeomagnetic data, using techniques similar to those applied to the historical data, and then to investigate whether features observed in the historical maps are also characteristic of the geomagnetic field over the last few million years .

There have been many investigations of the structure of the geomagnetic field, averaged over periods of a few million years, using palaeomagnetic data from sediments and lava flows (see later for a summary). These studies used a wide variety of datasets and analysis techniques, and many reached quite different conclusions regarding the nature of the time-averaged field. Some studies [*e.g., Opdyke and Henry*, 1969; *Schneider and Kent*, 1990] suggest that the field over the last 2 – 5 million years has on average exhibited an axisymmetric geometry; others [*e.g., Livermore et al.*, 1983; *Gubbins and Kelly*, 1993] suggest that longitudinal structure in the time-averaged field is required to fit the observations. Maps of the normal polarity average field structure (produced using a technique similar to that applied to the historical data) for the past 2.5 million years [*Gubbins and Kelly*, 1993] do show some features observed in the historical data, however little attempt has been made to investigate the robustness of smaller scale features in the maps of the palaeo field. Here we address the issue of the time-averaged geomagnetic field, as recorded by palaeomagnetic directions in lava flows over the last 5 million years (Myr).

Both sedimentary and igneous rocks can be used in studies of the time-averaged field (TAF) and long period variations in the field (palaeosecular variation or PSV), and both rock types provide constraints on paleofield directions. Palaeointensities are technically difficult to acquire from igneous rocks; for sedimentary materials paleointensity estimates are easily made, but it is often difficult to assess their validity. Thus the number of reliable palaeointensity data remains rather small, and is at present inadequate for global field modeling. In sediments the magnetic remanence is presumed detrital and is acquired during deposition and compaction. This results in smoothed, but continuous records. High sedimentation rates result in records which can be used for PSV studies, however these records typically span only a few thousand years (for example lake sediment data). In contrast, many deep sea sediment cores span a much longer time interval over which the sedimentation rate has been low. These records are useful for TAF studies and investigations of very long period secular variation. Sedimentary records of reversals have been studied, but the details of such records are controversial due to the temporal smoothing inherent in the record. Deep-sea sediment cores typically provide only inclinations (and relative declinations). This is problematic because non-zonal fields

are more difficult to detect using inclination data alone, compared with both inclination and declination data, unless the data are both accurate and well-distributed spatially. Igneous rocks carry a remanence which is thermal in origin, and flows and thin intrusives acquire this remanence virtually instantaneously on geological timescales. Thus lava flow data can be used to investigate PSV, the TAF, and reversals. The main disadvantage associated with lava flows is that the data distribution is discontinuous in space and time. We have recently compiled a database of lava flow records of PSV, spanning the last 5 Myr which is suitable for both PSV and TAF studies [*Johnson & Constable*, 1994]. A similar database compiled by *Quidelleur et al.* [1994] shows the same first order features, but differs in detail because of the selection criteria used.

In this paper we present models for the time-averaged geomagnetic field, using the lava flow data from our new database [*Johnson & Constable*, 1994]. We review previous studies of the TAF, emphasising the data and methods used, so that the results of these studies can be compared in a meaningful way. The criteria used in compiling our lava flow database are summarized along with the temporal and spatial data distribution. Some gross properties of the TAF, as deduced from these data, are discussed in order to motivate the more detailed modeling we have undertaken. The construction of regularized field models using a non-linear inversion technique is described, and the resulting models for several subsets of the data are presented. Of particular concern in this type of study is the robustness of particular features observed in the models obtained. We explore the effect of removing individual sites from the inversion, in order to provide some estimate of the sensitivity of the models to the data distribution and quality. Finally, we discuss the significance of our results in terms of possible core-mantle coupling and the timescales for secular variation.

PREVIOUS STUDIES OF THE TIME-AVERAGED FIELD

Studies of the TAF have used palaeomagnetic data from sedimentary and/or igneous rocks and have involved several different techniques. It is commonly agreed that the first order structure in the TAF can be described by a GAD. Deviations from this field are often reported as inclination or declination anomalies – the observed inclination/declination at a particular site minus that predicted at the site location by a geocentric axial dipole field. The geomagnetic field at the Earth's surface can be described by a spherical harmonic expansion: the magnetic scalar potential due to an internally generated field is given by

$$\Psi\,(r,\theta,\phi) = r_a \sum_{l=1}^{\infty} \sum_{m=0}^{l} \left(\frac{a}{r}\right)^{l+1} (g_l^m \cos m\phi + h_l^m \sin m\phi)\;\; P_l^m(\cos\theta) \qquad (1)$$

where g_l^m and h_l^m are the Schmidt partially normalized Gauss coefficients, r_a is the radius of the Earth, r, θ and ϕ are radius, colatitude and longitude respectively, and P_l^m are the partially normalized Schmidt functions.

The m=0 terms in the expansion of (1) correspond to spherical harmonic functions with no azimuthal structure - *i.e.*, they are axially symmetric or zonal. In geomagnetism, low degree zonal spherical harmonic fields are often used and the g_1^0, g_2^0, and g_3^0 terms are frequently referred to as the axial dipole, axial quadrupole and axial octupole terms respectively. The magnetic field is simply the gradient of the potential

$$\mathbf{B} = -\nabla\Psi \tag{2}$$

so

$$B_r = -\frac{\partial\Psi}{\partial r} \qquad B_\theta = -\frac{1}{r}\frac{\partial\Psi}{\partial\theta} \qquad B_\phi = -\frac{1}{r\sin\theta}\frac{\partial\Psi}{\partial\phi} \tag{3}$$

In palaeomagnetism, it is the field directions which are measured, and the inclination (I) and declination (D) are given by (4) and (5) respectively.

$$D = \tan^{-1}\left(\frac{B_\phi}{-B_\theta}\right) \tag{4}$$

$$I = \tan^{-1}\left(\frac{-B_r}{\left(B_\theta^2 + B_\phi^2\right)^{\frac{1}{2}}}\right). \tag{5}$$

For an axisymmetric field geometry B_ϕ and hence declination are identically zero, and inclination is a function only of latitude.

Studies using data from deep-sea sediment cores alone have generally inferred or assumed an axisymmetric structure for the TAF [*Opdyke and Henry*, 1969; *Opdyke*, 1972; *Schneider and Kent*, 1988, 1990]. Only inclination data were used in these studies making longitudinal structure in the field difficult to detect unless there is extensive coverage of accurate, consistent data. *Opdyke and Henry* [1969] and *Opdyke* [1972] concluded that the TAF could be described by a GAD, and that a period of 25,000 years is sufficient to average out palaeosecular variation in the field. *Schneider and Kent* [1988, 1990] concluded that there is an inclination anomaly in the time-averaged field, which can be described by a field composed of axial dipole, axial quadrupole and axial octupole terms. *Schneider and Kent* [1990] also concluded that the normal and reverse polarity fields for the Brunhes and Matuyama epochs are significantly different. Values for the axial quadrupole and axial octupole coefficients were obtained by a non-linear least squares fit of a truncated spherical harmonic expansion to the inclination data.

Other studies used both inclination and declination data from igneous rocks [*e.g., Merrill and McElhinny*, 1977; *Coupland and Van der Voo*, 1980; *Livermore et al.*, 1983; *Gubbins and Kelly*, 1993]. Most of these involved fitting the data with a truncated spherical harmonic expansion, usually up to degree 3. This technique

can produce misleading results since truncation of the spherical harmonic expansion leads to any real short (spatial) wavelength power in the data being aliased into the low degree terms included in the model. Some studies [*e.g., Livermore et al.*, 1983] estimated non-zonal as well as zonal terms in the spherical harmonic expansion; however estimates of non-zonal terms were not possible in other investigations because of poor data quality or distribution, and/or the methods employed to establish plate motion corrections [*e.g., Coupland and Van der Voo*, 1980]. *Livermore et al.* [1983] were able to describe inclination-only data from deep sea sediment cores with non-zonal models, when these data were combined with the lava flow data.

The most recent study of the time-averaged field has used palaeomagnetic directions from both lava flows and deep sea sediments spanning the last 2.5 million years, as the input to a regularized non-linear inversion [*Gubbins and Kelly*, 1993]. This type of modeling approach produces a spatially smooth field model; this is desirable as unnecessary structure in the model is minimized. Smooth models have been constructed for historical data and the application of this type of technique to palaeomagnetic data allows direct comparison of the historical and palaeo-fields. *Gubbins and Kelly* [1993] propose that the two northern flux lobes seen in the historical field maps have persisted over the last 2.5 million years and that the absence of southern flux lobes (observed in some historical maps) in the palaeo-field maps is the result of rapid secular variation in the southern hemisphere. However, the data distribution for both lava flows and deep-sea sediment cores is substantially different in the northern and southern hemispheres: there are very few lava flow data from the southern hemisphere suitable for time-averaged field modeling, whereas there are a substantial number of deep-sea sediment cores. As noted earlier, it is much more difficult to detect longitudinal structure in the field using noisy inclination data alone, and so the smooth nature of the field in the southern hemisphere obtained by *Gubbins and Kelly* [1993] may be an artefact of the data distribution, rather than the result of temporal variations in the geomagnetic field. The presence or absence of two southern hemisphere flux lobes in the historical field maps does appear to be related to the data distribution.

DATABASE

It is evident from the above review that the type, quality and distribution of data which are used in any study of the TAF or PSV have a profound influence on any resulting models or inferences. In this study we use palaeomagnetic directions from lava flows spanning the last 5 million years [*Johnson and Constable*, 1994]. We choose to use only lava flow data as these provide both declination and inclination information and we are specifically investigating the question of possible non-zonal structure in the TAF. Details of the data compilation are given in *Johnson and Constable* [1994]. The data are all taken from references published

during the period 1965 – 1992, and the individual magnetically cleaned directions must be published. To ensure the mean direction for each flow is reliable, at least 3 samples per flow must have been taken in the field. The VGP latitude is required to be greater than 55^o, to establish that the field direction corresponds to a stable polarity epoch. At each study location the temporal sampling must span at least 10,000 years and sufficient information must have been given in the original reference to establish temporal independence of the flows. Finally, we required that there are field directions from at least 5 flows at a given location satisfying all these criteria. The main aim of the criteria is to establish a database where the palaeomagnetic information at any location can be used to obtain a reliable estimate of the palaeosecular variation and the time-averaged field at that location.

The database comprises 2187 records from 104 distinct locations – 1528 normal polarity records and 659 reverse polarity records. Data sources were the *Lee* [1983] database, the Global Paleomagnetic Database [*Lock and McElhinny*, 1991], and additional library search by *Johnson and Constable* for post-1988 data. The spatial distribution of the normal and reverse polarity data is shown in figure 1. For some studies radiometric ages of some flows are given, for others only relative stratigraphic ages are available. The temporal distribution for the combined normal and reverse polarity data is shown in figure 2. A summary of the contributing data is given in table 1 – details concerning individual locations are found in *Johnson and Constable* [1994].

PROPERTIES OF THE DATABASE

Inclination and Declination Residuals

Figures 3 and 4 show the inclination and declination residuals, with respect to a GAD reference model, for three subsets of the palaeomagnetic data used in this paper. The residuals are computed as follows. At each location the site mean inclination and declination are computed from the contributing flow directions (Table 1). Uncertainties associated with these mean inclinations and declinations include a component due to secular variation of the field (the standard error in the mean inclination/declination) and a component due to within-site measurement errors. Details concerning the computation of each component of the uncertainty are given in appendix A.

Typically, the within-site component of uncertainty is about 1° for inclination at all latitudes, and 1° – 2° for declination at latitudes less than about 45°. At high latitudes the within-site component of uncertainty for declination data increases due to a geometrical effect and is typically around 6° at 65° N. The component of uncertainty due to secular variation, estimated from (A7) and (A8) is typically 3° for inclination (all latitudes)

and 3° – 4° for declination at low-mid latitudes, increasing to about 10° on average at 65° N. Thus, at almost all locations, the component of uncertainty due to secular variation is substantially larger than the within-site error, which is necessary if the data are to be used in any palaeosecular variation studies. The inclination and declination residuals shown in figures (3) and (4) are calculated from

$$\Delta(x) = \frac{x_{obs} - x_{pred}}{\sigma_x} \tag{6}$$

where x_{obs} is the mean observed declination or inclination, x_{pred} is the declination/inclination predicted by a spherical harmonic reference model, and σ_x is the estimate of uncertainty in declination/inclination at the given location. Hence, figures 3 and 4 display weighted inclination and declination anomalies respectively. We use residuals rather than the raw anomalies, as weighting the anomaly by the average uncertainty in the data from that location provides an indication of the significance of the measured anomaly. Also, by plotting the residuals before and after modeling (rather than the actual anomalies), it is obvious which data are fit by a particular model. Later we will show maps of the inclination and declination anomalies for our final models (the declination / inclination predicted by our model minus that predicted by a GAD model), which can be used to compare observed inclination / declination anomalies from future studies with those predicted by our models.

Inclination residuals relative to a geocentric axial dipole model are shown in figure 3 for (a) the Brunhes normal polarity data (all normal polarity data with an age less than 0.78 Myr), (b) all of the normal polarity data for the past 5 Myr, and (c) all of the reverse polarity data for the past 5 Myr. Negative inclination residuals are seen to dominate the normal polarity data, whereas positive inclination residuals dominate the reverse polarity data. This observation has been noted by many workers in the past [*e.g., Wilson*, 1970,1971, 1972; *McElhinny*, 1973; *Gubbins*, 1988]. It is often referred to as the "far-sided" effect, since the effect of the shallow inclinations is to cause a virtual geomagnetic pole (VGP) calculated from the field directions to plot on the far side of the geographic pole from the observation site. (A VGP is the pole position computed by assuming that the field direction at a given site is due to a geocentric dipole; see *e.g., Merrill and McElhinny*, [1983]). In truncated, zonal spherical harmonic models of the field, these inclination residuals are described by a model in which there is a non-zero axial quadrupole term of the same sign as the axial dipole term. A first-order physical approximation of such a model is that the field is due to an axial dipole which is not geocentric but is offset along the earth's rotation axis. Other non-zero higher order terms have been calculated in some studies but are often not well resolved [*Schneider and Kent*, 1990; *Merrill et al.*, 1990]. Figure 3

also shows that inclination residuals from the same or nearby locations usually have the same sign but are sometimes quite different in magnitude. Several residuals may be available from the same location (see *e.g.*, Hawaii and Iceland, Figure 3b) if there are sufficient data spanning different, but sufficiently long time periods (the number of data and required time period to be spanned are defined in our compilation criteria). The fact that residuals from the same or nearby locations are sometimes substantially different may be the result of real spatial variability in the field, but is likely also to be a manifestation of inadequate temporal sampling in one or more of the studies, resulting in a biased mean direction. This point is discussed further in the context of more detailed modeling. The magnitudes of the inclination anomalies themselves, rather than the residuals, vary from about -10° to +10° (table 1), which is compatible with previous studies using a variety of different datasets [*Merrill and McElhinny*, 1977; *Gubbins*, 1988; *Merrill et al.*, 1990; *Schneider and Kent*, 1990]. The distribution of inclination anomalies with latitude for the 79 normal polarity locations is strikingly similar to that observed from Brunhes age sediment cores [*Schneider and Kent*, 1990]. The inclination anomalies for the reverse data from our database, are similar in magnitude and distribution to the Matuyama sediment data reported by *Schneider and Kent* [1990], but the large difference in number of available data (our 34 points versus their 125 points) precludes a quantitative comparison.

The declination residuals for the same subsets of the whole dataset (Figure 4) show less well-defined patterns than the inclination residuals. Uncertainties associated with declination data are generally slightly greater than those associated with inclination data for latitudes less than about 45°, and increase with latitude. This is due to a variety of reasons – declination data often have higher uncertainties than the corresponding inclination data, due to orientation uncertainties. There is also a geometrical effect – in appendix A, equation (22) indicates that our estimate of within-site uncertainty in declination will increase with latitude. Previous PSV analysis [*Constable and Parker*, 1988] supports the notion of increasing variability in declination data with latitude. However, the component of uncertainty due to field variations is again much larger than that due to within-site measurement error. Unlike the inclination residuals, declination residuals from the same or nearby sites are quite often of a different sign. *Wilson* [1971] noted that there is a tendency for palaeomagnetic directions to exhibit a "right-handed" effect (positive declination residuals), corresponding to VGPs which plot to the east of the geographic pole, relative to the site location. Although this "right-handed" effect has been observed in palaeomagnetic directions for many local studies, it does not appear to be a global property of the data [*Merrill and McElhinny*, 1977; *Johnson and Constable*, 1994], and may in fact be an artifact of the data distribution [*Merrill and McElhinny*, 1977]. It is also a difficult phenomenon to explain from a theoretical perspective. Figure 4 and the VGP positions calculated for the raw data used here [appendix figures 1 –

11, *Johnson and Constable*, 1994] indicate that although positive declination residuals are observed at many locations, a global "right-handed" effect is not observed in the data used here. There is a suggestion of some longitudinal structure in the declination residuals in figure 4, particularly in the normal polarity data. For all of the normal polarity data and the Brunhes data alone, there is a preponderance of small, positive declination residuals in western N. America and positive residuals through Africa, whereas negative declination residuals are observed in eastern S. America and in the S. Indian Ocean. The declination residuals show a less clear distinction between normal and reverse polarity zones than the inclination residuals.

VGP latitude distributions

In the past several studies have noted that the time-averaged field structure is different for normal and reverse polarity zones [*Schneider and Kent*, 1990; *Merrill and McElhinny*, 1977; *Merrill et al.*, 1990]. If the geomagnetic field observed at the Earth's surface were solely the result of convection in a spherical outer core which was independent of processes in the lower mantle, then we would not only expect the field to average out to an axisymmetric geometry over the time period of a stable polarity zone, but we would also expect the field during different stable polarity zones of the same sign to be very similar. Most studies which have investigated the question of different field geometries for different polarity states have assumed or inferred an axisymmetric geometry for the field. Before presenting any detailed field models for the lava flow data used here, we show the results of a simple statistical test (known as the Kolmogorov-Smirnov or K-S test [*Massey*, 1951; *Kendall and Stuart*, 1979; *Press et al.*, 1992]) on the VGP latitude distributions calculated for different subsets of the data. The main objective of this test is to determine whether two distributions are significantly different, in the sense of being drawn from different underlying distributions. The K-S test can also be used to determine whether a given data sample is likely to be drawn from a specific theoretical distribution.

When applied to two data samples (S_{N_1}, S_{N_2}), the Kolmogorov-Smirnov test compares the sample cumulative distribution functions (cdf) for the two data sets. The sample distribution function is scaled in such a way that the ordinate represents the fraction of data with a value less than or equal to the abscissa. The Kolomogorov-Smirnov statistic then provides a measure of the "difference" between the two distributions. This statistic, commonly referred to as the d statistic is the maximum absolute difference between the two distributions, or the sup norm

$$d = max_{-\infty<x<\infty} |S_{N_1}(x) - S_{N_2}(x)| \tag{7}$$

The probability that d is larger than observed by chance is given by

$$P = 2\sum_{n=1}^{\infty}(-1)^{n-1}\exp\left(-2n^2\left(\frac{N_1N_2}{N_1+N_2}\right)d^2\right) \tag{8}$$

where N_1 and N_2 are the number of samples in the two sample distributions. Thus if the probability computed from (8) is very small, it is unlikely that the two observed data distributions are drawn from the same (possibly unknown) statistical distribution.

We can use this test to investigate whether the VGP latitude distributions for *e.g.,* the normal and reverse polarity data are significantly different. We choose to apply the test to VGP latitude distributions for distinct subsets of the 0 – 5 Myr data as these are much smoother than the VGP longitude distributions, and also provide the clearest information on the zonal part of the field. Figure 5a shows the results of this test applied to the VGP latitude distributions for normal and reverse polarity data from the same locations. There are roughly equal numbers of data in each distribution (624 normal data versus 592 reverse data). The distributions are visibly different, the computed value of d is 0.1309 and the probability that d is as large as this if the two distributions are drawn from the same underlying distribution is 6.0 x 10^{-5}. Thus these distributions are different at a very high significance level. In figure 5(b) we compare the Brunhes normal polarity data with all the remaining normal polarity data (0.78 – 5 Ma). Note that not all of these data are from the same locations. We do not refer to the remaining normal polarity data as Gauss normal polarity, since some of the data correspond to normal polarity events in the Matuyama and Gilbert reverse polarity epochs. In contrast to figure 5(a), the two distributions are strikingly similar and there is an 82% probability that the value of d observed is this large when random samples of size N_1 and N_2 are drawn from the same theoretical distribution. Thus the two distributions are not significantly different and we might expect a similar axisymmetric field geometry for these two subsets of the normal polarity data. In figure 5(b) there is the problem of comparing data from different locations, as well as from different time periods: we have not performed the comparison of different age normal polarity data from the same locations as there are insufficient common locations for the result to be meaningful.

In theory, performing K-S tests on VGP longitude distributions for the same subsets of the data would provide further information concerning properties of the time-averaged field. We have not performed such tests, as the effect of data distribution and our relatively small statistical samples preclude obtaining robust results. The VGP longitude distributions for the data subsets used above, are much less smooth than the

corresponding VGP latitude distributions; this is simply due to the fact that the VGP longitude distributions span 360^o whereas the VGP latitude distributions span only 35^o. VGP longitude distributions are strongly affected by both zonal and non-zonal contributions to the field and so the effect of site locations becomes even more critical.

The results shown in figures 3 – 5 suggest first, that the time-averaged field can be modeled to first order by a geocentric axial dipole model, but that there are systematic departures from this simple model. The "far-sided" effect is observed in the inclination residuals. A consistent "right-handed" effect is not observed in the declination residuals, but rather there is a suggestion of possible longitudinal structure in these residuals. Second, the normal and reverse polarity data have significantly different VGP latitude distributions from a statistical viewpoint, indicating that the second order field structure for these two polarities may be quite different. Third, the Brunhes data VGP latitude distribution is similar to the VGP latitude distribution for the remaining normal polarity data, and the hypothesis that the normal polarity field morphology has been the same over the last 5 million years cannot be rejected on the basis of this test. These results demonstrate the need for more detailed modeling and quantification of the second order structure in the time-averaged field.

GENERATION OF REGULARIZED FIELD MODELS

The primary goal of the modeling presented in this paper is to construct field models at the core surface which are spatially smooth in some quantifiable sense, and which also fit the palaeomagnetic observations at the earth's surface, to within some specified tolerance level. The inclusion of a regularization constraint in field modeling was first suggested by *Shure et al.* [1982] and has since been applied to observatory, MAGSAT and, most recently palaeomagnetic data by several workers [e.g. *Shure et al.*, 1985; *Bloxham et al.*, 1989; *Constable et al.*, 1993; *Gubbins and Kelly*, 1993].

In order to model palaeomagnetic field directions we parameterize the field in terms of the spherical harmonic coefficients g_l^m, h_l^m. Equations (1) – (5) can then be used to write down the forward problem, in which declination and inclination are non-linear functions of these spherical harmonic coefficients. If we denote our observations D and I by a data vector $\mathbf{s}$ and the spherical harmonic coefficients by a model vector, $\mathbf{c}$ then we can express the forward problem as

$$\mathbf{s} = F[\mathbf{c}] \tag{9}.$$

Each observation s_i (either declination or inclination) has an associated uncertainty σ_i. Regularized field

models at the top of the core are constructed by minimising the following functional, U

$$U = \|W\mathbf{s} - WF[\mathbf{c}]\|^2 - T^2 + \lambda R[\mathbf{c}] \tag{10}$$

where W is the diagonal matrix

$$W = diag\{1/\sigma_1, 1/\sigma_2, ..., 1/\sigma_N\} \tag{11}.$$

On the right hand side of equation (10) the left term denotes the misfit of the model to the data as measured by the Euclidean or 2-norm, T is the desired tolerance level, and the right term describes the regularization constraint, which is some function of the model vector. We choose our regularization constraint to be one which minimizes the root mean square (RMS) value of the radial field (B_r) at the CMB (R_1), or the RMS value of the spatial gradient of B_r (R_2). These are both physically reasonable smoothness criteria and have the added attraction that the regularization constraint is a 2-norm of the model vector, weighted by a function which depends only on spherical harmonic degree. Thus the regularization explicitly downweights high spatial frequencies at each step during the inversion. The two regularization constraints are given by

$$R_{1l} = \left(\frac{r_a}{r_c}\right)^{2(l+2)} \frac{(l+1)^2}{2l+1} \sum_m \left(g_l^{m2} + h_l^{m2}\right) \tag{12}$$

$$R_{2l} = \left(\frac{r_a}{r_c}\right)^{2(l+2)} \frac{l\,(l+1)^3}{2l+1} \sum_m \left(g_l^{m2} + h_l^{m2}\right) \tag{13}.$$

where r_a is the radius of the earth and r_c is the radius of the core. In equation (10) λ is the Lagrange multiplier which describes the trade-off between the regularization constraint and the requirement that the data are fit to within a specified tolerance level. Thus we can rewrite equation (10) as

$$U = \sum_{i=1}^{N} \left[\frac{s_i - F_i[\mathbf{c}]}{\sigma_i}\right]^2 - T^2 + \lambda \sum_{j=1}^{M} (R_j c_j)^2 \tag{14}$$

where N is the total number of data (*i.e.*, there are $N/2$ pairs of declination and inclination measurements), and M is the total number of model coefficients. If we assume that the errors are independent, zero-mean, Gaussian variables with variances σ_i^2, then the misfit of the model to our data as measured by the 2-norm should correspond to the expected value of χ^2_N. Unfortunately we have no a priori reason for assuming such statistics about the noise in our data; however as we cannot justify a more complicated statistical description of the uncertainties either, we make the assumption of Gaussian noise on the basis of simplicity. We note later

any indications that this description of the noise may be inadequate. We choose our tolerance level, T to be consistent with the 95% confidence limits on the expected value of χ^2_N, so our RMS misfit level is chosen as $1 \pm 2/\sqrt{N}$, where are N are the number of data in the inversion. The uncertainties in equation (14) are estimated by including contributions from both secular variation and within-site errors, as described in the previous section and appendix A.

We now have all the necessary information to perform the minimization of (14), but there is one further complication, resulting from the fact that our forward problem (9) is non-linear. If we had a linear problem, then the forward functional $F[\mathbf{c}]$ could be written as a matrix multiplication $G\mathbf{c}$ where G is the design matrix. Equation (12) could then be minimized easily, and the model vector $\mathbf{c}$ found from

$$\mathbf{c} = \left[\lambda R^T R + (WG)^T WG\right]^{-1} (WG)^T W\mathbf{s} \tag{15}$$

Our problem is non-linear and so the minimization of (14) is an iterative process, as the gradient of F with respect to the model vector $\mathbf{c}$ depends on $\mathbf{c}$, *i.e.*,we need to introduce the Jacobian, J

$$J = \nabla_c F[\mathbf{c}] \quad or \quad J_{ij} = \frac{\partial F_i[\mathbf{c}]}{\partial c_j} \tag{16}$$

The computation of the Jacobian for our forward problem, (9) is outlined in appendix B. We minimize (14) using Occam, an approach developed by *Constable et al.* [1987]. The problem is linearized about a starting model, and then successive iterations are performed, each time linearizing about the updated model. If we denote the starting model by $\mathbf{c_0}$, the model increment by $\mathbf{\Delta}$, and the new model ($= \mathbf{c_0} + \mathbf{\Delta}$) by $\mathbf{c_1}$ then the forward problem can be approximated to first order by

$$F[\mathbf{c_0} + \mathbf{\Delta}] = F[\mathbf{c_0}] + J_0 \tag{17}$$

where J_0 represents the Jacobian evaluated at the vector $\mathbf{c_0}$. Following *Constable et al.* [1987] we can substitute (17) into (14) to obtain a linear problem in $\mathbf{c_1}$

$$U = \|W\,\hat{\mathbf{s}}_0 - W\,J_0\mathbf{c_1}\|^2 - T^2 + \lambda\,\|R\mathbf{c}\|^2 \tag{18}$$

where $\hat{\mathbf{s}}_0 = \mathbf{s} - F[\mathbf{c_0}] + J_0\mathbf{c_0}$. (18) can be minimized to solve for $\mathbf{c_1}$

$$\mathbf{c_1} = \left[\lambda R^t R + (WJ_0)^T (WJ_0)\right]^{-1} (WJ_0)^T W\hat{\mathbf{s}}_0 \tag{19}$$

If the solution, $\mathbf{c_1}$, converges then if there is a unique minimum the final solution should be independent of the starting model [*Constable et al.*, 1987]. Our problem is extremely non-linear, and during the inversion procedure local minima were found. To ensure a thorough computational search, the minimization procedure involved sweeping through a large range of values for the Lagrange multiplier, λ, at each iteration, k, and computing the new model c_k^* corresponding to each value of λ_k^* at the $k'th$ iteration. The RMS misfit, X_k^*, of each of these models, c_k^*, to the data was computed, and the new model for the $k'th$ iteration was the vector c_k^* for which X_k^* was a minimum. Figure 6 shows the change in model roughness (as measured by R_1, equation (12)), RMS misfit, and Langrange multiplier as a function of iteration during a typical inversion. Figure 6 is taken from an actual inversion of the Brunhes normal polarity data. This iterative procedure was continued until the minimum misfit X_{last} at the last iteration was less than or equal to the required tolerance level, T (dashed line, figure 6b). The final model was then computed by finding the model from this last iteration corresponding to the largest value of λ for which the RMS misfit was less than or equal to the required tolerance level: this ensures that the final model is the smoothest possible model which just fits the data to within the required tolerance level. Note that an RMS misfit of unity (dotted line) in figure 6 corresponds to the expected value of χ_N^2, whereas the tolerance level, T (dashed line) corresponds to the 95% confidence limit on the expected value of χ_N^2. If we fit the data to the expected value of χ_N^2 our resulting model is almost an order of magnitude more rough than if we fit only to the 95% confidence limit. This sharp increase in model roughness between these two misfit levels is typical of almost all of the inversions performed. In fact, figure 6c shows that above iteration 33 for this inversion, the Langrange multiplier is always very small, resulting in only small improvements in RMS misfit at the expense of a steady increase in model roughness. The largest percentage drop in RMS misfit occurs on the first iteration – again this is typical of almost all the inversions performed. We choose to use a tolerance level equal to the 95% confidence level for χ_N^2 as this gives the "smoothest" model compatible with the observations. Then we know that models compatible with the data must be at least as complicated as our "smooth" models.

We have performed this regularized inversion procedure on three subsets of our data - the Brunhes normal polarity data only, all of the normal polarity data together and all of the reverse polarity data. In the next sections we discuss the results of the modeling, and the sensitivity of the models to the temporal and spatial data distributions.

FIELD MODELS FOR THE LAST 5 MILLION YEARS

Earlier, we presented basic properties of the lava flow database, and noted that there is evidence that non-zonal structure may be required in a description of the TAF. We tested this hypothesis further using the method outlined in the previous section to try to obtain regularized zonal models which would fit the time-averaged field data. Based on the inclination and declination residuals shown in figures 3 and 4, and also on some early results from our field inversions, we made the following modifications to the three data subsets.

For the Brunhes data, we combined two datasets from Hawaii: one dataset included 28 flows from Kahuka, the other included 29 flows from Polulu [both from *Doell and Cox*, 1965]. At each site the time period spanned by the data was at the lower limit of what we consider acceptable for inclusion in the database, and the very different mean directions obtained from the two sites may be an indication that the temporal sampling is insufficient. We combined the data from 16 flows at Medicine Lakes [*Brown and Mertzman*, 1979], and 33 flows [*Mankinen et al.*, 1986] at Long Valley Caldera, California for the same reason. Five records from France [*Doell*, 1970] were deleted based on their anomalous directions. These modifications lead to the original 34 locations being reduced to 31.

When modeling all the normal or reverse polarity data we binned these data geographically into 5° bins. Figures 3 and 4 indicate that there are several areas where studies from nearby locations yield quite different mean directions. It is possible that these differences are real, alternatively they may again reflect inadequate temporal sampling. By binning the data, we are effectively using spatial averaging as a proxy for temporal averaging. The binning reduced the number of normal polarity locations from 79 to 39, and the number of reverse polarity locations from 34 to 22.

Table 2 shows the results from modeling each of these modified subsets of data using zonal regularized inversions. For each subset of data, the original misfit of the data to the model is given (starting RMS) and also the required tolerance level, which is the 95% confidence limit on the expected value of χ^2_N, as described in the previous section. If we required the data be fit to the expected level of χ^2_N then the required RMS would be equal to 1. Note that as the number of data in our inversion decreases, the required tolerance level increases; in other words fitting the data to the same statistical level is different from fitting the data to the same RMS misfit level. This just reflects the number of degrees of freedom in the χ^2_N distribution. The number of spherical harmonic degrees in the inversion was successively increased; however, for all subsets of data and both choices of regularization constraint, although the models converge toward the same solution, they do not

fit the data, *i.e.*,zonal models are unacceptable.

We now consider the full non-zonal inversions for each of the data subsets. Because of the regularization constraint imposed during the inversion, the effective number of degrees of freedom in the model is less than the number of spherical harmonic coefficients in the model vector. To ensure that the model has sufficient degrees of freedom to describe the data adequately, then for each subset of data several inversions were performed, successively increasing the maximum number of spherical harmonic degrees, l_{max}. For small l_{max}, the inversion converges to a solution which does not fit the data to within the required tolerance level. Even when l_{max} was sufficiently large to allow a model to be found which did fit the data to within the required tolerance level, we continued to increase l_{max}. (The required tolerance levels for each data subset are the same as those given in Table 2 for the zonal models.) At this stage for each inversion the change in misfit, Langrange multiplier, and roughness at each iteration (see figure 6 for an example) were examined, along with the final model. Inversions were continued until a value of l_{max} was reached above which the character of the inversions (*i.e.*, the change in misfit, roughness and Lagrange multiplier as a function of iteration), and the final model did not change. At this point the final solution is not affected by the truncation level in the spherical harmonic expansion and there are adequate degrees of freedom in the model. We found that a maximum spherical harmonic degree of 10 was sufficient to describe the data in all our inversions. For brevity from now on our discussion refers only to the results obtained using the constraint that minimizes R_1 (equation (12)).

The results for the inversions, out to degree and order 10, for the three subsets of data are shown in figures 7 – 9. The field model (lower plot) is given in terms of B_r at the CMB in microteslas, for comparison with the historical field maps [*Bloxham et al.*, 1989; *Constable et al.*, 1993] and a recent palaeofield map [*Gubbins and Kelly*, 1993]. The upper two plots in each figure show the declination and inclination residuals relative to the final model, computed using equation (6). The RMS misfit of the model to the data is given, along with the RMS value of B_r in microteslas at the CMB. These models will be referred to as MB1 (Brunhes model 1), MN1 (normal polarity model 1) and MR1 (reverse polarity model 1).

An overall reduction in the declination and inclination residuals relative to the new models is evident for each subset of data, compared with the residuals relative to a GAD (figures 3 and 4). If the residuals were samples from zero mean Gaussian processes, with a standard deviation equal to the standard error in the mean declination or inclination at each location, then we would expect only 5% of the residuals to have a magnitude greater than 2 standard errors in the mean. Hence for the combined declination and inclination residuals for

the Brunhes data we would expect about 3 locations to have residuals bigger than two standard errors in the mean. Figure 7 shows that there are actually 5 such large residuals. Similarly for the binned normal polarity data we would expect a total of about 4 large residuals, whereas there are 8 (figure 8). For the binned reverse data we expect about 2 large residuals, whereas there are 4 (figure 9). For the Brunhes data all except one of the large residuals occur at locations where there are inconsistent data from two or more series of flows; this is suggestive of the previously mentioned problem of inadequate temporal sampling in individual studies. The large residuals for the binned normal polarity data correspond to inconsistent observations from the S. W. Pacific, to one site in Libya and to studies with a small number of suitable flows from the Carribean and the S. Atlantic. Large reverse data residuals occur for sites in Africa, Sicily (small number of flows), and S. Australia and the S. W. Pacific. Data from some of these sites were found to be critical to the resulting field models and these locations will be discussed further in the next section

The field models in figures 7 – 9 appear quite different. The model with the most structure is that obtained for the binned normal data (MN1), which has the best spatial data coverage of the three data subsets. The radial field map at the CMB is similar to that obtained by *Gubbins and Kelly*, [1993] which was produced using a different database (and also only 0 – 2.5 Ma data) from the one used here. However, there are some differences. First, our field map shows a patch of positive B_r or flux over Mexico and the Central Eastern Pacific which is not present in the *Gubbins and Kelly* [1993] map. Second, the larger amplitude flux lobes in the northern hemisphere are different in the two inversions. *Gubbins and Kelly* found two major northern hemisphere flux lobes, roughly coincident with those seen in the historical field maps [*Bloxham and Gubbins*, 1985; *Gubbins and Bloxham* 1987; *Bloxham et al.*, 1989]. Figure 8 shows three flux lobes (N. America, central Europe, N. Asia), with the one in N. America centered to the west of the corresponding lobe in the *Gubbins and Kelly* field map. The flux patch over Mexico in our map is of low amplitude and is probably not significant (see next section). The southern hemisphere field calculated from MN1 contains more structure than that in the *Gubbins and Kelly* inversion. In contrast, our model for the Brunhes polarity data alone, MB1, (figure 7) is much smoother than both our model obtained by binning all the normal polarity data (figure 8) and the *Gubbins and Kelly* model. Although there is some asymmetry in the field toward the North pole, there are no flux lobes in the radial field map computed from MB1, and the southern hemisphere field is very smooth.

The reverse polarity field model appears quite different in structure from the field models for either the Brunhes data alone, or all of the normal polarity data combined. Differences between normal and reverse polarity field morphology have been inferred by other investigators based on differences in the magnitude of

inclination anomalies [*McElhinny and Merrill*, 1977; *Merrill et al.*, 1990; *Schneider and Kent*, 1990] . The main problem with obtaining a robust description of the field (from lava flow data) during reverse polarities is the poor data coverage - there are almost no S. hemisphere data and the N. hemisphere data are extremely confined in longitude.

It appears that the complexity of the normal polarity field models MN1 and MB1 correlates with the number of lava flow data locations available. To investigate the question of whether our Brunhes only and binned normal polarity data are consistent with the same underlying field model we performed the following test. MN1 was expanded as far as degree and order 6 to produce synthetic declination and inclination data at the locations where we have Brunhes data (figure 10, lower). Forty observations were generated at each site (approximately the mean number of flows per site in our database), by assuming that the declination and inclination data at each location are drawn from a Gaussian process with a mean specified by the input normal polarity field model, and a standard deviation which resulted in the same average standard error in the mean inclination and declination as observed in the real data. These synthetic data were then inverted in exactly the same way as the real data, using a field model with l_{max} equal to 10. We allowed a higher maximum degree in the output field relative to the input field in order to account for the noise which was added to the synthetic observations. The resulting field was found to be much smoother than the input field and qualitatively very similar to the actual field model obtained from the real Brunhes polarity data (figure 10, upper). The results of this test are consistent with our earlier inference from the Kolmogorov-Smirnov tests, that the field properties during the Brunhes chron are unlikely to be significantly different from those during the Gauss chron. If the two field geometries are in fact dissimilar, then our results indicate that the current data distribution is insufficient to detect these differences.

Figure 11 shows the power in the geomagnetic field as a function of spherical harmonic degree, for the field models in figures 7 – 9, compared with the power spectrum for the present day field as computed from the PHS80 model. PHS80 is the result of a regularized inversion of MAGSAT data in which the regularization constraint R_1 (equation 12) was applied [*Shure et al.*, 1985]. The power is calculated from the *Lowes* [1974] power spectrum:

$$P(l) = \left(\frac{a}{r}\right)^{2(l+2)} (l+1) \sum_{m} \left(g_l^{m\,2} + h_l^{m\,2}\right) \tag{20}$$

The power spectra for the palaeomagnetic data are consistent with a white source at the CMB, for spherical harmonic degrees less than or equal to 6. The drop-off in power above degree 6 is due to the effect of the regularization constraint on the inversion. The power in the normal and reverse fields is noticeably different

for degrees one and two (note that in figure 11 the power for degree one does not include the GAD term), but is very similar above degree two. Differences in the power at degree 2 are consistent with previous studies which noted differences in the magnitude of the axial quadrupole term, g_2^0, estimated for normal and reverse polarity fields [*McElhinny and Merrill*, 1977; *Merrill et al.*, 1990; *Schneider and Kent*, 1990]. The power in the field model obtained from only the Brunhes data is very similar to that from all the normal polarity data combined for degrees one and two, differences at higher degrees are presumably due to the differences in data distribution. At spherical harmonic degrees greater than 2 the power in the non-zonal terms is larger than the power in the zonal term alone, for all subsets of data. In general the ratio of the power in the non-zonal terms to that in the zonal terms lies between 1 and 100; however the ratio is extremely variable from one degree to the next and for different data subsets. The high percentage of power in the non-zonal terms may seem surprising at first, given the field maps in figures 7 – 9, but recall that our regularization constraint penalizes non-zonal and zonal terms equally at a given spherical harmonic degree, and there are more non-zonal than zonal coefficients. For the palaeofield models the total power in the non-GAD terms is between 1% and 5% of that in the GAD term, approximately an order of magnitude less than the corresponding percentage in the PHS80 model. The shape of the power spectrum for all the palaeofield models is similar to that for the present day field for degrees 2 – 6, and is consistent with a white spectrum at the core-mantle boundary. The reduction in overall power in the palaeofield relative to the 1980 field is to be expected from the temporal averaging.

The predicted inclination and declination anomalies at the surface of the Earth for the models in figures 7 – 9, are shown in figure 12. The largest anomalies are for the reverse polarity field model, the smallest anomalies are for the Brunhes model. Inclination anomalies are predominantly negative for the normal polarity data and positive for the reverse data as we would expect from the raw residuals in figures 3 and 4. There is obvious non-zonal structure in the inclination anomaly maps and comparison of figure 12 with the field maps in figures 7 – 9 shows that as expected the negative inclination anomalies correspond to northward deflections of the magnetic equator. The very large positive inclination anomalies predicted over the central S. Atlantic for the reverse polarity epochs are constrained by observations from the W. Atlantic and from Africa, rather than from observations in the central S. Atlantic. The inclination anomalies in the raw data from sites around the S. Atlantic are greater than 10° ; however at one of the sites (Fernando de Noronha) there are only 5 contributing flows. The declination anomaly maps again exhibit substantial longitudinal structure, with 2 or 3 main bands of positive and negative anomalies. Care should be taken when interpreting these maps: in particular the very large amplitude declination anomaly lobes occur where there are few data to constrain them. Large amplitude declination anomalies can be expected near the poles if there is non-zonal structure in the field. Remember

also though, that within-site measurement uncertainties in declination increase poleward, so that declination data from high latitude regions alone are of limited use in constructing or verifying field models. Anomaly maps such as those in figure 12 are useful as they allow palaeomagnetic directions from other studies to be compared directly with the models obtained here. They also provide an indication of locations from which it would be useful to have further palaeomagnetic data in order to establish the reliability of certain features in the TAF models.

SENSITIVITY ANALYSIS

So far we have concluded that palaeomagnetic directions recorded by lava flows over the last 5 million years require that the TAF contains longitudinal structure. The details of this structure appear to depend on which subset of the data is inverted, leading us to question the robustness of some of the features in the resulting models. Another possible concern is whether inversions of a particular subset of the data converge toward the same solution, independent of the starting model. In a highly non-linear problem, such as ours, it is likely that there are many local minima in the parameter space which we wish to explore, and the inversion algorithm may get "stuck" in one of these local minima. We performed several inversions for each subset of data, using different starting models and verified that the results did not vary with our choice of starting model.

We next addressed the problem of investigating which, if any, data are critical to the model obtained from the inversion of each data subset. To do this, we used a jackknife approach: for a given data subset all the palaeomagnetic directions from one data group were deleted and the inversion performed. The resulting model was stored and the procedure repeated deleting the data from each group in turn in the subset. Thus 31 delete-one (or jackknife) estimates of the model were obtained for the Brunhes data, 39 for the binned normal data and 22 for the binned reverse data. Each of these models was examined and compared with the field model obtained by inverting the complete data subset (figures 7 – 9). Maps of B_r at the CMB were made, and the corresponding RMS value of B_r recorded.

For the Brunhes data we found that 4 data groups (1 each from Hawaii, Pagan Island, Crozet Island, Japan) had a significant effect on the model obtained from the inversion. The field maps obtained from these jackknife estimates appeared qualitatively different from that in figure 7 and there was up to 1% variation in the RMS value of B_r at the CMB. As the RMS value of B_r is dominated by the axial dipole term a 1% variation can be the result of a substantial variation in one or more of the other spherical harmonic terms (recall that the power in the non-GAD terms is in the range 1 – 5 % of the power in the GAD term) . The

removal of each of three data groups (Hawaii, Pagan Island, Crozet Island) resulted in a smoother model than was obtained when all the data were inverted. The removal of 35 records from Japan actually resulted in a slightly rougher model. As previously mentioned, some records from Hawaii may not span a sufficiently long time period to obtain an accurate estimate of the time-averaged field direction at that location. The Hawaiian group which we found to be anomalous was the group which we modified earlier to include data from two locations in an effort to improve the temporal data distribution. The results of our jackknife models suggest that the data from Hawaii still do not provide a self-consistent picture of the TAF. Some records from the Crozet Islands have a lower value of the precision parameter, than most flows in our database, indicating less reliable field directions – this may at least partly explain why the data from this site are anomalous. It is not clear from our literature research why the data from Japan or Pagan Island exert substantial influence over the resulting field model.

Five data groups were found to have a significant effect on the field model obtained from inverting the normal polarity data. Three of these sites (Carribean, Fernando de Noronha in the S. Atlantic, Libya) have 10 or fewer flows contributing to the estimated mean direction. The data from Norfolk Island, SW Pacific, appear to be incompatible with other SW Pacific and Australian sites. This incompatibility is evident in the raw residuals (figures 3 and 4), as well as in the residuals after modeling (figure 8). A similar incompatibility occurs for data from Madagascar and the SW Indian ocean.

The delete-one estimates of the reverse polarity field suggested that three data groups had a significant effect on the model shown in figure 9. Data from Libya were again found to be anomalous. In contrast to the normal polarity data from Libya which comprise only 10 records, the reverse polarity data consist of 54 records. The data from Sicily consists of only 6 flows. Again, data from the SW Pacific appears to be influential - 12 records from Norfolk Island have a substantial effect on the resulting field model.

The jackknife estimates of the field models for each of the three models were used to compute a jackknife estimate of the mean model vector. The mean model vector is the simple arithmetic average of the delete-one estimates of the model. The jackknife estimate of the mean was compared with the "true" field models - *i.e.,* those obtained by inverting all the data in each subset, and in all cases the jackknife mean provided an excellent estimate of the model vector. The delete-one estimates were then used to compute the standard error in the mean for each spherical harmonic coefficient. These standard errors are not true uncertainties in the model parameters, rather they give an estimate of the uncertainties due to data quality and distribution. Table 3 gives the resulting mean coefficients and associated standard error out to degree and order 4, for each of the

data subsets. Note that as stated previously the inversions included spherical harmonic terms as far as degree 10. The full field models are available on request from the authors.

Finally, we produced field models for the Brunhes data, binned normal polarity data, and the binned reverse polarity data removing the anomalous sites identified above. The resulting field models are shown in figures 13 – 15. These are conservative estimates of the minimum structure in the TAF required by the lava flow data from the past 5 Myr. We refer to these new models as MB2, MN2 and MR2 for brevity. As in figures 7 – 9, the field model is shown in terms of B_r at the CMB, and the declination and inclination residuals with respect to this final model are given. The sites removed from this final inversion are marked by asterisks. Note that as the number of data locations in the inversion has decreased for each subset of data, the absolute value of the RMS misfit in figures 13 – 15 is higher than that in figures 7 – 9 respectively, although the data are still fit to the same statistical significance level. All the field models in figures 13 – 15 are smoother than those in figures 7 – 9. Note that in particular, the MN2 field map (figure 14) for the binned normal polarity data is very similar to that for the earlier Brunhes model, MB1 (figure 7), and the northern hemisphere flux patches seen in the field map obtained from MN1 (figure 8) are no longer required by the data. There is still some significant non-zonal structure in the binned normal polarity field. The reverse polarity field map in figure 15 is smoother than that in figure 9 and the amplitude of the field where there are no data has been reduced.

Inclination and declination anomaly maps for the new field models are shown in figure 16. They show the same general features as previously, although they have the added desirable property that the anomaly magnitudes are reduced where there are no data constraining them.

DISCUSSION

Non-zonal models constructed for the Brunhes polarity data alone are much smoother than the corresponding models for all of the normal polarity data. The normal polarity field, MN1, is qualitatively very similar to the field model obtained by *Gubbins and Kelly*, 1993, using normal polarity flows spanning the last 2.5 Myr (figure 2a, *Gubbins and Kelly* [1993]. MN1 is also similar to the *Gubbins and Kelly* normal polarity field model which combined 0 – 2.5 Ma sedimentary and lava flow data. However, our model shows three northern hemisphere flux lobes as opposed to the two seen in the *Gubbins and Kelly* [1993] field map, and there is more structure in our southern hemisphere field. In contrast our Brunhes field model, MB1, is more smooth. The apparent dependence of field model complexity on the data distribution means that it is crucial to examine how robust certain features in the field are before attempting to interpret them in terms of

core flow models and possible core-mantle coupling. Our study assigns individual uncertainties to the mean declination and inclination at each site: the computed uncertainties include an estimate of secular variation and within-site measurement error. Typically our within-site uncertainties are on the order of 1° – 2° and the uncertainty due to secular variation is greater than the within-site error. The average uncertainty in the inclination data is approximately 3° at all latitudes, whereas for declination data the average uncertainty is 3° – 4° at low-mid latitudes, and up to about 10° at high latitudes. In contrast, *Gubbins and Kelly* assigned an average uncertainty of 1° to all the inclination and declination data from lavas and an average uncertainty of 4° to all the inclination data available from deep-sea sediment cores. Our field models spanning the last 5 Myr use data which has been binned spatially into 5° bins. Our reverse polarity field, MR1, appears quite different from the fields MB1 and MN1, as expected on the basis of the earlier Kolmogorov-Smirnov tests, however the spatial distribution of reverse data is poor. *Gubbins and Kelly* combined normal and reverse data from the last 2.5 Myr by changing the sign of the reverse polarity directions. We tested whether our field models MB1 and MN1 are compatible with the reverse polarity data – the sign of every coefficient in the models MB1 and MN1 was reversed and the misfit of these new models (MB1' and MN1' respectively) to the binned reverse polarity data computed. Remember that the RMS misfit of a GAD model to the reverse data is 4.06, and the misfit of model MR1 to the reverse data is 1.30. The RMS misfit for model MB1' is 2.98 and for MN1' is 3.44. Thus the normal polarity field models are incompatible with the reverse polarity data for the last 5 Myr.

In the PHS80 model of the present-day field, the southern part of the flux lobe over central Asia does in fact extent westwards toward central and southern Europe, where we find an additional lobe in model MN1. The deflection of the magnetic equator southward over S. America in the model MN1 is also qualitatively compatible with model PHS80. It is interesting to note that over historical times, the flux lobe over N. America has not remained completely stationary and has in fact oscillated in a west-east manner [*Bloxham et al.*, 1989; *Bloxham and Jackson*, 1992]. The position of this flux lobe in model MN1 is consistent with the westerly limit of the oscillation seen in the historical field maps. The variability in position of the flux lobes is probably due in part to differences in data coverage and the choice of regularization constraint, although these effects have not been investigated quantitatively to date. The low amplitude field and rather poorly defined position of the equator over the Pacific in model MN1 are also observed in the historical field maps.

Jackknife estimates of the field models suggest that data from a few locations are consistently influential, *e.g.*, data from the SW Pacific, from Libya and some Hawaiian data. New models with all of these sites removed were made (models MB2, MN2, MR2). All new models are smoother than their earlier counterparts

(MB1, MN1, MR1), but all three subsets of data still required a non-zonal model. The revised normal polarity model, MN2, no longer displays the northern hemisphere flux lobes, but still has the same general non-zonal structure as MN1. The revised Brunhes and reverse polarity field models (MB2 and MR2) are not substantially different from MR1 and MB1. It is important to note that there is no reason to exclude the sites indicated by asterisks in figures 13 – 15 from the inversions, except that the data at these sites require more complicated models than the data the remaining locations. Thus we believe that the models MB1, MN1, and MR1 are representative of the normal and reverse field morphology over the last 0.78 (MB1) and 5 Myr (MN1 and MR1). However, if a conservative estimate of the time-averaged field is required, models MB2, MN2 and MR2 should be used. The normal and reverse polarity fields for MN2 and MR2 are quite different, indicating that the polarity asymmetry is not due to a few anomalous data.

CONCLUSIONS

Investigation of the time-averaged field as recorded by lava flows over the last 5 Myr indicates that the geocentric dipole hypothesis is still a good first order approximation to the field geometry. A recently compiled database [*Johnson and Constable*, 1994] suggests that there are significant, persistent, higher order features detectable in the time-averaged field. Raw inclination anomalies are predominantly negative for normal polarity data, and positive for reverse polarity data (the "far-sided" effect), and the anomaly magnitudes are comparable to those found in previous studies which used different data compilations [*Merrill and McElhinny*, 1977; *Merrill et al.*, 1990; *Schneider and Kent*, 1990]. Raw declination anomaly plots do not display a global "right-handed" effect (positive declinations); however, the declination anomalies do not average to zero. There is evidence for non-zonal structure in the field in both the inclination and declination anomalies.

Application of the Kolmogorov-Smirnov test to VGP latitude distributions for different subsets of the database leads to the following conclusions. First, the normal and reverse polarity distributions are inconsistent with the hypothesis that the underlying field structure is the same for normal and reverse epochs. Second, the VGP latitude distributions for Brunhes normal polarity data and all of the remaining normal polarity data combined, indicate that either the underlying field structure during normal polarity periods (epochs and longer events) over the last 5 Myr has been the same, or any differences that do exist are undetectable given the current data distribution.

A regularized inversion algorithm was used to construct both zonal and non-zonal field models for different subsets of the palaeomagnetic data. Three subsets of the data were modeled: the Brunhes normal

polarity data, all of the normal polarity data and all of the reverse polarity data. When modeling all of the reverse or all of the normal polarity data, spatial binning was used so that inconsistent observations from nearby sites did not introduce unnecessary structure into the field models. In many cases the spatial binning effectively increased the temporal distribution of the data in the bin. All of our resulting models were required to fit the data to within the 95% confidence limits on the expected value of χ^2_N. We found that zonal models could not fit the data for any of the three subsets modeled.

Maps of the radial field at the core-mantle boundary from non-zonal field models indicate that the normal polarity data for the last 5 Myr are compatible with the presence of 3 northern hemisphere flux lobes (model MN1), however the flux lobes are not required when the data from 5 critical sites are removed from the inversion (model MN2). The Brunhes data alone also do not require the presence of these lobes (models MB1 and MB2). Brunhes field models are smoother than those obtained from all of the normal polarity data, the differences are consistent with the less extensive data distribution for the Brunhes data. No flux lobes are seen from inversions of the reverse polarity data (MR1, MR2).

All field models for the database used here suggest that there is non-zonal structure in the field over timescales of several million years, suggestive of possible core-mantle coupling. Further investigation of the details of long-term field morphology would be greatly aided by collection of 0 – 5 Ma palaeomagnetic data from the former Soviet Union, oceanic islands in the Atlantic, Indian, and S.W. Pacific Oceans and from western S. America.

APPENDIX A: *Calculation of Uncertainties in the Mean Directions*

Remember that at each location we have a sequence of, say, N_L lava flows, where the average direction for the *j'th* flow is computed from several (n_j) samples. It is this average direction which is usually quoted in the original reference. We can estimate a 95% confidence cone (α_{95}) about the mean direction for the *j'th* flow from the precision parameter, k_j (equation 21). The 95% confidence cone can be used to obtain estimates of the within-site measurement error in declination and inclination respectively [*Tarling*, 1983] from

$$\alpha_{95} = \frac{140}{\sqrt{(k_j n_j)}} \tag{21}$$

$$\sigma_j^{wi}(D_j) = \frac{\alpha_{95}}{\cos I_j} \tag{22}$$

$$\sigma_j^{wi}(I_j) = \alpha_{95} \tag{23}$$

where n_j is the number of samples from the given (*j'th*) flow, α_{95} is the 95% confidence cone, and k_j is the precision parameter

$$k_j = \frac{n_j - 1}{n_j - |R_j|} \tag{24}$$

In equation (24) $|R_j|$ is the magnitude of the resultant vector **R**, of the field directions for the n_j samples for the given flow. In the palaeomagnetic literature, the individual sample directions are rarely given: usually the average flow direction (D_j and I_j) and n_j and $|R_j|$ are quoted. At a given location we estimate $\sigma_j^{wi}(D_j)$ and $\sigma_j^{wi}(I_j)$ for each flow from (21-23) and then compute the arithmetic average of the N_L estimates,

$$\sigma_{wi}(D) = \frac{1}{N_L}\sum_{j=1}^{N_L}\sigma_j^{wi}(D_j) \tag{25}$$

$$\sigma_{wi}(I) = \frac{1}{N_L}\sum_{j=1}^{N_L}\sigma_j^{wi}(I_j) \tag{26}$$

Equations (25) and (26) describe the mean within-site measurement error in declination and inclination at a given location.

We estimate the uncertainty associated with the secular variation, σ_{sv}, as simply the standard error in the mean inclination and declination for the N_L lava flows at a given location,

$$\sigma_{sv}^2(D) = \frac{1}{N_L(N_L-1)}\sum_{j=1}^{N_L}\left(D_j - \bar{D}\right)^2 \tag{27}$$

$$\sigma_{sv}^2(I) = \frac{1}{N_L\left(N_L-1\right)} \sum_{j=1}^{N_L} \left(I_j - \bar{I}\right)^2 \tag{28}$$

where D_j and I_j are the average field directions from the *j'th* lava flow and $\bar{D}$ and $\bar{I}$ are the mean of these N_L contributing flow directions.

Finally, the total uncertainty in declination and inclination at a given site are calculated from

$$\sigma = \left({\sigma_{wi}}^2 + {\sigma_{sv}}^2\right)^{\frac{1}{2}} \tag{29}$$

APPENDIX B: *Computation of the Jacobian*

Our non-linear inversion requires the computation of the partial derivatives of declination and inclination (our observations) with respect to the Schmidt normalized spherical harmonic coefficients (our model parameters). In many problems the computation of the Jacobian requires the implementation of a finite difference algorithm, however for our problem there are fortuitously analytical solutions for the elements of the Jacobian.

The forward problem is given by equations (3)–(5) of the main text, where the field elements B_r, B_θ, and B_ϕ are written explicitly as

$$B_r\left(r,\theta,\phi\right) = \sum_{l=1}^{lmax} \left(\frac{r_a}{r}\right)^{l+2} (l+1) \sum_{m=0}^{l} \left(g_l^m cosm\phi + h_l^m sinm\phi\right) P_l^m(cos\theta) \tag{30}$$

$$B_\theta\left(r,\theta,\phi\right) = -\sum_{l=1}^{lmax} \left(\frac{r_a}{r}\right)^{l+2} \sum_{m=0}^{l} \left(g_l^m cosm\phi + h_l^m sinm\phi\right) \frac{\partial P_l^m(cos\theta)}{\partial\theta} \tag{31}$$

$$B_\phi\left(r,\theta,\phi\right) = \frac{1}{sin\theta} \sum_{l=1}^{lmax} \left(\frac{r_a}{r}\right)^{l+2} \sum_{m=0}^{l} \left(m g_l^m sinm\phi - m h_l^m cosm\phi\right) P_l^m(cos\theta) \tag{32}.$$

The elements of the Jacobian are the following partial derivatives evaluated at each location where we have data

$$\frac{\partial I}{\partial g_l^m}, \quad \frac{\partial I}{\partial h_l^m}, \quad \frac{\partial D}{\partial g_l^m}, \quad \frac{\partial D}{\partial h_l^m} \tag{33}.$$

We can make the following substitutions for brevity

$$\alpha = \frac{B_\phi\left(g_l^m, h_l^m\right)}{-B_\theta\left(g_l^m, h_l^m\right)} \tag{34}$$

and

$$\beta = \frac{-B_r\left(g_l^m, h_l^m\right)}{\left({B_\theta}^2\left(g_l^m, h_l^m\right) + {B_\phi}^2\left(g_l^m, h_l^m\right)\right)^{1/2}} \tag{35}$$

so that $D = tan^{-1}\alpha$ and $I = tan^{-1}\beta$. Using the chain rule and considering the partial derivatives of declination with respect to the model parameters first

$$\frac{\partial D}{\partial g_l^m} = \frac{\partial D}{\partial \alpha}\frac{\partial \alpha}{\partial g_l^m} \tag{36}$$

and similarly for $\frac{\partial D}{\partial h_l^m}$. Now $D = tan^{-1}\alpha$ so

$$\frac{\partial D}{\partial \alpha} = \frac{1}{1+\alpha^2} = \frac{{B_\theta}^2}{{B_\phi}^2 + {B_\theta}^2} \tag{37}.$$

$$\frac{\partial \alpha}{\partial g_l^m} = \left(-B_\theta \frac{\partial(-B_\phi)}{\partial g_l^m} - B_\theta \frac{\partial B_\phi}{\partial g_l^m}\right) \cdot \frac{1}{{B_\theta}^2} \tag{38}$$

Thus the element of the Jacobian is

$$\frac{\partial D}{\partial g_l^m} = \frac{1}{{B_\phi}^2 + {B_\theta}^2}\left(B_\phi \frac{\partial B_\theta}{\partial g_l^m} - B_\theta \frac{\partial B_\phi}{\partial g_l^m}\right) \tag{39}.$$

The corresponding partial derivatives of D with respect to the coefficients h_l^m can be found by substituting g_l^m by h_l^m in equation (39). The partial derivatives of inclination are a little more laborious

$$\frac{\partial I}{\partial g_l^m} = \frac{\partial I}{\partial \beta}\frac{\partial \beta}{\partial g_l^m} \tag{40}$$

and similarly for $\frac{\partial I}{\partial h_l^m}$. Remember that $I = tan^{-1}\beta$ so

$$\frac{\partial I}{\partial \beta} = \frac{1}{1+\beta^2} = \frac{{B_\theta}^2 + {B_\phi}^2}{{B_r}^2 + {B_\theta}^2 + {B_\phi}^2} \tag{41}.$$

Partial differentiation and further application of the chain rule yields

$$\frac{\partial \beta}{\partial g_l^m} = \frac{B_r}{\left({B_\theta}^2 + {B_\phi}^2\right)^{(3/2)}}\left[B_\theta \frac{\partial B_\theta}{\partial g_l^m} + B_\phi \frac{\partial B_\phi}{\partial g_l^m} - \left({B_\theta}^2 + {B_\phi}^2\right)^{(1/2)}\frac{\partial B_r}{\partial g_l^m}\right] \tag{42}.$$

Hence

$$\frac{\partial I}{\partial g_l^m} = \frac{1}{\left({B_r}^2 + {B_\theta}^2 + {B_\phi}^2\right)\left({B_\theta}^2 + {B_\phi}^2\right)^{(1/2)}}\left[B_r\left(B_\theta \frac{\partial B_\theta}{\partial g_l^m} + B_\phi \frac{\partial B_\phi}{\partial g_l^m}\right) - \left({B_\theta}^2 + {B_\phi}^2\right)^{(1/2)}\frac{\partial B_r}{\partial g_l^m}\right] \tag{43}.$$

The corresponding partial derivatives of I with respect to the coefficients h_l^m can be found by replacing g_l^m by h_l^m in equation (43). The computation of the partial derivatives of the field elements B_r, B_θ, B_ϕ with respect to the spherical harmonic coefficients follows easily from equations (30) – (32) above.

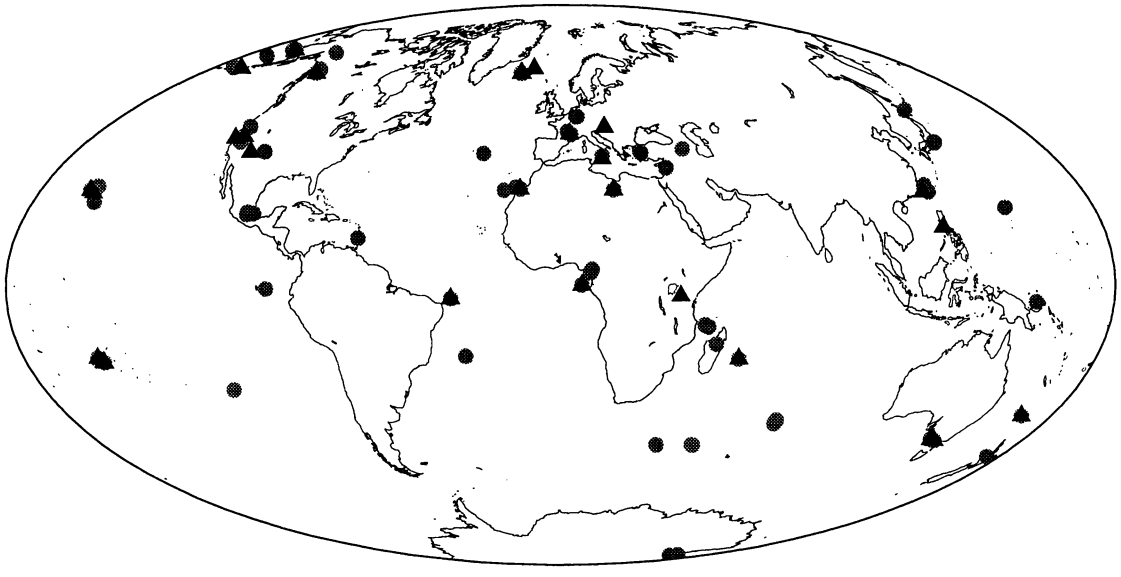

Figure 3.1: Location map for the data comprising the revised database. The circles denote normal polarity data locations, the triangles denote reverse polarity data locations.

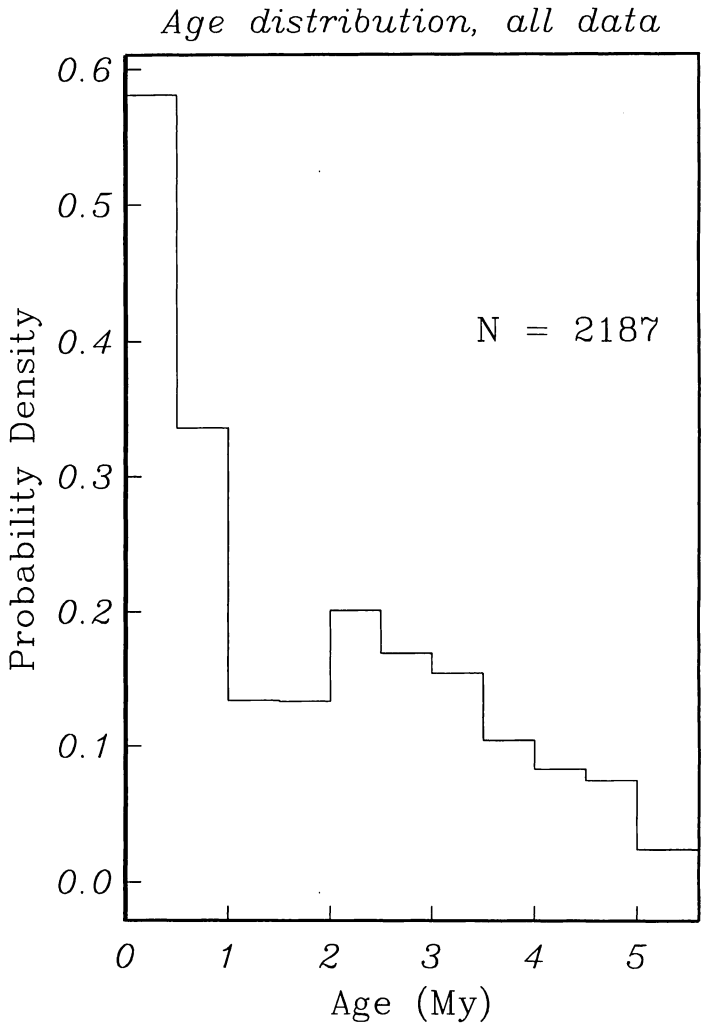

Figure 3.2: Age distribution of data, normal and reverse polarities combined. Data from each location is assumed to be uniformly distributed over the age interval quoted, and is binned into 0.5 Myr bins. Normalized so that total area under histogram is unity. Note that almost 50% of the data lies in the interval 0 - 0.8 Myr.

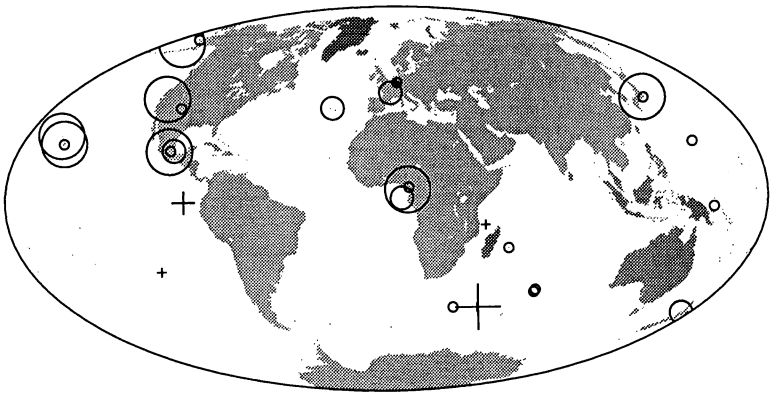

(a) Brunhes Data: N = 34

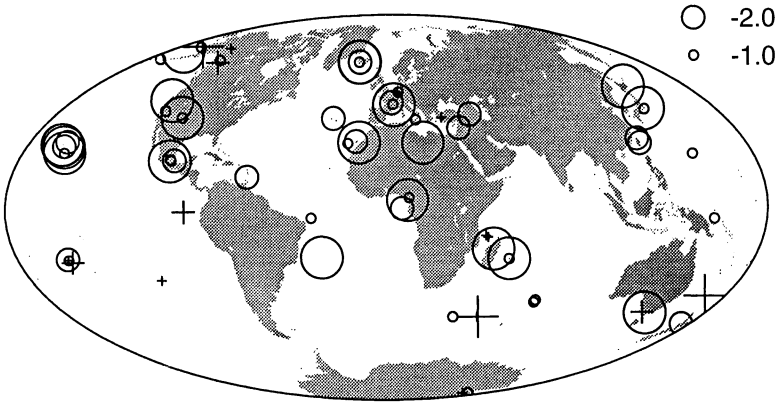

(b) All Normal Data: N = 79

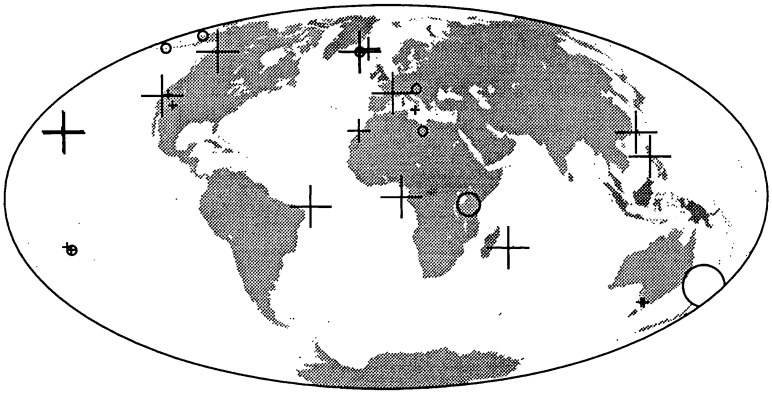

(c) All Reverse Data: N = 34

Figure 3.3: Inclination Residuals for (a) Brunhes, (b) all normal, (c) reverse data relative to a GAD model. Residuals are normalized by the uncertainty in the mean inclination at each site. Circles denote negative residuals, plus signs denote positive residuals; symbol size is magnitude.

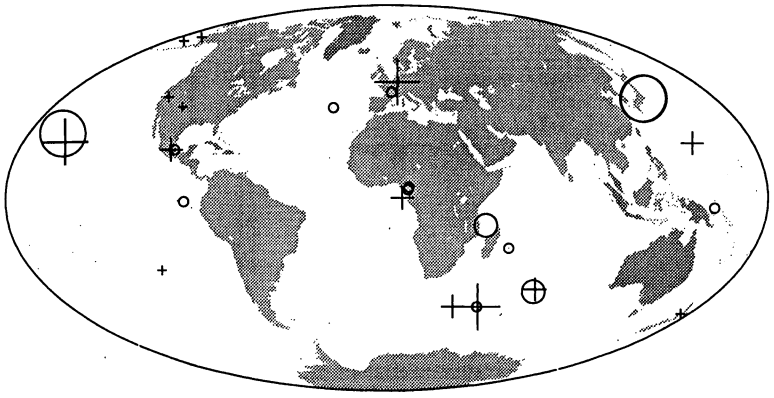

(a) Brunhes Data: N = 34

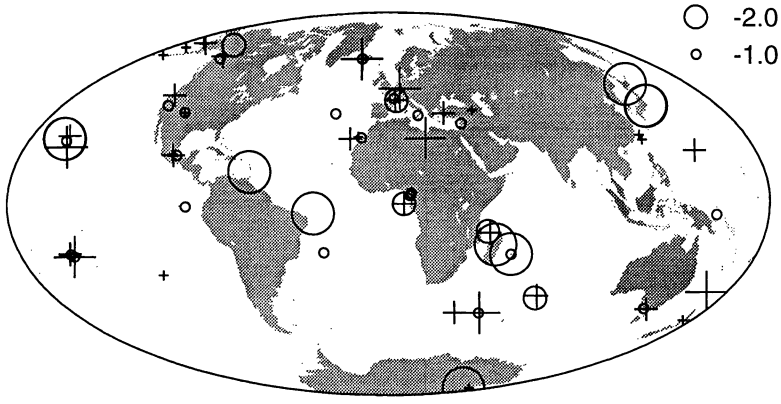

(b) All Normal Data: N = 79

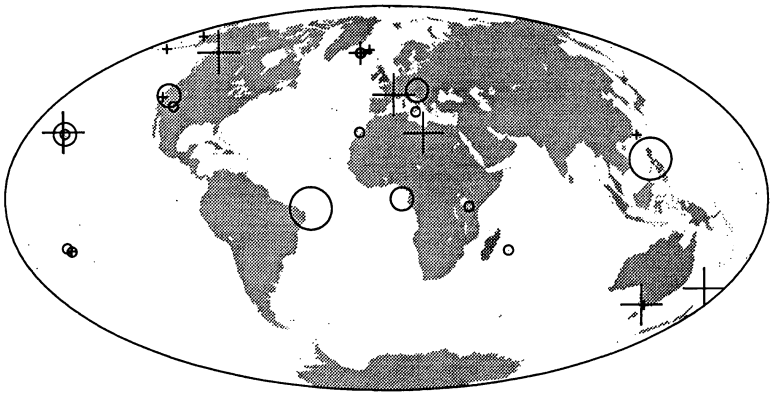

(c) All Reverse Data: N = 34

Figure 3.4: Declination residuals relative to a GAD model. Same three subsets of the database and normalization as in figure 3.3.

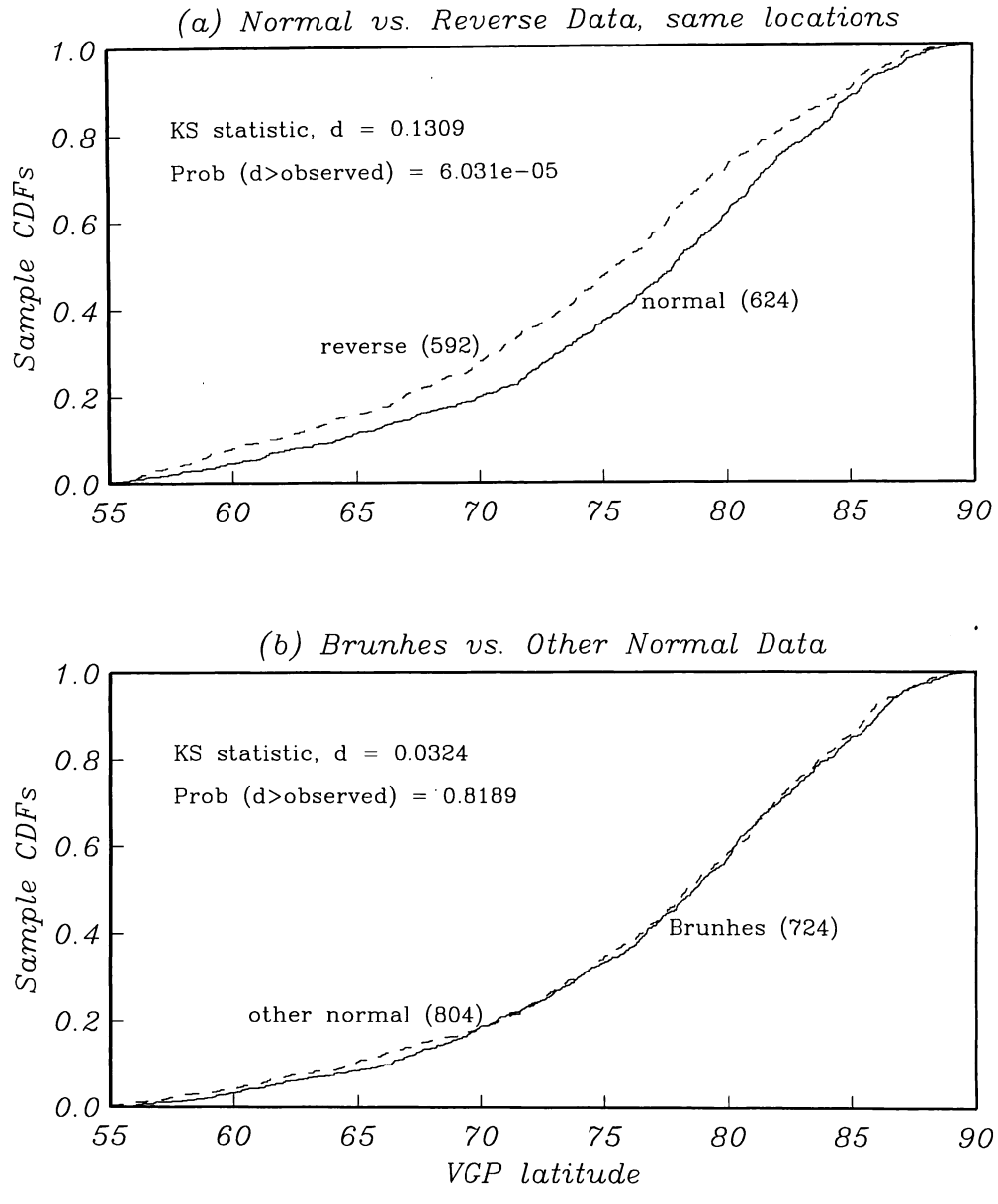

Figure 3.5: Results of Kolmogorov-Smirnov test applied to different subsets of database. (a) Normal (solid) and reverse (dashed) from same locations, (b) Brunhes (solid) and rest of normal (dashed) data. Sample cumulative distribution function shown for the two subsets being compared. KS statistic, d, is given, along with the probability that d is larger than observed, which is a measure of the similarity of the distributions (see text).

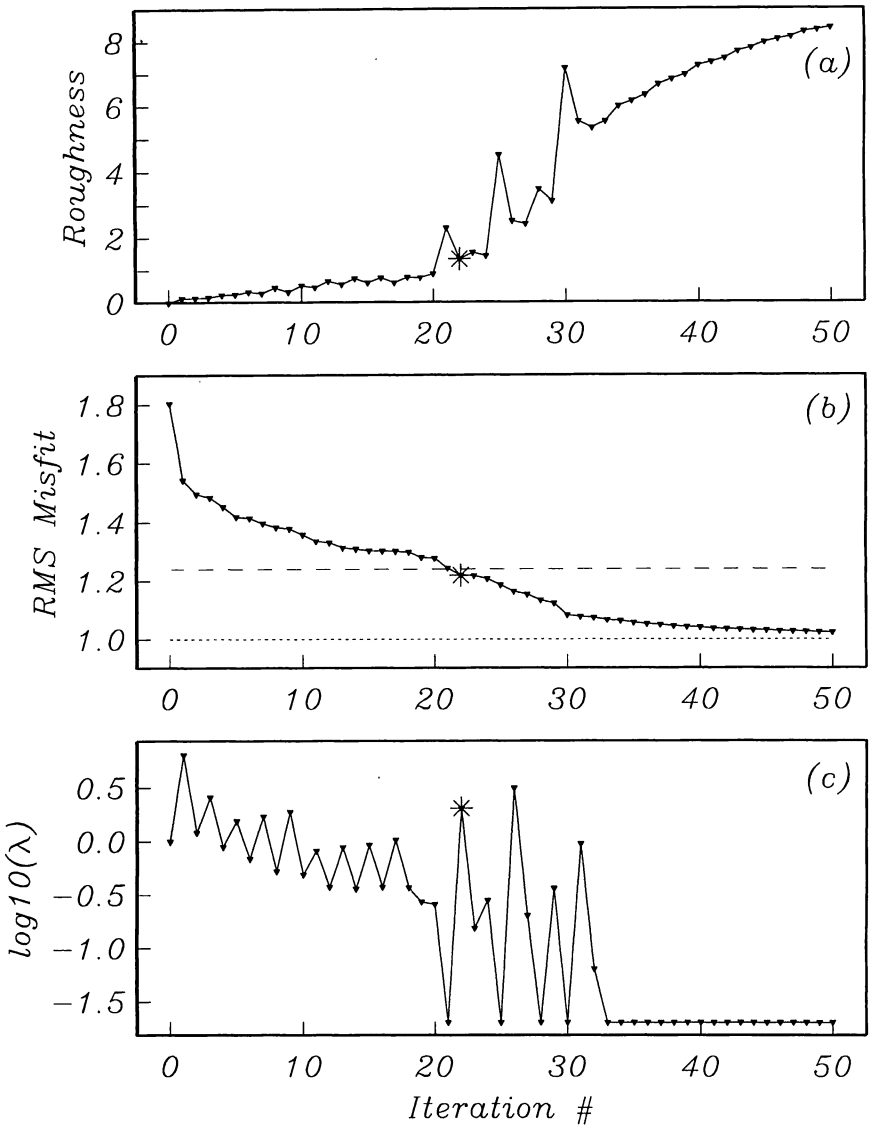

Figure 3.6: Change in (a) model roughness, (b) RMS misfit of model to data and (c) Lagrange multiplier as a function of iteration number during a typical regularized non-linear inversion. This example is taken from an inversion of the Brunhes data using a GAD starting model. As the iteration proceeds, λ typically decreases as the RMS misfit can only be reduced at the expense of increasing model roughness. The dashed line in (b) is the required tolerance level (95% limit on expected value of chi-squared). RMS of unity (dotted) corresponds to a tolerance level equal to the expected value of chi-squared. The preferred model has a roughness indicated by the asterisk in (a), and the corresponding misfit in (b).

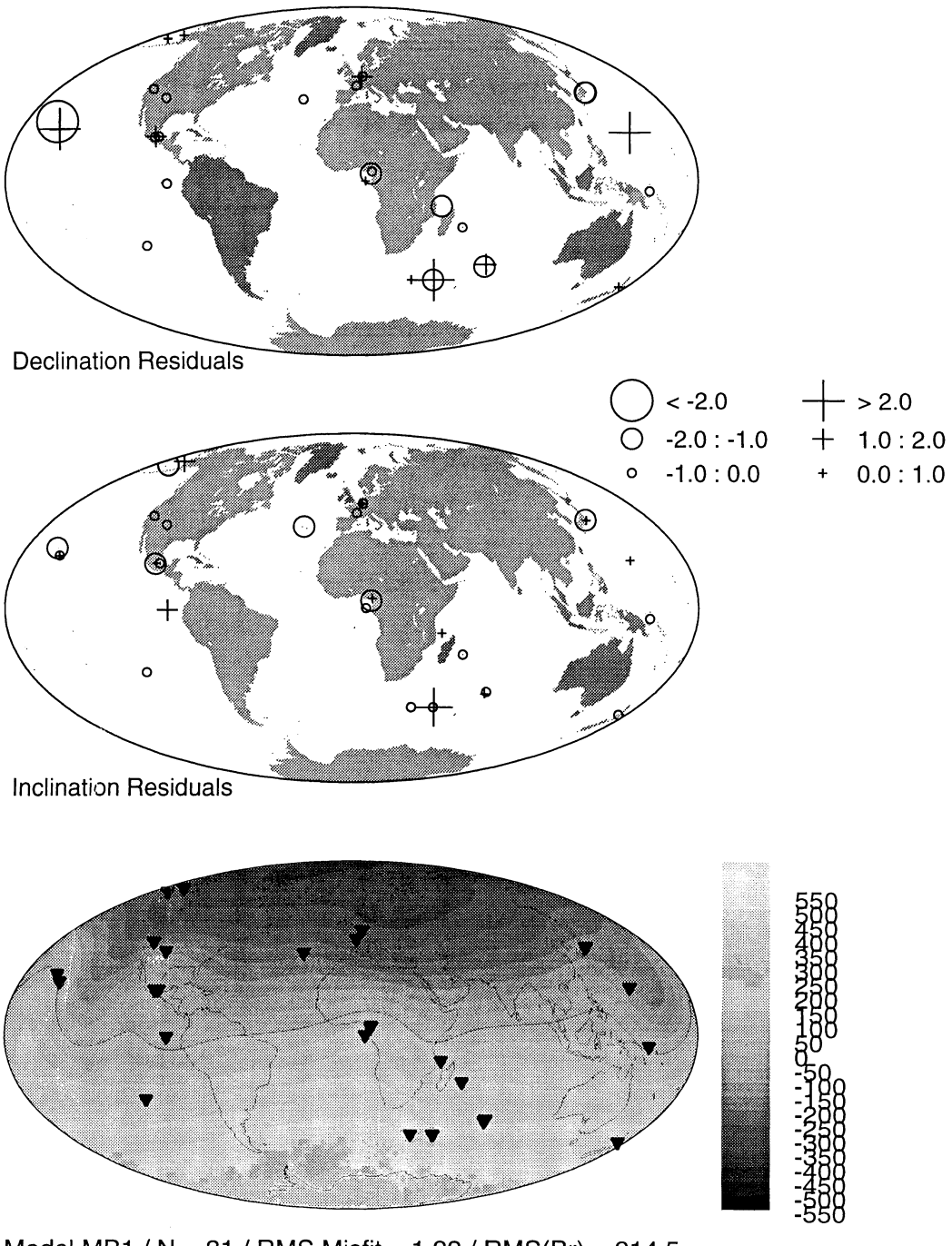

Figure 3.7: Inversion of Brunhes normal polarity data. Lower figure is the resulting field model (MB1), shown in terms of Br at the CMB, units are μT, contour interval is 50 μT. Triangles denote data locations. N is the number of locations. Upper two figures show inclination and declination residuals (normalized by uncertainty) relative to MB1.

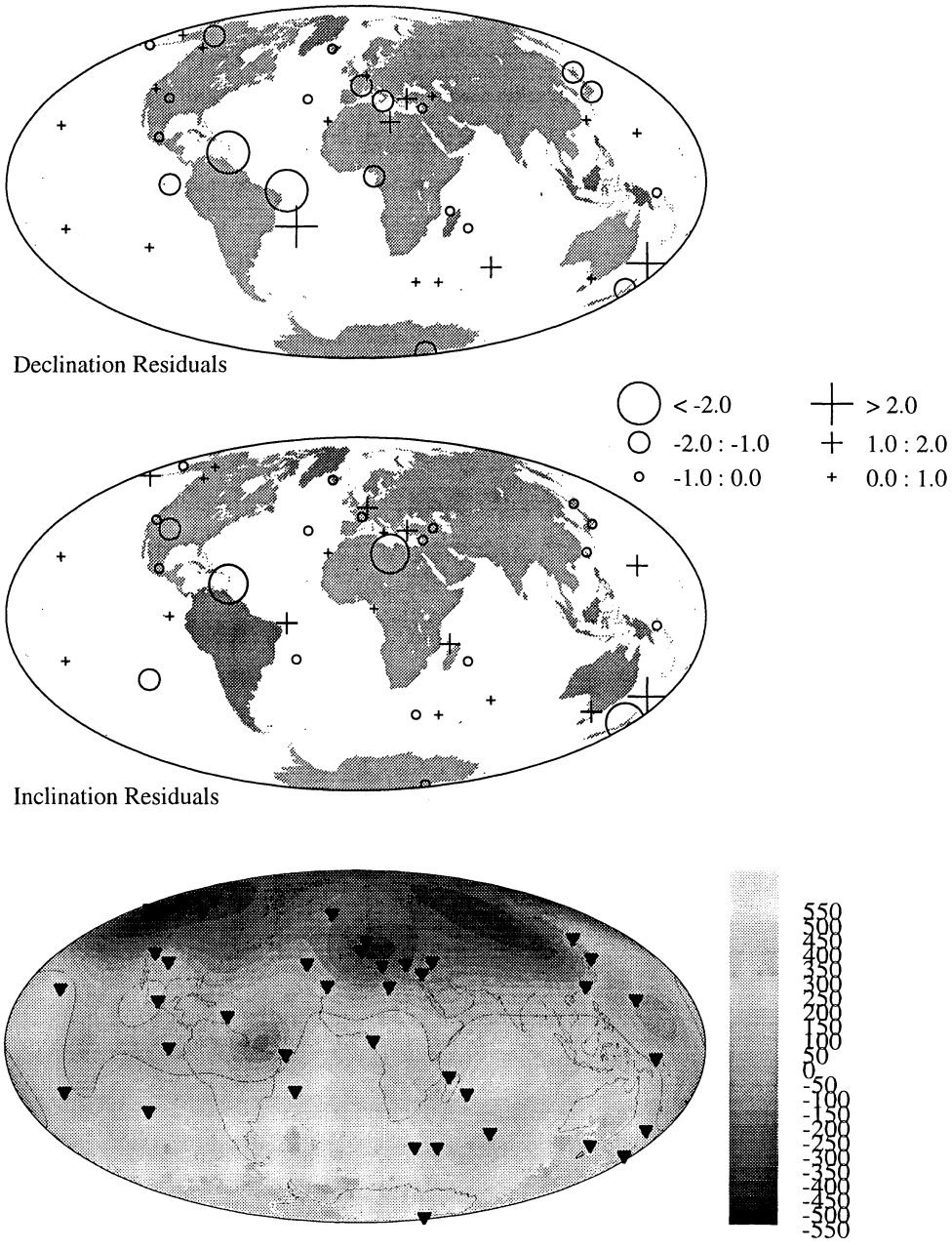

Figure 3.8: Inversion of binned (5 degree bins) normal polarity data (model MN1).

Inclination, declination residuals relative to MN1.

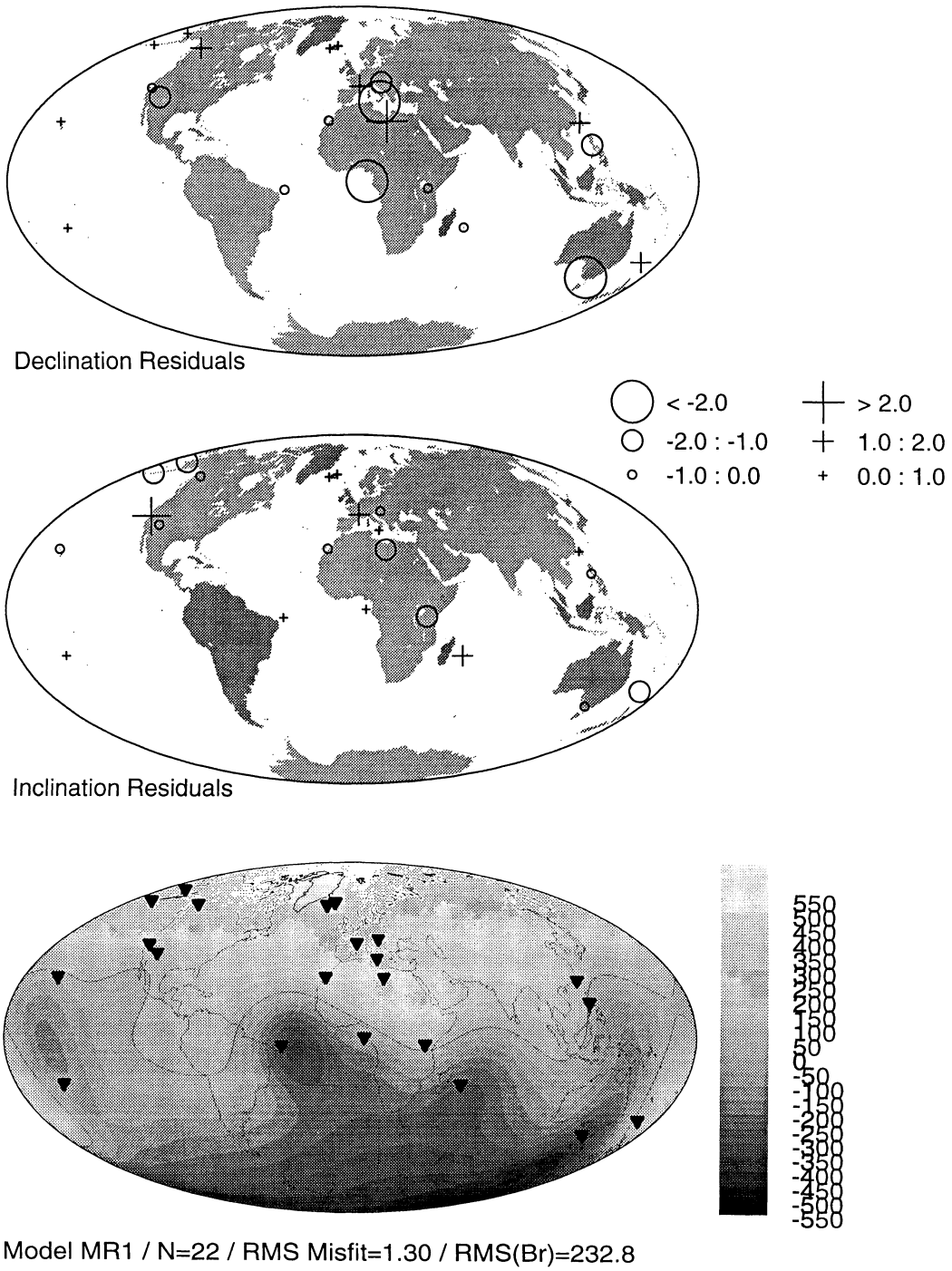

Figure 3.9: Inversion of binned (5 degree bins) reverse polarity data (model MR1). Inclination, declination residuals relative to MR1.

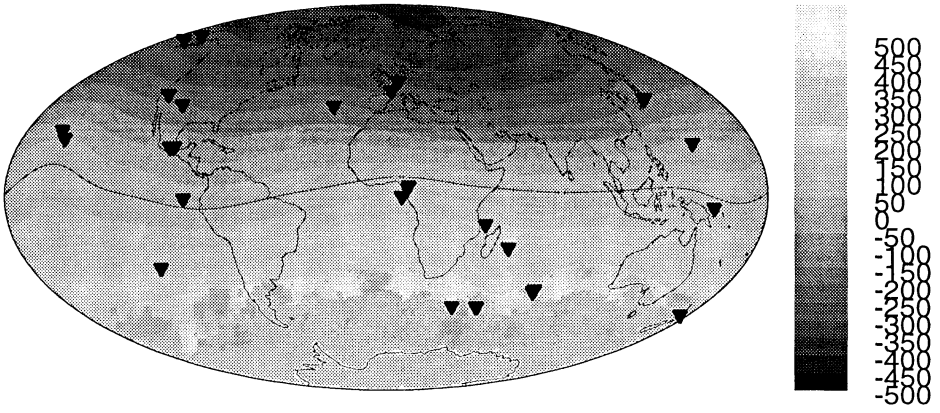

Output: noisy D, I data at 31 Brunhes locations inverted / l = 10

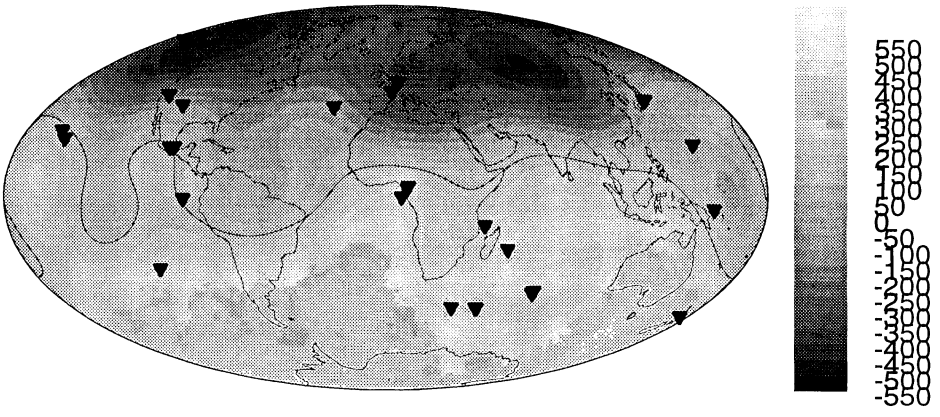

Input = Field from binned normal data expanded to l = 6

Figure 3.10: Lower figure is model field from inversion of all the normal data, expanded to degree and order 6. Synthetic observations with noise were generated from this model. A non-linear inversion of the synthetic observations to degree and order 10 resulted in the upper field model, which is strikingly similar to the Brunhes polarity field model, MB1 (figure 7).

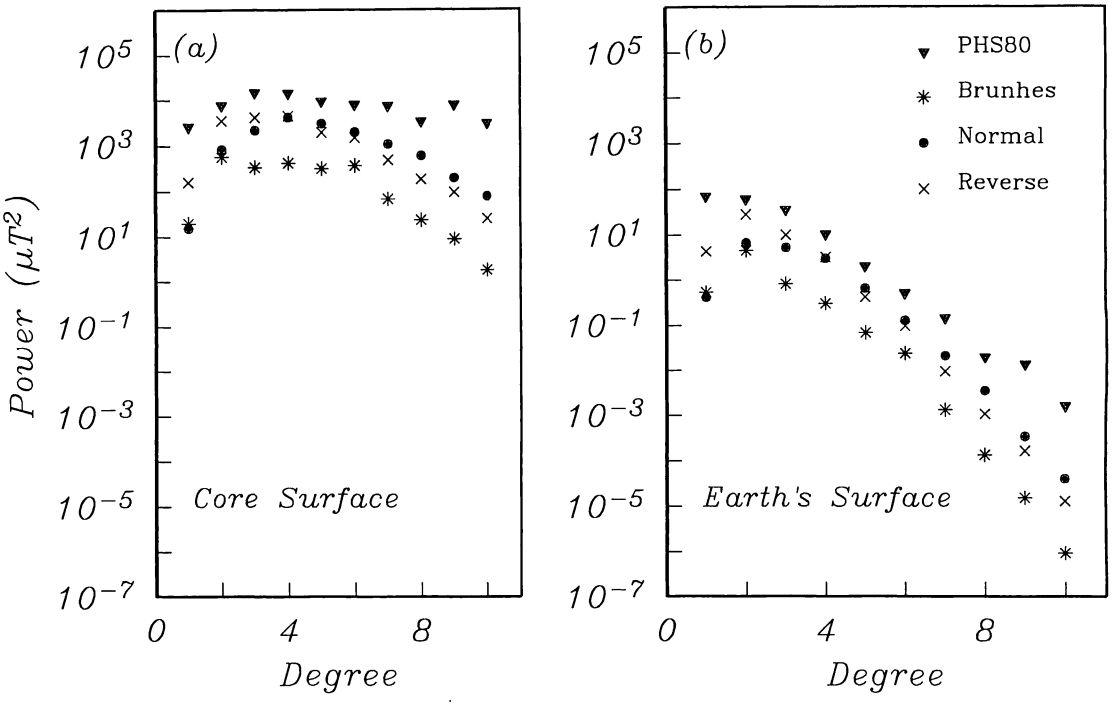

Figure 3.11: Power in resulting field models for Brunhes (asterisks), all normal (solid circles), and all reverse (crosses) data, computed using *Lowes* [1974] power spectrum. Corresponding power spectrum for the present day field as described by the PHS80 model (triangles) is also shown.

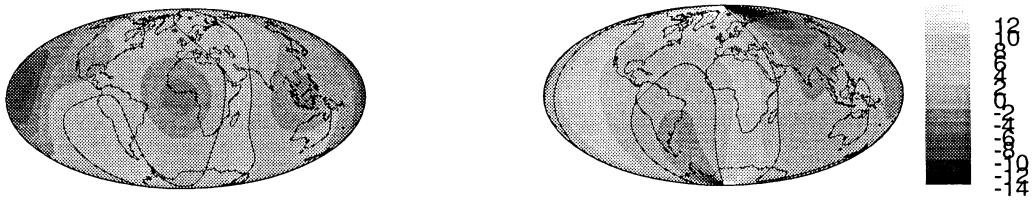

(a) Brunhes Inclination Anomaly (MB1-GAD)

Brunhes Declination Anomaly (MB1-GAD)

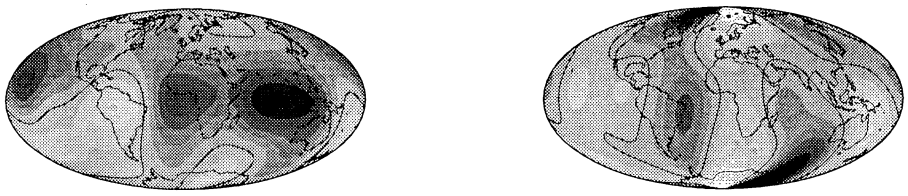

(b) Normal Inclination Anomaly (MN1-GAD)

Normal Declination Anomaly (MN1-GAD)

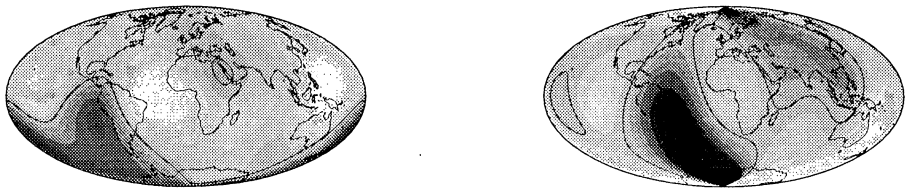

(c) Reverse Inclination Anomaly (MR1-GAD)

Reverse Declination Anomaly (MR1-GAD)

Figure 3.12: Maps of declination and inclination anomalies (model minus GAD model) for models (a) MB1, Bunhes, (b) MN1, normal and (c) MR1, reverse. Contour interval is 2 degrees.

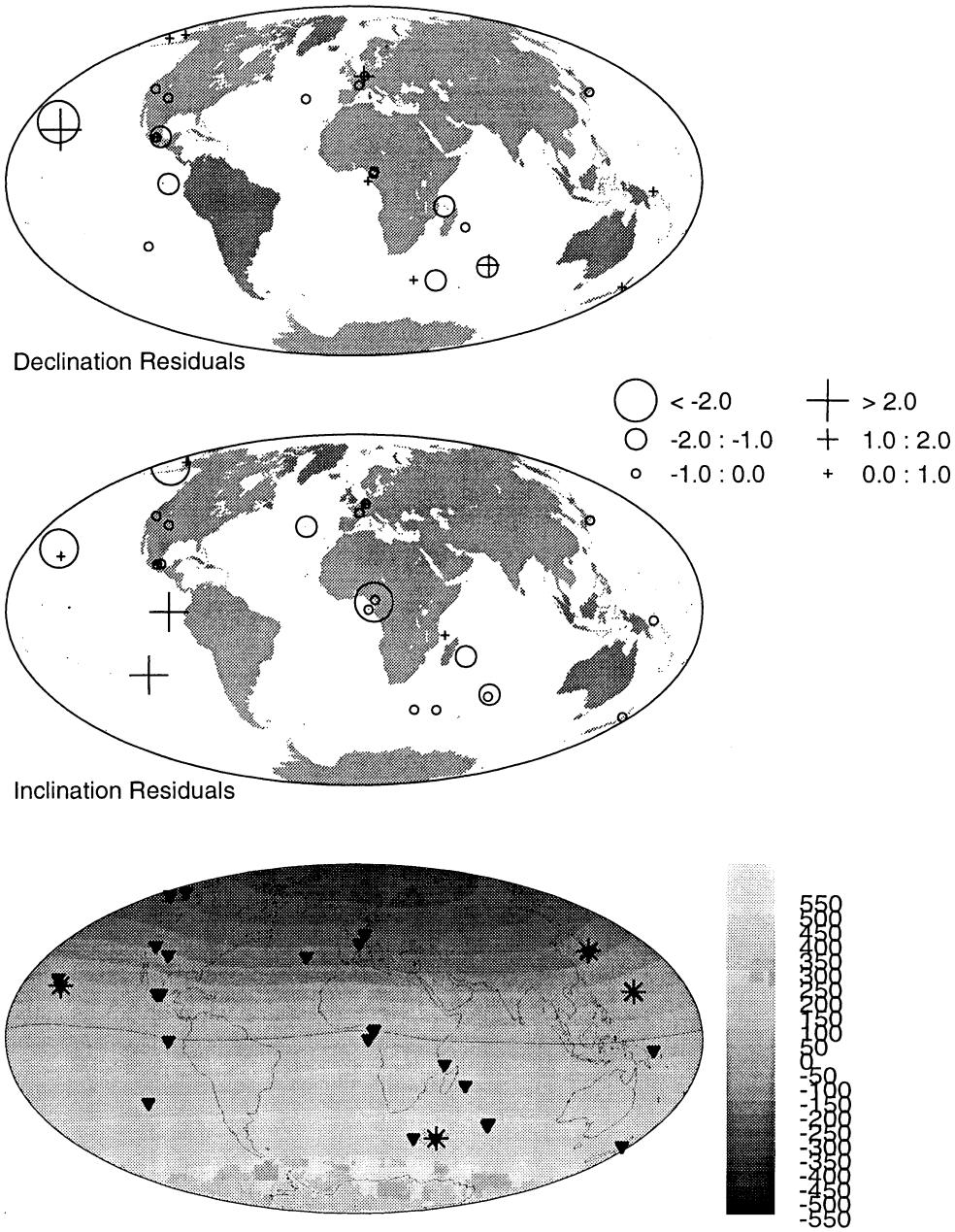

Figure 3.13: Brunhes field model (MB2) and inclination, declination residuals for an inversion in which all 4 anomalous sites (asterisks) were deleted. Figure format as for figure 3.7.

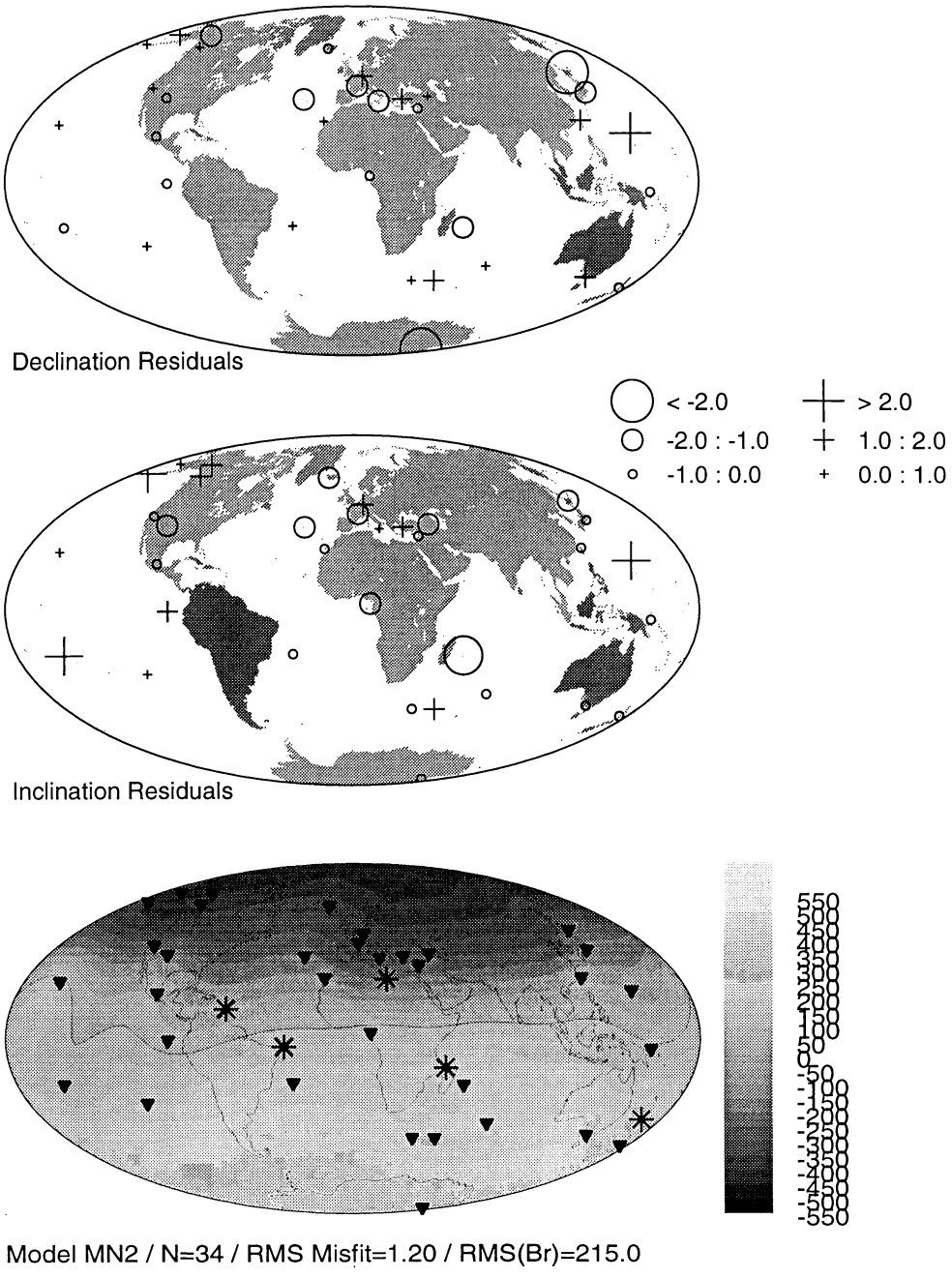

Figure 3.14: Normal polarity field model (MN2) and inclination, declination residuals for an inversion in which all 5 anomalous sites (asterisks) were deleted. Figure format as for figure 8.

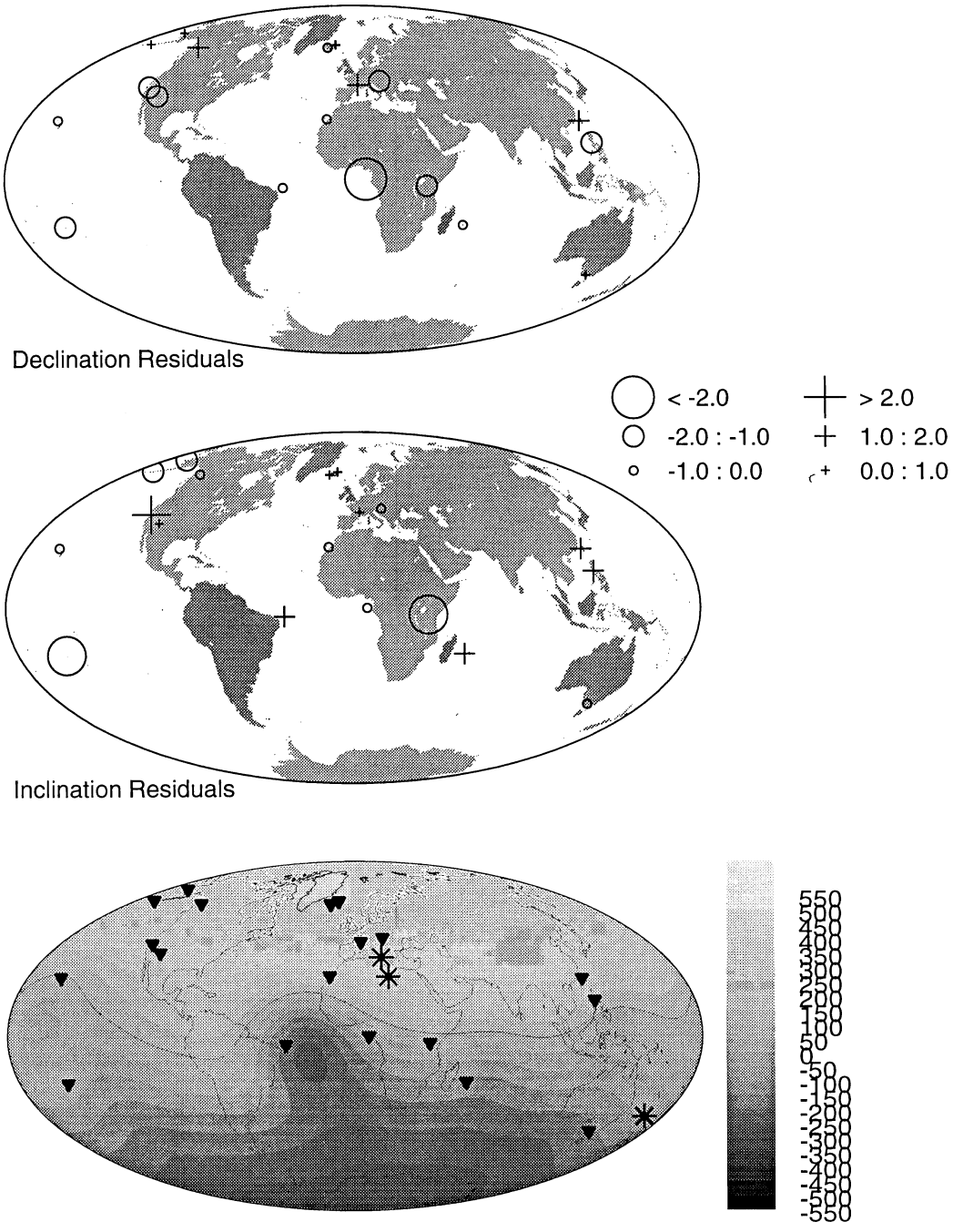

Figure 3.15: Reverse polarity field model (MR2) and declination, inclination residuals for an inversion in which all 3 anomalous sites (asterisks) were deleted. Format as for figure 3.9.

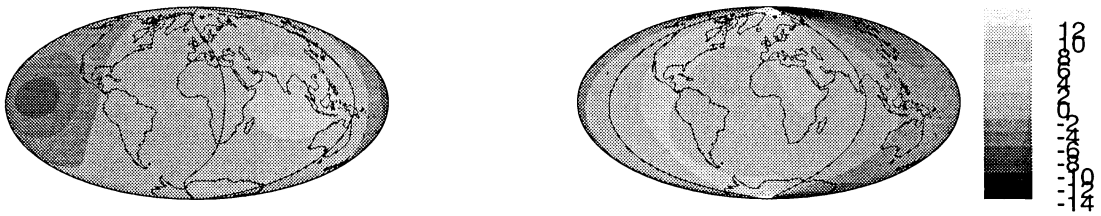

(a) Brunhes Inclination Anomaly (MB2-GAD)

Brunhes Declination Anomaly (MB2-GAD)

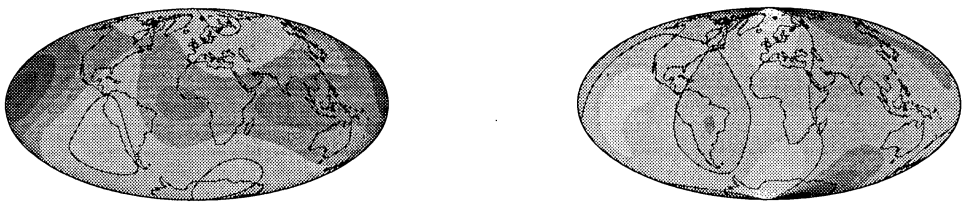

(b) Normal Inclination Anomaly (MN2-GAD)

Normal Declination Anomaly (MN2-GAD)

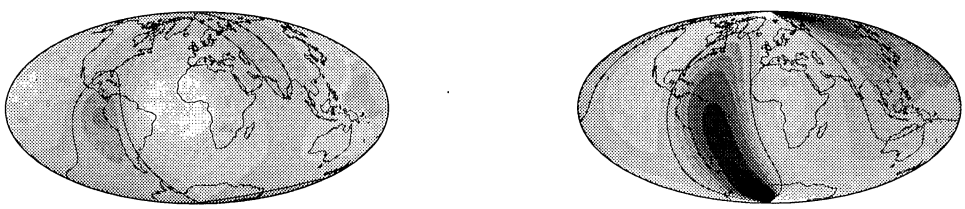

(c) Reverse Inclination Anomaly (MR2-GAD)

Reverse Declination Anomaly (MR2-GAD)

Figure 3.16: Inclination and declination anomalies for models MB2, MN2, MR2 shown in figures 13 - 15. (a) MB2, Brunhes, (b) MN2, normal, (c) MR2, reverse.

Table 3.1: Data Summary

Brunhes Normal Polarity Data

N	λ	ϕ	D	σ_D	I	σ_I	ΔI	$LoAge$	$HiAge$
15	-46.9	37.8	7.89	7.04	-67.30	3.04	-2.37	0.00	0.70
32	-46.5	51.7	-2.66	3.48	-64.50	1.58	0.12	0.00	0.70
37	-46.5	52.2	10.14	3.70	-60.52	1.63	4.1	0.00	0.70
14	-38.8	77.5	-10.80	6.94	-58.14	3.44	-0.02	0.00	0.70
19	-38.5	175.0	0.53	3.41	-60.73	1.58	-2.88	0.00	0.70
24	-37.8	77.5	5.33	3.50	-59.25	2.18	-2.03	0.00	0.70
53	-27.1	-109.2	1.04	2.51	-45.00	1.42	0.66	0.00	0.70
17	-21.1	55.5	-1.17	3.85	-38.94	3.05	-1.28	0.00	0.70
12	-11.6	43.3	-2.97	2.52	-20.16	2.64	2.16	0.00	0.70
5	-4.0	150.0	-2.39	10.51	-14.95	8.34	-6.99	0.00	0.01
18	-0.8	-88.4	-1.00	2.21	2.91	2.45	4.57	0.00	0.70
14	0.0	6.5	3.94	3.50	-5.37	4.80	-5.37	0.00	0.70
38	3.5	9.0	-0.34	2.13	-2.31	2.48	-9.28	0.00	0.70
15	4.5	9.5	-0.58	4.74	5.18	5.44	-3.77	0.00	0.70
23	18.1	145.7	1.97	1.32	32.16	1.49	-1.01	0.00	0.70
30	19.0	-99.0	1.31	2.41	29.43	2.15	-5.12	0.00	0.70
21	19.2	-98.6	3.73	2.18	34.17	3.28	-0.69	0.00	0.70
20	19.3	-96.9	-0.73	2.23	30.83	2.42	-4.18	0.00	0.70
7	19.4	-155.5	10.19	4.58	31.45	7.23	-3.71	0.00	0.02
28	19.5	-155.5	8.38	2.73	21.66	2.33	-13.65	0.01	0.02
29	19.5	-155.5	7.50	1.43	31.72	1.79	-3.59	0.20	0.30
11	22.0	-160.0	-7.23	2.73	26.79	2.72	-11.49	0.30	0.70
14	23.1	-158.0	2.70	2.20	35.62	4.32	-4.85	3.00	0.00
13	35.0	139.0	-5.52	2.06	53.70	1.99	-0.77	0.00	0.70
35	35.2	138.8	-4.99	2.40	49.82	1.68	-4.86	0.00	0.70
6	35.9	-106.5	-1.77	2.39	43.88	1.88	-11.49	0.40	0.60
33	37.7	-119.0	-0.59	3.08	55.80	1.98	-1.27	0.00	0.75

20	38.7	-27.2	-2.83	4.13	52.48	2.81	-5.55	0.00	0.70
16	41.8	-121.9	4.50	2.67	50.82	2.24	-9.92	0.00	0.70
5	44.7	4.3	-10.52	9.46	51.51	3.12	-11.68	0.00	0.70
26	45.7	3.0	-0.18	3.54	61.90	1.80	-2.1	0.00	0.70
37	50.3	6.8	10.03	3.90	67.97	1.25	0.51	0.00	0.70
30	50.4	7.3	3.06	3.22	67.17	1.41	-0.36	0.00	0.70

Remaining Normal Polarity Data

13	-78.4	164.2	-59.10	20.39	-83.85	1.77	0.28	0.00	1.54
5	-77.6	166.3	6.90	38.54	-87.32	3.65	-3.61	0.56	1.39
17	-38.0	144.5	5.90	4.05	-61.14	1.40	-3.76	0.00	4.50
5	-38.0	142.8	-1.33	9.80	-55.03	2.28	2.35	0.00	4.50
25	-29.1	167.9	11.42	1.89	-42.14	1.59	5.93	2.40	3.10
27	-21.0	55.5	-4.28	1.94	-47.20	1.62	-9.69	0.00	0.98
5	-20.5	-29.3	-0.43	2.51	-40.99	1.12	-4.17	2.30	3.30
23	-17.7	-149.6	3.92	1.37	-29.09	2.34	1.48	0.40	1.60
8	-17.7	-149.6	-2.65	4.60	-31.02	4.26	3.41	0.60	1.20
14	-17.0	47.5	-10.20	4.80	-43.63	3.69	-12.19	0.00	1.60
32	-16.8	-151.0	-0.07	2.07	-31.93	1.60	-0.88	2.30	2.50
8	-16.8	-151.5	4.45	4.05	-30.87	3.45	0.3	2.01	3.00
7	-16.5	-151.3	5.64	4.28	-34.03	3.38	-3.39	3.10	3.40
23	-12.2	44.4	2.81	2.79	-22.08	2.71	1.3	0.00	1.62
7	-3.9	-32.4	-9.68	1.31	-8.56	1.24	-0.89	1.70	5.10
9	0.0	6.5	-7.33	4.27	-8.91	5.56	-8.91	2.50	4.00
9	13.3	-61.2	-9.14	3.30	18.10	4.78	-7.2	0.29	1.28
25	19.5	-155.5	0.46	1.63	25.05	3.00	-10.26	0.01	5.00
23	19.6	-99.0	1.95	3.15	33.94	3.33	-1.52	1.60	5.30
25	21.3	-157.8	-0.08	1.87	32.10	1.92	-5.85	0.03	0.85
31	21.5	-158.1	-0.43	2.33	33.98	2.17	-4.25	2.40	3.60
46	22.0	-159.5	-3.57	1.47	27.45	2.19	-12.15	3.50	5.60
12	23.5	121.4	3.86	5.22	31.99	5.36	-9.02	0.01	5.00
27	25.3	121.5	1.27	2.88	38.50	2.80	-4.89	0.01	3.40

10	27.8	-18.0	6.72	6.05	45.62	5.19	-0.9	0.00	1.60
10	27.8	17.3	5.07	2.22	34.09	3.01	-12.43	0.40	2.20
18	28.2	-12.8	-2.05	3.67	40.55	2.39	-6.45	0.00	1.60
14	28.7	-14.2	3.27	5.03	41.94	2.91	-5.66	0.00	1.66
9	34.0	36.0	-3.66	5.24	49.09	3.61	-4.36	1.60	5.00
6	35.9	-106.5	0.38	5.30	51.44	4.16	-3.93	0.00	1.60
14	38.0	15.0	-1.74	3.39	56.26	1.35	-1.12	0.00	1.60
5	38.6	28.7	11.60	7.71	61.60	4.05	3.66	0.00	1.60
5	39.5	44.0	3.44	7.39	51.33	5.83	-7.43	0.00	1.60
13	43.5	143.5	-13.48	5.33	57.45	1.84	-4.77	0.00	1.60
7	45.0	3.8	8.18	7.76	61.56	3.61	-1.87	0.00	2.30
53	53.0	-172.0	0.07	3.18	69.35	1.13	0	0.00	5.00
8	57.2	-170.4	3.82	8.41	63.31	3.18	-8.82	0.00	0.80
16	57.5	-130.0	-6.21	11.32	75.00	2.34	2.67	0.00	5.00
11	58.5	-131.5	13.48	9.19	69.82	3.48	-3.14	0.00	5.00
13	60.0	-165.9	1.69	7.51	73.20	1.82	-0.69	0.00	0.80
8	60.3	-166.1	18.09	12.46	78.46	1.40	4.36	0.80	2.40
9	62.9	-143.2	-6.98	3.96	75.97	1.92	0.31	3.00	4.00
10	64.5	-22.0	26.56	8.97	71.72	1.42	-0.72	3.40	5.00
29	64.5	-21.5	-7.37	7.86	73.61	1.77	-2.98	2.40	3.40
52	64.5	-21.5	4.44	4.05	71.44	1.15	-4.87	1.80	2.40
65	64.5	-22.0	5.64	4.70	75.87	0.81	-5.15	2.40	3.40

Reverse Polarity Data

N	λ	ϕ	D	σ_D	I	σ_I	ΔI	$LoAge$	$HiAge$
14	-38.0	144.5	180.62	2.74	57.81	2.07	0.43	0.00	4.50
5	-38.0	142.8	194.80	7.33	59.11	6.26	1.73	0.00	4.50
12	-29.1	167.9	195.92	2.27	38.62	1.96	-9.45	2.40	3.10
13	-21.0	55.5	178.81	4.86	45.83	3.41	8.32	2.00	2.11
39	-17.7	-149.6	179.31	1.33	32.36	2.02	-0.14	0.60	1.20
6	-17.5	-149.9	184.42	4.43	34.94	5.50	2.66	1.40	1.60

6	-16.5	-151.3	178.18	5.69	32.99	4.83	2.35	3.10	3.40
5	-3.9	-32.4	171.43	0.77	26.93	1.08	19.26	1.70	5.10
12	-3.2	35.5	179.97	4.96	-5.22	7.53	-11.6	0.70	2.45
14	0.0	6.5	172.11	4.33	14.29	3.98	14.29	0.00	4.00
5	14.5	120.6	172.85	2.21	-17.40	4.05	9.87	0.00	5.00
27	21.5	-158.1	177.44	2.30	-24.31	3.11	13.92	2.40	3.60
33	21.5	-158.1	178.86	1.60	-29.83	2.31	8.4	1.80	2.60
42	22.0	-159.5	183.27	1.26	-29.87	0.88	0.69	3.00	5.00
5	22.0	-160.0	188.97	2.87	-38.25	3.59	9.07	3.50	5.60
7	23.6	119.5	180.20	3.20	-28.67	5.57	12.48	0.01	5.00
54	27.8	17.3	189.29	1.70	-47.09	1.73	-0.57	0.40	2.20
6	28.2	-12.8	178.04	6.22	-38.94	5.73	8.06	0.81	1.74
9	35.5	-111.6	173.52	7.24	-51.87	3.75	3.1	3.62	4.38
6	37.2	14.8	178.61	1.45	-54.03	2.74	2.6	1.40	3.60
13	38.5	-122.5	181.64	4.25	-42.78	2.07	15.07	4.00	5.50
6	39.3	-120.0	170.76	9.02	-54.91	4.68	3.62	0.70	5.00
13	45.0	3.8	190.88	4.87	-56.47	3.18	6.96	0.70	2.41
6	46.9	17.5	168.67	9.71	-65.17	5.00	-0.24	0.00	5.00
8	53.5	-168.1	188.53	15.50	-71.92	4.00	-2.22	1.50	2.30
44	57.5	-130.0	191.34	5.30	-68.96	1.57	3.37	0.00	5.00
8	60.3	-166.1	188.39	11.25	-74.95	4.06	-0.85	0.80	2.40
103	64.5	-22.0	179.48	4.15	-74.66	0.94	-1.6	2.40	3.40
12	64.5	-21.5	190.02	14.31	-78.19	2.34	0.81	3.40	5.00
15	64.5	-22.0	189.56	7.35	-69.70	2.30	1.93	1.57	2.40
16	64.5	-22.0	185.22	6.08	-71.51	2.25	5.08	1.80	2.40
68	64.5	-21.5	180.76	5.07	-75.78	1.04	6.89	2.40	3.40
8	64.5	-21.5	175.89	12.09	-67.91	2.76	8.68	3.40	4.00
19	66.2	-15.2	185.30	9.10	-74.28	2.31	3.28	1.09	2.00

N = number of flows; λ, ϕ = site latitude, longitude; D, I = mean declination, inclination in degrees; σ_D, σ_I = standard error in mean declination, inclination; ΔI = inclination anomaly in degrees; $LoAge$, $HiAge$ = minimum, maximum age of flows in MYr.

Table 3.2: Zonal Models

l_{max}	*Brunhes (N=31)*		*All Normal (N=39)*		*All Reverse (N=22)*	
	RMS (R_1)	*RMS (R_2)*	*RMS (R_1)*	*RMS (R_2)*	*RMS (R_1)*	*RMS (R_2)*
Starting RMS	1.804	1.804	2.314	2.314	4.056	4.056
2	1.639	1.640	2.050	2.046	3.164	3.164
3	1.568	1.577	1.947	1.950	3.113	3.112
4	1.563	1.575	1.945	1.950	2.895	3.111
5	1.542	1.572	1.929	1.947	2.883	3.077
6	1.535	1.572	1.928	1.947	2.791	3.085
7	1.532	1.572	1.923	1.947	2.787	3.085
8	1.533	1.572	1.913	1.946	2.778	3.085
9	1.533	1.572	1.913	1.946	2.778	3.085
10	1.533	1.572	1.913	1.946	2.782	3.085
11	1.533	1.572	1.913	1.946	2.778	3.085
Required RMS	1.25	1.25	1.22	1.22	1.30	1.30

Table 3.3: Jackknife Estimates of Mean Spherical Harmonic Coefficients with Standard Errors

(a) Brunhes Field Model, MB1

l	m	g_l^m	h_l^m	$S_{g_l^m}$	$S_{h_l^m}$
1	0	-30.0000	0	0	0
1	1	-0.4367	-0.0902	0.0458	0.0331
2	0	-0.9879	0	0.0225	0
2	1	-0.4848	-0.2630	0.0177	0.0103
2	2	0.5648	-0.1359	0.0170	0.0104
3	0	-0.3106	0	0.0103	0
3	1	-0.0275	-0.0993	0.0055	0.0066
3	2	-0.0439	0.0007	0.0085	0.0043
3	3	0.0738	-0.2234	0.0063	0.0127
4	0	0.0364	0	0.0027	0
4	1	0.0044	0.0800	0.0021	0.0036
4	2	0.0275	-0.0911	0.0035	0.0044
4	3	-0.0002	-0.0051	0.0023	0.0021
4	4	0.1325	0.1046	0.0065	0.0053

(b) Normal Field Model, MN1

1	0	-30.0000	0	0	0
1	1	0.2090	0.3950	0.0184	0.0209
2	0	-1.3344	0	0.0147	0
2	1	0.0370	-0.2828	0.0155	0.0190
2	2	0.2644	-0.2129	0.0108	0.0090
3	0	-0.4673	0	0.0110	0
3	1	-0.0456	-0.8221	0.0113	0.0135
3	2	-0.0560	0.3130	0.0081	0.0094
3	3	0.3887	-0.2921	0.0092	0.0053
4	0	0.1392	0	0.0066	0
4	1	0.3130	0.2652	0.0072	0.0066
4	2	0.2312	-0.4662	0.0095	0.0072
4	3	-0.2907	-0.0337	0.0075	0.0053

4	4	0.1049	-0.0771	0.0063	0.0053

(c) Reverse Field Model, MR1

1	0	30.0000	0	0	0
1	1	-0.9116	-1.2209	0.0542	0.0489
2	0	1.9800	0	0.0480	0
2	1	1.5314	1.2344	0.0352	0.0474
2	2	-0.6799	0.7043	0.0369	0.0296
3	0	1.0973	0	0.0398	0
3	1	0.0003	-0.6514	0.0232	0.0339
3	2	0.1191	0.0868	0.0362	0.0182
3	3	-0.5543	0.4740	0.0146	0.0318
4	0	-0.0858	0	0.0073	0
4	1	-0.4853	-0.2122	0.0171	0.0101
4	2	0.1811	-0.0081	0.0096	0.0117
4	3	0.1419	0.0789	0.0133	0.0134
4	4	0.3089	0.3313	0.0181	0.0185

l = spherical harmonic degree; m = order; g_l^m, h_l^m = mean sphercial harmonic coefficients in μT computed from jackknife estimates of field; $S_{g_l^m}$, $S_{h_l^m}$ standard error in mean spherical harmonic coefficients.

REFERENCES

Bloxham, J., & D. Gubbins, (1985). The secular variation of Earth's magnetic field. *Nature*, **317**, 777–781.

Bloxham, J., D. Gubbins & A. Jackson, (1989). Geomagnetic secular variation. *Phil. Trans. Roy. Soc. London, A*, **329**, 415–502.

Bloxham, J. & A. Jackson, 1992. Time-dependent mapping of the magnetic field at the core-mantle boundary. *J. Geophys. Res.*, **97**, 19537–19563.

Brown, L. & S. A. Mertzman, 1979. Negative inclination anomalies from the Medicine Lake Highland lavas, Northern California. *Earth Planet. Sci. Lett.*, **42**, 121–126.

Constable, S. C., R. L. Parker & C. G. Constable, (1987). Occam's inversion: A practical algorithm for generating smooth models from electromagnetic sounding data. *Geophysics*, **52**, 289-300.

Constable, C. G. & R. L. Parker, (1988). Statistics of the geomagnetic secular variation for the past 5 m.y.. *J. Geophys. Res.*, **93**, 11569–11581.

Constable, C. G., R. L. Parker & P. B. Stark, (1993). Geomagnetic field models incorporating frozen flux constraints. *Geophys. J. Int.*, **113**, 419-433.

Coupland, D. H. & R. Van der Voo, (1980). Long-term nondipole components in the geomagnetic field during the last 130 Myr. *J. Geophys. Res.*, **85**, 3529–3548.

Doell, R. R., 1970. Paleomagnetic secular variation study of lavas from the Massif Central, France. *Earth Planet. Sci. Lett.*, **8**, 352–362.

Doell, R. R. & A. Cox, 1965. Paleomagnetism of Hawaiian lava flows. *J. Geophys. Res.*, **70**, 3377–3405.

Gubbins, D., (1988). Thermal core-mantle interactions and the time-averaged paleomagnetic field. *J. Geophys. Res.*, **93**, 3413–3420.

Gubbins, D. & J. Bloxham, (1987). Morphology of the geomagnetic field and implications for the geodynamo. *Nature*, **325**, 509–511.

Gubbins, D. & P. Kelly, (1993). Persistent patterns in the geomagnetic field over the past 2.5 Myr. *Nature*, **365**, 829-832.

Johnson, C. L. & C. G. Constable, (1994). Paleosecular variation recorded by lava flows over the last 5 Myr. *Philos. Trans. R. Soc. London Ser. A* , in press.

Kendall, M. & A. Stuart, (1979). *The advanced theory of statistics, vol. 2, Inference and relationship.* 4th ed., MacMillan, New York.

Langel, R.A., (1989). Satellite magnetic measurements. **In** "*Encyclopedia of Solid Earth Geophysics*", ed. D.E. James, 977–989, pp. Van Nostrand, 107 Reinhold, New York.

Lee, S., (1983). A study of the time-averaged paleomagnetic field for the last 195 million years. *PhD Thesis.* Australian National University

Livermore, R.A., F. J. Vine & A. G. Smith, (1983). Plate motions and the geomagnetic field – I. Quaternary and late Tertiary. *Geophys. J.R. astr. Soc.*, **73**, 153–171.

Lock, J. & M. W. McElhinny, (1991). The global paleomagnetic database. *Surveys in Geophysics*, **12**, 317–491.

Lowes, F. J., 1974. Spatial power spectrum of the main geomagnetic field and extrapolation to the core. *Geophys. J.R. astr. Soc.*, **36**, 717–730.

Massey, F. J., (1951). The Kolmogorov-Smirnov test for goodness of fit. *J. Am. Stat. Assoc.*, **46**, 68–78.

Mankinen, E. A., C. S. Grommé, G. B. Dalrymple, M. A. Lanphere & R. A. Bailey, 1986. Paleomagnetism and K-Ar ages of volcanic rocks from Long Valley Caldera, California. *J. Geophys. Res.*, **91**, 633–652.

McElhinny, M. W., (1973). *Paleomagnetism and plate tectonics.* Cambridge University Press, New York.

Merrill, R. T. & M. W. McElhinny, (1977). Anomalies in the time averaged paleomagnetic field and their implications for the lower mantle. *Rev. Geophys. Space Phys.*, **15**, 309–323.

Merrill, R. T. & M. W. McElhinny, 1983. *The Earth's magnetic field.* Academic Press.

Merrill, R. T., P. L. McFadden & M. W. McElhinny, (1990). Paleomagnetic tomography of the core-mantle boundary. *Phys. Earth Planet. Inter.*, **64**, 87–101.

Opdyke, N. D., (1972). Paleomagnetism of deep-sea cores. *Rev. Geophys. Space Phys.*, **10**, 213–249.

Opdyke, N. D. & K. W. Henry, (1969). A test of the dipole hypothesis. *Earth Planet. Sci. Lett.*, **6**, 139–151.

Press, W. H., B. P. Flannery, S. A. Teukolsky & W. T. Vetterling, 1992. *Numerical Recipes, 2nd Edition.* Cambridge University Press.

Quidelleur, X., J-P. Valet, V. Courtillot & G. Hulot, (1994). Long-term geometry of the geomagnetic field for the last 5 million years; an updated secular variation database from volcanic sequences.. *Geophys. Res. Lett.*, in press.

Schneider, D. A. & D. V. Kent, (1988). Inclination anomalies from Indian Ocean sediments and the possibility of a standing non-dipole field. *J. Geophys. Res.*, **93**, 11621–11630.

Schneider, D. A. & D. V. Kent, (1990). The time-averaged paleomagnetic field. *Rev. Geophys.*, **28**, 71–96.

Shure, L., R. L. Parker & G. E. Backus, (1982). Harmonic splines for geomagnetic modelling. *Phys. Earth Planet. Inter.*, **28**, 215–229.

Shure, L., R. L. Parker & R. A. Langel, 1985. A preliminary harmonic spline model for MAGSAT data. *J. Geophys. Res.*, **90**, 11505–11512.

Tarling, D. H., (1983). *Palaeomagnetism. Principles and applications in geology, geophysics and archaeology.* Chapman and Hall, London.

Wilson, R. L., (1970). Permanent aspects of the earth's non-dipole magnetic field over Upper Tertiary times. *Geophys. J.R. astr. Soc.*, **19**, 417–439.

Wilson, R. L., (1971). Dipole offset – the time-averaged field over the past 25 million years. *Geophys. J.R. astr. Soc.*, **22**, 491–504.

Wilson, R. L., (1972). Paleomagnetic differences between normal and reversed field sources, and the problem of far-sided and right-handed pole positions. *Geophys. J.R. astr. Soc.*, **28**, 295–304.

CHAPTER 4

JOINTS IN VENUSIAN LAVA FLOWS

ABSTRACT

Venusian plains regions, as imaged by the Magellan spacecraft, display many styles of tectonic and volcanic deformation. Radar images of several volcanic plains reveal polygonal patterns of bright lineations. Intersection geometries of the lineations defining the polygonal patterns are typical of those found in tensile networks and the patterns exhibit no preferred orientation, implying that they are the result of horizontally isotropic stress fields. Such stress fields arise on the Earth as a consequence of desiccation, freeze-thaw cycles or cooling and produce mud cracks, ice-wedge polygons and columnar joints respectively. We propose that the polygonal patterns seen in the Magellan images of some of the volcanic plains are the result of thermal stresses. We consider two alternative scenarios which would generate sufficient tensile thermal stresses to cause failure. The first scenario is that of a cooling lava flow; the residual thermal stress which would develop (assuming no failure of the rock) is tensional and on the order of 400 MPa. This is much greater than the strength of unfractured terrestrial basalt (~10 MPa), so we can expect joints to form during cooling of Venusian lava flows. However, the spacing of the polygonal lineations seen in Magellan images is typically 1 - 2 km, much larger than the largest spacings of decimeters for joints in terrestrial lavas. The second scenario involves an increased heat flux to the base of the lithosphere; the resulting thermal stresses cause the upper lithosphere to be in tension and the lower lithosphere to be in compression. Brittle tensile failure occurs near the surface due to the finite yield strength of the lithosphere. The maximum depth to which failure occurs increases with increasing elevation of the temperature gradient. For an initially 25 km thick lithosphere and temperature gradient of 11°/km, this maximum depth varies from 0.5 km to 2 km as the temperature gradient is increased to 12°/km and 22°/km respectively. Both the cooling flow scenario and the heated lithosphere scenario produce isotropic tensile surface stress patterns, but the heated lithosphere model is more compatible with the kilometer scale of the polygonal patterns seen in Magellan images.

INTRODUCTION

Radar images obtained from the Magellan spacecraft reveal extensive plains displaying both tectonic and volcanic deformation. Some plains terrains are smooth and featureless, some show lobate areas of differing radar brightness, and some display radar bright lineations of compressional and/or extensional origin [*Saunders et al* ., 1991]. Radar bright lineaments identifiable as graben may extend for hundreds of kilometers. Other bright sinuous features are compressional in origin and similar to 'wrinkle' ridges seen on the moon. Some plains display intersecting sinuous features which are not identifiable as compressional or extensional. In several areas (figure 1) intersecting bright lineations form polygonal patterns (figure 2), which resemble fracture networks often developed in terrestrial rocks and soils.

Polygonal fracture networks on Earth commonly result from desiccation (e.g. mud cracks), freeze-thaw cycles (e.g. ice-wedge polygons), or cooling (e.g. columnar joints). Such fracture networks are usually dominated by tetragonal, pentagonal and hexagonal polygons [*Peck and Minakami*, 1968; *Ryan and Sammis*, 1978; *Aydin and DeGraff*, 1988]. Although the surface pattern of two types of shrinkage cracks may be the same, the ratio of the horizontal crack spacing to the crack depth may be different. For example, it can be observed that the ratio of crack spacing to crack depth for mud cracks is usually much greater than one, whereas for joints in terrestrial lava flows it is much less than one. On Venus, the surface conditions prohibit dessication or freeze-thaw cycles as causes of the polygonal fracture patterns. However, extensive lava flows and many volcanic edifices are evident supporting the possibility that the polygonal patterns may be of thermal origin.

On the earth, columnar jointing in lava flows and sills is common - e.g. the Giants Causeway in Northern Ireland, the Columbia River Basalts, and the lava lakes in Hawaii. Such jointing is the result of thermal stresses which develop as the lava cools and solidifies. Extensive research has been done, examining the evolution of polygonal joint patterns [*Aydin and DeGraff* , 1988], the relationship of jointing structures to cooling history [*Long and Wood* , 1986], observations of joint formation in Hawaiian lava lakes [*Peck and Minakami* , 1968], the mechanics of joint growth from observations of small scale structures on joint faces [*DeGraff and Aydin* , 1987] and the

relationship of joint spacing to cooling rate and joint growth increment [*DeGraff and Aydin*, 1986]. The processes of joint formation, interaction, propagation and arrest are not yet well understood, but substantial progress has been made over the last 15 years [*Nemat-Nasser et al .*, 1978; *Keer et al .*, 1978; *Nemat-Nasser et al .*, 1980].

On the basis of morphology, we propose that the bright polygonal patterns seen in some Magellan images of the volcanic plains are joint networks. We identify several areas displaying such patterns, noting their areal extent, the presence of volcanic features, and the regional topography. One area with well-developed polygonal patterns is described in detail, presenting evidence to suggest the patterns are tensional networks. We demonstrate that sufficient tensile stresses develop in a cooling Venusian flow to allow joints to form and that the thermal strain predicted is not incompatible with that observed. The major difference between the polygonal fracture patterns seen in the Magellan data and joints in terrestrial lavas is one of scale. The spacing of the Venusian features is on the order of kilometers, whereas the spacing of joints in terrestrial lavas varies from decimeters to centimeters. Factors which may cause such a difference in scale are discussed. It is possible that the tensional networks are the result of a thermally stressed layer much thicker than a single lava flow. We consider a second model in which thermal stresses develop as a result of regional elevation of the temperature gradient. In this case a layer several kilometres thick undergoes brittle tensile failure.

DATA ANALYSIS

A preliminary analysis of Magellan SAR and altimeter data has revealed 15 areas displaying bright polygonal patterns (figure 1). If the polygonal patterns are tensional fracture networks, resulting from the cooling and contraction of lava flows, then the fracture patterns should occur in areas that have been resurfaced by lava flows (identify flow source(s) and extent) and the edges of the fracture patterns should correlate with the margins of the flows. Alternatively, if the polygonal patterns are the result of thermal stresses in a thicker layer (upper crust or lithosphere) the edge of the patterns will not necessarily correlate with the limits of a lava flow. Below we discuss one area in detail, presenting evidence to support the hypothesis of a thermal contraction origin for the polygonal patterns.

The area which we have selected for detailed discussion is a region southeast of Nightingale Corona, at ~60°N, 135°E (figure 2) as polygonal patterns are clearly identifiable and are not obscured by contemporaneous or later volcanism/tectonism. The edge of the corona is seen as a bright feature in the top left of the image, and is associated with a flexural signature in the topography [*Johnson and Sandwell*, 1992]. Aside from this flexure, the region is extremely flat with regional slopes of < 1°. Figure 3 shows Magellan topography profiles [*Ford and Pettengill*, this issue] along sections XX', YY', ZZ' of figure 2. Bright polygonal patterns are evident on the dark plains. Possible origins for such smooth (radar-dark) flat areas include resurfacing by extremely fluid lavas (analogous to terrestrial flood basalts) ash cover, or tuffs. It is evident from thin mantling deposits identified in some areas that pyroclastic eruptions do occur on Venus [*Guest and Bulmer*, 1992]. However, it is currently believed that this type of eruption is unlikely to occur under Venusian conditions unless the volatile content of the ascending magma is in the range 2 - 4 % ; when pyroclastic eruptions do occur the pyroclasts themselves will be much less widely distributed than on Earth [*Head and Wilson*, 1986]. It is thus more likely that the dark background in the radar image is the result of lava flow(s) rather than ash cover or nuee ardente type flows. Although difficult to discern in figure 2, the edge of the polygonal patterns (very southern part of the image) appears to coincide with a boundary between areas of slightly different radar brightness. We propose this is the edge of one or more lava flows. Smaller, brighter flows occur closer to the corona edge and are easily identified by their lobate forms (FMIDR_60N132, Jet Propulsion Laboratory). Lava flows and other volcanic features are commonly seen in and around coronae on Venus [*Stofan et al.*, this issue]. It is therefore feasible that the extensive flows to the southeast of Nightingale are associated with the corona. The radial lineations which terminate at the edge of the corona and are distinguishable as depressions may be dikes - possible feeders for volcanic flows.

Polygonal patterns over the eastern part of the area are shown at higher resolution in Figure 4. The intersections of the bright lineations defining the polygons show geometries identical to those of shrinkage cracks on Earth: 'T' intersections, curved - 'T' intersections and 'Y' intersections [*Aydin and DeGraff*, 1988]. Examples of these intersection types are shown in figure 4 with interpretation sketches alongside the image. On Earth, the order of joint formation at 'T' and

curved - 'T' intersections is through joint first followed by the truncated joint, as the later joint cannot propagate across an existing fracture. Such 'T' and curved - 'T' intersections are common at the surface of terrestrial lava lakes where joints form sequentially [*Aydin and DeGraff*, 1988]. Examples A and B (figure 4) show such a geometry - one bright lineation is truncated against another continuous lineation. 'Y' - type intersections may result from 3 joints initiating at a common weak point in the material, from branching of a propagating joint, or from joints growing toward one another. Example C (figure 4) is typical of a 'Y' intersection although it is not possible to distinguish by which of the above mechanisms it was formed. Example D may represent an early stage in the formation of 'Y' intersection. Here 3 bright lineations of similar lengths terminate just short of a common intersection point. Few 'Y' intersections are present (figures 2 and 4). This is consistent with observations of terrestrial flows, where 'Y' intersections are more common in the interior of a flow than at the surface [*Aydin and DeGraff*, 1988]. In cases where terrestrial joints approach one another they curve away from each other and form overlappers. Examples E and F (figure 4) are typical of such overlappers.

The variation in mean spacing of the lineaments (polygon widths) in the area (figures 2 and 4) was made by estimating the average spacing of these lineaments on lines taken at varying orientations across different parts of the region. Although crude, this method provides a sufficiently accurate result for the purpose of this study. Mean spacings range from 1 - 2 km (southern portion of the area) to 8 km (close to the corona edge). An interesting observation is that the wider polygons are associated with the edge of the topographic flexural signature around the corona. The smaller polygons occur where the topography is extremely flat. The width of the lineations themselves range from less than the resolution of one pixel (75 m) in the southern portion of the image, to 500m close to Nightingale Corona. The lower limit on lineation width is not known as a topographic feature significantly narrower than 75 m may be detected by the SAR if the energy returned from the feature is substantially more than that returned from the immediately surrounding terrain. An obvious feature of the polygonal patterns in figure 2 is that narrower lineations are associated with smaller polygons.

We have proposed above that the plains to the southeast of Nightingale Corona are the result of extensive lava flows, probably associated with the corona itself. Unfortunately, most of the

lineations comprising the bright polygonal patterns associated with the flow(s) are too narrow to be distinguishable as ridges or depressions. However, close to the corona edge a few wider lineations are just discernable as depressions - the more westerly side of the lineation is dark compared with the more easterly side. Intersection geometries of the lineations comprising the polygonal patterns are typical of the geometries found in tensional networks. We do not believe the patterns seen here are the result of regional tectonic stress fields because they are isotropic. The observations and arguments above strongly support the hypothesis that these polygonal patterns are analogous to joint networks found in terrestrial lava flows.

For 7 of the15 areas shown in figure 1 the flow source(s)/extent could be identified and the edge of the area of polygonal patterns was seen to correlate with the edge of the lava flow(s). The major characteristics of these 7 areas are summarised in table 1. Polygon and lineament widths were measured for each area as described above. It can be seen that the the smaller polygon widths (1 - 3 km) and lineament widths (< 75 m - 150 m) in the polygonal patterns around Nightingale Corona are typical of those identified in other areas, but the larger scale patterns at Nightingale are not observed elsewhere. All the areas identified in table 1 are extremely flat (slopes < 1°), and lie at elevations between +/- 1 km of the mean planetary radius (6051.9 km). This is not particularly suprising as most of the highland regions on Venus are extremely tectonically deformed. Lakshmi Planum is the only extensive upland area which has low topographic relief and a smooth radar-dark surface, but it does not display polygonal networks. In 5 regions clusters of small shield volcanoes were present, further evidence that the regions exhibiting polygonal networks are associated with substantial volcanic activity. Possible collapsed lava tubes are present in the corona centered at 31.5°S, 259.5°E, coincident with an area displaying polygonal networks (table 1). In some regions tectonic and/or volcanic processes postdate the formation of the polyonal patterns. Such an example occurs in part of Guinevere Planitia - part of this area is shown in figure 5. The polygonal patterns can be seen, but later tectonic deformation has resulted in closely spaced (~1 km) N-S and NW-SE trending bright lineations. The shield volcano in the centre of the image is one of many in the region and appears to postdate both the polygonal patterns and the later lineations. In portions of this area there appears to be some orientation to the polygonal patterns, with lineations being preferentially aligned along and perpendicular to the regional topographic gradient (< 1°, downhill to the SW).

In summary 15 regions have so far been identified as displaying polygonal patterns in the Magellan SAR images. Seven of these areas can be identified as regions of extensive lava flow(s), where the limits of the lava flow(s) correlate well with the spatial extent of the polygonal patterns. Furthermore the polygonal patterns are identified as tensional and probably unrelated to local and regional tectonics due to their lack of preferred orientation.

DISCUSSION

We have presented observational evidence supporting the idea that polygonal patterns seen in Magellan SAR images are tensional networks. Spatial correlation of the patterns with volcanic flows, the isotropic nature of the patterns and the joint intersection geometries described in detail above suggest an analogy with terrestrial lava flow joints in 7 areas. In the remaining 8 areas, correlation of the edge of the patterns with flow limits is poor but the patterns are still associated with extensive volcanism. The major difference between terrestrial joints and the tensional networks seen in the Magellan data is the width of the polygons (joint spacing) and the lineations defining them (joint width). On Earth, joints in lava flows have typical spacings of decimeters to a meter and widths of a few centimeters [e.g. *Peck and Minakami,* 1968] The Venusian features typically have spacings of 1 - 2 km and widths of less than 75 m - 150 m (i.e. less than 2 pixels). In this section we consider possible origins for the Venusian polygonal patterns. If the patterns are directly analogous to terrestrial joints then sufficient thermal stresses must be generated in a cooling flow to cause tensile failure of the rock, the predicted thermal strain must be compatible with that observed and the difference in scale between the Venusian patterns and columnar joints on the Earth must be explained. Alternatively, the patterns may be the result of thermal stresses generated in the upper crust/lithosphere rather than in a single lava flow. If this is so the mechanism producing the thermal stress must be investigated and an estimate of the yield strength envelope for the Venusian lithosphere is needed to determine whether failure would occur for a given thermal stress profile. These issues are discussed in detail below.

In an ideal case, a cooling lava flow solidifies but cannot retain any thermal stress until it cools through an elastic 'blocking temperature'; below this temperature elastic stresses accumulate according to

$$\sigma_{xx}(z,t) = \alpha * \frac{E}{1-\nu} * \Delta T(z,t) \qquad (1)$$

$$\text{where} \quad \Delta T(z,t) = T(z,t) - T_e$$

[*Boley and Weiner*, 1960; *Parmentier and Haxby,* 1986]. T_e is the elastic blocking temperature, α is the coefficient of linear thermal expansion , E is Young's modulus and υ is Poisson's ratio. We use terrestrial values of 10^{-5} $°C^{-1}$ for α, 7 x 10^{10} Nm^{-2} for E, and 0.25 for υ.

Joints have been observed to initiate in Hawaiian lava lakes at temperatures between 900°C and 980°C [*Peck and Minakami*, 1968]. Assuming a similar 'blocking temperature' range for Venusian lavas and no failure of the rock, residual tensional stresses on the order of 400 MPa are predicted. This greatly exceeds the tensile strength of unfractured terrestrial basalt (~10 MPa) [*Peck and Minakami*, 1968]. Thus, if Venusian lavas are of comparable strength to terrestrial basalts the thermal stresses generated in a cooling flow will cause the flow to fail in tension from the top surface downward and the bottom surface upward. This is exactly how joints form in terrestrial flows [*Peck and Minakami*, 1968; *Ryan and Sammis*, 1978; *DeGraff and Aydin*, 1988; *Pollard and Aydin*, 1988].

The thermal strain generated in a cooling flow is equal to α ΔT l, where l is the joint spacing. For a joint spacing on the order of 1 km, we would expect the final joint width to be ~ 5 m . As seen in figure 2 the widths of individual fractures seems to increase as the spacings of the fractures increases. Fracture spacings on the order of 1 km are generally associated with fractures that are less than or equal to the pixel spacing (75 m). However, a linear feature less than 75 m can be detected by the SAR, as long as the energy return from the feature is much greater than the radar return from the surrounding terrain [Sabins 1978, N. Izenberg and R. Brackett, personal communication, 1992]. Although comparison with terrestrial joints would suggest that we would not expect significant widening of a tensional crack by weathering, we need to remember that the

features seen in the Venusian images are much wider than terrestrial joints which could lead to some failure and slumping, thus increasing the width of the feature at the surface.

The arguments above indicate that the thermal stresses generated in a cooling lava flow under Venusian surface conditions exceed the (terrestrial) tensile strength of the rock and that the thermal strain predicted may be compatible with that observed in the SAR images. If the tensional networks are lava flow joint networks we need to explain the major difference in scales between the Venusian features (~ 10^3 m) and terrestrial columnar joints (~ 1 m); this is hampered by the fact that there is currently no simple physical model for the typical widths and spacings of joints on Earth. We next consider factors which might cause joints on Venus to be much more widely spaced than on Earth.

On earth a relationship between lava flow joint spacing and cooling rate is observed: polygon widths are generally greater at the base of a flow than at the top, due to the relatively slower cooling of the base [*James*, 1920; *Spry*, 1962; *Pollard and Aydin*, 1988]. Where quenching of a flow by rainfall has occured joints are more closely spaced and in extreme cases the regular columnar structure may be replaced a more irregular pattern of joints known as an entablature structure [*Long and Wood*, 1986]. On Venus, the high surface temperature means that the cooling rate of a flow will be lower than on earth. Also the absence of water on the surface of Venus means that cooling of a flow will be entirely by conduction as compared with terrestrial flows where cooling is often accelerated due to convective cooling following flooding events. We would therefore expect Venusian joints to be spaced somewhat wider than at the upper surface of terrestrial flows, however a 500-fold increase does not seem plausible. It should also be noted that the thermo-mechanical properties of a 'dry' basalt at Venusian surface conditions are not known. It is possible that lava flows on Venus may be stronger than their terrestrial counterparts, although what effect this would have on joint spacing is not clear.

No dependence of joint spacing on lava flow thickness is observed for terrestrial lava flows - joints initiate before the flow has completely solidified [*Peck and Minakami*, 1968]. *Head and Wilson* [1992] suggest that magma reservoirs may be larger on Venus than on Earth which could give rise to either thicker or more extensive flows. However, there are currently few estimates of

thickness for Venusian flows - some have been estimated to be 56 m to several hundred metres thick [*Moore and Schenk*, 1992], although these flows are believed to be more silicic (due to their ridged surface morphologies) than the flows we have considered here. The smooth surfaces and extensive nature of the flows associated with the polygonal patterns are more indicative of a basaltic composition such as that measured by 5 of the Soviet Venera landers [*Basilevsky and Surkov*, 1989]. A mechanism which could result in a relationship between joint spacing and lava flow thickness is described in studies on the propagation of tensional cracks in a brittle solid [*Nemat-Nasser et al.*, 1980; *Keer et al.*, 1978; *Nemat-Nasser et al.*, 1978]; we give a brief summary. For an initial crack configuration of parallel, equally spaced fractures of the same length and a conduction temperature profile, the fractures will grow until a critical state is reached. At this critical state, every alternate crack will stop growing, snap shut and the remaining cracks will continue to propagate, until a second similar critical state is reached and so on. In this way a final fracture spacing is obtained which is greater than the initial spacing and is dependent on the thickness of the brittle layer (via the number of critical states reached). Calculation of the initial crack spacing in a cooling Venusian lava (by assuming a fraction of the thermo-elastic energy is used to initiate a fracture) gives a value on the order of millimetres. Extrapolation of millimeter spacing to kilometer spacing is unlikely. Even if the flows considered are one hundred metres thick, the ratio of polygon width to flow thickness is on the order of 10. However, if the flows are comparable in thickness to terrestrial flood basalts then this ratio is on the order of 100 and the width of the tensile cracks is likely to be greater than the thickness of the flow.

Extrapolation of typical terrestrial joint spacings of decimetres to those of 1 - 2 km for Venus by any of the above mechanisms seems improbable. Spacings on the order of kilometers are more compatible with deformation of a layer thicker than that typical of terrestrial (and presumably Venusian) lava flows. The isotropic nature of the Venusian polygonal patterns is a strong reason for invoking a thermal origin; we next consider the thermal stresses resulting from regional heating of the lithosphere and an increased thermal gradient. As noted earlier, many of the areas exhibiting polygonal networks are areas of extensive volcanism, often in the form of shield fields. It has been suggested by *Aubele et al.* [1992] that shield fields represent areas of anomalous melting. We consider a less drastic scenario in which the temperature gradient in the regions of polygonal patterns is elevated due to an increased heat flux at the base of the lithosphere; the

lithosphere thins and thermal stresses develop. We assume that the lithosphere is free to relieve the depth integrated stress. Stresses develop in the lithosphere according to

$$\Delta \sigma_{xx}(z,t) = - \alpha * \frac{E}{1-\nu} * \Delta T(z,t) + \frac{1}{h_e} \int_0^{h_e} \alpha * \frac{E}{1-\nu} * \Delta T(z,t)\, dz \qquad (2)$$

[*Boley and Weiner*, 1960; *Parmentier and Haxby,* 1986], where h_e is the thickness of the elastic lithosphere. Other variables are as defined previously and tensional stresses are positive. For an increased temperature gradient and assuming linear geotherms before and after the lithosphere is heated, equation (2) reduces to

$$\Delta \sigma_{xx}(z,t) = \alpha * \frac{E}{1-\nu} * (c_2 - c_1) * \left(\frac{h_e}{2} - z\right) \qquad (3)$$

where c_1 and c_2 are the original and elevated temperature gradients respectively. Compressional stresses develop in the lower half of the thinned lithosphere and tensional stresses in the upper half. This process is shown schematically in figure 6.

To investigate the failure associated with lithospheric thinning we compare the thermo-elastic stresses (equation 2) with a yield strength envelope model of the Venusian lithosphere. Without a good knowledge of lithospheric rheology on Venus, one can only adopt characteristic values used for the Earth's oceanic lithosphere [*Goetze and Evans,* 1979]. Here we follow *Solomon and Head* [1990] where they characterized the strength of the upper brittle portion of the lithosphere using a frictional sliding law [*Byerlee*, 1978] and the strength of the lower lithosphere using a ductile flow law for dry olivine (10^{-16} s^{-1} strain rate). These two failure criterion define a yield strength envelope (YSE) [*Goetze and Evans,* 1979] where the base of the YSE is approximately defined by the 740°K isotherm [*McAdoo et al.,* 1985]. Thus a higher temperature gradient results in a weaker, thinner lithosphere.

As an example we consider a 25 km thick lithosphere, which is the mean mechanical thickness derived from modeling of flexure at Nightingale Corona [*Johnson and Sandwell*, 1992]. The base of the elastic lithosphere is defined by the 740°C isotherm, so the resulting average

temperature gradient at Nightingale is ~11°/km. Figure 7 shows the stress profiles obtained from (3) when the temperature gradient is elevated to 12°/km, 14°/km and 22°/km, representing increasing amounts of reheating and lithospheric thinning. In all cases the upper half of the thinned lithosphere is in tension and the lower half in compression. The maximum tensile stress, which occurs at z = 0 increases with increasing lithospheric thinning. The yield strength envelope (YSE) for dry olivine [*Kirby and Kronenberg*, 1987] for the elevated temperature gradient is also plotted. Brittle failure (dashed line) is assumed in the upper lithosphere [*Byerlee*, 1978] - this is independent of temperature gradient. Ductile flow (dotted line) is assumed in the lower lithosphere. The effect of increasing temperature gradient on the thickness and strength of the lower lithosphere can clearly be seen. Failure by ductile flow begins at increasingly shallower depths as the temperature gradient increases and the net strength of the lithosphere in both compression and tension (area within the YSE) also decreases. In this model we are not interested in what happens beneath the base of the thinned elastic lithosphere so the ductile flow part of the YSE is not considered further.

Brittle failure in the upper lithosphere will occur wherever the thermal stress given by (3) exceeds the yield strength, given by

$$S_t = 0.8 * \rho\, g\, z \qquad (4)$$

[*Byerlee*, 1968; *Kirby*, 1983]. It can be seen from figure 7 that the maximum depth to which failure will occur increases with the elevation in temperature gradient. In the case of linear geotherms there is a simple analytical solution for this depth. Equating (3) and (4) gives the maximum depth of failure as a function of the thickness of the thinned lithosphere, h_e and temperature gradient increase, $(c_2\text{-}c_1)$

$$z_{max} = \frac{47\,(c_2 - c_1)\,h_e}{(1.99 + 93\,(c_2 - c_1))} \qquad (5)$$

We used a value of 8.86 ms^{-2} for g and 2800 kgm^{-3} for ρ. For the three degrees of thinning 12°/km, 14°/km and 22°/km the maximum depth to which tensile failure will occur is 0.52 km , 1.2

km and 2.1 km, respectively. The elevated temperature gradient of 14°/km would seem reasonable, predicting tensile failure of the upper 1.2 km of the lithosphere.

In the heated lithosphere model the crack width is much less than the thickness of the deformed layer . At Nightingale Corona if we take the range of polygon widths as 1 - 8 km and the range in the thickness of the deformed layer as 0.5 - 2 km (depending on the amount of reheating) we can get a crude estimate of the range in the ratio of polygon width to thickness of the deformed layer. This ratio varies from 0.5 to 16. It is interesting to note that this ratio is of the same order of magnitude as the ratio of wavlength of (dominant mode of) deformation to layer thickness in studies of deformation of thin layers under uniaxial compression/tension [*Ricard and Froidevaux*, 1986; *Zuber et al.,* 1986]. These studies predict that the deformation wavelength will be about 4 times the layer thickness.

The variation in spacing at Nightingale Corona is not explained by either the cooling flow or heated lithosphere scenario. However, in the heated lithosphere model the depth of failure is governed by the intensity of the increased heat flux and so wider polygons could be the result of greater heating. This would imply a large lateral gradient in heat flow south of Nightingale Corona to account for the spatial variation in polygon size. Alternatively, the variation in polygon width may be related to the topographic flexure at Nightingale Corona. We have no quantitative explanation for this but the idea is supported by the observation that the wide polygons (> 3 km) are observed only at Nightingale Corona. In all other locations identified in figure 1 the typical polygon widths are < 3 km and in all these regions the topography is extremely flat.

CONCLUSIONS

The Venusian volcanic plains, as imaged by the Magellan spacecraft show a wide range of tectonic and volcanic deformation patterns. We have considered a possible evolution for polygonal patterns identified in 15 regions. The polygonal patterns must arise as a result of an isotropic stress field and we have proposed that they are tensional networks. The fractures defining the polygons have typical mean spacings of 1 - 2 km and widths at the resolution of the image pixels (75 m). Consideration of possible origins of an isotropic stress field in the volcanic plains

leads to two possible scenarios. Firstly, the patterns may be the result of residual thermal stress which would develop in a cooling lava flow. Residual tensional stresses which are much greater than the strength of unfractured terrestrial lava flows are predicted. The strain observed in the images is compatible with the thermal strain predicted only if the lineations defining the polygons are much less than 75 m wide. Secondly, the polygonal patterns may reflect deformation of a much thicker layer, such as brittle failure of the upper crust/lithosphere. A possible scenario involves an increased thermal gradient as a result of increased heat flux to the base of the lithosphere. Such an increase in heat flux is compatible with the evidence for extensive lava flows and shield fields in the regions exhibiting polygonal patterns. Assuming the lithosphere relieves the depth integrated stress, the increased temperature gradient predicts tensile stresses in the upper lithosphere and compressive stresses in the lower lithosphere. We have computed stress profiles for an initially 25 km thick lithosphere with a temperature gradient of 11°/km, by allowing the temperature gradient to increase to between 12°/km and 22°/km. The yield strength envelope for dry olivine corresponding to the increased temperature gradient was also computed. Brittle tensile failure occurs in the upper part of the lithosphere wherever the thermal stresses predicted exceed the yield strength. The maximum depth at which failure occurs increases with increasing elevation of the temperature gradient. In our numerical example this depth increased from 0.5 km for the temperature gradient of 12°/km to 2 km for the temperature gradient of 22°/km.

The cooling lava flow model can explain the existence, but not the scale, of isotropic patterns at the 7 locations described in table 1. This model requires that the limits of the polygonal patterns can be identified and correlated with individual flows. In most areas this is a difficult task due to later tectonic and volcanic events and the fact that the fractures defining some of the polygonal patterns are at the resolution of the radar. The heated lithosphere model does not require the same correlation of flows and polygonal patterns and so could account for all the areas identified in figure 1. Neither model predicts the polygon widths or explains the variation in the polygonal patterns at Nightingale Corona. However, it is worth noting at this point that there is still progress to be made in our understanding of the evolution of joints in terrestrial columnar basalts, especially in explaining the final widths of the columns. Modeling of any kind of surface deformation on Venus would be aided greatly by better knowledge of the typical lithospheric

thickness and strength, and of the thermo-mechanical properties of lavas under Venusian conditions.

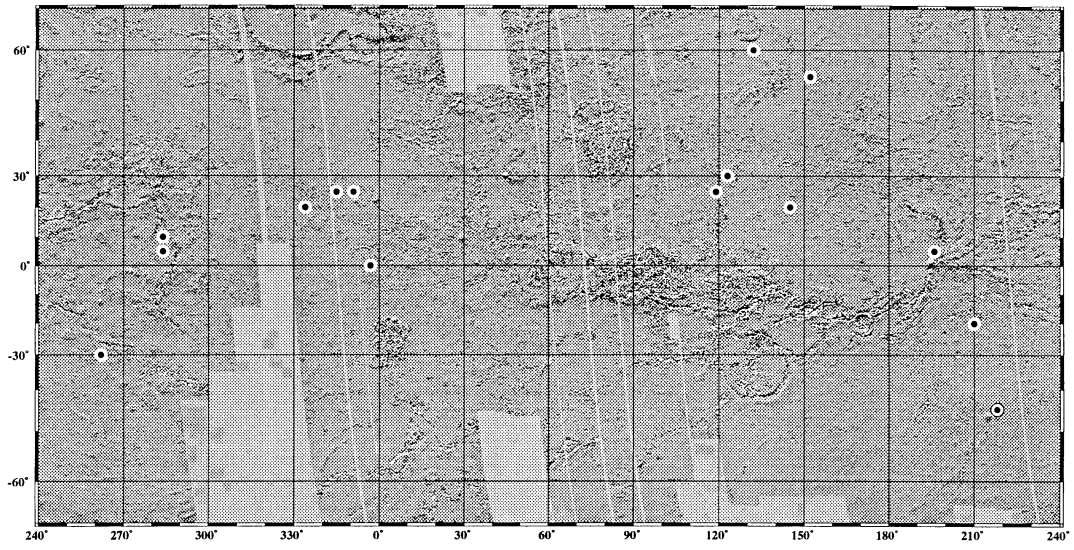

Figure 4.1: Mercator projection topography map of Venus [*Ford and Pettengill*, 1992]. Illumination is from the north along altimeter tracks; thus gray shade indicates topographic slope. Dots indicate areas identified in the high resolution Magellan synthetic aperture radar images as exhbiting polygonal patterns. Areas which overlap two adjacent images are shown as one dot only. All areas lie within 1 km of the mean planetary radius for Venus (6051.9 km), but appear to be randomly distributed and uncorrelated with particular geographical features.

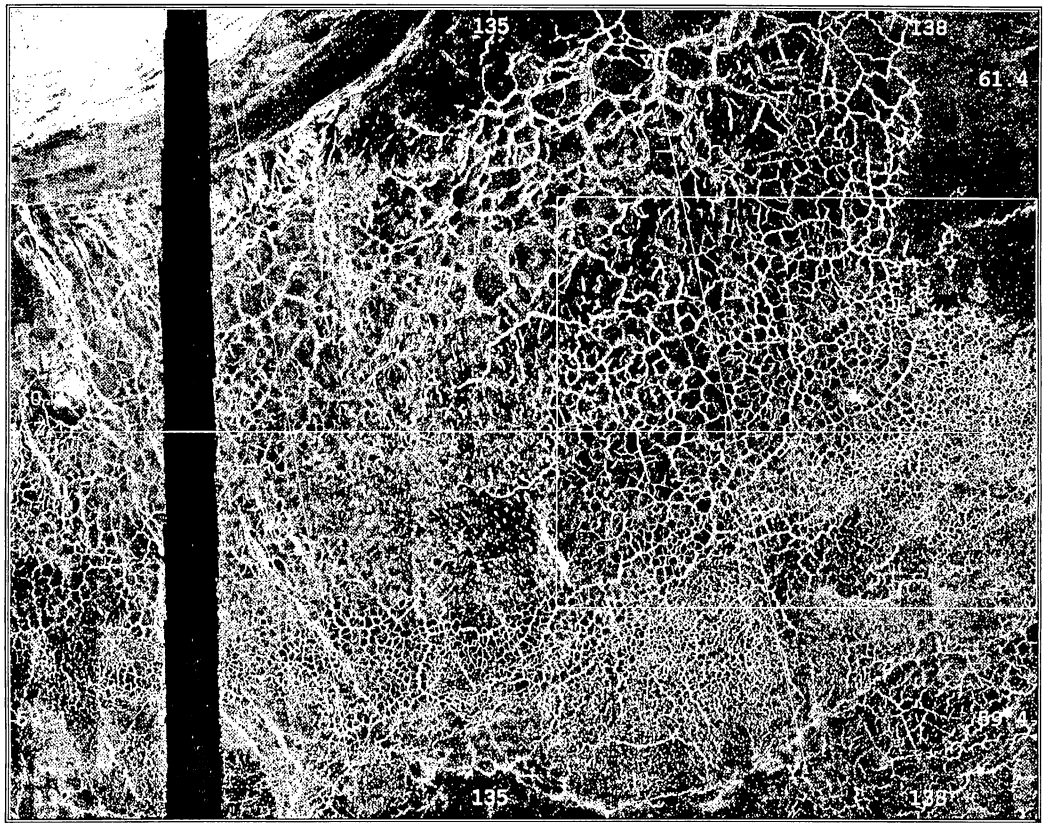

Figure 4.2: Portion of JPL Magellan image FMIDR 60N132 (look direction is left) showing part of the venusian plains southeast of Nightingale corona. The edge of the corona can be seen in the upper left corner of the image. The area is about 350 km in longitude by 270 km in latitude. Altimetry profiles along XX', YY', ZZ' are shown in figure 4.3. The boxed region in the eastern part of the image is shown in more detail in figure 4.4.

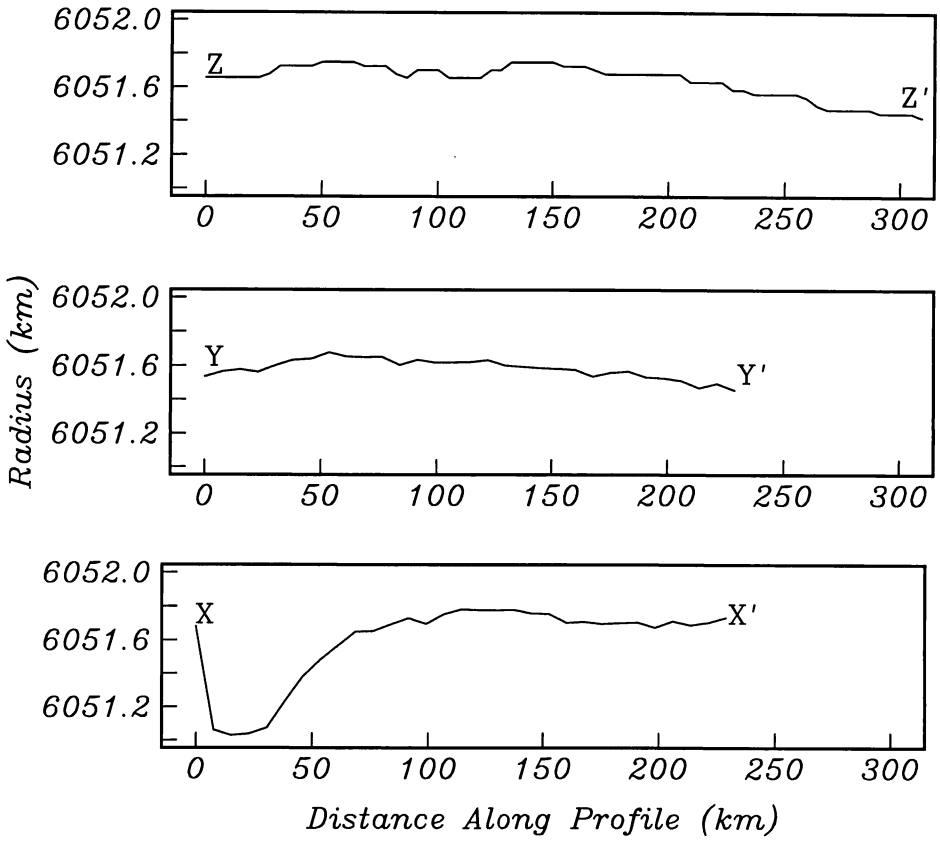

Figure 4.3: Magellan altimetry profiles XX', YY', ZZ' as indicated in figure 4.2. Profile XX' is along orbit 1232. The topographic low outboard of Nightingale corona can be seen between 10 km and 30 km along the profile. Beyond 100 km the topography is extremely flat. Profile YY' is along orbit 1246. Profile ZZ' was taken from the gridded altimetry [Ford and Pettengill, 1992] along a line of latitude. The regional slope is less than 1° downhill to the southeast.

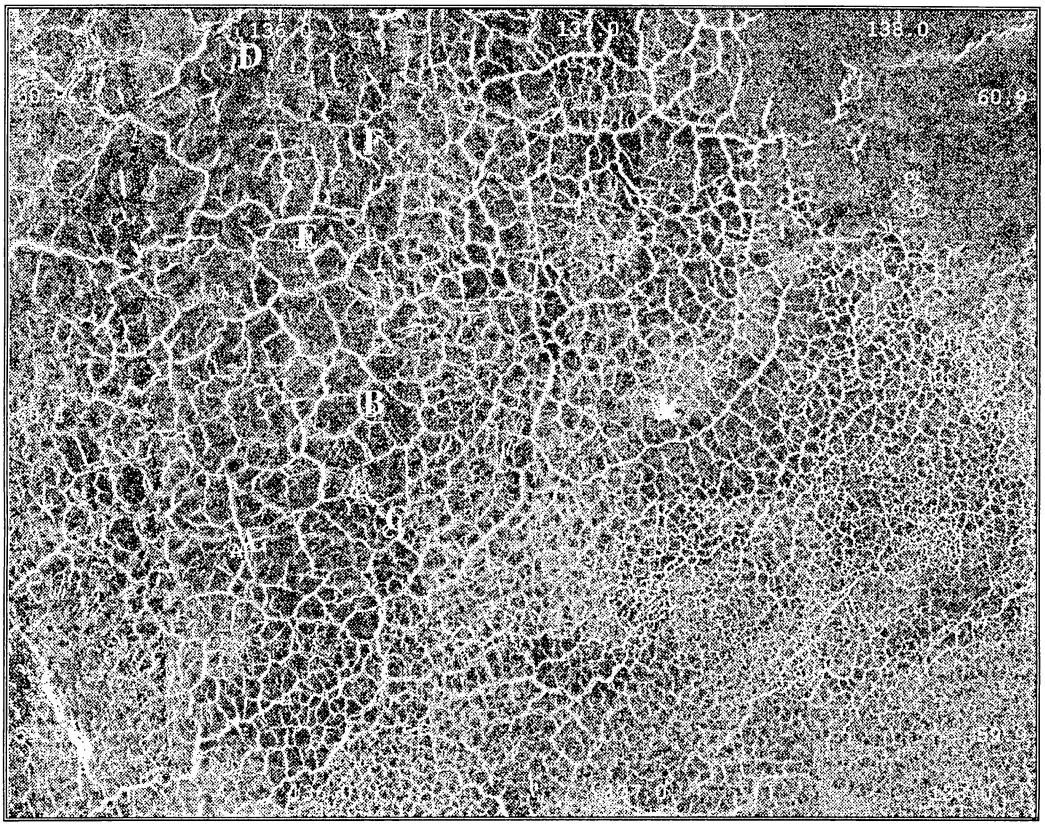

Figure 4.4a: Boxed region in figure 4.2 is shown in more detail. Points marked A, B, C, D, E, F are referred to in the text and correspond to the labeled interpretation sketches in figure 4.4b.

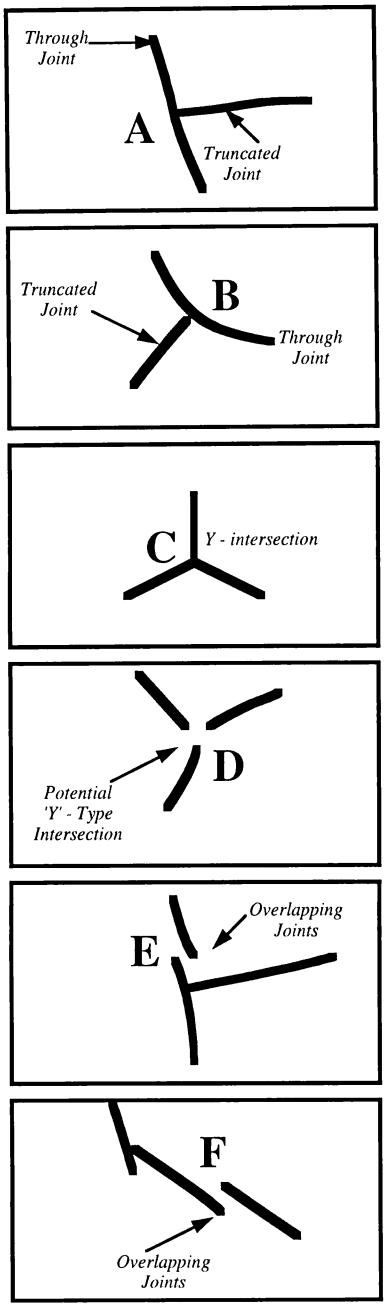

Figure 4.4b: Interpretation sketches for 4.4a.

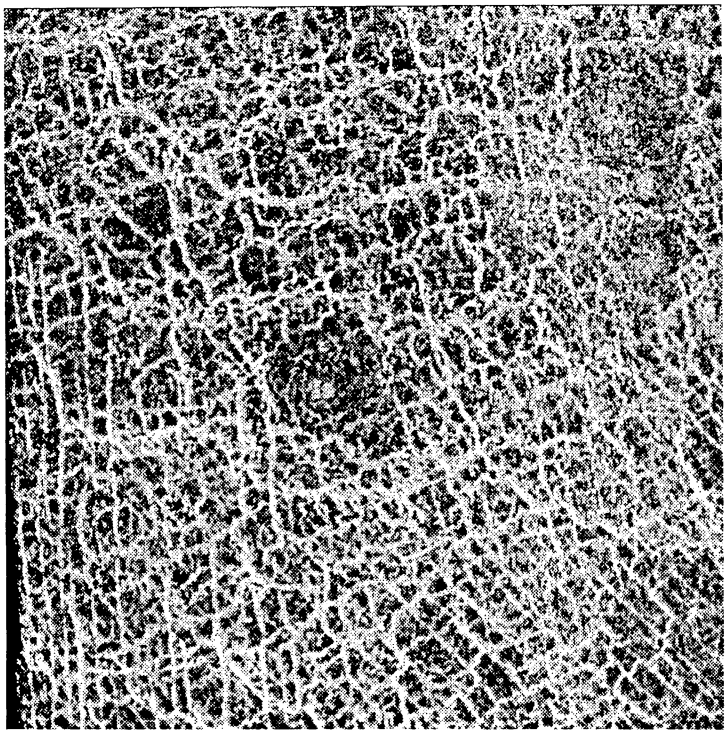

Figure 4.5: Portion of JPL Magellan image 20N334 (look direction is left). Image is 39 km (E-W) by 38 km (N-S). The polygonal patterns are overlain by two sets of bright parallel lineations spaced at ~1 km; one set trending N-S, the other NW-SE. Several shield volcanoes are present, the most prominent of which is in the center of the image. These volcanoes appear to postdate the polygonal patterns and the lineations, rendering detailed analysis of polygon widths difficult.

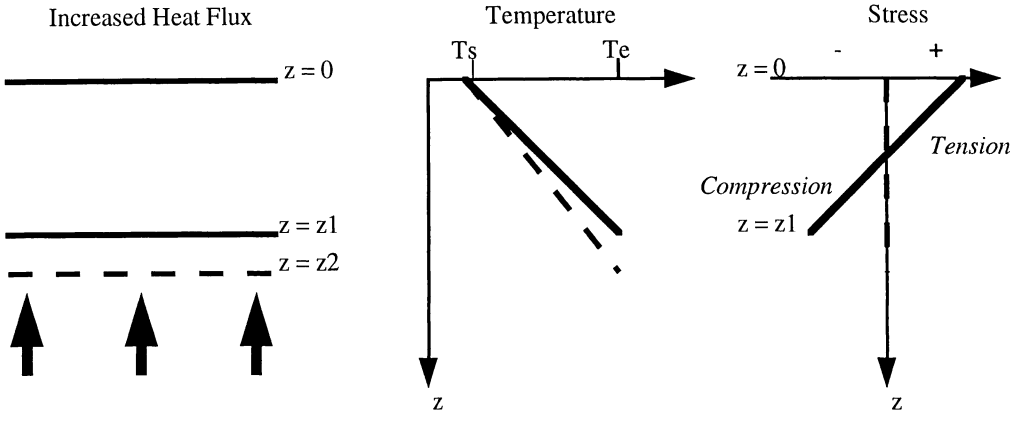

a) Heat and thin lithosphere from z2 to z1.

b) Temperature gradient increases - dashed line to solid line - as lithosphere thins.

c) Thermal stresses develop Top of lithosphere is in tension, base is in compression

Figure 4.6: Schematic representation of the development of thermal stress in the lithosphere as a result of an increased temperature gradient to the base of the lithosphere. (a) Increased heat flux thins the lithosphere, (b) the temperature gradient (assumed linear) increases and thermal stresses develop, (c) the lithosphere is assumed to relieve the depth-integrated stress, so tensional stresses result at the surface and compressional stresses at depth as shown.

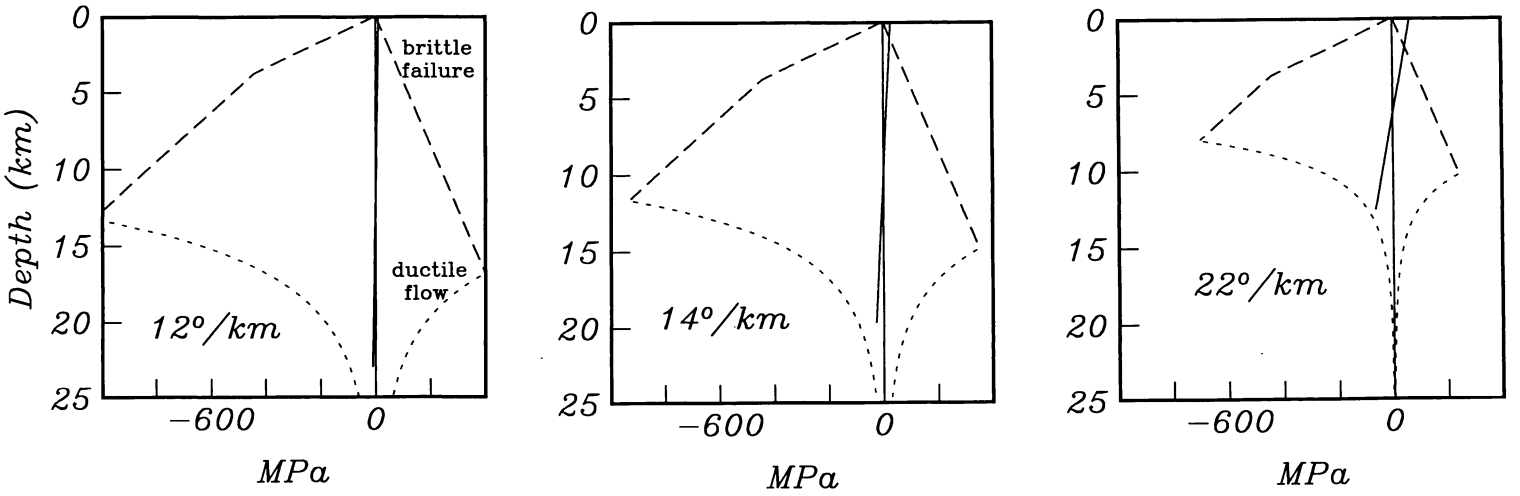

Figure 4.7: Stress profiles and yield strength envelopes (for a dry olivine rheology) for elevation of the temperature gradient from 11° / km to (a) 12° / km, (b) 14° / km, (c) 22° / km. The dashed lines indicate the part of the YSE defined by brittle failure, the dotted lines indicate ductile flow. The stress profiles before (zero stress), and after the temperature gradient increase are shown as solid lines. Failure of the lithosphere occurs where the thermal stresses exceed the yield strength.

Table 4.1 Major Characteristics of Polygonal Pattern Regions

FMIDR	*Areal Extent*	*Mean Radius*	*Fracture Spacings*	*Fracture Widths*
F45S 218 (46.5S, 219.0E)	110 km (EW) 110 km (NS)	6052.5 km	1 km - 2 km	<= 75 m
F30S262 (31.4S,259.2E)	100 km (EW) 80 km (NS)	6051.5 km	1 km - 3 km	<75 m - 150 m
F20S210 (20.0S,211.3)	a) 80 km (EW) 70 km (NS)	6051.9km	1 km - 3 km	<75 m - 150 m
	b) 30 km (EW) 40 km (NS)	6051.1km	1 km - 3 km	<75 m - 150 m
F05N195 (6.6N, 192.5E)	200 km (EW) 200 km (NS)	6052.7 km	1km - 2km	<= 75 m
F10N284 (7.9N, 282.9E)	25 km (EW) 25 km (NS)	6050.7 km	500 m - 1.5 km	<75 m - 150 m
(10.5N, 283.9E)	25 km (EW) 25 km (NS)	6050.4 km	500 m - 1.5 km	<75 m - 150 m
F20N334 (21.0N, 334.0E)	220 km (EW) 300 km (NS)	6050.7 km	1 km - 2 km	<75 m - 150 m
F60N132 (60.5N, 137.0E)	330km (EW)	6051.6km	1 km - 8 km	<75 m - 500 m

REFERENCES

Aubele, J. C., L. S. Crumpler, and J. W. Head, Venus Shield Fields: Characteristics and Implications, *EOS, Trans. , AGU,* 73, 178, 1992.

Aydin, A., and J. M. DeGraff, Evolution of Polygonal Fracture Patterns in Lava Flows, *Science, 239,* 471-476, 1988.

Basilevsky, A. T., and Y. A. Surkov, Chemical Composition of Venusian Rocks and some Geochemical Implications. *Magellan project V-Gram, Jet Propulsion Laboratroy, 15,* 2-4, 1989.

Boley, B. A., and J. H. Weiner, Theory of Thermal Stresses. Wiley, 1960.

Byerlee, J. D., Friction of rocks, *Pageoph,* 116, 615-626, 1978.

DeGraff, J. M., and A. Aydin, Dependence of Columnar Joint Spacing and Growth Increment on Cooling Rate in Lava Flows, *EOS, Trans. AGU, 67,* 1211, 1986.

DeGraff, J. M., and A. Aydin, Surface morphology of columnar joints and its significance to mechanics and direction of joint growth, *G.S.A. Bull., 99,* 605-617, 1987.

Ford, P. G., and G. H. Pettengill, Venus Topography and Kilometer-Scale Slopes, *J. Geophys. Res., 97,* 13,103 - 13,114, 1992.

Goetze, C. and B. Evans, Stress and temperature in the bending lithosphere as constrained by experimental rock mechanics, *Geophys. J. R. astr. Soc., 59,* 463-478, 1979.

Guest, J. E., and M. H. Bulmer, Volcanic Edifices and Volcanism in the Plains of Venus, *EOS, Trans, AGU,* 73, 178, 1992.

Head, J. W., and L. Wilson, Volcanic Processes and Landforms on Venus: Theory, Predictions and Observations, *J. Geophys. Res., 91,* 9407-9446, 1986.

James, A. V. G., Factors Producing Columnar Structure in Lavas and its Occurrence near Melbourne, Australia, *J. Geology,* 28, 458 - 469, 1920.

Johnson, C. L., and D. T. Sandwell, Flexure on Venus: Implications for Lithospheric Elastic Thickness and Strength, *LPSC,* XXIII, 619 - 620, 1992.

Keer, L. M., S. Nemat-Nasser, and A. Oranratnachai, Unstable Growth of Thermally Induced Interacting Cracks in Brittle Solids: Further Results, *Int. J. Solids Structures, 15,* 111-126, 1978.

Kirby, S. H., Rheology of the Lithosphere, *Rev. Geophys.*, 21, 1458 - 1487, 1983.

Kirby, S. H., and A. K. Kronenberg, Rheology of the Lithosphere: Selected Topics, *Rev. Geophys.*, 25, 1219 - 1244, 1987.

Long, P. E., and B. J. Wood, Structures, textures, and cooling histories of Columbia River basalt flows, *G.S.A. Bull., 97*, 1144-1155, 1986.

McAdoo, D. C., C. F. Martin and S. Poulouse, Seasat observations of flexure: Evidence for a strong lithosphere, *Tectonophysics, 116*, 209-222, 1985.

Moore, H. J., and P. Schenk, Thick Lava Flows on Venus: Distribution, Morphology and Terrestrial Comparisons, *EOS, Trans, AGU*, 73, 179, 1992.

Nemat-Nasser, S., L. M. Keer, and K. S. Parihar, Unstable Growth of Thermally Induced Interacting Cracks in Brittle Solids, *Int. J. Solids Structures, 14*, 409-430, 1978.

Nemat-Nasser, S., Y. Sumi, and L. M. Keer, Unstable Growth of Tension Cracks in Brittle Solids: Stable and Unstable Bifurcations, Snap-Through, and Imperfection Sensitivity, *Int. J. Solids Structures, 16*, 1017-1035, 1980.

Parmentier, E. M., and W. F. Haxby, Thermal Stresses in the Oceanic Lithosphere: Evidence From Geoid Anomalies at Fracture Zones, *J. Geophys. Res., 91*, 7193-7204, 1986.

Peck, D. L., and T. Minakami, The Formation of Columnar Joints in the Upper Part of Kilauean Lava Lakes, Hawaii, *G.S.A. Bull., 79*, 1151-1166, 1968.

Pollard, D. P., and A. Aydin, Progress in Understanding Jointing over the Past Century, *G.S.A. Bull., 100*, 1181 - 1204, 1988.

Ricard, Y., and C. Froidevaux, Stretching Instabilities and Lithospheric Boudinage, *J. Geophys. Res.*, 91, 8314-8324, 1986.

Ryan, M. P., and C. G. Sammis, Cyclic Fracture Mechanisms in Cooling Basalt, *G. S. A. Bull, 89*, 1295 - 1308, 1978.

Sabins, F. F., Remote Sensing Principles and Interpretation. Freeman and Co., 1978.

Saunders, R. S., R. E. Arvidson, J. W. Head, G. G. Schaber, E. R. Stofan, and S. C. Solomon, An Overview of Venus Geology. *Science, 252*, 249-252, 1991.

Solomon, S. C. and J. W. Head, Lithospheric flexure beneath the Freyja Montes foredeep, Venus: Constraints on lithospheric thermal gradient and heat flow, *Geophys. Res. Lett. 17*, 1393-1396, 1990.

Stofan, E. R., G. Sharpton, G. Schubert, G. Baer, D. L. Bindschadler, D. M. Janes, and S. W. Squyres, Global distribution and characteristics of coronae and related features on Venus: Implications for origin and relation to mantle processes, *J. Geophys. Res.*, *97*, 13,347 - 13,378, 1992.

Spry, A. H., The Origin of Columnar Jointing, Particularly in Basalt Flows, *Geol. Soc. Australia Journal*, 8, 191 - 216, 1962.

Zuber, M. T., E. M. Parmentier, and R. C. Fletcher, Extension of continental lithosphere: A model for two scales of Basin and Range deformation, *J. Geophys. Res.*, 91, 4826-4838, 1986.

CHAPTER 4

LITHOSPHERIC FLEXURE ON VENUS

ABSTRACT

Topographic flexural signatures on Venus are generally associated with the outer edges of coronae, with some chasmata and with rift zones. Using Magellan altimetry profiles and grids of venusian topography, we identified 17 potential flexure sites. Both 2-D cartesian and 2-D axisymmetric, thin-elastic plate models were used to establish the flexural parameter and applied load/bending moment. These parameters can be used to infer the thickness, strength and possibly the dynamics of the venusian lithosphere. Numerical simulations show that the 2-D model provides an accurate representation of the flexural parameter as long as the radius of the feature is several times the flexural parameter. However, an axisymmetric model must be used to obtain a reliable estimate of load/bending moment. Twelve of the 17 areas were modeled with a 2-D thin elastic plate model, yielding best-fit effective elastic thicknesses in the range 12 to 34 km. We find no convincing evidence for flexure around smaller coronae, though five possible candidates have been identified. These five features show circumferential topographic signatures which, if interpreted as flexure, yield mean elastic thicknesses ranging from 6 to 22 km. We adopt a yield strength envelope for the venusian lithosphere based on a dry olivine rheology and on the additional assumption that strain rates on Venus are similar to, or lower than, strain rates on Earth. Many of the flexural signatures correspond to relatively high plate-bending curvatures so the upper and lower parts of the lithosphere should theoretically exhibit brittle fracture and flow, respectively. For areas where the curvatures are not too extreme, the estimated elastic thickness is used to estimate the larger mechanical thickness of the lithosphere. The large amplitude flexures in Aphrodite Terra predict complete failure of the plate, rendering mechanical thickness estimates from these features unreliable. One smaller corona also yielded an unreliable mechanical thickness estimate based on the marginal quality of the profile data. Reliable mechanical thicknesses found by forward modeling in this study are 21 km - 37 km, significantly greater than the 13 km - 20 km predictions based on heat flow scaling arguments and chondritic

thermal models. If the modeled topography is the result of lithospheric flexure, then our results for mechanical thickness, combined with the lack of evidence for flexure around smaller features, are consistent with a venusian lithosphere somewhat thicker than predicted. Dynamical models for bending of a viscous lithosphere at low strain rates predict a thick lithosphere, also consistent with low temperature gradients. Recent laboratory measurements indicate that dry crustal materials are much stronger than previously believed. Corresponding timescales for gravitational relaxation are 10^8-10^9 years, making gravitational relaxation an unlikely mechanism for the generation of the few inferred flexural features. If dry olivine is also found to be stronger than previously believed, the mechanical thickness estimates for Venus will be reduced, and will be more consistent with the predictions of global heat scaling models.

INTRODUCTION

Lithospheric flexure can result from static or dynamic processes and provides constraints on spatial and/or temporal variations in lithospheric thickness and strength. Lithospheric thickness may be determined solely from modeling topographic flexure or by combining gravity and topography data. On Venus, the highest resolution Magellan gravity data is insufficient for modeling all but the longest wavelength flexural features so we rely heavily on altimetry data [*Ford and Pettengill*, 1992] for information about lithospheric thickness. Lithospheric flexure on Venus was first inferred from the Pioneer Venus altimetry data over Freyja Montes [*Solomon and Head*, 1990]. Magellan altimetry has revealed additional sites of possible flexural signatures; these are associated with coronae [*Johnson and Sandwell*, 1992a,1993; *Sandwell and Schubert*, 1992a], chasmata [*McKenzie et al.*, 1992] and rifts [*Evans et al.*, 1992].

Coronae are unique to Venus and are circular to elongate features, at least partially surrounded by an annulus of ridges and grooves [*Pronin and Stofan*, 1990]. They have complex interiors, which often exhibit substantial tectonic deformation and volcanism. The interior elevations range from local topographic highs to local topographic lows surrounded by an elevated ring. Some larger coronae have an elevated outer ring or elevated interior surrounded by a trench-outer rise signature which is characteristic of plate flexure.

On Earth, flexure is predominantly observed at seamounts and subduction zones. If the flexure has persisted on geological timescales, models involving the bending of a thin elastic or elastic-plastic plate may be appropriate and may provide an estimate of the elastic plate thickness. A purely elastic flexure model also assumes that the lithosphere can sustain infinite stresses; however, laboratory studies suggest that the strength of the upper lithosphere is limited by pressure-dependent brittle failure [*Byerlee*, 1978] and the strength of the lower lithosphere is limited by temperature and strain-rate dependent ductile flow [*Goetze and Evans*, 1979]. We are interested in that part of the lithosphere which can support stresses over geological timescales: this is known as the mechanical lithospheric thickness. *McNutt* [1984] developed a method for using inferred elastic plate thicknesses and plate curvatures to estimate mechanical thicknesses; this has been applied to many terrestrial examples of flexure [for a review see *Wessel* 1992]. While purely elastic models can explain trench/outer rise topography at most subduction zones [*Caldwell and*

Turcotte, 1979], they predict that the thin elastic part of the lithosphere must maintain large fibre stresses over long timescales. To reduce the maximum stress and also account for plate motion at subduction zones, several authors [e.g. *DeBremaecker*, 1977; *Melosh*, 1978] have proposed dynamical models in which the observed topography is supported by the horizontal motion of a thick viscous/visco-elastic lithosphere. The important parameters are the strain rate, viscosity and viscous/visco-elastic plate thickness as compared with the strain, flexural rigidity and elastic-plate thickness of the elastic models. Both static and dynamical models fit the observations equally well, and so one cannot discriminate between these models using topography data alone.

Preliminary results involving simple 2-D cartesian elastic plate models [*Solomon and Head*, 1990; *Evans et al.*, 1992; *Johnson and Sandwell*, 1992a,1993; *Sandwell and Schubert*, 1992a; *Brown and Grimm*, 1993] and 2-D axisymmetric models [*Moore et al.*, 1992] have been reported for some topographic flexures on Venus. In this paper we present the results of a global study of possible flexural features as identified in the Magellan data. Initially we model 7 features using a 2-D cartesian elastic model and summarise the results for 5 features previously modeled in this way [*Sandwell and Schubert*, 1992a]. Many of these flexural signatures are associated with the outer edges of coronae and thus the question of the validity of a 2-D cartesian model is important. Axisymmetric models for simple loading geometries have previously been derived [*Brotchie and Sylvester*, 1969; *Brotchie*, 1971; *Turcotte*, 1979], and we address quantitatively the limiting cases for which a 2-D cartesian model is valid. Based on these results we re-examine the topography around one corona with an axisymmetric model and compare these results with the earlier 2-D results. Flexure associated with smaller coronae requires either a full 3-D model, or a 2-D axisymmetric model: we consider a few 2-D axisymmetric cases. Elastic thicknesses and curvatures obtained from these models are used to estimate mechanical thicknesses [*Solomon and Head*, 1990]. *Mueller and Phillips* [1992] suggest modifications to the approach used in the conversion of elastic to mechanical thickness [*McNutt*, 1984] which result in a more reliable estimate of mechanical thickness. We discuss these different approaches applied to our study areas. We consider flexure of a viscous lithosphere, using a simple model developed for terrestrial flexure [*DeBremaecker*, 1977]. Timescales for viscous relaxation consistent with the number and form of the inferred flexural signatures are derived, and the corresponding viscous plate thicknesses calculated. Finally we discuss the implications of gravitational relaxation as a mechanism for generating flexural topography.

DATA

Locations of all our study areas are shown in Figure 1 [*Ford and Pettengill*, 1992]. Twenty three potential flexure areas were initially identified in the gridded topography images. Results from five of these sites have been reported elsewhere [*Sandwell and Schubert*, 1992a]. All altimetry profiles crossing each site were extracted from the publicly available Magellan CDs [*Saunders et al.*, 1992]. We selected features with a large planform radius of curvature which could be approximated as 2-dimensional (Figure 1, squares); smaller quasi-circular features were also selected (Figure 1, circles). One restriction on our selection of areas was that we looked for topographic flexures with profiles oriented roughly along the satellite ground tracks, so that original profiles could be used rather than the gridded topography. The gridded data are smoother than the profiles and may contain cross-track errors due to radial orbit error. Inspection of the topography map shows that in practice this restriction was not too severe: the strike of most of the major features modeled has a significant east-west component. The main disadvantage of this approach is in the modeling of small axisymmetric features where it would be much easier to take radial profiles from a regular grid than to work with the original along-track profiles.

Profiles were selected based on their trench-outer rise signature which consists of a topographic low (generally referred to in flexure literature as a moat or trench) adjacent to a lower amplitude topographic high. In practice however, topographic noise can mask the low amplitude outer rise. Another complication is that faulting on the outer trench wall can lead to very rough topographic profiles which are difficult to model. After examining the altimetry profiles across all of the 23 areas initally identified as potential flexure sites, we rejected 6 areas because topographic noise would have made it difficult to obtain any reliable estimates of lithospheric thickness based on flexure models.

Magellan synthetic aperture radar (SAR) data is also useful in flexure modeling as the fracture patterns may reflect the regional tectonics. For each area chosen, we superposed the SAR and altimetry data to produce an image with topography represented by color and SAR backscatter represented by brightness. This facilitated correlation of surface stresses and topography and allowed comparison with the locations of stresses predicted by the various flexure models.

A summary of each of the 12 new areas retained for modeling (after examining the gridded topography and the profile data) is provided in Appendix 1. (Descriptions of the 5 areas previously modeled are given in *Sandwell and Schubert*, [1992a]) A brief description of the topography and the SAR characteristics of the possible flexure and the feature with which it is associated are given.

THIN ELASTIC PLATE MODELS

Thin elastic plate models are based on the assumption that the plate thickness is small compared with the flexural wavelength. While this type of model provides a good first order fit to the available data, *Turcotte* [1979] has noted that the 'thin' plate approximation is often only marginally valid. We have modeled flexural features on Venus using either cartesian models in which the topography is assumed to be continuous along-strike or axisymmetric models (ring or disk loads).

2-D Cartesian Model

The differential equation for flexure problems where there is no in-plane force is

$$D \frac{d^4 w}{d x^4} + \Delta\rho \, g \, w = 0 \qquad (1)$$

where x is horizontal distance perpendicular to the strike of the trench, w is the vertical deflection, $\Delta\rho$ is the density difference at the upper horizontal boundary, g is the gravitational acceleration and D is the flexural rigidity . (1) has the following general solution

$$w(x) = c_1 \exp\left(-\left(\frac{x-x_0}{\alpha}\right)\right)\cos\left(\frac{x-x_0}{\alpha}\right) + c_2 \exp\left(-\left(\frac{x-x_0}{\alpha}\right)\right)\sin\left(\frac{x-x_0}{\alpha}\right) \qquad (2)$$

In terrestrial problems the flexure is usually modeled as due to: (a) a line load on a continuous plate ($c_1 = c_2$), or (b) a line load on a broken plate ($c_2 = 0$), or (c) a line load and a bending moment applied to the end of a plate ($c_1 \neq c_2 \neq 0$). The load and/or bending moment are applied at x_0 and α is the flexural parameter. Given a particular flexure profile we can solve for x_0, α, c_1, c_2. However, in practice the position of the load is known at least approximately and so it is not

necessary to solve explicitly for x_0. When fitting the Magellan profiles we also included the mean and regional gradient terms. A regional gradient term was included because many of the larger amplitude flexures have a prominent regional slope that is downward away from the trench axis. The complete solution is

$$w(x) = d_1 \exp\left(\frac{-x}{\alpha}\right)\cos\left(\frac{x}{\alpha}\right) + d_2 \exp\left(\frac{-x}{\alpha}\right)\sin\left(\frac{x}{\alpha}\right) + d_3 x + d_4 \qquad (3)$$

where d_1 and d_2 now incorporate both the magnitude of the sinusoidal terms and small changes in the estimated origin position, and d_3 and d_4 are the gradient and mean respectively. It is important to note that in any flexure problem we cannot obtain independent estimates of the load, origin position and flexural parameter as the individual terms in (2) and (3) are not orthogonal even though they are linearly independent.

Expressions for the flexural parameter α (in terms of the elastic plate thickness h_e), the bending moment, M, and the surface stresses $\sigma_{xx,}$ are given in *Turcotte and Schubert* [1982], and in equations (2) - (5) of *Sandwell and Schubert* [1992a]. Values for all the parameters used in this paper are given in Table 1.

The cartesian solution was used to model features having large planform radius; profiles across each feature were modeled by setting h_e and then minimizing the RMS misfit between the model and the observations, thereby solving linearly for the coefficients d_1 - d_4. This procedure was repeated for a range of h_e to establish the RMS misfit versus elastic thickness. Surface stress, bending moment, and curvature were also computed for the minimum misfit model. Plate curvature at the first zero crossing of the model topography profile (or the maximum curvature) was used with the elastic plate thickness estimate to convert elastic thickness to mechanical thickness.

2-D Axisymmetric Model

The model presented above is valid for linear loads or loads with a sufficiently large radius of curvature. However, most coronae have an elevated outer ring, or partial ring [*Stofan et al.*, 1992, *Squyres et al.*, 1992, *Janes et al.*, 1992], so a 2-D axisymmetric model or even a full 3-D flexure model may be more appropriate. To establish the validity of the linear load geometry, we

investigate flexure due to an axisymmetric load for which some solutions have already been derived [*Brotchie and Sylvester*, 1969; *Brotchie*, 1971; *Turcotte*, 1977]. On Venus, where there is a large range in the size of coronae, it is important to determine how large the planform radius of curvature needs to be before a cartesian approximation is valid. For readers primarily interested in the venusian results we suggest skimming over this section briefly. The results are summarised in Figure 3 which illustrates the percentage errors introduced in estimating the load and flexural wavelength from a 2-D model when the real load geometry is axisymmetric. Note that our analysis does not take into account failure of the plate.

Consider a topographic flexural signature due to a ring load of outer radius a and ring width Δa, on a continuous plate (Figure 2). For a given radius a, as Δa increases the ring load behaves more and more like a disk load of radius a. Alternatively we can imagine fixing Δa and increasing a. As a becomes very large relative to Δa the ring can be approximated by a bar load of width Δa. In fact, it can be shown that as a tends to infinity the limit of the ring load is indeed a bar load of width Δa (Figure 2) - the proof is given in Appendix 2.

We investigated the effect of approximating a ring load by a bar load for different ring load geometries using the following approach. First, a synthetic flexure profile due to a ring geometry of known outer radius, width and load was generated. The deflection due to a ring load, outer radius a and width Δa can be derived by subtracting the effect of a disk load, radius $a - \Delta a$ from that of a disk load, radius a. The deflection due to a disk load, radius a is given by (4) and that due to a ring load, outer radius a and width Δa is given by (5):

$$w(r) = \frac{p_0}{\Delta\rho\, g}\,\frac{a}{\alpha}\left\{\mathrm{ber}'\left(\frac{a}{\alpha}\right)\mathrm{ker}\left(\frac{r}{\alpha}\right) + \mathrm{bei}'\left(\frac{a}{\alpha}\right)\mathrm{kei}\left(\frac{r}{\alpha}\right)\right\} \qquad r \geq a \qquad (4)$$

$$w(r) = \frac{p_0}{\Delta\rho\, g}\left\{c_1\,\mathrm{ker}\left(\frac{r}{\alpha}\right) + c_2\,\mathrm{kei}\left(\frac{r}{\alpha}\right)\right\} \qquad r \geq a$$

$$c_1 = \left[\left(\frac{a}{\alpha}\right)\mathrm{ber}'\left(\frac{a}{\alpha}\right) - \left(\frac{a-\Delta a}{\alpha}\right)\mathrm{ber}'\left(\frac{a-\Delta a}{\alpha}\right)\right] \qquad (5)$$

$$c_2 = \left[\left(\frac{a-\Delta a}{\alpha}\right)\mathrm{bei}'\left(\frac{a-\Delta a}{\alpha}\right) - \left(\frac{a}{\alpha}\right)\mathrm{bei}'\left(\frac{a}{\alpha}\right)\right]$$

Here p_0 is the loading force per unit area; *ber, bei, ker, kei* are Bessel - Kelvin functions of zero order and r is the radial distance from the center of the ring or disk load.

As the outer ring radius increases the ring load behaves more like a bar load if the outer ring radius is also large compared with both the flexural parameter, α, and the ring width, Δa. It should be noted that the flexural parameter defined in the literature for axisymmetric models α_{axi} (equations 4 and 5) differs from that defined for cartesian models α_{car} (equations 2 and 3) by a constant factor :

$$\alpha_{axi} = \frac{\alpha_{car}}{\sqrt{2}} \tag{6}$$

To avoid confusion, results quoted for the flexural parameter α in this paper will always refer to the cartesian flexural parameter or the axisymmetric parameter multiplied by $\sqrt{2}$ to facilitate comparisons between different models.

Flexure due to a bar load can be described by convolving a bar load geometry with the response due to a line load (Green's function for a cartesian flexure model):

$$w(x) = B(x) * s(x) \tag{7}$$

where $s(x)$ describes the response due to a line load (V_0) on a continuous plate

$$s(x) = \frac{V_0}{\Delta\rho\, g\, \alpha} \exp\left(-\frac{x}{\alpha}\right)\left[\cos\left(\frac{x}{\alpha}\right) + \sin\left(\frac{x}{\alpha}\right)\right] \qquad x \geq 0 \tag{8}$$

and $B(x)$ describes the bar load, width $2l$ and centered on the origin (box-car function)

$$B(x) = \Pi\left(\frac{x}{l}\right) \tag{9}$$

Thus flexure due to a bar load is given by

$$w(x) = \frac{p_0}{\Delta\rho\, g}\left[\exp\left(-\left(\frac{x-l}{\alpha}\right)\right)\cos\left(\frac{x-l}{\alpha}\right) - \exp\left(-\left(\frac{x+l}{\alpha}\right)\right)\cos\left(\frac{x+l}{\alpha}\right)\right] \tag{10}$$

where p_0 is defined earlier.

To investigate the effect of approximating a truly axisymmetric load by a cartesian load we next modeled the synthetic data profile with a bar load solution (10). The best-fit profile in a least squares sense was sought, simultaneously solving for the load (p_0) and origin position (x_0) of the assumed bar load and for the flexural parameter. This procedure was repeated for several different ratios of ring load width to flexural parameter ($\Delta a/\alpha$); for each ratio a series of profiles was generated where the ratio of outer ring radius to the flexural parameter (a/α) was varied. Results for 4 choices of $\Delta a/\alpha$ and for a disk load are shown in Figure 3. In all cases we expect that as a/α increases, our approximation of a truly axisymmetric load by a cartesian load is increasingly valid and so we should be better able to retrieve x_0, p_0 and α. This can indeed be seen to be the case from Figures 3a - 3c. The misfit of the cartesian model to the synthetic profile generated from a ring load decreases as a/α increases for a given $\Delta a/\alpha$ (Figure 3d). For a given a/α both p_0 and α are better estimated for a thin ring as expected. While α can always be estimated to within about 10% of the true value using a cartesian model, the magnitude of the load is severely underestimated. For example, modeling a disk load with $a/\alpha = 2$ using a cartesian model results in less than a 10% error in estimating the flexural parameter but approximately a 40% error in estimating the magnitude of the load.

It can be seen that the validity of a cartesian approximation to an axisymmetric geometry is dependent on the specifics of the axisymmetric geometry. Say we choose certain "acceptable" limits to the errors introduced in estimating x_0, p_0 and α. Our study suggests that the errors introduced in estimating α are always less than 10% for any detectable axisymmetric load, providing virtually no constraint on when the cartesian approximation is valid. When modeling real topographic flexure profiles, noise in the data usually results in variations much greater than 10% in the flexural parameter estimated for a particular feature. It should also be noted that we have not taken into account the fact that topographic profiles may not pass through the center of the axisymmetric feature. This is the case for most of the Magellan orbit tracks across venusian features. In these cases the topographic profile may change considerably when elevation is plotted against distance from the center of the feature rather than against distance along the profile. Plotting topography versus distance along the profile, rather than topography versus radial distance, gives an apparent flexural wavelength which is longer than the true flexural wavelength.

In contrast to the results concerning the flexural parameter, errors in estimating the magnitude of the load, p_0, can be large. If we choose a cut-off of say 20% for our allowed error then we see that we need $a/\alpha > \sim 2$ for a thin ring load and $> \sim 6$ for a disk load. In estimating the origin position a sensible choice of allowable error is 25%, i.e. we are specifying that the origin position must be correctly estimated to within a quarter of the flexural parameter. This means we require a/α to be $> \sim 3.5$ for any axisymmetric load - ring or disk. The misfit of the cartesian model to the axisymmetric synthetic shown in Figure 3d is the root mean square (r.m.s.) misfit calculated over the outer rise expressed as a percentage of the maximum true deflection on the outer rise (i.e. we are looking at the r.m.s. misfit relative to the signal). This misfit is always less for a disk load than for a ring load of the same outer radius since the outer rise is larger for the disk load. Thus if we choose say 40% as our cut-off we would require $a/\alpha > \sim 2$ for a disk and $> \sim 3$ for a thin ring.

The above discussion demonstrates that it is not easy to establish a general rule for when an axisymmetric model is required. If we can assume that the flexural parameter estimated by a cartesian analysis is roughly correct, as Figure 3a suggests, we can use α_{car} to get an estimate of a/α and $\Delta a/\alpha$ for a given feature. Then the curves in Figure 3 can be used as master curves and our given feature plotted on each figure. Using this approach a more quantitative estimate of the validity of the cartesian approximation to the axisymmetric geometry can be obtained. It should be remembered that this is a "best-case" scenario, assuming that (a) the profiles pass though the center of the feature and (b) that the effect of topographic noise is negligible.

Our results contrast somewhat with those of *Watts et al.* [1988], who investigated the effect of the assumed load geometry on flexure inferred from SEASAT gravity data across the Louisville Ridge. They investigated only the effect on the flexural parameter of incorrectly using a cartesian approximation where the data warrant an axisymmetric model. Their analysis was based on the fact that there is a significant difference in the theoretical gravity/topography admittance corresponding to cartesian and axisymmetric topography [*Ribe*, 1982]. Their gravity/topography analysis found that the cartesian approximation could lead to overestimation of the flexural parameter and the effective elastic thickness. As mentioned above our topography analysis using synthetic profiles illustrated that the cartesian approximation results in estimating the flexural parameter to within 10%. The gravity/topography analysis is more sensitive to the model geometry because it attempts to match the gravity amplitude, especially over the load. Thus in

these analyses the load is matched at the expense of the flexural parameter. We also show that load estimates are very sensitive to the ratio of a/α. Thus, topographic studies attempting to estimate the flexural wavelength are less sensitive to an accurate geometrical representation of the load than are gravity/topography studies.

Flexure due to a disk load or a ring load is given by (4) or (5) respectively. The corresponding bending moment is given by

$$M(r) = -D \frac{d^2w}{dr^2} + \frac{\nu}{r} \frac{dw}{dr} \qquad (11)$$

Again when modeling Magellan altimetry data we include the mean and regional gradient and the fitting procedure is analogous to that performed for the cartesian model. As discussed later only one feature was modeled with an axisymmetric load geometry.

ELASTIC PLATE MODELING RESULTS

Cartesian Features

Inspection of the gridded Magellan topography led to the identification of 10 new candidates for cartesian flexure modeling. Of these 3 were rejected after analysing the altimetry orbit data, based on a lack of clear evidence for flexure. The best-fit cartesian elastic models and the altimetry profiles are shown in Figure 4. The results for best-fit thickness, RMS misfit, the first zero crossing of the profile (x_0) and the curvature (K_0) and bending moment (M_0) at this position are tabulated in Table 2. The best-fit elastic thicknesses for each feature and the range of acceptable thicknesses are given in Table 3. The best-fit elastic thicknesses range from 12 km for Nishtigri Corona to 34 km for West Dali Chasma. We defined the range of acceptable thicknesses to be that over which the RMS misfit was within 10% of its minimum value. It can be seen that there is a wide variation in the goodness of fit of the models to the profiles (Figure 5). The absolute value of the RMS misfit increases in topographically rough areas. The predicted surface stresses at 5 of the 7 areas are extremely high and could not be sustained by the lithosphere. Fracturing at these locations (Neyterkob Corona, Demeter Corona and W. Dali Chasma) is evident in the SAR images. At Nightingale Corona and Nishtigri Corona lower surface stresses are

predicted, although they are still sufficiently high to suggest some faulting. At Nightingale Corona no concentric fractures associated with the flexure can be identified in the SAR images. There is evidence for volcanism postdating the flexure with polygonal fracture patterns possibly related to this later lithospheric reheating, [*Johnson and Sandwell*, 1992b]; these fractures may obscure earlier flexure-related deformation. Concentric fractures possibly associated with the flexure are seen at Nishtigri Corona. On the north side of Demeter Corona there appears to be extensive tectonism and volcanism and the relative stratigraphy of the different events is difficult to identify. West Dali Chasma lies in an intensely tectonised region. This, coupled with the very high curvatures and surface stresses predicted by the flexure model, implies that either the lithosphere here was indeed flexed, but was flexed past its elastic limit, or that the faulting and lithospheric failure is associated with some other tectonic process.

Table 3 shows the best-fit elastic thickness, the corresponding values of the flexural parameter α, and the disk radius a, and ring width Δa, for the 7 areas modeled in this paper with a cartesian model. Four of the features are coronae; however, the inferred flexure north and south of Demeter corona corresponds to a part of the elevated rim which is almost linear in geometry. Thus there are three features (Nishtigri, Nightingale and Neyterkob coronae) for which the validity of the cartesian approximation is important and a/α_{car} and $\Delta a/\alpha_{car}$ are also given for these features. We use the results from the numerical simulations to justify the assumption that the ratio a/α_{car} is approximately equal to a/α_{axi} and similarly for $\Delta a/\alpha_{car}$. The parameters a/α_{car} and $\Delta a/\alpha_{car}$ can then be used together with the master curves in Figure 3 to investigate errors in the estimated parameters (load and flexural wavelength) introduced by assuming a cartesian geometry.

Nishtigri Corona has the largest errors associated with estimating the parameters x_0, p_0 and α. The cartesian model appears only marginally valid, consistent with the small corona size and the fact that it is better approximated by a disk load as compared with the ring load geometry of Neyterkob and Nightingale Coronae. We remodeled the topography to the south of Nishtigri Corona as flexure due to a disk. First, distance along each orbit track was recalculated as distance from the corona center (effectively radial distance) and then a flexure profile described by (4) but including the mean and regional gradient was fit to the recalculated profile. A gray scale image of Nishtigri corona with the orbits modeled is shown in Figure 6a. The results of the cartesian modeling are shown in Figure 6b, where distance is calculated from the highest point

just inboard of the coronal moat. In the cartesian models the profiles are always projected onto the normal to the topographic moat. The results of the axisymmetric model are shown in Figure 6c, where distance is radial distance. The main point to notice is that plotting elevation against radial distance effectively compresses the profile more at small radial distances than at large radial distances, having a marked effect on the best-fit elastic thickness. We recalculated distances along the profile using this method rather than the simpler reprojection used for the cartesian model as the corona is not perfectly circular. Thus the normal to the moat will not necessarily pass through the corona center and distance along a normal is not radial distance. Also the profiles shown in Figures 6b and 6c are only marginally acceptable in terms of being regarded as flexure because they have topographic noise on a critical part of the flexure. This last point is common to altimetry orbits across many of the smaller coronae, rendering these features unsuitable for detailed flexural modeling.

Axisymmetric Features

Initially 8 small coronae were identified from the gridded topography as possible candidates for flexure modeling. Three of these were rejected after inspecting the orbit data, as the signal-to-noise ratio meant that it was difficult to identify a clear consistent flexural signature. Brief descriptions of the remaining 5 features and the surrounding areas are given in Appendix 1. The 5 coronae are shown in Figure 7; for each feature a gray scale image of the topography is given, together with the altimetry orbits analysed. As in Figure 6c, distance is calculated relative to the corona center. The gray scale image for each corona suggests a fairly continuous moat around the corona which is easily identified in the orbit data. However, although some of the profiles exhibit flexure-like signals, these signals can vary substantially from one orbit to the next. In some cases the amplitude of the topographic signal is small making it difficult to distinguish, e.g. the north side of Fatua Corona. Other features have more periodic topography with amplitudes which do not decay exponentially with radius as predicted by simple flexure models. As a result, we consider these data unsuitable detailed flexure modeling. Nevertheless, there does appear to be a characteristic wavelength associated with these smaller features. We use this characteristic wavelength to provide a crude estimate of the elastic plate thickness. The distance between the deepest part of the moat around the corona and the maximum deflection outboard of the moat, i.e. the peak of the possible outer rise is given by the following approximate expression

$$\beta = r_b - r_t \approx \frac{\pi\alpha}{2} \qquad (12)$$

where r_b is the distance to the point of maximum deflection on the outer rise and r_t is the distance to the deepest part of the moat. We can thus obtain the equivalent elastic plate thickness h_e using (4). The distances r_b and r_t were determined for as many profiles as possible for each of the 5 coronae and then α and h_e were calculated. The results are given in Table 4. If the topography represents flexure of the lithosphere the mean elastic plate thickness varies from ~6 km to ~22 km. Note that the result of ~8 km for Fatua Corona differs from the 15 km derived previously by *Moore et al* [1992]. This could be due to the fact that the topography north of Fatua has a longer wavelength than the topography that we modeled on the south side. However, on the north side the amplitude of the outer rise (and also the moat) is extremely small rendering it difficult to obtain a well constrained flexural wavelength for the corona as a whole.

MECHANICAL THICKNESS ESTIMATES

The parameters of the best fitting thin elastic plate models can be used to estimate the depth to the base of the mechanically strong layer. Assuming this corresponds to an isotherm, the geothermal gradient can also be calculated. However, this conversion from elastic thickness to mechanical thickness is highly dependent on the rheological properties of the ductile lower lithosphere. Without a good knowledge of lithospheric rheology on Venus, one can only adopt characteristic values used for the Earth's oceanic lithosphere [*Goetze and Evans,* 1979; *Brace and Kohlstedt,* 1980]. Here we follow *McNutt* [1984] and *Solomon and Head* [1990] where they characterised the strength of the upper brittle portion of the lithosphere using a frictional sliding law, zero pore pressure, [*Byerlee*, 1978] and the strength of the lower lithosphere using a ductile flow law for dry olivine (10^{-16} s^{-1} strain rate). These two failure criteria define a yield strength envelope (YSE) [*Goetze and Evans,* 1979], where the base of the YSE is defined as the depth where the ductile yield strength drops below 50-100 MPa. This corresponds to the 740°C isotherm, and is consistent with the observation that the maximum depths of earthquakes in the oceanic lithosphere correspond roughly to the 740°C isotherm.

When the lithosphere is flexed, the largest deviatoric stresses occur at the top and bottom of the layer. For moderate plate curvatures (~10^{-7} m^{-1}), significant yielding occurs in both the uppermost and lowermost parts of the mechanical lithosphere which are weak. This yielding causes the effective elastic thickness of the lithosphere (i.e. that derived from flexure modeling) to be less than the actual mechanical thickness of the lithosphere *McNutt* [1984]. Complete lithospheric failure occurs when the plate curvature exceeds about 10^{-6} m^{-1}. *Solomon and Head* [1990] adapted this YSE model for the parameters appropriate to Venus and provide a diagram to map the elastic thickness into mechanical thickness using the plate curvature at the first zero crossing of the flexure model (Figure 4 of their paper). Based on synthetic models of bending of plates with realistic nonlinear rheologies, *Mueller and Phillips* [1992] proposed that it is better to use the maximum curvature along the flexure profile, rather than the curvature at the first zero crossing, when converting elastic thickness to mechanical thickness; we use both the first zero crossing of the synthetic profile and the point of maximum curvature of the synthetic profile. The results for the 7 new features modeled with a cartesian model are shown in Figure 8, together with the 5 earlier results of *Sandwell and Schubert* [1992a] for comparison. For a given feature the conversion was performed using the curvatures and moments corresponding to the best fit model for each profile. The uncertainties in Figure 8 represent the range of h_m for each feature. Note that if we used the range in h_e given in table 3 (based on the 10% increase in misfit criteria) some of the uncertainties in h_m would be substantially larger. We prefer the former method as there is a specific curvature associated with each value of h_e: we caution that the the error bars in Figure 8 are in most cases minimum uncertainty estimates. The conversion of h_e to h_m was not possible for the 5 smaller coronae, as curvatures could not be reliably estimated. However, the crude estimates for elastic thickness provide a lower bound on h_m at these locations.

DISCUSSION

The global study presented in this paper has revealed surprisingly few examples of lithospheric flexure on Venus. (Note that we have excluded flexure at rift zones as this study is currently being pursued by *Evans et al.* [1992]). We have found only 7 areas exhibiting well-defined flexure, in addition to the 5 areas previously found by *Sandwell and Schubert* [1992a]. These areas give values for effective elastic thickness ranging from 12 km to 34 km. Of these 7 examples the result

for Nishtigri Corona should be regarded with caution based on the profile data and the cartesian versus axisymmetric analysis described earlier. The remaining 6 areas have sufficiently large radii of curvature to be modeled with a cartesian model. The result obtained for West Dali Chasma is similar to that obtained for Latona and Artemis Coronae by *Sandwell and Schubert* [1992a]. Profiles across other parts of Aphrodite were extracted, e.g. Diana Chasma to the west of Dali Chasma. Although initially appearing very similar to the profiles from W. Dali Chasma the profiles from other parts of Aphrodite could not be satisfactorily fit with a flexure model due to extensive faulting evident in the SAR images and reflected in the topography. It should be noted that the best-fit models for West Dali Chasma, Artemis and Latona Coronae do not extend to the base of what should be the trench. There appears to be a step in the topography part way down the trench wall, corresponding to extensive faulting evident in the radar images. If the profiles are fit to the base of the trench the result is unconvincing. These characteristics, common to altimetry profiles from several parts of Aphrodite, including the larger coronae, suggest that either the lithosphere in this area is flexed but moment saturated, or has been extensively deformed as the result of other processes. The 5 remaining features provide more reliable estimates of the mechanical thickness of the lithosphere. From Figure 8 the mean thicknesses are in the range 21 - 37 km. The corresponding range of average thermal gradients is 14 - 8 K / km and the range of surface heat flow is 46.2 - 26.4 mW m^{-2} (using the parameters given in Table 1). It should be noted that these values for mechanical thickness, and the derived thermal gradient and heat flow may not be the current lithospheric conditions, they rather reflect the conditions at the time the flexural signature was frozen in.

Predictions for the average surface heat flux / thermal gradient / lithospheric thickness were made on the basis of heat flow scaling arguments and chondritic thermal models [*Solomon and Head*, 1982; *Phillips and Malin*, 1983]. Heat flux estimates ranged from 50 mW m^{-2} from the chondritic thermal models to 74 mW m^{-2} from the heat flow scaling argument, with equivalent mechanical thicknesses of 21 - 13 km. Our results for static flexure suggest a thicker lithosphere than predicted, although not as thick as that proposed by *Sandwell and Schubert* [1992a]. Surface stresses predicted by thin elastic plate models are much higher (in most cases) than could be supported by the lithosphere, and there is evidence in the SAR images of failure at the appropriate locations. A thicker lithosphere is consistent with the general lack of evidence for flexural signatures around smaller coronae - we would not expect small loads to be able to deflect a thick

plate. Thinner values for elastic thickness around two large volcanoes on Venus [*McGovern and Solomon,* 1992] could be associated with lithospheric reheating and thinning of the plate. Localised thermal rejuvenation would explain some of the smaller values for elastic thickness in Table 4, and is consistent with plume models for coronae formation and evolution. The large gravity signatures over some of the smaller coronae require either a thick lithosphere (based on preliminary results from isostatic compensation models [*Moore*, personal communication 1993]) or dynamic support.

An important consideration is that the assumed rheological properties of the venusian lithosphere are based on our knowledge of oceanic lithosphere. The extremely low abundance of water at the surface of Venus relative to the Earth [*Oyama et al.*, 1980], suggests that models for the venusian lithosphere require a dry rheology such as that used by *Solomon and Head* [1990]. It is known that dry olivine is stronger than wet olivine [*Goetze and Evans*, 1979] under terrestrial conditions; however it is quite possible that the venusian lithosphere is drier than could be attainable in a laboratory. Although the difference in the percentage of water present in the Venus lithosphere and terrestrial laboratory experiments may be small, it may have significant effects on the rheology, especially given the venusian surface conditions. In particular, the venusian lithosphere could be much stronger than predicted. Recent measurements suggest that dry diabase is much stronger than previously believed [*Mackwell et al.*, 1993]; it is quite feasible that the same will be found to be true of dry olivine.

Flexure of a Viscous Plate

The flexure model assumes that the trench/outer rise features are statically maintained by large fiber stresses within a thin elastic lithosphere. However, it is possible that the flexure inferred from topography is the result of deformation of a viscous lithosphere. We discuss three mechanisms which can produce apparent topographic flexural signatures. In the first two cases the lithosphere is currently dynamically supported and the estimated viscous plate thickness depends upon the assumed strain rate or stress distribution. In the third case the process generating the flexural signature has ceased recently, relative to the characteristic timescales for viscous relaxation.

In the first scenario, flexural signatures can be generated by a hydrostatically supported viscous lithosphere, loaded at the trench and moving horizontally toward the trench [*DeBremaecker,* 1977]. This type of model has been applied to terrestrial subduction zones, and predicts a thick viscous lithosphere (on the order of 120 km) in which the deviatoric stresses are lower [*Melosh,* 1978] than the stresses predicted by the elastic flexure model. The equation describing the vertical deflection is

$$w(x) = d_1 \exp\left[-\left(\frac{x - x_0}{\beta}\right) \cos\left(\frac{\pi}{5}\right)\right] \sin\left[\left(\frac{x - x_0}{\beta}\right) \sin\left(\frac{\pi}{5}\right)\right] + d_2 x + d_3 \qquad (13)$$

[*DeBremaecker*, 1977], where $\beta^5 = (\eta\ U\ h_v^3) / (27\ \rho\ g)$; η is the viscosity, h_v is the viscous plate thickness and U the horizontal velocity. As an example we fit such a model to Latona Corona as this has been proposed to be the site of possible subduction on Venus [*McKenzie et al.*, 1992; *Sandwell and Schubert* 1992a, 1992b], and appears to display evidence for back-arc type extension [*Sandwell and Schubert*, 1993]. If we fix the viscosity to the terrestrial value of 10^{23} Ns m^{-2}, the best-fit model has a viscous plate thickness of 80 km for U = 50 mm/yr and 172 km for U = 5 mm/yr. Latona has a mean radius of approximately 400 km, and so a plate velocity of 50 mm/yr would imply the corona has developed only over the last 8 Myr, whereas the lower velocity of 5 mm/yr would imply development over the last 80 Myr. The main problem with this kind of model for Venus is that at most locations with flexural-like topography there is no evidence for retrograde subduction, and as yet, no independent evidence for plate motions has been observed. These considerations lead us to favour low horizontal strain rates, which in turn imply a thick viscous lithosphere at most of our study areas. Thus viscous plate models, like the elastic plate models, are compatible with low temperature gradients in the lithosphere.

In a second scenario, the inferred flexural signatures result from vertical stresses, acting on the base of a viscous lithosphere. Flexure inferred around coronae would imply a ring geometry to the stress field; it is difficult to imagine how this could be generated by a mantle flow field consistent with models for coronae evolution. Regardless of the mechanism by which the stresses could be generated, the resulting models would produce results analogous to those of the previous discussion. That is, low bending stresses would imply a thick viscous lithosphere, high stresses would correspond to a thin viscous lithosphere.

In a third scenario, the inferred flexures are the result of dynamic processes which are no longer active. One concern with an elastic plate flexure model is that only a small percentage of coronae exhibit topographic signatures consistent with flexure. The size distribution of coronae is described by a power law decay [*Stofan et al.*, 1992]. Smaller loads (coronae) will result in a smaller deflection of an elastic plate and it is possible that the topography around many coronae contains a low amplitude flexural signature which is masked by topographic noise. It is very likely that coronae are at different stages of evolution, and also that different coronae may be generated by different processes, so we would not expect flexural signatures to be associated with all coronae. However, it is possible that a topographic flexural signature, associated with most or all coronae when they are formed, relaxes due to viscous flow, once it is no longer dynamically maintained. If this is the case, then we can make some predictions concerning the characteristic timescales for viscous flow, based on the percentage of coronae with associated inferred flexure.

The governing equation for flexure of a viscous plate is

$$F \frac{\partial^5 w}{\partial t \, \partial x^4} + \Delta\rho \; g \; w = 0 \qquad (14)$$

where $F = \eta \; h_v^3 \; / \; 27$ is the instantaneous flexural rigidity. We assume that sinusoidal topography of wavelength α decays exponetially with time with a time constant of λ:

$$w(x,t) = A \cos(x \; / \; \alpha) \exp(-\lambda \; t) \qquad (15)$$

The characteristic decay time of this topography is given by

$$\tau_\alpha = \frac{1}{\lambda} = \frac{\eta \; h_v^3}{27 \; \Delta\rho \; g \; \alpha^4} \qquad (16)$$

Thus an initial flexural signature will be undetectable (due to viscous flow) after a time which depends upon the initial amplitude of the flexure. If we assume that typical initial outer rise heights are on the order of 100 - 300m (consistent with the larger inferred flexural signatures from Aphrodite Terra), then the outer rise will be undetectable after a time, T_f equal to twice the

characteristic decay time. If we also assume that the production rate of coronae has been uniform over the mean surface age of the planet, then we can calculate T_f from the number of coronae with inferred flexural signals, N_f, and the total number of coronae, N_t (approximately 250 [*Stofan et al.*, 1992]):

$$T_f = \frac{T * N_f}{N_t} \tag{17}$$

T is the mean surface age of the planet, which we take to be 500 million years [*Phillips et al.*, 1992; *Schaber et al.*, 1992]. This gives T_f = 18 Myr, so τ = 9 Myr. Thus if we assume the flexural wavelength has not changed significantly as the topography has relaxed, we can use (16) and the flexural wavelengths given in tables 3 and 4 to obtain the corresponding viscous plate thickness for each feature. Values for h_v calculated in this manner (assuming $\eta = 10^{23}$ Pa s) are in the range 69 - 291 km.

It is evident that we can calculate viscous plate thicknesses consistent with the observed number and form of inferred flexural features, however the results are dependent on many assumptions which cannot be independently verified. Relaxation timescales consistent with the observed number of inferred flexural features predict a thick lithosphere at most of the sites, again consistent with a low temperature gradient in the lithosphere. If the viscous plate thicknesses are lower than this analysis suggests, the corresponding timescales for relaxation would be much shorter. It is possible that there are smaller lateral variations in viscous thickness than the above analysis suggests: however, we would then expect a larger percentage of short wavelength flexural signatures compared with the long wavelngth flexural signals, due to the shorter characteristic decay time of long wavelength topography. Our study has not revealed such a distribution of features, however the statistics may be biased by the fact that low amplitude, short wavelength signals are not easily detectable above the topographic noise.

The above discussion concerned relaxation of a flexural signature previously generated in a viscous lithosphere. Gravitational relaxation of surface topography produces vertical stresses which can result in very similar topographic signatures to those which would be generated by flexure of an elastic, visco-elastic or viscous plate. This mechanism has been proposed to account for the topography around coronae on Venus [*Stofan et al.*, 1991; *Janes et al.*, 1992]. The timescales

for crustal flow for Venus are 10,000 - 100,000 years [*Smrekar and Solomon*, 1992], based on previous experimental results for diabase rheology. However, recent measurements on dry diabase [*Mackwell et al.*, 1993] suggest a much stronger rheology, comparable to that previously published for websterite. *Smrekar and Solomon* [1992] found that the timescales for gravitational relaxation assuming a websterite rheology were on the order of several hundred million years. These long timescales would predict a much higher abundance of flexure-like topographic signals than is observed.

CONCLUSIONS

We have presented results from a global study of flexure on Venus, excluding flexure at rift zones and around volcanoes. Most prominent examples of downward flexure are associated with the outer edges of coronae. As coronae vary considerably in diameter, we investigated the validity of a cartesian approximation to an axisymmetric load geometry. The important parameters are the ratio of outer load radius to the flexural parameter a/α, and, if a ring load is appropriate, the ratio of ring load width to the flexural parameter $\Delta a/\alpha$. Our analysis indicates that for a given a/α, loads with a smaller value of $\Delta a/\alpha$ (thin rings) are better approximated with a cartesian model than loads with a larger value of $\Delta a/\alpha$ (wide rings or disks). As a/α increases for any given $\Delta a/\alpha$ the cartesian approximation becomes increasingly valid, especially for estimating α when a/α is greater than about 2. In contrast, the magnitude of the load is severely underestimated even when a/α is about 5; this is important as it directly translates into an underestimation of the bending moment. Modeling of profiles which do not pass through the center of the axisymmetric feature, with a cartesian model can overestimate the flexural wavelength. Criteria can be set up specifying the acceptable error in each of the parameters estimated by the flexure model - load magnitude, load position and flexural parameter. These criteria can then be used together with the curves in Figure 3 to establish critical values of a/α and $\Delta a/\alpha$ for which a cartesian approximation to a ring load or disk load geometry is acceptable.

We modeled 7 features, in addition to 5 previously modeled, with a cartesian model. We remodeled one of these features, Nishtigri Corona, with a disk load model and found significantly different results. The difference can be partly attributed to the fact that the cartesian approximation was, in this case, a poor approximation and partly to the fact that this was a poor

example of flexure. Based on the curvatures and surface stresses obtained from thin elastic plate models, the topography at W. Dali Chasma, Latona and Artemis Coronae is either representative of extreme flexure (the lithosphere is moment saturated) or it is the result of a tectonic history not involving lithospheric flexure. Mean mechanical thicknesses calculated for the remaining examples fall in the range 21 km - 37 km, reflecting lithospheric thicknesses at the time of loading. We found no clear examples of flexure around smaller corona, though 5 areas could not be completely ruled out. Estimates of effective elastic thickness based on a flexure model for these examples fell in the range 4 km - 28 km and did not correlate with corona diameter. The elastic thicknesses provide a lower bound on mechanical thickness at these sites. Of these 5 examples, only Fatua Corona has a strong gravity signal which is well correlated with the topography [*Moore*, personal communication 1993].

An alternative interpretation of the apparent flexural signatures modeled in this paper is that they are the result of flexure of a viscous lithosphere. A dynamical model derived for terrestrial subduction zones [*DeBremaecker*, 1977] was applied to the topographic profiles from Latona Corona. The viscous plate thickness corresponding to low strain rates was found to be 170 km, greater than the comparable thickness derived for terrestrial subduction zones. The number of observed apparent flexural signatures is consistent with characteristic timescales for viscous relaxation of 9 million years. Based on these timescales the derived viscous plate thicknesses are again high. Thus, viscous plate models are also consistent with low temperature gradients in the lithosphere. The main problem with viscous models is that there is a trade-off between the strain-rate (or stress distribution or relaxation timescales) and the viscous plate thickness. Unfortunately, we have almost no information on timescales on Venus, so if a viscous rheology is appropriate we can, at best, propose a family of models consistent with the observations.

Models for the formation of coronae have suggested that an apparent flexural signature may form during the late stages of evolution, as a result of gravitational relaxation [*Stofan et al.*, 1991; *Janes et al.*, 1992]. However, recent measurments on dry diabase indicate that dry crustal materials are much stronger than previously believed [*Mackwell*, 1993]. Timescales for gravitational relaxation of a strong venusian crust are on the order of 10^8 - 10^9 years [*Smrekar and Solomon* , 1992], comparable to the inferred average surface age of approximately 500 million

years [*Phillips et al.*, 1992; *Schaber et al.*, 1992]. Thus, based on the current available information, it is unlikely that flexural topography is generated by gravitational relaxation.

Another possibility is that the trench and outer rise signatures could be Airy-compensated and simply reflect variations in crustal thickness. The improved gravity anomaly data being collected by Magellan may shed light on this final possibility. On Earth, gravity anomaly data are used to reject this hypothesis.

Assuming the trench and outer rise topographic features that we have identified are supported by large fiber stresses within a thin plate, our results indicate that the venusian elastic lithosphere is thicker than predicted based on the global heat scaling argument. This has implications for the style and timing of tectonic acitivity on Venus. Scenarios consistent with a thick lithosphere have been proposed in which either most of the heat escapes through localized heat pipes [*Turcotte*, 1989], or mantle convection on Venus is highly episodic [*Turcotte*, 1992; *Parmentier and Hess*, 1992]. The localized heat pipe model is problematic as it predicts a global volcanic flux much greater than that inferred from radar observations [*Solomon and Head*, 1991; *Head et al.*, 1992]. Also a natural choice of locations for such heat pipes would be the coronae themselves and this model would then predict hotter thinner lithosphere at coronae. Current episodic convection models require global synchroneity of the initiation and termination of convection. It is more realistic to expect regional variations in the extent and duration of the episodes of increased convection. Such modifications to the current models would be more consistent with the range in lithospheric thicknesses reported here and with the fact that many coronae do not exhibit any flexural signature. A recent tectonic model for resurfacing on Venus has been proposed in which a period of rapid crustal deformation existed in the past due to a higher surface heat flux than at present and a correspondingly weaker lower crust [*Solomon*, 1993]. In this model a gradual decrease in surface heat flux can lead to a much more abrupt change in the crustal deformation rates because of the exponential dependence of strain rate upon temperature. High strain rates would be expected to persist over a longer time period in elevated regions, (compared with the lowlands) due to a weaker crust. Our results are broadly consistent with this model as the features exhibiting apparent flexural signatures are mostly in or around the edge of the lowlands, where a lower heat flux and thicker lithosphere would be expected. Recent laboratory experiments on terrestrial diabase indicate that dry crustal materials are significantly stronger than previously

believed [*Mackwell*, 1993]. If similar results are found for dry olivine, this will suggest a strong venusian lithosphere, and the mechanical thickness estimates in this paper will be reduced. Finally, although it will not be able to directly model flexure profiles using the Magellan gravity data we hope that it will provide more information on variations in lithospheric thickness on Venus and on the relative contributions of static and dynamic processes to the support of topographic features.

APPENDIX 1: Descriptions of Flexure Locations

(a) Larger Features Modeled with a cartesian Flexure Model

Nishtigri Corona (24.5°S, 72.0°E)

Asymmetric corona with maximum radius of 140 km. The interior is elevated about 1 km above surrounding plains regions. The topographic moat around the corona is about 45 km wide. The topography to the north of the corona is elevated and rough, so no flexure signature could be detected. Possible flexure is visible on the south side of Nishtigri. A moderate number of volcanic features associated with Nishtigri are evident in the SAR image (C1MIDR 30S063;1) mostly small domes in the elevated interior and flows surrounding the corona. Concentric fractures around Nishtigri coincide with the location of the outer rise in the flexure profiles.

Nightingale Corona (63.0°N, 132.0°E)

Concentric corona (a well-defined tectonic annulus [*Stofan et al.*, 1992]) with a maximum radius of ~280 km. The tectonic annulus is elevated up to ~2.5 km above the surrounding plains. This elevated rim is extremely tectonically disturbed as evidenced in the SAR images (e.g. C1MIDR 60N125E;1). Tessera-like terrain to the north of the corona masks any flexure which may have been associated with Nightingale. There is a well defined flexural signature to the south, superposed on a regional slope which is downhill in the SSE direction. No concentric fractures associated with the flexure are seen, however there is substantial volcanism associated with Nightingale both interior to and exterior to the corona. In particular there is evidence for flows possibly postdating the flexure on the south side of the corona. Polygonal fracture patterns rather than fractures concentric to the corona are seen.

Demeter Corona (55.0°N, 295°E)

Concentric elongate corona with maximum radii ~335 km (NE-SW direction) and ~165 km (NW-SE direction). The corona interior is at approximately the same elevation as the surrounding plains but the corona rim is elevated by up to 1 km. Flexure is evident to the north and south of the corona and the coronal rim at these locations is almost straight. Concentric fractures associated with the rim and the flexural moat are evident in the SAR images (e.g.

C1MIDR 60N291). To the north of the corona there is considerable tectonism probably unassociated with the corona. Volcanism is visible in the form of small volcanoes in the corona interior and flows in the surrounding plains.

Neyterkob Corona (49.0°N, 203.0°E)

Neyterkob is defined as a multiple corona [*Stofan et al.*, 1992], the east and west parts being distinct. The interior of both parts of the corona is not elevated but there is a topographically high rim defining the edge of the corona. The topography surrounding the corona is very rough. However to the south and south-east of the eastern part of the corona the topography is relatively flat and there is evidence for flexure associated with the coronal outer rim. Volcanism is evident in the SAR images (e.g. C1MIDR 45N202;1) and there is extensive tectonism associated with the corona and with the ridge belts in the surrounding plains. Concentric fractures possibly associated with the topographic flexure can be seen though they are somewhat masked by other tectonic features and lava flows.

Ridge (19.0°N, 70.0°E)

This is a narrow east-west trending ridge reaching a maximum height of about 1km above the plains to the north. There is no evidence of a flexural moat to the south but a possible low amplitude flexure to the north can be seen in the gridded topography. Some fracturing parallel to the ridge and to the north can be identified in the SAR image (C1MIDR 15N077;1) Volcanism in the areas immmediately adjacent to the ridge is mainly in the form of flows of small areal extent.

W. Dali Chasma (18°N, 160°E)

West Dali Chasma is located in Eastern Aphrodite Terra and is an extremely deep (~xx km) roughly east-west trending asymmetric chasma. The highest part of the topography is just to the north of the chasma. The topography on the south side of the chasma was identified as a possible example of flexure. The region is extremely tectonically deformed as evidenced in the SAR images of this area. The tectonic deformation appears to postdate several volcanic flows. An extremely bright region in the SAR image correlates with the highest topography in agreement with previous observations of an increase in reflectivity at high elevations [*Pettengill et al., 1992*].

Extensive closely spaced fractures on the south side of the chasma and parallel to it are easily identified in the SAR data.

(b) Smaller Axisymmetric Features (Coronae)

Fatua Corona (16.5°S, 17.2°E)

Concentric corona with interior high ring (up to ~1km), surrounding moat and outer elevated ring. Maximum radius is ~ 155 km. Gridded topography suggests outer lower amplitude ring may be a flexural feature, although the part of the outer ring to the SW of the corona has too high an amplitude to be flexure caused by the inner corona load. SAR image (C1MIDR 15S026;1) shows concentric fractures associated with the corona moat and outer elevated rim. Small volcanoes are evident in the corona interior and flows associated with the corona can be seen.

Beyla Corona (27.0°N, 16.0°E)

Asymmetric corona (elongate in a NW-SE direction) with maximum radius of 145 km. Has little associated volcanism. The center of the corona is less than 500 m above the surrounding plains. There is a pronounced moat around the northern edge of the corona, although the topography to the north is too rough to distinguish any topographic flexure. The gridded topography suggests possible flexure to the south. The SAR image (C1MIDR 30N009;1) shows almost no concentric fractures around the southern edge of the corona. Quasi-concentric fractures are seen associate with the moat around the northern edge. Corona interior exhibits roughly NW-SE trending bright lineations.

Indrani Corona (37.5°S, 70.5°E)

Concentric corona with a maximum radius of ~100 km. The topography surrounding the corona is moderately rough making flexure difficult to identify. There is a narrow moat which is almost continuous around the corona. There are no distinguishing features associated with the corona evident in the SAR images (C1MIDR 45S074;1).

Bhumidevi Corona (17.0°S, 343.0°E)

Concentric corona with maximum radius of 100 km. The center of the corona is low relative to the surrounding plains, but there is an elevated rim (up to ~1 km) surrounded by a moat which is continuous except on the south east side of the corona. There is evidence in the gridded topography for possible flexure associated with the moat around the north west side of the corona. A narrow band of concentric fractures around the outer edge of the corona are visible in the SAR image (C1MIDR 15S352;1).

Unnamed Corona (37.0°N, 257.0°E)

Concentric corona with maximum radius of ~100km. Moderate volcanism is associated with the corona, although the corona itself is difficult to identify in the SAR data alone. The corona lies to the north of a region of rough topography. The interior is at approximately the same elevation as the plains to the north but there is an elevated ring surrounded by a topographic low on the northern side of the corona. Possible flexure to the north.

APPENDIX 2: The bar load approximation to the ring load

In this appendix we demonstrate that in the limit of large a/α a ring load of outer radius a and width Δa can be approximated by a bar load width Δa.

The expression for deflection due to a ring load outer radius a and width Δa (equation (8) in the main text) can be written explicitly as the deflection due to a disk load of radius a minus the deflection due to a disk load of radius $a - \Delta a$:

$$w(r) = \frac{p_0}{\Delta\rho\, g}\left[\left(d\ ber'(d)\ ker(x) - \delta\ ber'(\delta)\ ker(x)\right) + \left(\delta\ bei'(\delta)\ kei(x) - d\ bei'(d)\ kei(x)\right)\right] \qquad x >= a/\alpha \tag{A1}$$

where

$$d = a/\alpha; \quad \delta = \frac{a-\Delta a}{\alpha}; \quad x = \frac{r}{\alpha}$$

We are interested in the limit of w(r) as a/α becomes very large. The limit of each of the terms inside the square brackets can be taken using the following relations

$$ber'(d)\ ker(x) = \frac{\exp\left(-\left(\frac{x-d}{\sqrt{2}}\right)\right)}{2\sqrt{d\,x}}\left[S_0(d)\cos(dd) - T_0(d)\sin(dd)\right]\left[L_0(-x)\cos(xx) + M_0(-x)\sin(xx)\right] \tag{A2}$$

$$bei'(d)\ kei(x) = \frac{\exp\left(-\left(\frac{x-d}{\sqrt{2}}\right)\right)}{2\sqrt{d\,x}}\left[T_0(d)\cos(dd) + S_0(d)\sin(dd)\right]\left[M_0(-x)\cos(xx) - L_0(-x)\sin(xx)\right] \tag{A3}$$

where

$$dd = \frac{d}{\sqrt{2}} + \frac{\pi}{8}; \qquad xx = \frac{x}{\sqrt{2}} + \frac{\pi}{8}; \qquad \delta\delta = \frac{\delta}{\sqrt{2}} + \frac{\pi}{8} \tag{A4}$$

$$S_0(x) = 1 - \frac{1.3}{1!\,8x}\cos\left(\frac{\pi}{4}\right) - \frac{1^2.3.5}{2!\,(8x)^2}\cos\left(\frac{2\pi}{4}\right) - \frac{1^2.3^2.5.7}{3!\,(8x)^3}\cos\left(\frac{3\pi}{4}\right) - \ldots\ldots, \tag{A5}$$

$$T_0(x) = \frac{1.3}{1!\,8x}\sin\left(\frac{\pi}{4}\right) + \frac{1^2.3.5}{2!\,(8x)^2}\sin\left(\frac{2\pi}{4}\right) + \frac{1^2.3^2.5.7}{3!\,(8x)^3}\sin\left(\frac{3\pi}{4}\right) + \ldots\ldots, \tag{A6}$$

$$L_0(x) = 1 + \frac{1^2}{1!\,8x}\cos\left(\frac{\pi}{4}\right) + \frac{1^2.3^2}{2!\,(8x)^2}\cos\left(\frac{2\pi}{4}\right) + \frac{1^2.3^2.5^2}{3!\,(8x)^3}\cos\left(\frac{3\pi}{4}\right) + \ldots\ldots, \tag{A7}$$

$$M_0(x) = -\frac{1^2}{1!\,8x}\sin\left(\frac{\pi}{4}\right) - \frac{1^2.3^2}{2!\,(8x)^2}\sin\left(\frac{2\pi}{4}\right) - \frac{1^2.3^2.5^2}{3!\,(8x)^3}\sin\left(\frac{3\pi}{4}\right) - \ldots\ldots, \tag{A8}$$

For large x, d, and δ the expressions (A2) and (A3) reduce respectively to

$$\text{ber}'(d)\,\text{ker}(x) = \frac{1}{2\sqrt{d\,x}}\exp\left(-\left(\frac{x-d}{\sqrt{2}}\right)\right)\cos(dd)\cos(xx) \tag{A9}$$

and

$$\text{bei}'(d)\,\text{kei}(x) = -\frac{1}{2\sqrt{d\,x}}\exp\left(-\left(\frac{x-d}{\sqrt{2}}\right)\right)\sin(dd)\sin(xx) \tag{A10}$$

Thus equation (A1) reduces to

$$w(x) = \frac{p_0}{\Delta\rho\, g}\frac{1}{2}\left[\sqrt{\frac{d}{x}}\exp\left[-\left(\frac{x-d}{\sqrt{2}}\right)\right]\cos\left(\frac{x-d}{\sqrt{2}}\right) - \sqrt{\frac{\delta}{x}}\exp\left[-\left(\frac{x-\delta}{\sqrt{2}}\right)\right]\cos\left(\frac{x-\delta}{\sqrt{2}}\right)\right] \tag{A11}$$

For large a/α (hence large d, δ and x)

$$\sqrt{\frac{d}{x}} \approx \sqrt{\frac{\delta}{x}} \approx 1$$

and we have

$$w(x) = \frac{p_0}{\Delta\rho\, g}\frac{1}{2}\left[\exp\left[-\left(\frac{x-d}{\sqrt{2}}\right)\right]\cos\left(\frac{x-d}{\sqrt{2}}\right) - \exp\left[-\left(\frac{x-\delta}{\sqrt{2}}\right)\right]\cos\left(\frac{x-\delta}{\sqrt{2}}\right)\right] \tag{A13}$$

Equation (A13) gives the ring load solution as a/α becomes very large, for an origin at the center of the ring. The origin, r = 0, for the ring load solution is defined as being the center of the circles defining the inner and outer edges of the ring load. For the bar load solution the bar load is centered on the origin, x = 0. Thus to compare the two solutions we need to make a shift of origin to r = a - Δa/2. Equation (A13) then becomes

$$w(x') = \frac{p_0}{\Delta\rho\, g}\frac{1}{2}\left[\exp\left[-\left(\frac{x'-\frac{\Delta d}{2}}{\sqrt{2}}\right)\right]\cos\left(\frac{x'-\frac{\Delta d}{2}}{\sqrt{2}}\right) - \exp\left[-\left(\frac{x'+\frac{\Delta d}{2}}{\sqrt{2}}\right)\right]\cos\left(\frac{x'+\frac{\Delta d}{2}}{\sqrt{2}}\right)\right] \tag{A14}$$

As the flexural parameter defined for axisymmetric geometries differs from that defined for cartesian geometries by a factor of $\sqrt{2}$ (equation (9) in main text) then (A14) can be rewritten

$$w(x) = \frac{p_0}{\Delta\rho\, g}\frac{1}{2}\left[\exp\left[-\left(\frac{x-\frac{\Delta a}{2}}{\alpha}\right)\right]\cos\left(\frac{x-\frac{\Delta a}{2}}{\alpha}\right) - \exp\left[-\left(\frac{x+\frac{\Delta a}{2}}{\alpha}\right)\right]\cos\left(\frac{x+\frac{\Delta a}{2}}{\alpha}\right)\right] \tag{A15}$$

Equation (A15) is simply the bar load solution (equation (13) in the main text with l replaced by Δa/2). Thus in the limit of large a/α the ring load geometry is identical to a bar load of the same width. We used a similar procedure to calculate the limit of a disk load as a/α becomes very large.

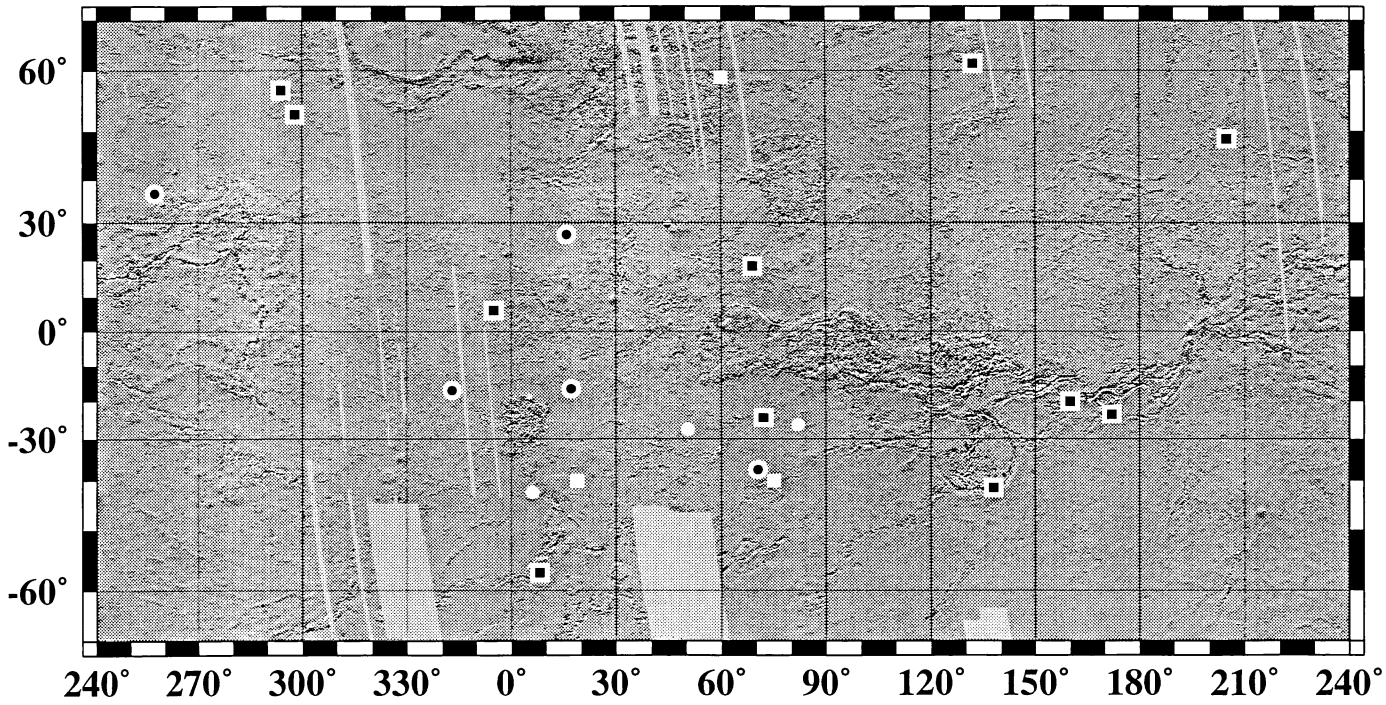

Figure 5.1: Mercator projection Venus topography map illuminated from the north [Ford and Pettengill, 1992]. Square symbols are 14 of the 15 linear flexural signatures (Freyja Montes is off the map, 78°N, 335°E). Solid white symbols are areas rejected after inspecting the altimetry orbit data. The larger black and white symbols represent areas modeled with a 2-D cartesian model. Black and white circles are smaller coronae for which axisymmetric models are discussed.

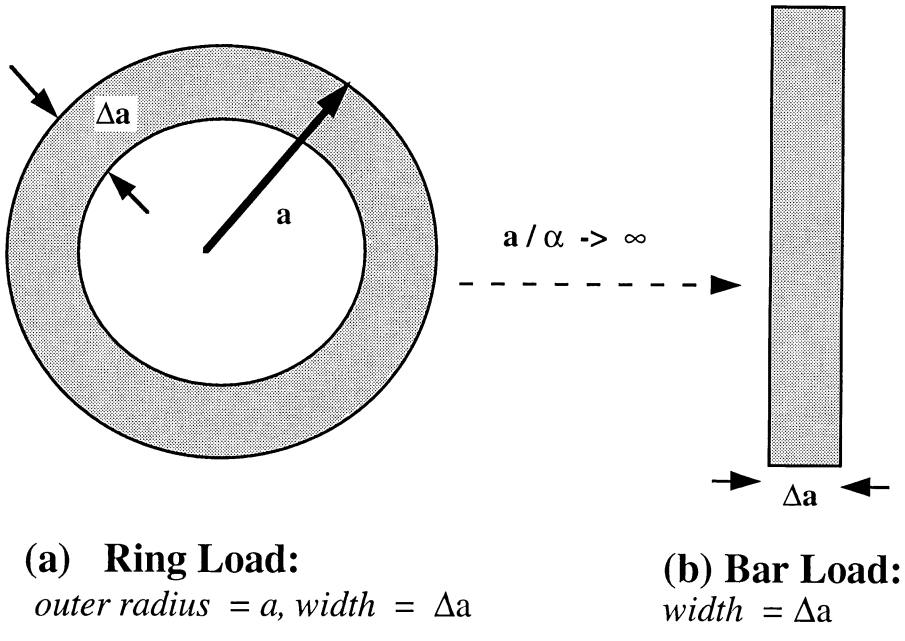

Figure 5.2: Schematic demonstrating the approximation of a ring load of outer radius a and width Da by a bar load with width Da. As the ratio of outer radius to flexural parameter tends to infinity, the ring load behaves like the equivalent bar load.

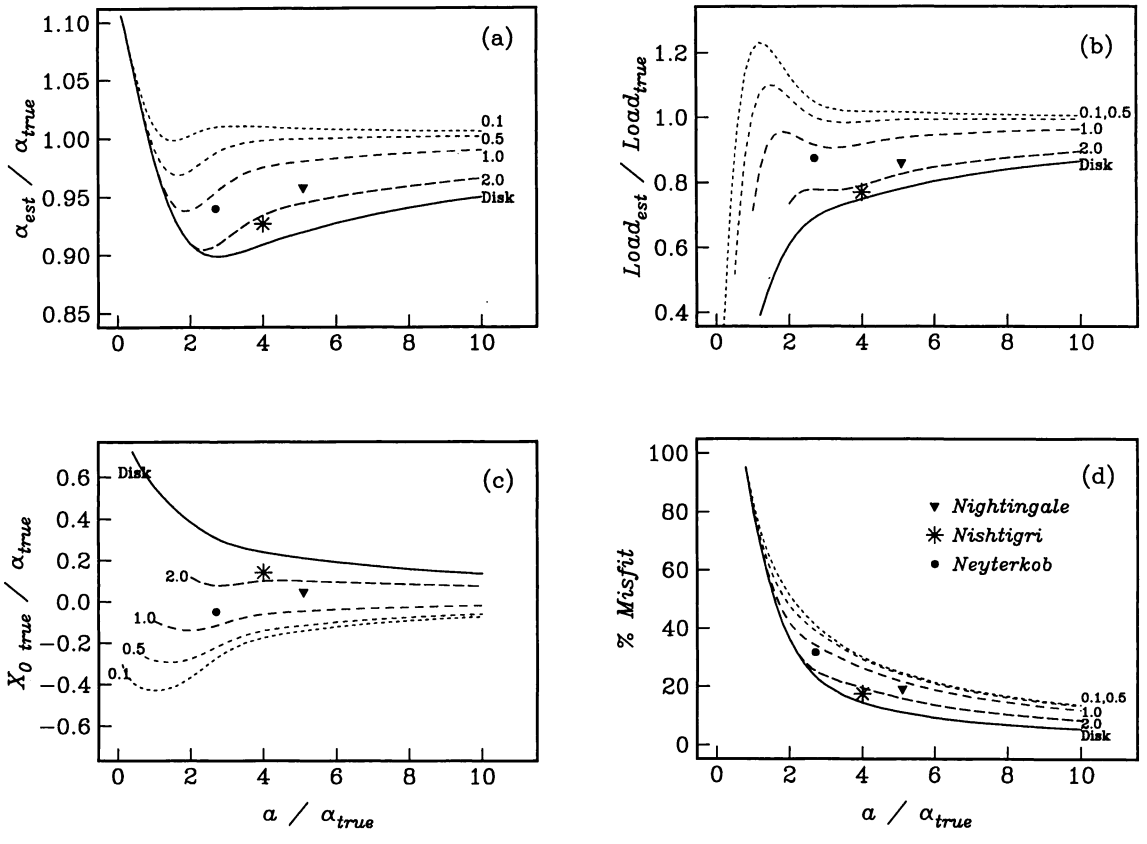

Figure 5.3: Effect of the cartesian approximation to an axisymmetric geometry on estimating model parameters; (a) flexural parameter, (b) load magnitude, (c) load position. Horizontal axis is the ratio of outer ring radius to true flexural parameter (axisymmetric flexural parameter). The vertical axis is normalized to indicate relative error in the particular parameter being estimated. Comparison of curves in (a), (b) and (c) demonstrates the inability of the flexure model to estimate the parameters independently. Figure (d) represents a "goodness of fit" criterion of the cartesian model to the axisymmetric geometry. Misfit over the outer rise was calculated and expressed as a percentage of the maximum deflection on the outer rise. Different curves in each figure correspond to different ratios of ring width to flexural parameter; the value of this ratio is given next to each curve. The results for a disk load are also shown. Three study areas have been plotted on each figure, to investigate the validity of the cartesian approximation.

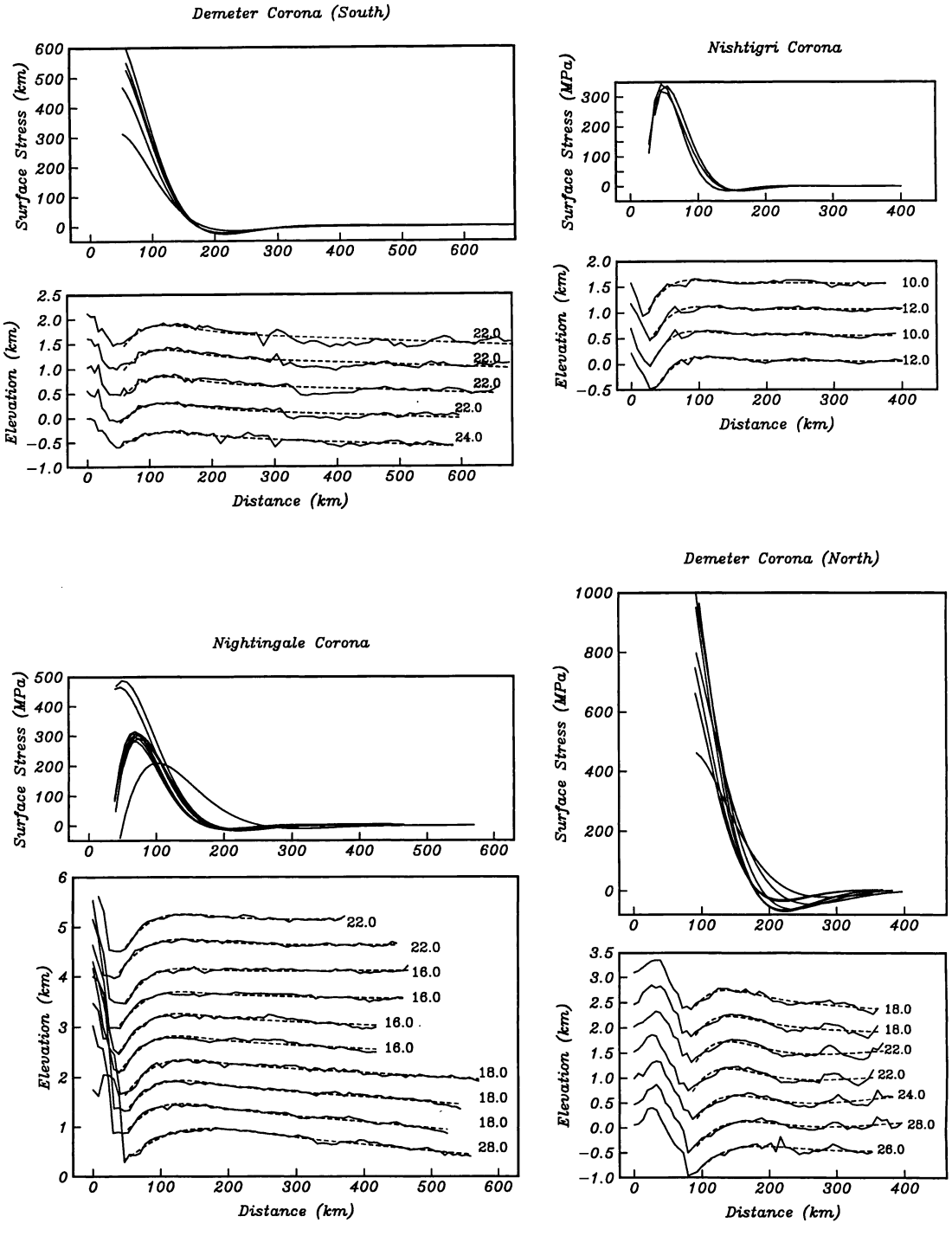

Figure 5.4a: Results of cartesian flexure modeling of 4 of the 7 areas. For each area the lower plot shows altimetry orbits modeled (solid line) with the best-fit cartesian elastic model (dashed line). Distance is calculated relative to the highest elevation inboard of the flexural moat. Elastic thickness corresponds to the best-fit model is given at the end of each profile. Upper figure shows surface stresses predicted by the best-fit models.

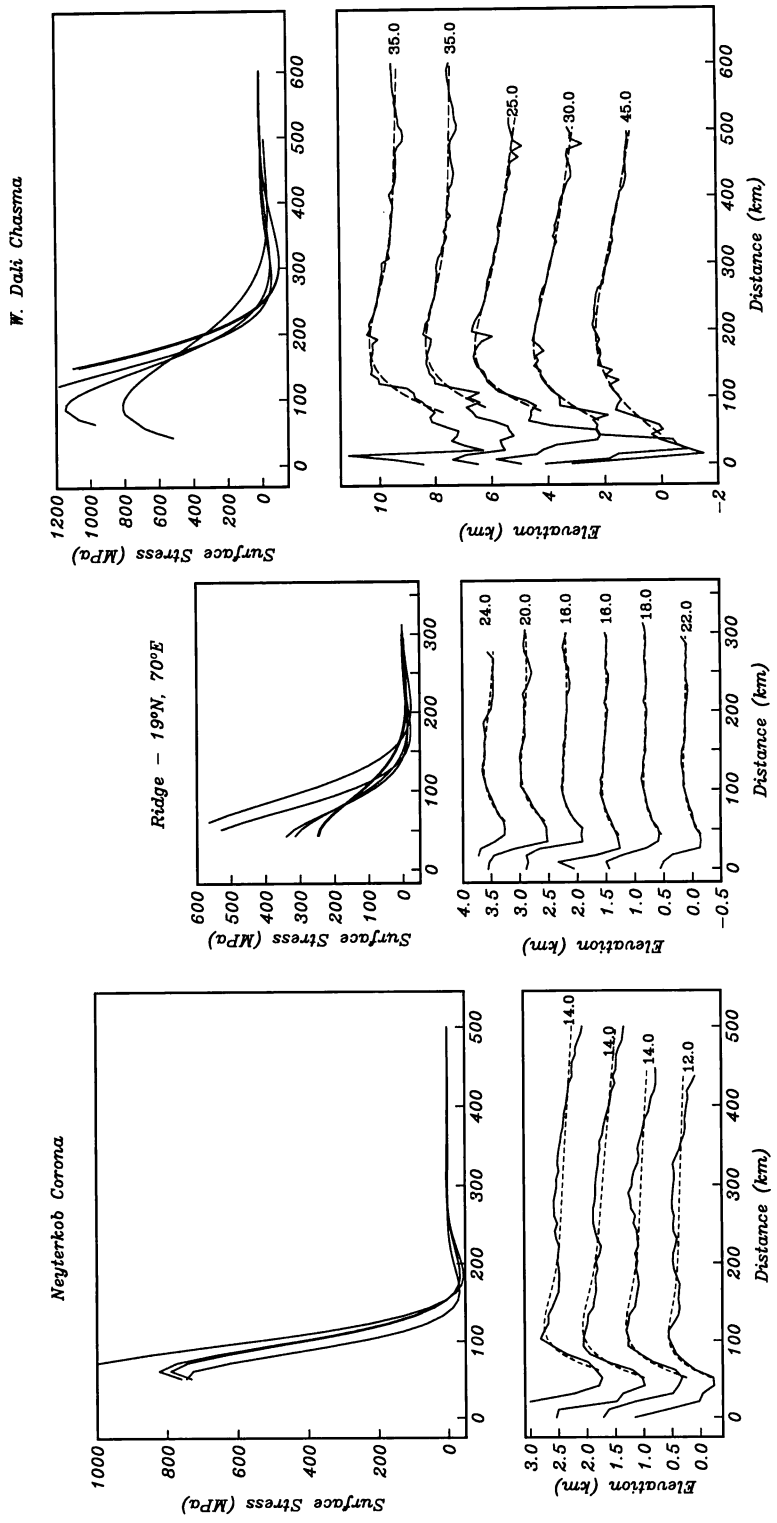

Figure 5.4b: Results of cartesian flexure modeling of 3 of the 7 areas. Figure format as in figure 5.4a.

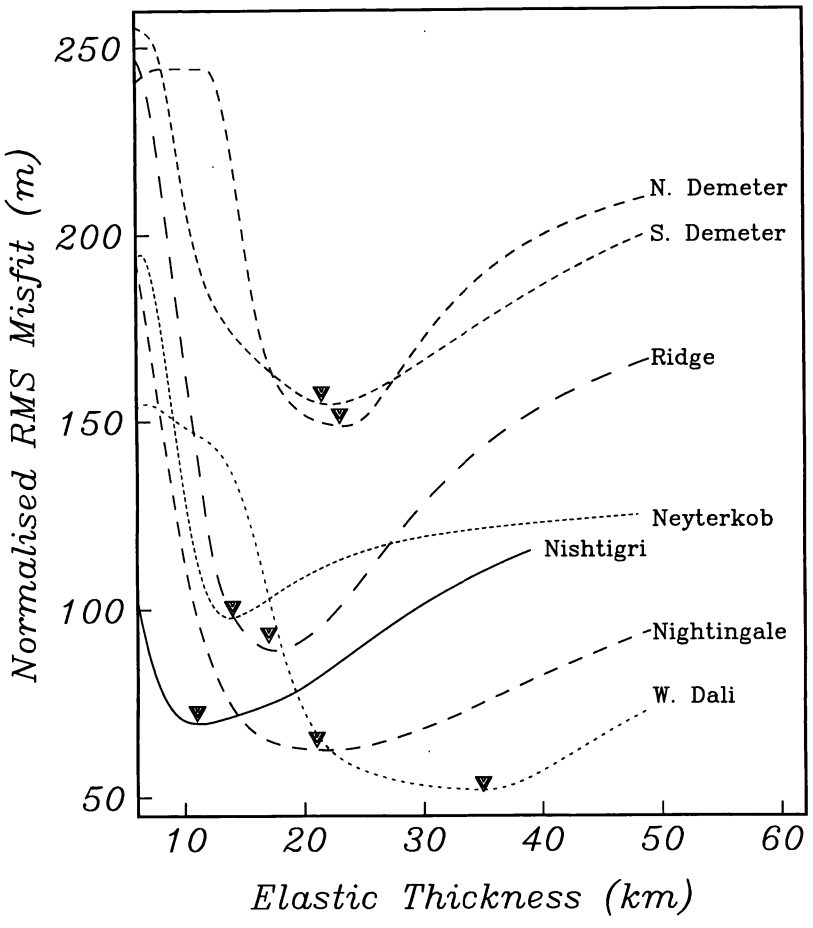

Figure 5.5: RMS misfit versus elastic thickness for each of the 7 areas. Misfit was calculated for 2 km increments in elastic thickness. Solid triangles denote average best-fit elastic thickness for each feature. Figures 5.5 and 5.4 together demonstrate the increase in the minimum RMS misfit in topographically rough areas. Figure 5.5 shows the variation in how well-constrained the best-fit models are.

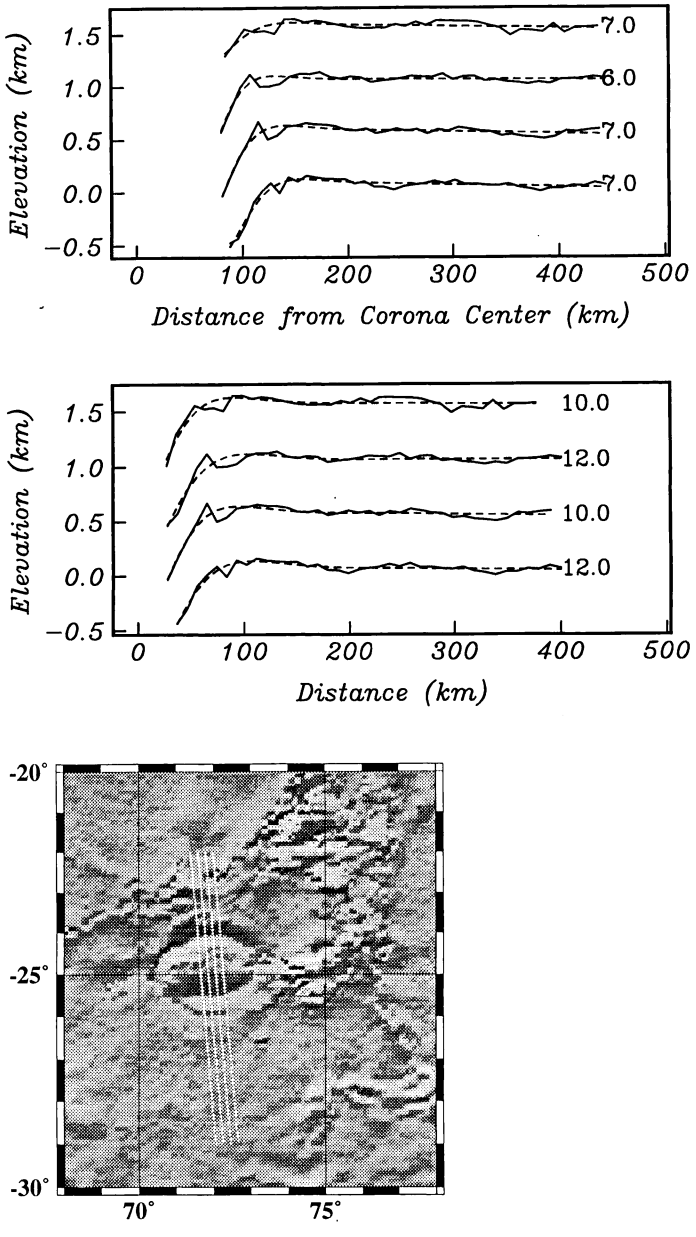

Figure 5.6: Comparison of cartesian and axisymmetric models for Nishtigri corona. The lower figure shows the corona with the tracks of the altimetry orbits modeled. Altimetry profiles with the best-fit cartesian models are shown in the middle plot. The upper plot shows the profile data replotted so that distance is now calculated from the center of the corona. The best-fit models calculated using a disk model are shown by the dashed lines, with the best-fit elastic thickness given at the end of each profile.

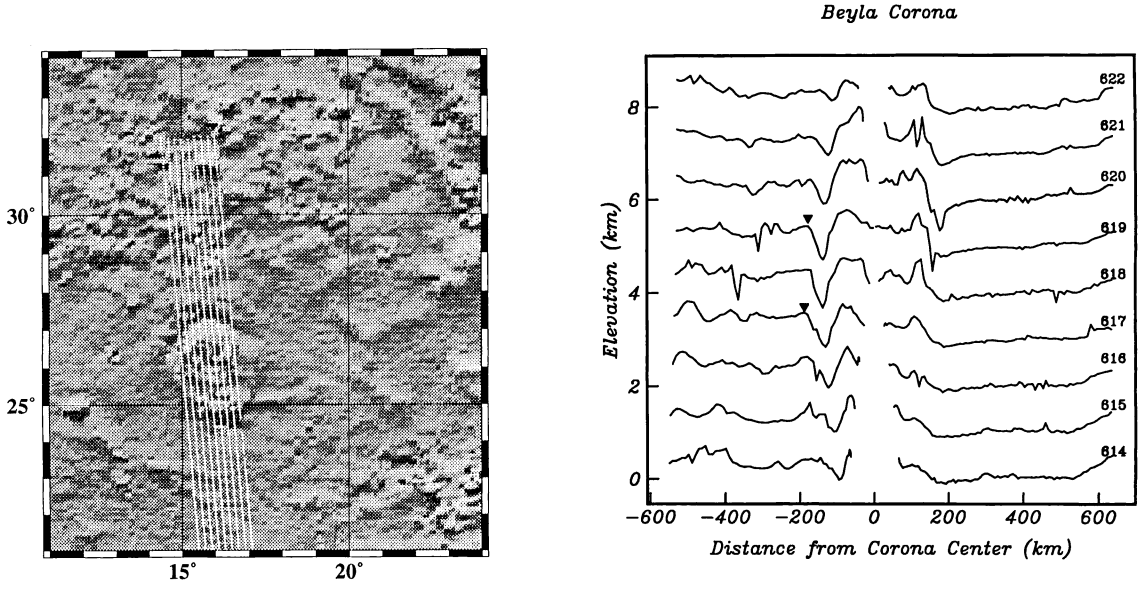

Figure 5.7a: Topography with the orbit tracks and profile data for Beyla corona. For each feature in figure 7 distance along the profile is calculated relative to the corona center. Gaps in the profiles are due to profiles passing at different distances from the corona center. Distances north of the corona center are again negative, distances south of the center are positive. The triangles mark the position of the possible outer rise measured and tabulated. The topographic highs inboard of the trench are the corona interior. The orbit number is given at the end of each profile.

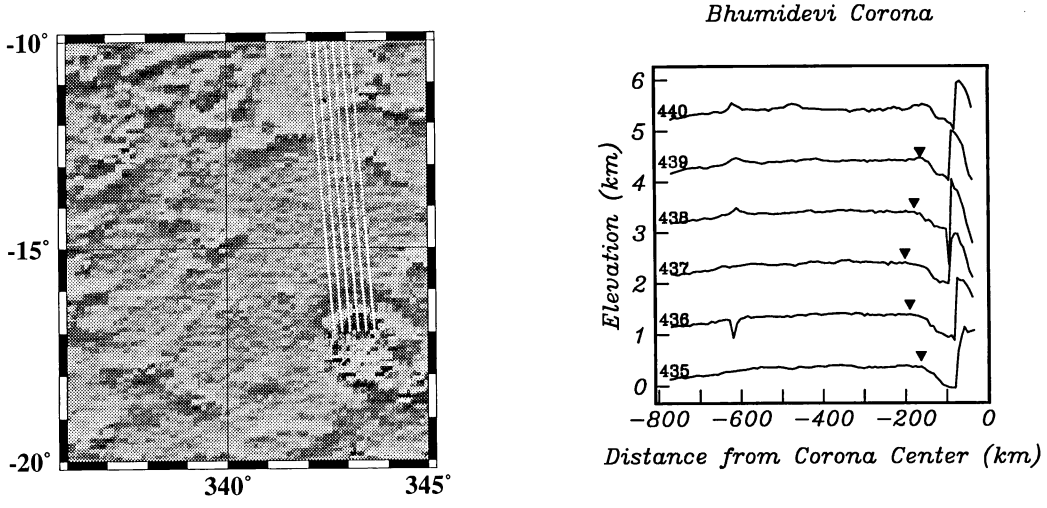

Figure 5.7b: Topography with the orbit tracks and profile data for Bhumidevi corona. Format as in figure 7a.

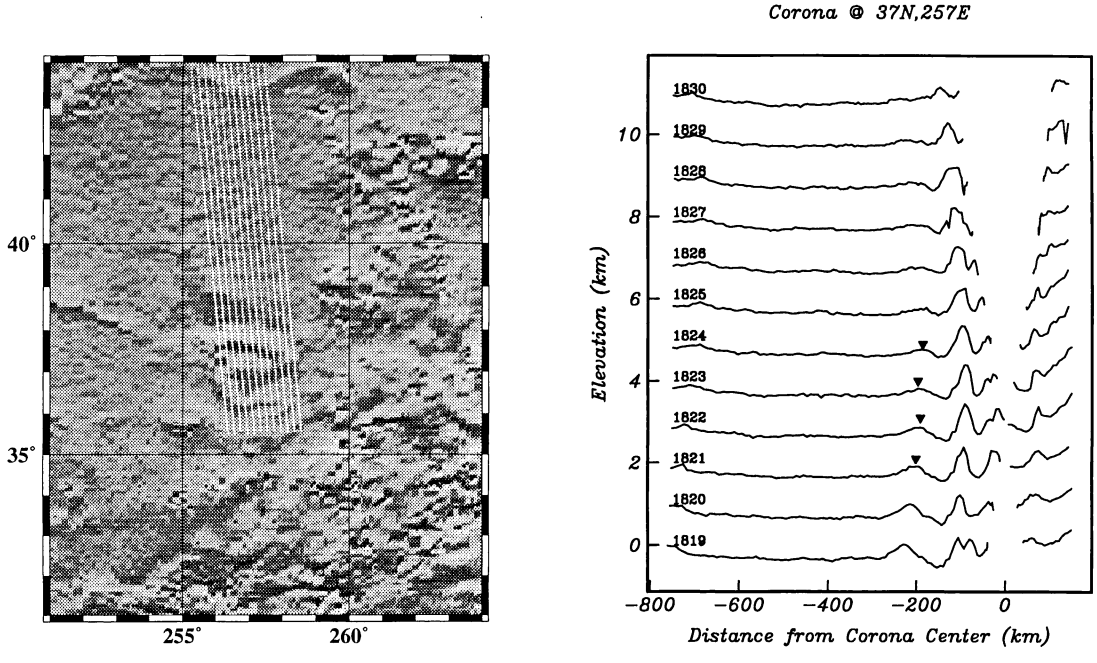

Figure 5.7c: Topography with the orbit tracks and profile data for 37°N,257°E corona. Format as in figure 7a.

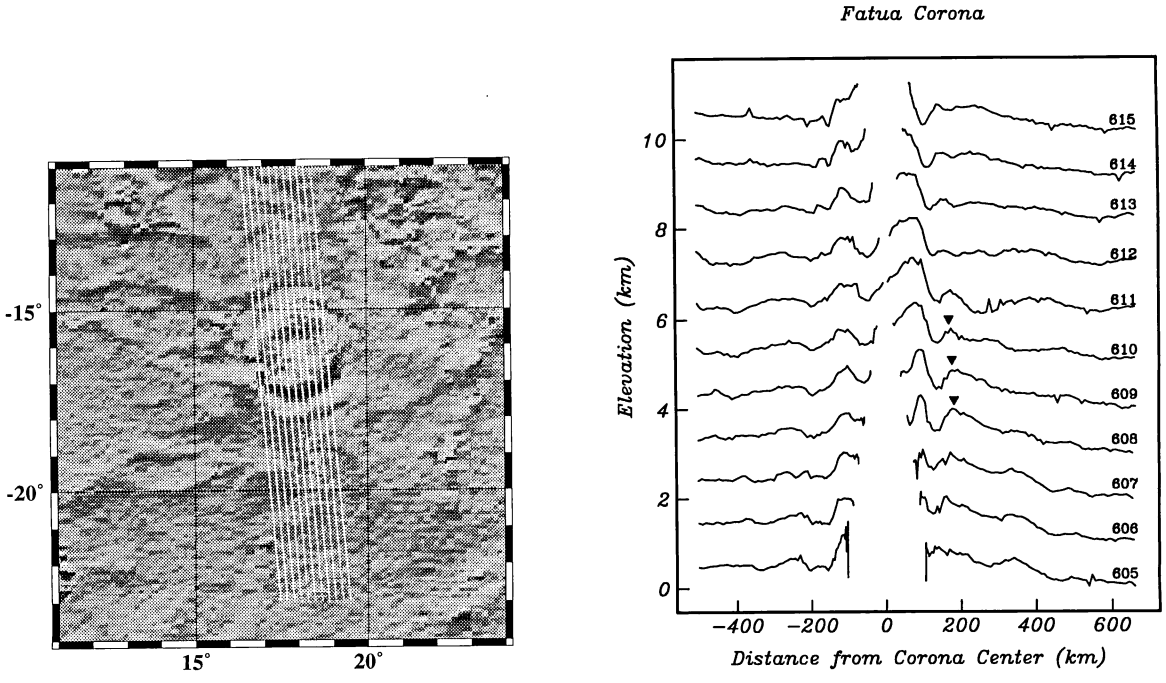

Figure 5.7d: Topography with the orbit tracks and profile data for Fatua corona. Format as in figure 7a.

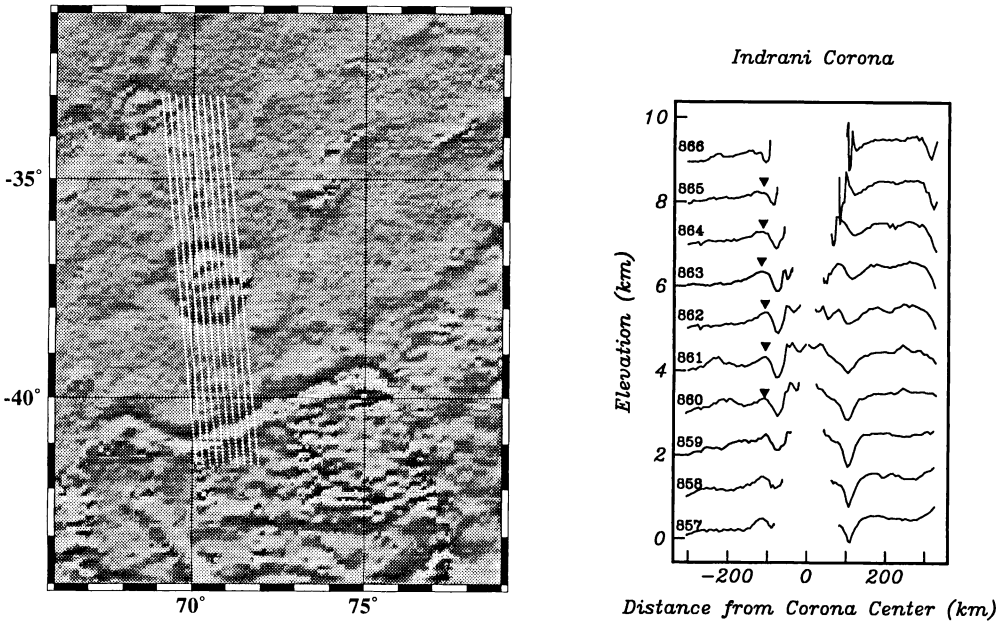

Figure 5.7e: Topography with the orbit tracks and profile data for Indrani corona. Format as in figure 7a.

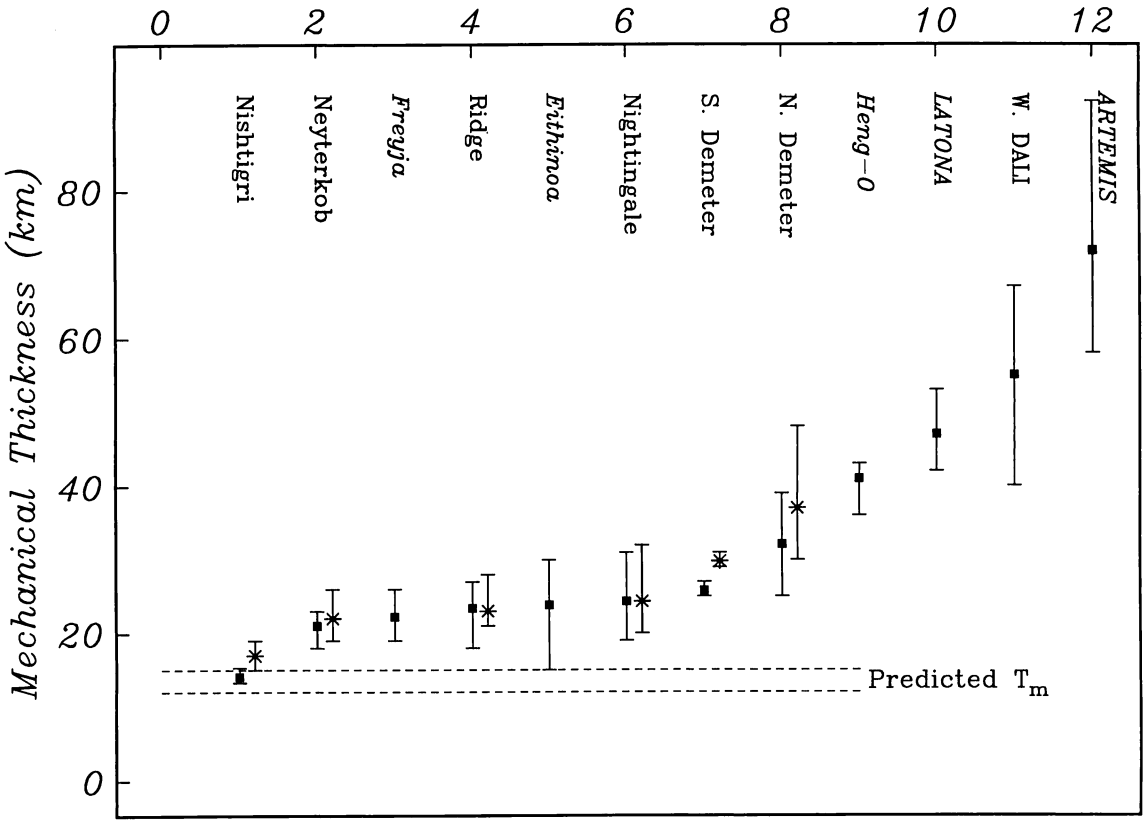

Figure 5.8: Mechanical thicknesses for all 12 areas modeled with a cartesian model. The area names in italics represent results presented previously [Sandwell and Schubert, 1992a]. Areas whose names are capitalised are believed to be moment saturated and thus do not provide a reliable estimate of mechanical thickness. The dashed lines represent the range of mechanical thickness predicted for Venus on the basis of heat flow scaling arguments [Solomon and Head, 1982]. The solid symbols represent the mean mechanical thickness for each area and the uncertainties are the range. Square symbols with errors are mechanical thicknesses obtained by performing the conversion from elastic to mechanical thickness at the first zero crossing of the synthetic profiles [McNutt, 1984]. Stars and errors are from the conversion using the point of maximum curvature along the synthetic. The latter method not used at W. Dali due to high curvatures.

Table 5.1: Parameters Relating to Venusian Lithosphere

	Parameter	*Value*
T_m	mantle temperature	1400°C
T_e	temperature at base of mechanical lithosphere	740°C
T_s	surface temperature	455°C
α	thermal expansivity	3.1×10^{-5} K^{-1}
E	Young's modulus	65 GPa
ρ_m	mantle density	3000 kg m^{-3}
k	thermal conductivity	3.3 W m^{-1} K^{-1}
ν	Poisson's ratio	0.25
g	gravitational acceleration	8.87 m s^{-2}

TABLE 5.2: Best-fit 2-D Models for (a) Demeter [N], (b) Demeter [S], (c) Nightingale, (d) Nishtigri, (e) Neyeterkob, (f) ridge, (g) W. Dali.

Orbit	he (km)	RMS (m)	X0 (km)	MO (1.e16N)	K0 (1.e-08/m)	hm (km)	dT/dz (K/km)
2036	26.0	60	134.65	1.70	16.70	30.0	9.7
2037	28.0	56	105.65	4.37	34.45	39.0	7.4
2038	24.0	63	96.98	4.45	55.77	36.0	8.1
2039	22.0	70	91.89	3.91	63.59	35.0	8.3
2040	22.0	76	92.94	4.25	69.12	34.0	8.5
2041	18.0	65	107.44	1.51	44.94	26.0	11.1
2042	18.0	52	108.15	1.33	39.42	25.0	11.6
2018	24.0	48	46.23	1.50	18.79	26.0	11.1
2020	22.0	53	43.31	1.89	30.66	25.0	11.6
2021	22.0	62	43.31	2.12	34.39	26.0	11.1
2022	22.0	65	43.31	2.21	35.93	25.0	11.6
2023	22.0	77	43.31	2.39	38.80	27.0	10.7
1212	28.0	36	153.89	0.88	6.97	30.0	9.7
1214	18.0	35	111.78	0.51	15.05	21.0	13.8
1216	18.0	33	108.28	0.57	16.98	21.0	13.8
1218	18.0	36	111.78	0.56	16.77	21.0	13.8
1220	16.0	45	102.33	0.43	18.18	19.0	15.3
1222	16.0	46	102.33	0.45	18.81	19.0	15.3
1224	16.0	37	101.88	0.39	16.28	19.0	15.3
1226	16.0	35	102.32	0.46	19.31	19.0	15.3
1228	22.0	30	89.00	1.20	19.53	25.0	11.6
1230	22.0	27	91.53	1.43	23.23	26.0	11.1
874	12.0	31	80.48	0.26	26.16	14.5	20.0
875	10.0	39	71.93	0.18	31.85	14.0	20.7
876	12.0	41	76.58	0.25	24.74	14.0	20.7
877	10.0	42	67.22	0.17	30.09	14.0	20.7
1570	12.0	89	82.47	0.58	58.31	18.0	16.1
1571	14.0	103	92.58	0.83	52.44	21.0	13.8
1572	14.0	91	92.58	0.87	54.56	22.0	13.2
1573	14.0	93	92.58	1.11	70.32	23.0	12.6
877	22.0	24	86.62	0.64	10.41	24.0	12.1
878	18.0	19	75.75	0.55	16.39	21.0	13.8
879	16.0	19	72.48	0.47	19.89	19.0	15.3
880	16.0	24	73.10	0.78	32.93	21.0	13.8
881	20.0	34	85.65	1.31	28.31	26.0	11.1
1315	45.0	148	165.41	8.83	16.77	57.0	5.1
1316	30.0	153	143.90	5.54	35.48	45.0	6.4
1317	25.0	146	143.01	4.68	51.86	40.0	7.3
1318	35.0	194	125.41	25.60	103.33	67.0	4.3
1319	35.0	166	122.71	16.44	66.35	66.0	4.4

Table 5.3 Best-fit 2-D models for larger features

Feature Name	h_e *(km)*		α *(km)*	*a (km)*	Δa *(km)*	a/α	$\Delta a/\alpha$
	Best-Fit	*Range*					
Nishtigri Corona	12	10 - 16	35.0	140	Disk	4.0	Disk
Neyterkob Corona	14	12 - 18	39.3	105	50	2.7	1.3
Ridge	18	14 - 22	47.4	----	-----	-----	----
Nightingale Corona	22	16 - 30	55.1	280	100	5.1	1.8
S. Demeter Corona	22	16 - 32	55.1	----	-----	----	----
N.Demeter Corona	24	18 - 28	58.8	----	----	----	----
W. Dali Chasma	34	26 - 40	76.4	----	----	----	----

Table 5.4: Smaller Axisymmetric Features (Coronae)

Feature Name	*Profile #*	r_b *(km)*	r_t *(km)*	β *(km)*	α *(km)*	h_e *(km)*
Indrani Corona	860	107.5	75.1	32.4	20.6	5.9
37.5°S, 70.5°E	861	106.5	79.4	27.1	17.3	4.6
	862	107.5	74.1	33.4	21.3	6.2
	863	116.9	79.2	37.7	24.0	7.3
	864	112.9	80.5	32.4	20.6	5.9
	865	112.8	87.7	25.1	16.0	4.2
Bhumidevi Corona	435	161.6	79.8	81.8	52.1	20.4
17.0°S, 343.0°E	436	189.5	96.2	93.3	59.4	24.3
	437	199.8	94.6	105.2	67.0	28.5
	438	176.8	93.5	83.3	53.0	20.9
	439	162.3	93.4	68.9	43.9	16.2
Unamed Corona	1821	201.0	143.1	57.9	36.9	12.8
37.0°N, 257.0°E	1822	191.2	133.1	58.1	37.0	12.9
	1823	197.3	132.9	64.4	41.0	14.8
	1824	185.8	144.1	41.7	26.5	8.3
Fatua Corona	608	179.3	130.8	48.5	30.9	9.9
16.5°S, 17.2°E	609	178.4	135.8	42.6	27.1	8.5
	610	161.9	134.0	27.9	17.8	4.9
Beyla Corona	617	187.2	130.0	57.2	36.4	12.7
27.0°N, 16.0°E	619	177.8	137.0	40.8	26.0	8.1

REFERENCES

Brace, W. F., and D. L. Kohlstedt, Limits on lithospheric stress imposed by laboratory experiments, *J. Geophys. Res., 85*, 6248-6252, 1980.

Brotchie, J. F., Flexure of a liquid filled spherical shell in a radial gravity field, *Modern Geology, 3*, 15-23, 1971

Brotchie, J.F. and R. Silvester, On crustal flexure, *J. Geophys. Res, 74*, 5240-5252, 1969

Brown, C.D. and R.E. Grimm, Flexure and the role of inplane force around coronae on Venus, *LPSC XXIV*, 199-200, 1993

Byerlee, J. D., Friction of rocks, *Pageoph., 116*, 615-626, 1978.

Caldwell, J. G., and D. L. Turcotte, Dependence of the thickness of the elastic oceanic lithosphere on age, *J. Geophys. Res., 84*, 7572-7576, 1979.

DeBremaecker, J. C., Is the oceanic lithosphere elastic or viscous?, *J. Geophys. Res., 82*, 2001-2004, 1977.

Evans, S.A., M. Simons and S.C. Solomon, Flexural Analysis of Uplifted Rift Flanks on Venus, *International Colloqium on Venus, LPI Contribution No. 789*, 30-32, 1992

Fletcher, J., L. Haar, T. Hanks, L. Baker, F. Vernon, J. Berger and J. Brune, The Digital Array at Anza, California: Processing and Initial Interpretation of Source Parameters, *J. Geophys. Res., 92*, 369-382, 1987

Ford, P. G., and G. H. Pettengill, Venus topography and kilometer-scale slopes, *J. Geophys. Res., 97*, 13103-13114, 1992.

Goetze, C., and B. Evans, Stress and temperature in the bending lithosphere as constrained by experimental rock mechanics, *Geophys. J. R. astr. Soc., 59*, 463-478, 1979.

Head, J.W., L.S. Crumpler, J.C. Aubele, J.E. Guest and R.S. Saunders, Venus Volcanism: Classification of volcanic features and structures, associations and global distribution from Magellan data, *J. Geophys. Res., 97*, 13,153-13,197, 1992

Janes, D. M., S. W. Squyres, D. L. Bindschadler, G. Baer, G. Schubert, V. L. Sharpton, and E. R. Stofan, Geophysical models for the formation and evolution of coronae on Venus, *J. Geophys. Res., 97*, 16,055-16,067, 1992.

Johnson, C.L. and D.T. Sandwell, Flexure on Venus: Implications for Lithospheric Elastic Thickness and Strength, *LPSC XXIII*, 619-620, 1992a

Johnson, C.L. and D.T. Sandwell, Joints in venusian Lava Flows, *J. Geophys. Res., 97*, 13,601-13,610, 1992b

Johnson, C.L. and D.T. Sandwell, Estimates of Lithospheric Thickness on Venus, *LPSC XXIV,* 721-722, 1993

Mackwell, S. J., D. L. Kohlstedt, D. S. Scherber, and M. E. Zimmerman, High temperature deformation of diabase: Implications for Tectonics on Venus, *EOS, Trans. A.G.U., 74*, #43, 378, 1993.

McKenzie, D. P., Some remarks on heat flow and gravity anomalies, *J. Geophys. Res., 72*, 6261-6273, 1967

McKenzie, D., P. G. Ford, C. Johnson, B. Parsons, G. H. Pettengill, D. Sandwell, S. Saunders, and S. C. Solomon, Features on Venus generated by plate boundary processes, *J. Geophys. Res., 97*, 13533-13544, 1992.

McNutt, M. K., Lithospheric flexure and thermal anomalies, *J. Geophys. Res., 89*, 11180-11194, 1984.

McNutt, M. K. and H. W. Menard, Constraints on yield strength in the oceanic lithosphere derived from observations of flexure, *Geophys. J. R. Astr. Soc., 71*, 363-394, 1982

Melosh, H. J., Dynamic support of outer rise topography, *Geophys. Res. Lett., 5*, 321-324, 1978.

McGovern, P.J. and S.C. Solomon, Estimates of elastic plate thicknesses beneath large volcanoes on Venus, *International Colloqium on Venus, LPI Contribution No. 789*, 68-70, 1992

Moore, W., G. Schubert and D.T. Sandwell, Flexural models of trench/outer rise topography of coronae on Venus with axisymmetric spherical shell thin elastic plates, *International Colloqium on Venus, LPI Contribution No. 789*, 72-73, 1992

Mueller, S., and R. J. Phillips, Inelastic Lithospheric Flexure, Submitted to Geophysical Journal International, February, 1992.

Oyama, V.I., G.C. Carle, F. Woeller, J.B. Pollack, R.T. Reynolds and R.A. Craig, Pioneer Venus gas chromatography of the lower atmosphere of Venus, *J. Geophys. Res., 85*, 7891-7902, 1980

Parmentier, E.M. and P.C. Hess, Chemical differentiation of a convecting planetary interior: Consequences for a one plate planet such as Venus, *Geophys. Res. Lett., 19*, 2015-2018, 1992

Parsons, B. and J. Sclater, An analysis of the variation of ocean floor bathymetry and heat flow with age, *J. Geophys. Res., 82*, 803-827, 1977

Pettengill, G.H., P.G. Ford and R.J. Wilt, Venus surface radiothermal emission as observed by Magellan, *J. Geophys. Res., 97*, 13,091-13,102, 1992

Phillips, R.J. and M.C. Malin, The interior of Venus and tectonic implications, in *Venus*, D.M. Hunten, L. Colin, T.M. Donahue, V.I. Moroz, Eds, (University of Arizona Press, Tuscon, 1983)

Phillips, R.J., R.E. Raubertas, R.E. Arvidson, I.C. Sarkar, R.R. Herrick, N. Izenberg and R.E. Grimm, Impact craters and Venus resurfacing history, *J. Geophys. Res., 97*, 15,923-15,948, 1922

Pronin, A. A., and E. R. Stofan, Coronae on Venus: Morphology and distribution, *Icarus, 87*, 452-474, 1990

Ribe, N. M., On the interpretation of frequench response functions for oceanic gravity and bathymetry, *Geophys. J. R. Astron. Soc., 70*, 273-294, 1982.

Sandwell, D. T., and G. Schubert, Flexural ridges, trenches and outer rises around Venus coronae, *J. Geophys. Res., 97*, 16069-16083, 1992a.

Sandwell, D. T., and G. Schubert, Evidence for retrograde lithospheric subduction on Venus, Science, 257, 766-770, 1992b.

Sandwell, D. T. and G. Schubert, A global survey of possible sites of subduction on Venus, *EOS, Trans. A.G.U., 74*, #43, 376, 1993

Saunders, R. S., A. J. Spear, P. C. Allin, R. S. Austin, A. L. Berman, R. C. Chandlee, J. Clark, A. V. deCharon, E. M. DeJong, D. G. Griffith, J. M. Gunn, S. Hensley, W. T. K. Johnson, C. E. Kirby, K. S. Leung, D. T. Lyons, G. A. Michaels, J. Miller, R. B. Morris, A. D. Morrison, R. G. Piereson, J. F. Scott, S. J. Shaffer, J. P. Slonski, E. R. Stofan, T. W. Thompson, and S. D. Wall, Magellan Mission Summary, *J. Geophys. Res., 97*, 13067-13090, 1992.

Schaber, G.G., R.G. Strom, H.J. Moore, L.A. Soderblom, R.L. Kirk, D.J. Chadwick, D.D. Dawson, L.R. Gaddis, J.M. Boyce and J. Russell, Geology and distribution of impact craters on Venus: What are they telling us?, *J. Geophys. Res., 97*, 13,257-13,301, 1992

Smrekar, S. E. and S.C. Solomon, Gravitational spreading of high terrain in Ishtar Terra, Venus, *J. Geophys. Res., 97*, 16,121-16,148, 1992

Solomon, S. C., and J. W. Head, Mechanisms for lithospheric heat transport on Venus: Implications for tectonic style and volcanism, *J. Geophys. Res., 87*, 9,236-9,246, 1982.

Solomon, S. C., and J. W. Head, Lithospheric flexure beneath the Freyja Montes foredeep, Venus: constraints on lithospheric thermal gradient and heat flow, *Geophys. Res. Lett., 17*, 1,393-1,396, 1990.

Solomon, S.C. and J.W. Head, Fundamental issues in the geology and geophysics of Venus, *Science, 252*, 252-260, 1991

Solomon, S.C., The geophysics of Venus, *Physics Today, 46*, 48-55, 1993

Squyres, S. W., D. M. Janes, G. Baer, D. L. Bindschadler, G. Schubert, V. L. Sharpton, and E. R. Stofan, The morphology and evolution of coronae and novae on Venus, *J. Geophys. Res., 97*, 13,611-13,634, 1992.

Stein, S., Introduction to seismology, earthquakes, and earth structure, *in press*

Stofan, E. R., D. L. Bindschadler, J. W. Head, and E. M. Parmentier, Corona Structures on Venus: Models of Origin, *J. Geophys. Res., 96,* 20,933-20,946, 1991

Stofan, E. R., G. Sharpton, G. Schubert, G. Baer, D. L. Bindschadler, D. M. Janes, and S. W. Squyres, Global distribution and characteristics of coronae and related features on Venus: Implications for origin and relation to mantle processes,*J. Geophys. Res., 97*, 13,347-13,378, 1992.

Turcotte, D. L., Flexure, *Advances in Geophysics, 21*, 51-86, 1979.

Turcotte, D.L., A heat pipe mechanism for volcanism and tectonics on Venus, *J. Geophys. Res., 94*, 2779-2785, 1989

Turcotte, D.L., Episodic plate tectonics on Venus, *Eos, Fall Suppl., 73*, 332, 1992

Watts, A. B., J. K. Weissel, R. A. Duncan, and R. L. Larson, Origin of the Louisville Ridge and its relationship to the Eltanin fracture zone system, *J. Geophys. Res., 93*, 3051-3077, 1988.

Wessel, P., Thermal stresses and the bimodal distribution of elastic thickness estimates of the oceanic lithosphere, *J. Geophys. Res., 10*, 14,177-14,193, 1992

CHAPTER 6

RESOLUTION ANALYSIS OF MAGELLAN CYCLE 5 GRAVITY DATA

INTRODUCTION

The previous two chapters have been concerned with inferences of the thickness of surface layers which deform due to topographic or thermal loads. These inferences have been made on the basis of wavelengths and characteristics of deformation observed in the Magellan synthetic aperture radar images (chapter 3), and on the basis of topography (chapter 4). On Earth we use observations of both gravity and topography to constrain the thickness of crustal and lithospheric layers. Cycles 4 and 5 of the Magellan mission have been devoted to the collection of gravity data by Doppler tracking of the spacecraft from Deep Space Network stations on Earth. Cycle 4 gravity data is of limited use as it was collected while Magellan was still in an extremely elliptical orbit; however between cycles 4 and 5, the orbit geometry was modified and the cycle 5 data comes from a nearly circular orbit. The gravity data is obtained from two-way X-band (3 cm radar) Doppler tracking of the spacecraft at Deep Space Network stations (Goldstone, California; Madrid, Spain; Canberra, Australia), with a sampling interval of 2 seconds. The data are processed and inverted to obtain spherical harmonic gravity models for Venus. Current gravity models include spherical harmonic coefficients out to degree and order 40 or 60. For Venus degree 40 corresponds to a wavelength of approximately 1000 km and degree 60 corresponds to a wavelength of approximately 630 km. Doppler residuals relative to a degree and order 40 model (MGN40E - see later) are available. These residuals are typically used in regional (as opposed to global) inversions to obtain surface gravity maps.

Many geophysical investigations of Venus are concerned, at least in part, with establishing an understanding of the mechanism by which topography is supported. Distinguishing between mechanisms in which the topography is supported solely by the strength of the lithosphere and those in which support is dynamic, require high resolution gravity measurements. In particular, features interpreted as flexure of the lithosphere (chapter 4) could be locally compensated, or they may be the result of dynamic support of a viscous lithosphere. Gravity data of sufficiently high resolution may confirm the proposed uncompensated nature of flexural features discussed in chapter 4. This chapter is a study of the maximum resolution available from the early cycle 5 gravity data, using the residuals to spherical harmonic model MGN40E. This work is still in progress as gravity data continues to be collected using the Magellan spacecraft.

MAGELLAN GRAVITY DATA

Cycle 4 and Cycle 5 Data

The first Magellan gravity data was acquired on September 14th, 1992, during cycle 4 of the Magellan mission. At this time the spacecraft was still in a highly elliptical orbit, with a periapsis altitude of 180 km (at about 10° N) and an apopasis altitude of approximately 8000 km. The precision of the Doppler tracking measurements is as good as 0.1 mms^{-1} for one minute compression intervals [*Nerem et al.*, 1993]. The noise level in a typical uncompressed orbit arc is 0.2 – 1 mms^{-1} [*Sjogren and Phillips*, 1994]. The spatial resolution of the gravity data varies primarily with spacecraft altitude, and as we shall show later is usually 2.5 – 3 times the spacecraft altitude. As a result, in cycle 4 the elliptical orbit geometry resulted in useful gravity measurements being confined to ± 40° latitude of periapsis.

During summer 1993, an experiment was conducted to make the spacecraft orbit as circular as possible. Periapsis altitude was lowered to 150 km, so that the spacecraft velocity was reduced due to atmospheric drag. This in turn caused the apoapsis altitude to be reduced. The aerobraking manouevre was successfully completed at the beginning of August 1993, at which time periapsis altitude was raised out of the venusian atmosphere, to about 180 km. The final orbit geometry is considerably more circular than previously, with an apoapsis altitude between 500 and 600 km. The spacecraft began collecting cycle 5 data on August 6th, 1993 and this cycle is now complete. For gravity data to be obtained the high gain antenna on Magellan must be visible from Earth. Often, part of the spacecraft orbit is not visible from Earth as it is hidden behind Venus. Because of the strong dependence of horizontal resolution of the gravity data on spacecraft altitude, we are most interested in the data collected close to periapsis. During cycle 5 periapsis was occulted until November 1st, 1993 when it was at a venusian longitude of 220° E. Near-periapsis data was obtained until April 1st, 1994, at which time periapsis was again occulted at a venusian longitude of 90° E.

Data Reduction

The Doppler data collected by Magellan (MGN) are processed at the Jet Propulsion Laboratory (JPL), Pasadena, using an orbit determination program [*Moyer*, 1971]. The program calculates spacecraft acceleration, velocity and position due to gravitational forces of Venus (spherical harmonic model) as well as time and space dependent drag forces due to atmospheric density. Construction of a smooth gravity field requires the use of an a priori constraint on the spherical harmonic coefficients. Traditionally, terrestrial gravity models have used a constraint proposed by *Kaula* [1966], in which the spherical harmonic

coefficients are assigned a variance which depends upon spherical harmonic degree. This type of constraint has also been applied to models for the venusian gravity field based on Pioneer Venus data (PVO) alone, MGN data alone and combinations of PVO and MGN data [*Ananda et al.*, 1980; *Konopliv et al.*, 1993; *Nerem et al.*, 1993; *McNamee et al.*, 1993; *Konopliv and Sjogren*, 1994].

One of the spherical harmonic models constructed using this technique is MGN40E, which is a degree and order 40 model, based solely on MGN data. The modified *Kaula* rule used in this model assigns an a priori uncertainty of $1.25/l^2$ to each spherical harmonic coefficient of degree l. For Venus, degree 40 corresponds to a spatial wavelength of approximately 950 km.

The most recent spherical harmonic gravity model (degree 60) incorporates MGN data collected prior to January 5th, 1994 and also PVO data. *Kaula's* rule was used in the generation of this model, but indirectly. First unconstrained (least squares) and constrained (penalized) models of the combined data set were constructed. The unconstrained inversion was used to generate a covariance matrix for the gravity field at the surface of Venus. A new hybrid data set was then made comprising original gravity measurements (PVO and MGN) in regions where the uncertainty in the unconstrained solution was less than 40 milligals, and synthetic gravity measurements in poorly constrained regions. The synthetic measurements were generated at 2° intervals from the constrained inversion, and assigned an uncertainty of 20 milligals. This hybrid data set was then inverted without an a priori constraint to yield the final model. This model is referred to as MGNP60FSAAP (**MaGellaN** and **P**ioneer data combined, degree and order **60**, series **F**, **S**urface **A**ccelerations **A P**riori).

Many geophysical investigations using the Magellan data require the availability of high resolution gravity data on a regional, rather than a global scale. For regions around periapsis, it is possible that there are resolvable features in the gravity data with a wavelength shorter than the 630 km available from MGNP60FSAAP. For a given spherical harmonic model, the Doppler residuals relative to this model can be calculated and any higher (spatial) frequency structure in the data investigated. Calculation of any spherical harmonic model and the corresponding residuals is computationally intensive. As a result only residuals relative to one spherical harmonic model, MGN40E, are available. These residuals are recorded on an orbit by orbit basis at JPL.

The work presented in this chapter is an attempt to establish the shortest resolvable wavelengths in the raw Magellan Doppler data. From now on, the term "raw" will refer to the Doppler residuals relative to MGN40E. These are line-of-site (LOS) data – *i.e.*,they measure the component of the residual

gravitational acceleration (relative to MGN40E) along the spacecraft-Earth vector. The term "viewing geometry" describes how the line-of-site vector deviates from the local vertical (the vertical to the venusian surface at the point directly below the spacecraft). A poor viewing geometry is one in which the line-of-site vector is at a high angle to the local normal, and a good viewing geometry is one in which the line-of-site vector is close to the local vertical direction. The Doppler residuals available from JPL are residuals in Hz along the LOS vector. At JPL spline fits to these "raw" data are produced; the splines are then differentiated to provide LOS accelerations. These smooth acceleration profiles have traditionally be used in regional inversion programs [*Phillips et al.*, 1978; *Grimm*, 1991] to obtain higher resolution gravity fields than available from the spherical harmonic models [*e.g., Herrick et al.*, 1989; *Grimm and Phillips*, 1992; *Smrekar*, 1994; *Phillips*, 1994]. A secondary purpose of this study is to compare the resolution available from the raw, pre-splined Doppler residuals with the resolution available from the splined data. Data within a 25° latitude band of periapsis has been analyzed, covering the venusian longitude band 220° E – 310° E; the results from two regions in this longitude band will be presented here. It is intended that this study will be extended to include all of the cycle 5 data.

METHOD

The maximum resolution of the gravity data can be investigated via a quantity known as the spectral coherence [*Bendat and Piersol*, 1986]. For two time series x(t) and y(t), the spectral coherence is given by the ratio of the cross spectrum of x(t) and y(t) to the product of the amplitude spectra of x(t) and y(t). For our purposes, the spectral coherence describes the consistency of a signal of a particular wavelength from one orbit to another, and is essentially the frequency domain equivalent of a correlation coefficient. Our time series x(t) and y(t) are nearby gravity tracks, where t=0 corresponds to the latitude which is 25° north of periapsis on each track. (This ensures that the spacecraft altitude variation along each track is the same.) Spectral coherence is a normalized quantity: a value of 1 indicates perfectly coherent signals at a given frequency, and a value of zero indicates completely incoherent signals. To compute the spectral coherence of the gravity data we need to estimate the cross spectrum and the power spectrum along parallel orbits that are nearly colinear (*i.e.*,they should measure the same gravity field). Unfortunately, we usually do not have complete gravity coverage of a given area – there are often orbits for which no data is available. In addition to this, the sampling interval for the X-band gravity data is 2 seconds, and so each orbit track covering a latitude band of ± 25° about periapsis contains only about 35 – 400 estimates of the gravity field. The analyses presented here are confined to a latitude band of ± 25° about periapsis, since the spacecraft altitude in this region is almost constant at 185 km – 200 km. Using longer orbit arcs introduces

a much greater variation in spacecraft altitude, which is undesirable as this has a significant effect on the spatial resolution of the gravity data. For spectral analysis purposes 300 points define a very short time series. This means that an estimate of the power spectrum computed using a traditional fourier transform approach will have large associated uncertainties. The problem can be alleviated in regions where there are many adjacent orbits by computing the cross spectra between pairs of adjacent orbits and averaging, thus reducing the variance of the spectral estimate. However, in many regions we have only a few tracks and so a different approach is required.

A very powerful tool exists for estimating the power spectrum of short time series (in our case part of one orbit), known as multi-taper spectral estimation. The mathematical basis for this approach is described in full elsewhere (see *Thomson*, [1982]) and is not repeated here. The basic difference between this method and a conventional spectral analysis approach is that in the conventional approach a time series is multiplied by a taper (e.g. a cosine taper) before the fourier transform is computed. This tapering of the series removes edge effects, but results in the loss of some data at the ends of the series. For a short time series this loss of data is extremely detrimental. The multi-taper approach avoids this problem by tapering the time series not once, but several times using a set of orthogonal tapers. Each taper samples the series differently, and the fourier transform is calculated for each tapered version of the original time series. These spectra are averaged, and the bias and variance of the resulting spectrum are extremely small, making this a powerful method for the spectral analysis of short series.

For the Magellan gravity data, the computation of power spectra and spectral coherence using the multi-taper approach has two advantages. First, because we can compute the spectral coherence on an orbit to orbit basis, the resolution of the data can be investigated in regions where we have only a few profiles. Second, we can not only compute the coherence between adjacent tracks but we can examine how the coherence of the along-track signals varies as the cross-track distance between orbit pairs increases.

RESULTS

Magellan altimetry over the region investigated in this study is shown in figure 1. The superimposed contours are the gravity field at the surface of Venus as predicted by spherical harmonic model MGN40E, and the locations of periapsis are marked. A high correlation of long-wavelength gravity with topography is evident, as previously noticed in the much poorer quality PVO data [*Phillips and Lambeck*, 1980]. This study is concerned with the minimum resolvable wavelengths in the residual gravity signal relative to the MGN40E spherical harmonic model. As described in the previous section, the resolution of the

data is investigated via the spectral coherence. Results from two regions are presented, with the objective of demonstrating (a) the advantage of the multi-taper approach to power spectral estimation, (b) that the minimum resolvable wavelengths in the Doppler residuals are in the range 450 – 500 km, and (c) that significant resolution is lost in the production of LOS accelerations from spline fits to the raw residuals.

The first region investigated here is shown in figure 2. Doppler residuals from seven orbits were analyzed, and the westerly and easterly limits of these orbits are marked by the two tracks on figure 2. Figure 3 shows the raw Doppler residuals to spherical harmonic model MGN40E for these seven orbits, along with the spline fits provided by JPL. As several adjacent orbits were available in this region, the single taper and multi-taper approaches to coherence estimation were compared. If the spectral coherence estimated from two time series is high at a given frequency, then signals at this frequency are well correlated. Recall that spectral coherence is a normalized quantity; traditionally in coherence studies an ad hoc value of 0.5 is taken as the critical value, below which signals are regarded as incoherent. We adopt this value of 0.5, noting that our results are insensitive to the choice of cut-off in the range 0.4 - 0.6. The power and phase spectra were always examined along with the spectral coherence, in order to check that the wavelength band in which the coherence is greater than 0.5 corresponds to real signal, and that the phase varies smoothly and is close to zero out to the critical, cut-off wavelength. An example of this is shown in figure 4 for a multi-taper estimate of the power, phase and coherence spectra for the data from two orbits in figure 3. The cut-off wavelength selected on the basis of coherence is 665 km. The power spectra indicate that there is real signal in the data out to this wavelength, whilst the phase spectrum indicates that these coherent signals are also in phase.

A comparison of the coherence estimated using the single-taper and multi-taper approaches is given in figure 5. Coherence is estimated for the single taper approach as follows. Gaps in each of the 7 orbit tracks were filled by linear interpolation, and the time series padded to a length 2^M. The first 6 orbits were stacked end-to-end to produce a new time series, X_1 and the second 6 orbits were stacked similarly to produce a second time series X_2. A single-taper cross-spectral analysis of X_1 and X_2 was performed, with section averaging. Section averaging resulted in the new time series X_1 and X_2 being split into the original 6 series again and each series was tapered and the FFT taken. The 6 estimates of the power spectrum for each series X_1 and X_2 were averaged to obtain final power spectra. The phase and coherence were computed similarly. The section averaging reduces the variance in the power spectral estimates.

To obtain a multi-taper estimate of coherence, two of the original orbits were selected, and gaps filled

by linear interpolation. Next, each of the two orbits was multiplied by a set of orthogonal tapers, and the discrete fourier transform of each tapered series computed. This resulted in several spectral estimates for each orbit, which were combined to produce one single smooth spectrum per orbit. An analogous approach was used to compute the cross-spectrum, and so a multi-taper estimate of the phase and coherence could be made. The bottom plot in figure 5 shows the coherence estimated for the six pairs of adjacent tracks using a single-taper approach. Note that this is an average coherence across the region spanned by the tracks. The upper 6 plots show the coherence computed using a multi-taper approach. The coherence is calculated for pairs of orbits at increasing cross-track distance. Figure 5 shows that first, the single-taper approach results in a conservative estimate of the minimum resolvable wavelength, as compared with the multi-taper approach. The comparison shown in figure 5 is not exact because the single taper estimate of coherence should really be compared with all the multi-taper coherence estimates computed for pairs of adjacent tracks. However, the multi-taper estimate of coherence for a cross track distance of 20 km shown in figure 5 is in fact representative of the multi-taper coherence computed for all the pairs of adjacent tracks. Second, the minimum resolvable wavelength indicated by the multi-taper approach is 665 km and is consistent over cross-track distances of 20 – 100 km. The lower coherence at long wavelengths for some pairs of orbits is due in part to small static shifts between adjacent orbits and to the fact that the residuals are relative to a degree and order 40 spherical harmonic model. (Degree 40 corresponds to a wavelength of about 1000 km.) The minimum resolvable wavelength is over 3 times the spacecraft altitude - however, this region was specifically chosen as an example of an area in which there are no large amplitude, short-wavelength gravity or topography signals.

The second area analyzed is shown in figure 6. The data coverage over this region is less extensive than that over region 1, and the profiles examined occur in one group of three to the west and one group of four to the east. Two topographic chasms are seen in the altimetry data: these lie to the west of a highland region known as Beta Regio, and they exhibit characteristics typical of terrestrial rift zones. Based on the topography, this area is a good candidate for the presence of short wavelength gravity anomalies. The raw LOS residuals and spline fits for the seven profiles are shown in figure 7. The western (lower) three profiles are quite different from the eastern (upper) four. Both topographic chasms appear to have associated short-wavelength LOS gravity signals in the western three profiles; however only the southern chasm has an associated gravity anomaly in the eastern four profiles. Closer examination of the topography coincident with the LOS profiles does indeed show that the relief across the northern chasm decreases toward the east. Because there are few adjacent profiles in this region only the multi-taper approach was

used to compute spectral coherence. The results for the two groups of profiles are shown in figure 8. The minimum resolvable wavelength computed from the western three profiles is in the range 426 – 559 km; that computed from the eastern four profiles is more consistent and is in the range 445 – 462 km over cross track distances of up to 80 km. Thus in this area, where there are stronger short wavelength gravity signatures, the minimum resolvable wavelength is about 2.5 times the spacecraft altitude.

Figure 9 shows the transfer functions between the spline fits to the data and the raw data themsleves for each of the seven orbits. In this case the transfer function is the ratio of the power in the spline fits to the power in the raw data as a function of frequency. Ideally, if the splines provide a complete description of the data the transfer function should be equal to one for all wavelengths longer than the minimum resolvable wavelength in the data. The figure shows that power is lost in the spline fits relative to the data for wavelengths less than approximately 1000 km. Up to 40% of the power in the real signal is lost in the wavelength band 500 – 1000 km. Examination of the transfer function between the splines and the raw data in other areas within the region shown in figure 1 indicate that the results presented in figure 9 are typical of the data. Thus regional inversions of the LOS accelerations derived from spline fits to the data do not provide a good description of the short-wavelength gravity field.

The importance of obtaining an accurate representation of short-wavelength features in the gravity field is demonstrated in figure 10. One of the outstanding questions concerning the geophysics of Venus is the problem of support of topographic loads. This was discussed earlier in chapter 4 of the thesis. Prior to Magellan it was proposed that the high surface temperature on Venus would lead to the lithosphere being thin and weak; however studies of topographic flexural signatures on Venus [*Sandwell and Schubert*, 1992; *Johnson and Sandwell*, 1994a], and preliminary studies using the Magellan gravity data [*Solomon et al.*, 1994; *Smrekar*, 1994; *Phillips*, 1994] suggest that the lithosphere may be much thicker than previously believed. The venusian lithosphere may be stronger than terrestrial lithosphere as a result of the absence of water [*Oyama et al.*, 1980; *Fowler*, 1990]. Recent laboratory measurements on diabase suggest that dry crustal rocks are significantly stronger than their hydrated counterparts [*Mackwell et al.*, 1993]. (These measurements are currently been extended to dry olivine [*Mackwell*, personal communication].) If the venusian lithosphere is indeed thick and strong, then static support of topographic loads is possible. However, if the lithosphere is weak, then the topography must be supported either locally by crustal thickness variations and/or by dynamic and viscous stresses. Distinguishing between these mechanisms of support requires accurate gravity data at wavelengths of a few hundred to a couple of thousand kilometers. Figure 10 shows the transfer function, at a spacecraft altitude of 200 km, between gravity and topography

for flexure of an elastic lithosphere. The transfer function in this case is the ratio of the cross spectrum of the gravity and topography to the power spectrum of the topography and has an analytical solution [*Banks et al.*, 1977]. Figure 10 shows transfer function curves for different elastic thicknesses given a crustal thickness of 10 or 30 km. (The crustal thickness on Venus is not well constrained but some estimate of the range of thicknesses expected has been made on the basis of impact crater relaxation [*Grimm and Solomon*, 1988] and wavelengths of deformation [*Zuber and Parmentier*, 1990].) The noise level in the gravity data is less than 1 mgal, and the results presented in chapter 4 suggest that the typical amplitude of flexural topography is on the order of 400m. The results presented in this chapter suggest that the minimum resolvable wavelengths in the gravity data are in the range 450 – 500 km. Thus figure 10 suggests that flexure of an elastic lithosphere should, in theory, be detectable in the Magellan gravity data, particularly if the lithosphere is indeed thick.

CONCLUSIONS

Magellan cycle 5 LOS Doppler residuals in the region 220° E – 310° E and 5° S – 50° N have been examined to investigate the maximum resolution available from the gravity data. In regions where gravity data from several (more than 6) adjacent orbits were available, both single-taper and multi-taper estimates of spectral coherence were made. The two methods agreed well in these regions, although the minimum resolvable wavelength estimated by the single taper method was longer than that estimated by the multi-taper method. The multi-taper method allows the estimation of along-track coherence in regions where few orbits are available, and also enables the investigation of the variation of along-track coherence with cross-track distance. The best resolution obtained was 410 km. Typical resolution of the data is 450 – 500 km over cross track distances of up to 80 – 170 km. The poorer coherence of long-wavelength signals in some regions results in a band-limited signal (500 km – 1200 km wavelength) of high coherence in the LOS residuals. The best resolution of the spline fits to the raw data varies, and in many cases there was found to be an amplitude loss of up to 40% in the splines relative to the raw data in the wavelength band 450 – 1000 km. These results suggest that the use of the splined data in regional inversions can lead to gravity fields which do not adequately represent the short-wavelength signals in the data. Comparison of the maximum resolution of the gravity data with theoretical transfer functions between gravity and topography for an elastic lithosphere, suggest that in regions within a 25° latitude band of periapsis it should be possible to distinguish between static and dynamic support of topographic flexural features on Venus.

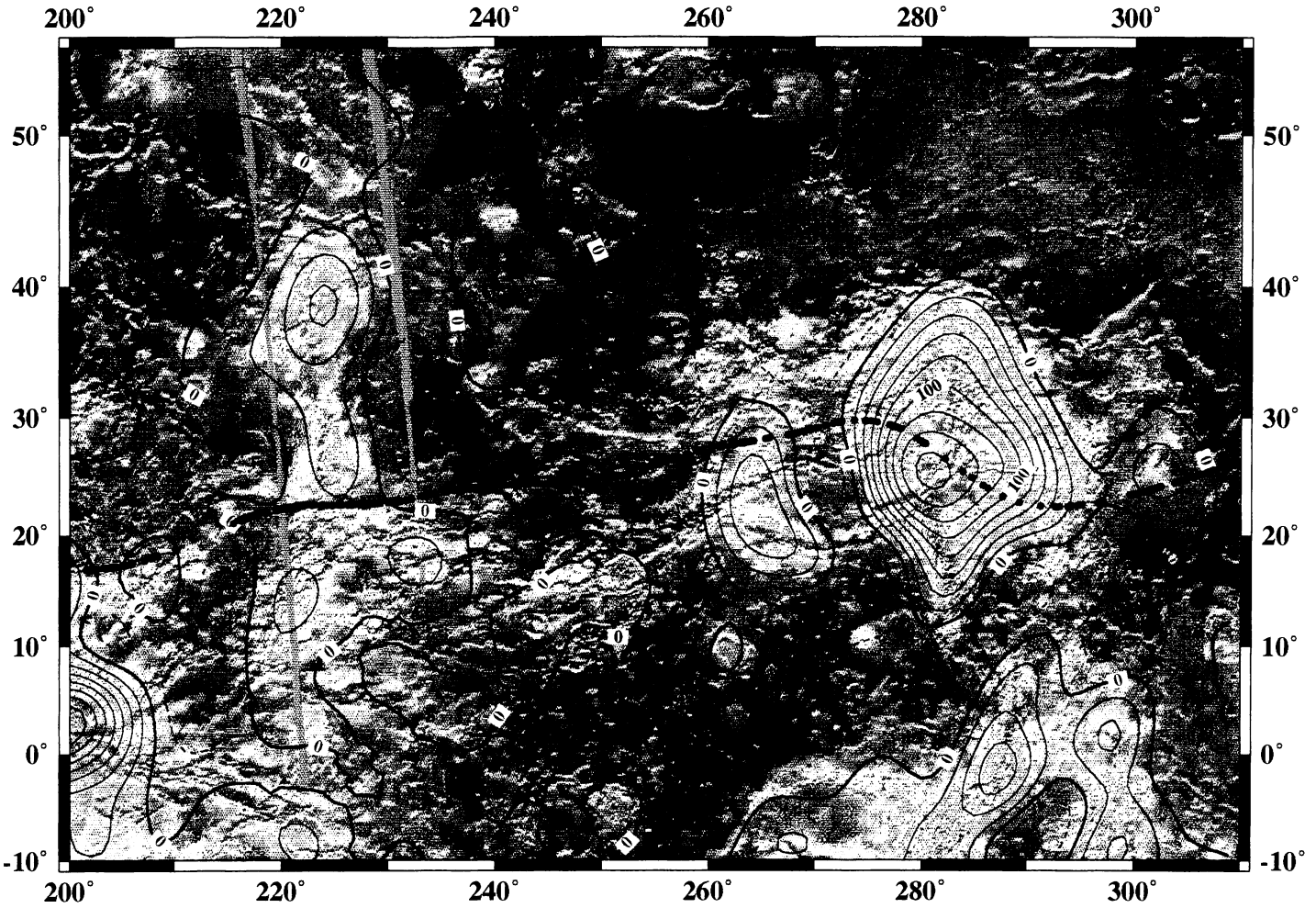

Figure 6.1: Magellan altimetry (color range spans 10 km altitude, from about 6048 km - 6058 km radius) with locations of cycle 5 periapsis marked (heavy circles). Contours are vertical gravity computed at the mean radius of Venus (6051.9 km) from the spherical harmonic model MGN40E. Dashed contours are negative, solid contours positive, contour interval is 20 mgal. Region is that covered by near-periapsis cycle 5 data from 9/93 - 1/94.

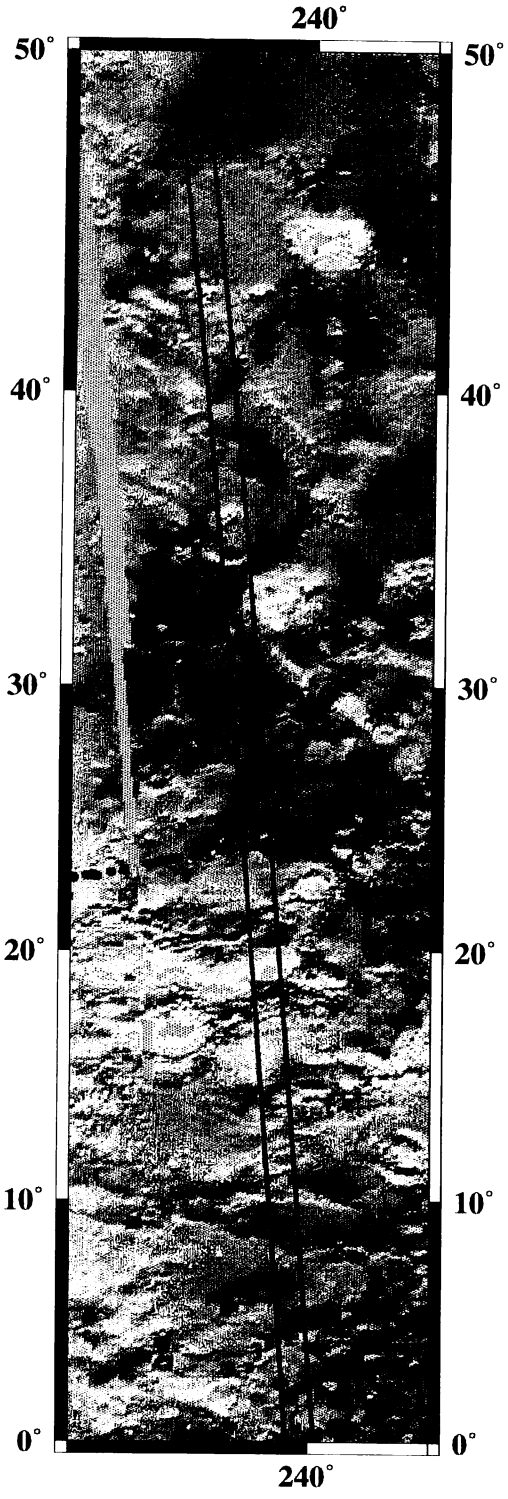

Figure 6.2: Magellan altimetry over the first region discussed. Color is altimetry as in figure 1. Periapsis locations are marked (solid circles). The two tracks are the locations of orbits 9906 and 9918 (figure 6.3)

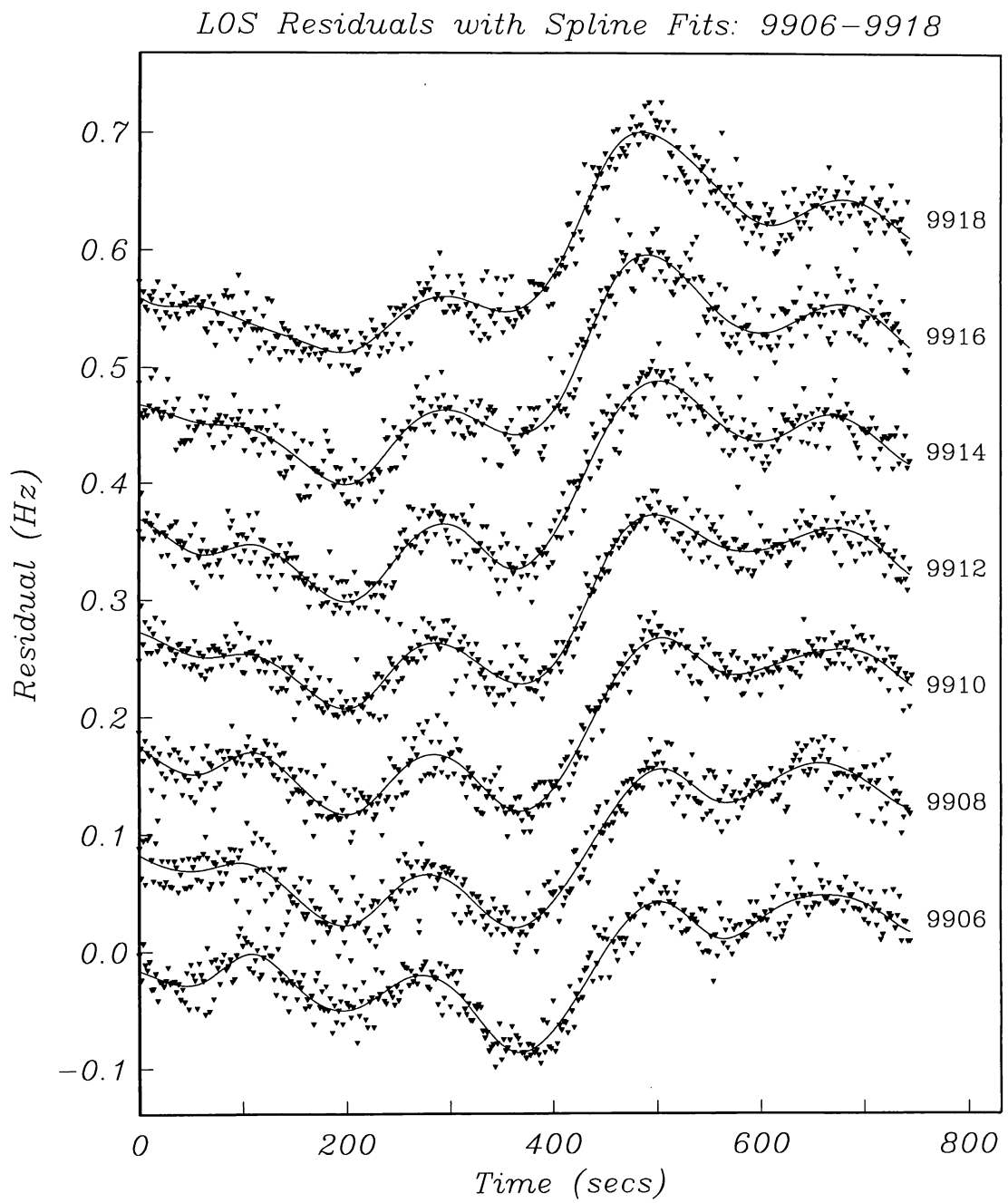

Figure 6.3: Raw Doppler residuals relative to MGN40E (triangles) and corresponding spline fits (solid lines) produced by JPL for orbits 9906 - 9918 (gravity data only available from every other orbit in this region). Data shown spans a 25° latitude band about periapsis. Successive orbits are offset vertically by 0.1 Hz. Sampling interval is 2 seconds.

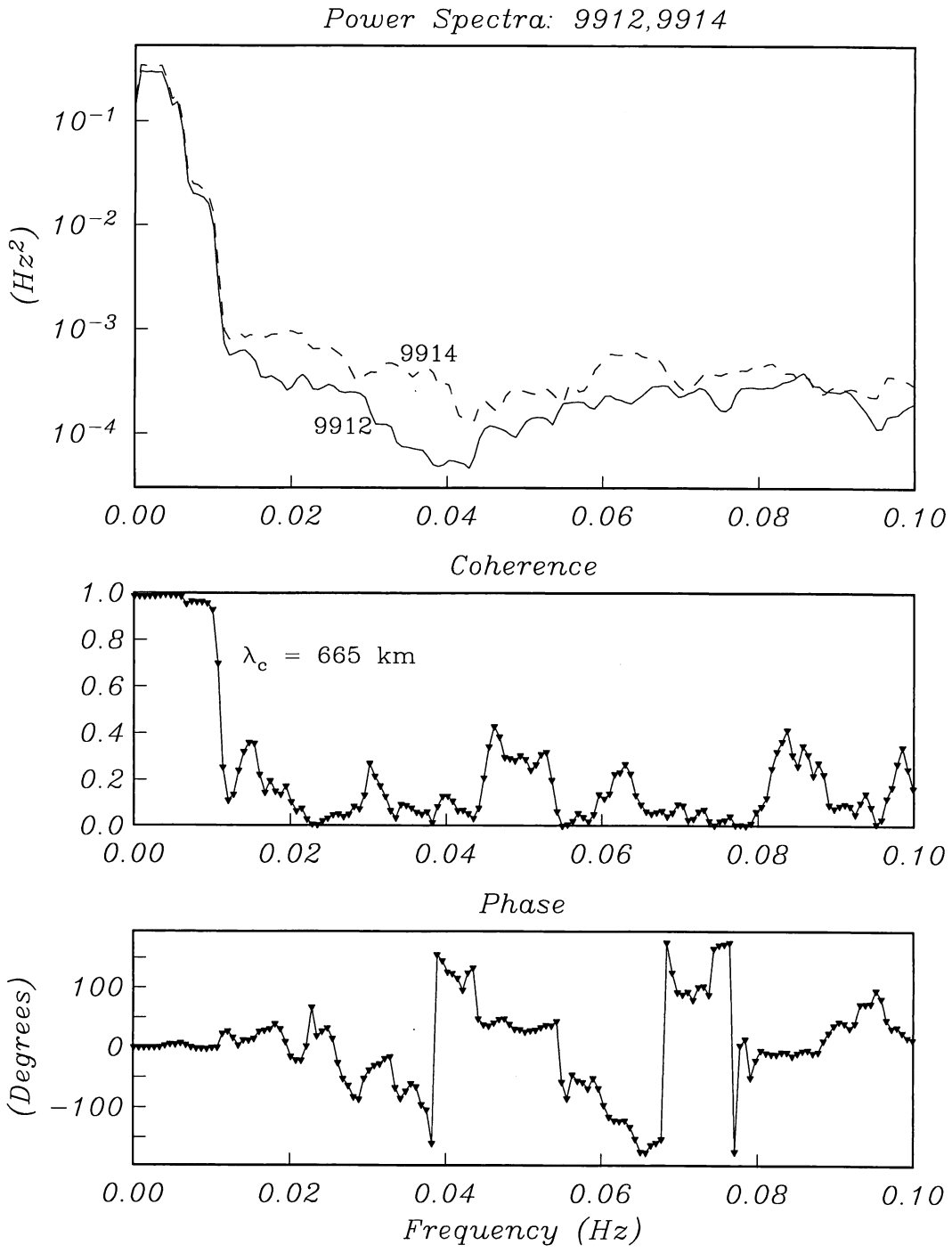

Figure 6.4: Power, coherence and phase spectra computed using the multi-taper approach for orbits 9912 and 9914. All four spectra are consistent with the conclusion that there are resolvable, coherent signals in the data out to a minimum wavelength of about 665 km. (Note: 1 second is equivalent to 7.1 km).

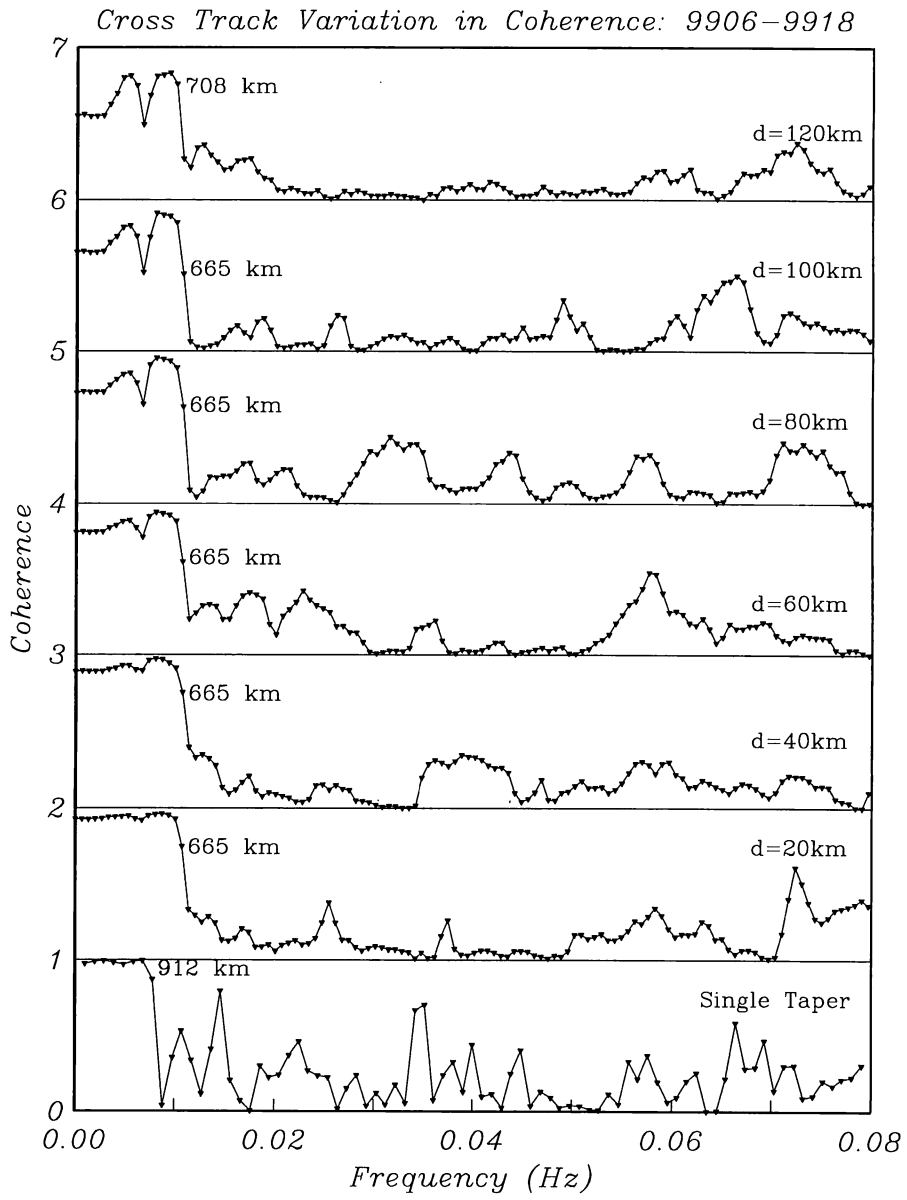

Figure 6.5: Comparison of the single-taper and multi-taper estimates of coherence, and also the variation of along-track coherence with cross-track distance. The lower figure shows the single taper estimate of coherence for all 7 orbits in figure 6.3. The minimum resolvable wavelength is 912 km. The upper figures show the (multi-taper) coherence estimated for two orbits at increasing cross-track distance. The coherence estimates are offset vertically by one unit. One orbit is always 9906, the second orbit varies from 9908 - 9918. d denotes the cross-track distance in kilometers. The cut-off wavelength estimated using the multi-taper method is consistently 665 km for cross-track distances up to 100 km.

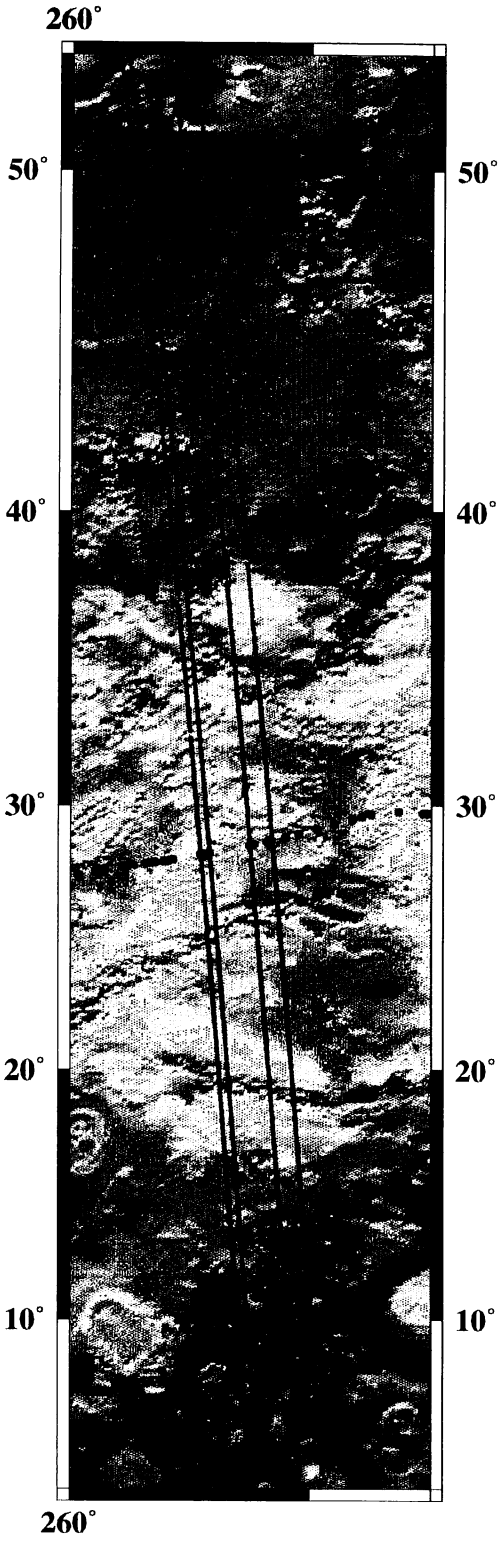

Figure 6.6: Magellan altimetry (as in figure 1) over the second region discussed. Periapsis locations marked (solid circles). Tracks are (from west to east) orbits 10204, 10208, 10226, 10236.

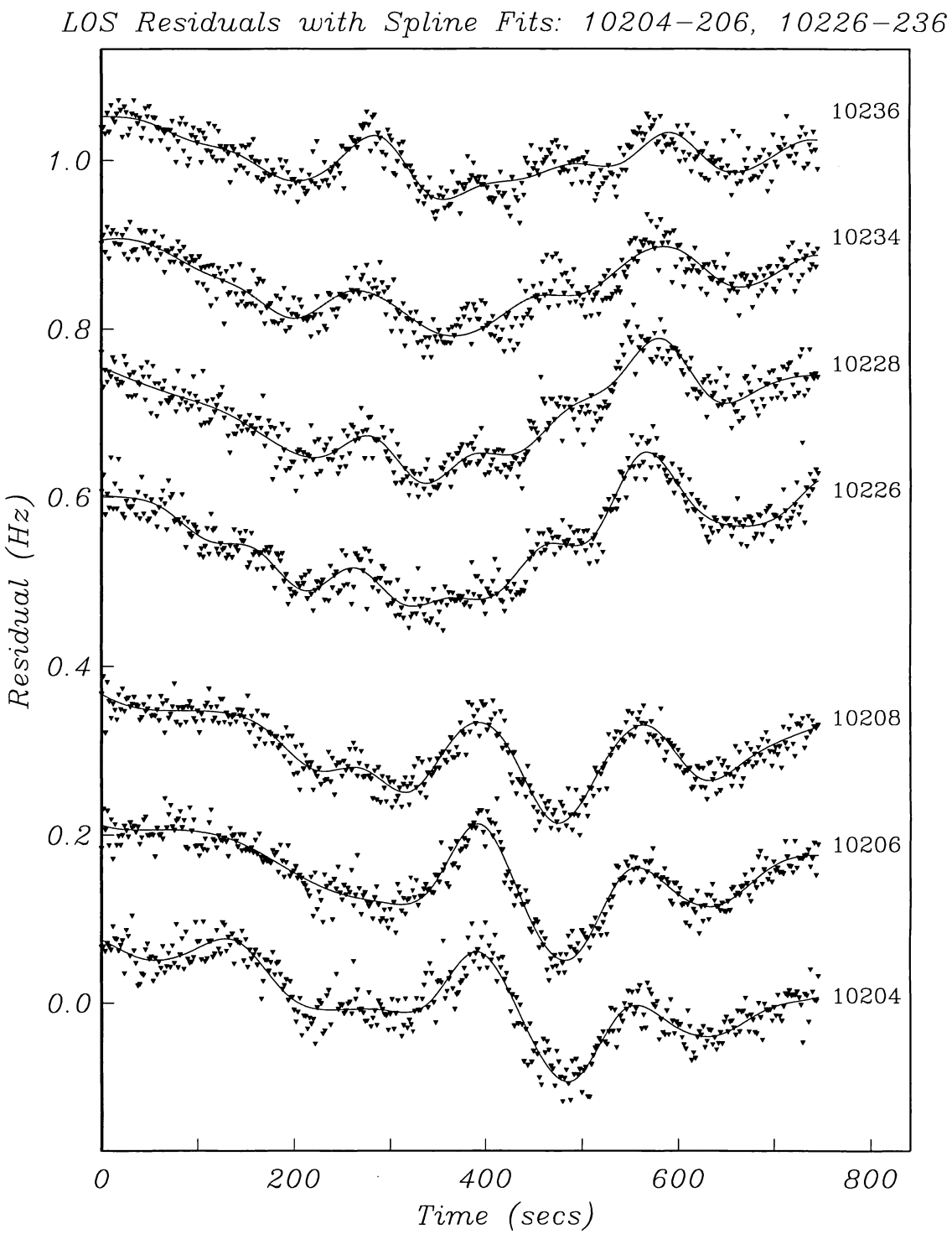

Figure 6.7: Raw Doppler residuals (triangles) relative to MGN40E, and the corresponding spline fits (solid lines) for the 7 orbits discussed. Successive orbits are offset vertically.

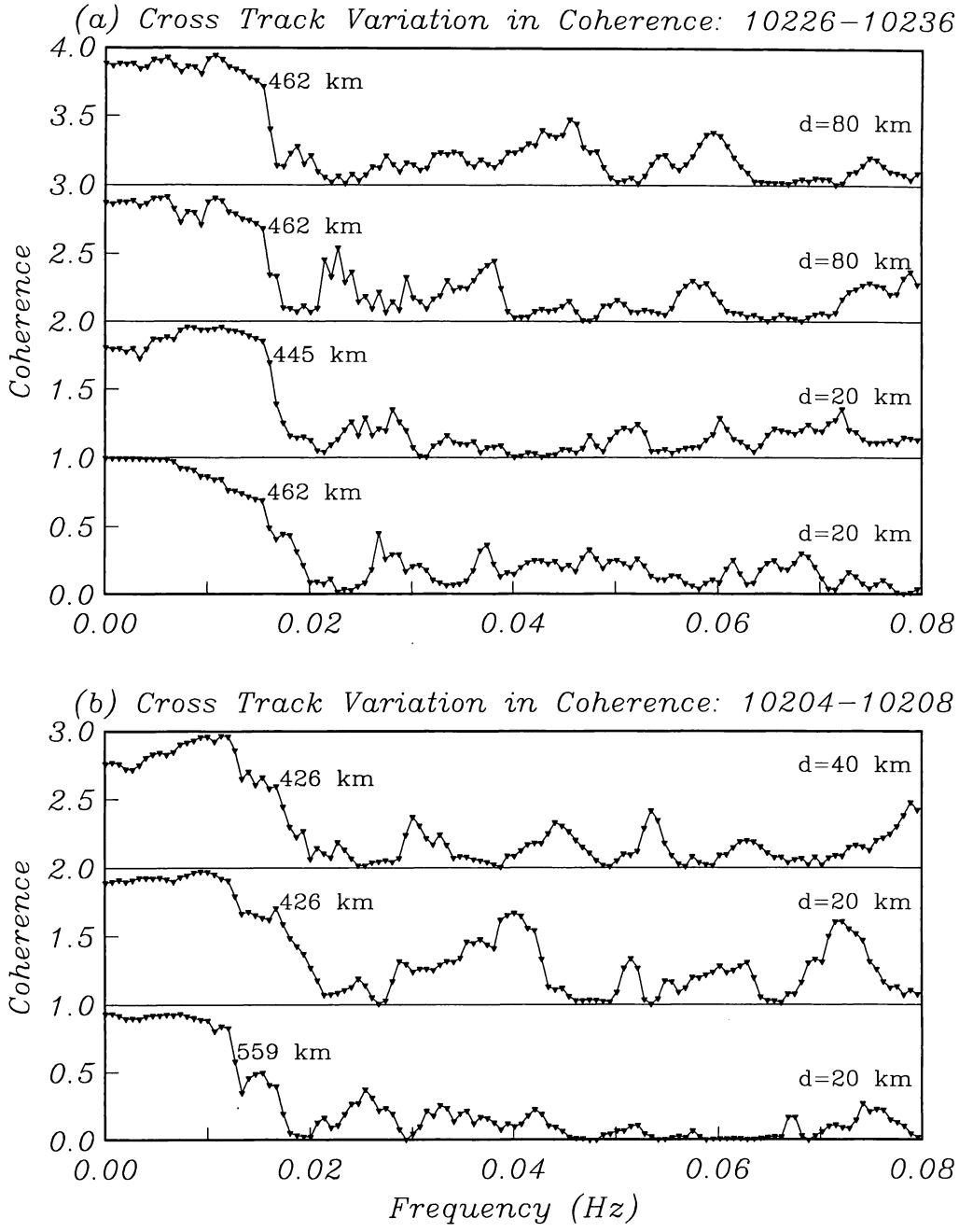

Figure 6.8: Coherence estimated between pairs of orbits using the multi-taper approach. The western three orbits and eastern four orbits are grouped separately. d is cross-track distance, and coherence estimates are offset vertically by one unit. For the western three orbits the minimum resolvable wavelength is in the range 426 - 559 km; for the eastern four orbits it is in the range 445 - 462 km.

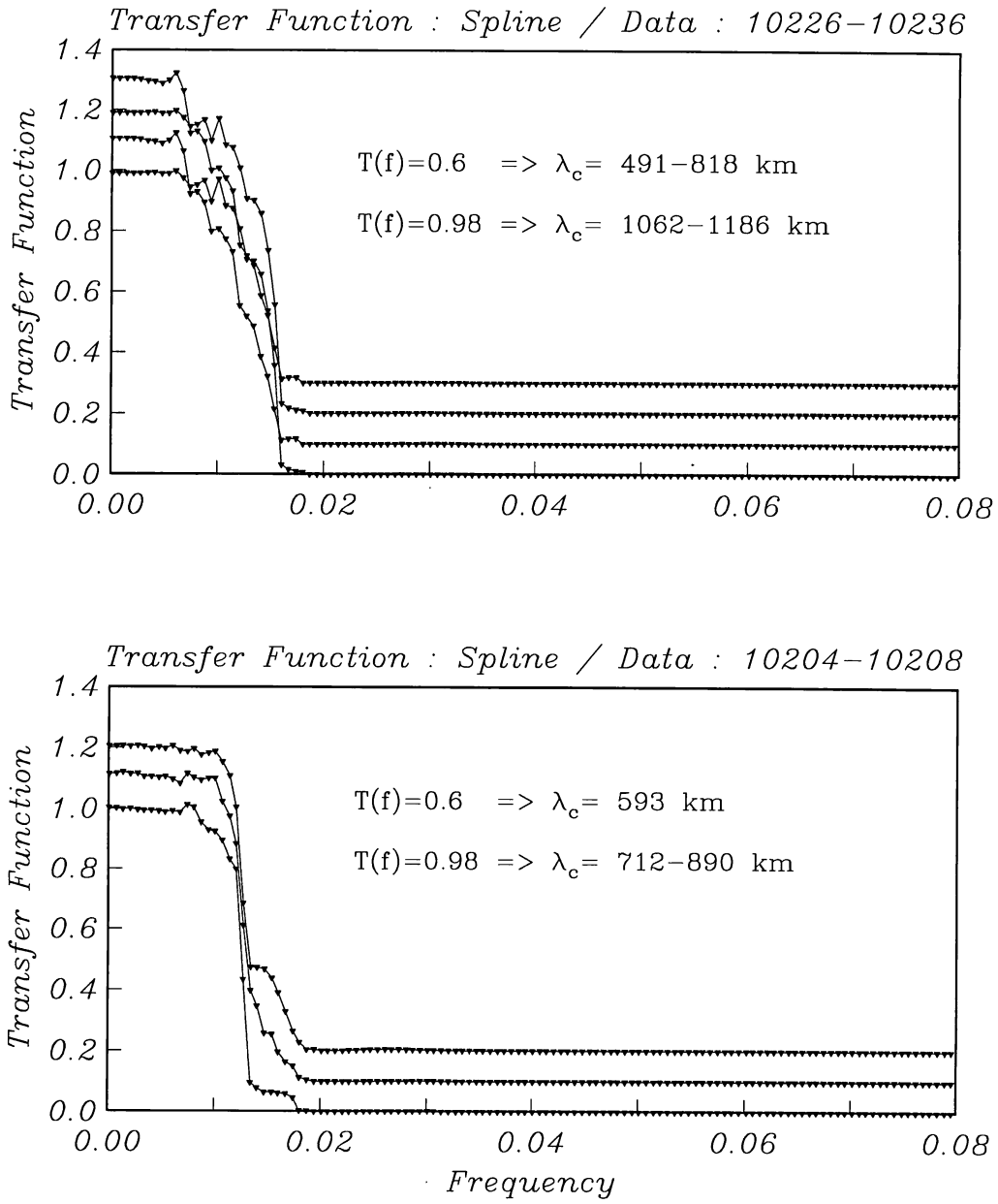

Figure 6.9: Transfer function between the spline fits and the raw data for the seven orbits in figure 6.3. The transfer function here is the ratio of the power in the spline to the power in the raw data. Notice that the transfer function has a value less than one at wavelengths which are still resolvable in the data.

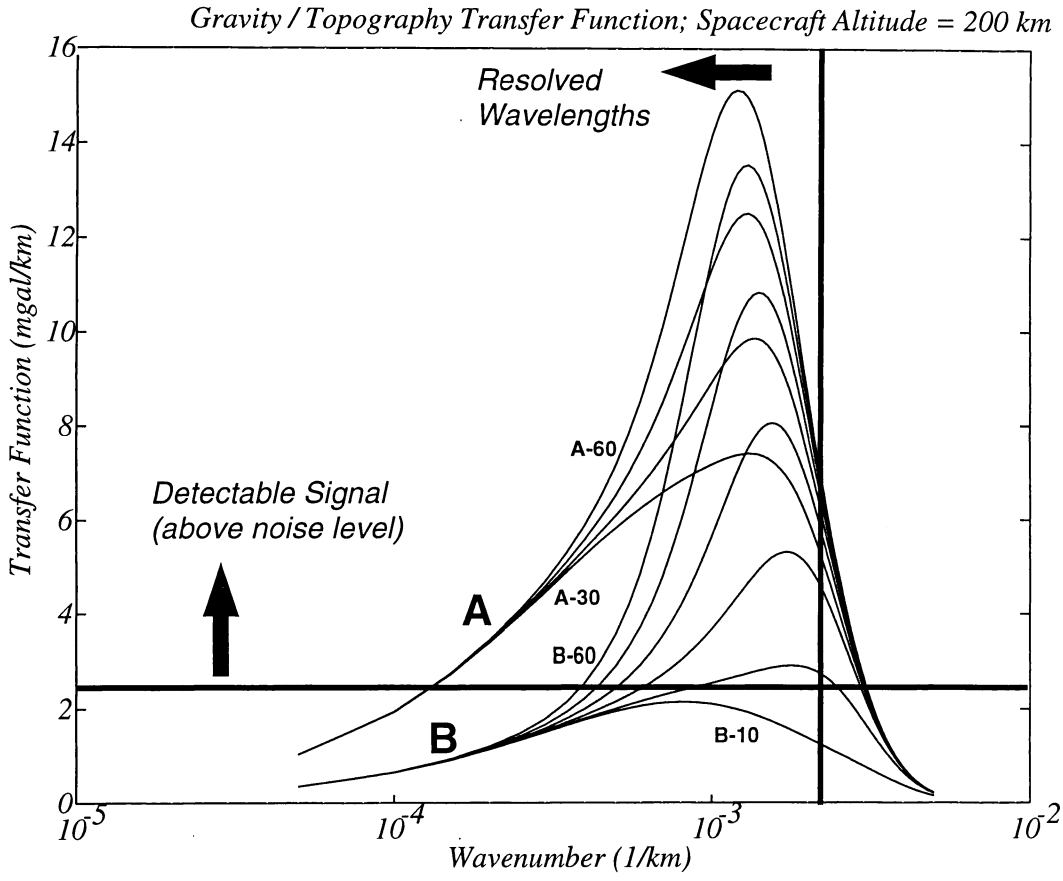

Figure 6.10: Gravity / topography transfer function for flexurally compensated topography for varying elastic plate thickness. Curves A are for an assumed crustal thickness of 30 km, and elastic plate thicknesses in the range 30 - 60 km (A-30, A-60); curves B are for an assumed crustal thickness of 10 km and elastic plate thicknesses 10 - 60 km (B-10, B-60). The vertical line marks the approximate boundary between resolvable and unresolvable wavelengths, based on preliminary spectral coherence studies. The horizontal line marks a conservative estimate of the minimum detectable amplitude of he transfer function, based on typical noise levels in the data.

REFERENCES

Ananda, M. P., W. L. Sjogren, R. J. Phillips, R. N. Wimberly & B. G. Bills, 1980. A low-order global gravity field of Venus and dynamical implications. *J. Geophys. Res.*, **85**, 8303–8318.

Banks, R. J., Parker, R. L., & J. P. Heustis, 1977. Isostatic compensation on a continental scale: Local versus regional mechanisms. *Geophys. J.R. astr. Soc.*, **51**, 431–452.

Bendat, J. S., & A. G. Piersol, 1986. *Random Data: Analysis and Measurement.* Wiley & Sons.

Fowler, C. M. R., 1990. *The Solid Earth. An introduction to global geophysics.* Cambridge University Press.

Grimm, R. E., 1991. Gravity Analysis and Simulation Package. *report, 13 pp., Southern Methodist Univ., Dallas, Tex.*

Grimm, R. E. & R. J. Phillips, 1992. Anatomy of a venusian hotspot: geology, gravity, and mantle dynamics of Eistla Regio. *J. Geophys. Res. Planets*, **97**, 16035–16054.

Grimm, R. E. & S. C. Solomon, 1988. Viscous relaxation of impact crater relief on Venus: Constraints on crustal thickness and thermal gradient. *J. Geophys. Res.*, **93**, 11911–11929.

Herrick, R. R., B. G. Bills & R. J. Phillips, 1989. Variations in effective compensation depth across Aphrodite Terra, Venus. *Geophys. Res. Lett.*, **16**, 543–546.

Johnson, C. L. & D. T. Sandwell, 1994a. Lithospheric Flexure on Venus. *Geophys. J. Int.*, in press.

Johnson, C. L. & D. T. Sandwell, 1994b. Resolution Analysis of Magellan Cycle 5 Gravity Data. *LPSC*, **XXV**, 625–626.

Kaula, W. M., 1966. *Theory of Satellite Geodesy.* Blaisdell Publishing Company, Waltham, Massacusetts.

Konopliv, A. S., N. J. Borderies, P. W. Chodas, E. J. Christensen, W. L. Sjogren & B. G. Williams, 1993. Venus gravity and topography: 60th degree and order model. *Geophys. Res. Lett.*, **20**, 2403–2406.

Konopliv, A. S. & W. L. Sjogren, 1994. Venus spherical harmonic gravity model to degree and order 60. submitted to *Icarus*.

Mackwell, S. J., D. L. Kohlstedt, D. S. Scherber, & M. E. Zimmerman, 1993. High temperature deformation

of diabase: Implications for Tectonics on Venus. *EOS, Trans. A.G.U.*, **74**, 378.

McNamee, J. B., N. J. Borderies & W. L. Sjogren, 1993. Venus: Global gravity and topography. *J. Geophys. Res. Planets*, **98**, 9113–9128.

Moyer, T. D., 1971. Mathematical formulation of the double-precision orbit determination program (DPODP). *Technical report 32-1527. Jet Propulsion Laboratory, California Institute of Technology, Pasadena, Ca.*

Nerem, R. S., B. G. Bills, J. B. McNamee, 1993. A high resolution gravity model for Venus: GVM-1. *Geophys. Res. Lett.*, **20**, 599–602.

Oyama, V.I., G.C. Carle, F. Woeller, J.B. Pollack, R.T. Reynolds & R.A. Craig, 1980. Pioneer Venus gas chromatography of the lower atmosphere of Venus. *J. Geophys. Res.*, **85**, 7891–7902.

Phillips, R. J., 1994. Estimating Lithospheric Properties at Atla Regio, Venus. submitted to *Icarus*.

Phillips, R. J. & K. Lambeck, 1980. Gravity fields of the terrestrial planets: long-wavelength anomalies and tectonics. *Rev. Geophys. Space Phys.*, **18**, 27–76.

Phillips, R. J., Sjogren, W. L., & E. A. Abbott, 1978. Simulation Gravity Modeling to Spacecraft-Tracking Data: Analysis and Application. *J. Geophys. Res.*, **83**, 5455–5464.

Sandwell, D. T., & G. Schubert, 1992. Flexural ridges, trenches and outer rises around Venus coronae. *J. Geophys. Res.*, **97**, 16069–16083.

Sjogren, W. L. & R. J. Phillips, 1994. The Magellan Gravity Experiment. submitted to *Icarus*.

Smrekar, S. E, 1994. Evidence for Active Hotspots on Venus from Analysis of Magellan Gravity Data. submitted to *Icarus*.

Solomon, S. C. McGovern, P. J., Simons, M. & J. W. Head, 1994. Gravity Anomalies over Volcanoes on Venus: Implications for Lithospheric Thickness and Volcano History. *LPSC*, **XXV**, 1317–1318.

Thomson, D. J., 1982. Spectrum Estimation and Harmonic Analysis. *Proc. IEEE*, **70**, 1055–1096.

Zuber, M. T. & E. M. Parmentier, 1990. On the relationship between isostatic elevation and the wavelengths of tectonic surface features on Venus. *Icarus*, **85**, 290–308.